UNIVERSITY OF SOUTHAMPTON

Investigation of the Potential for Sonar Detection in Bubbly Environments

James W L Clarke

Doctor of Philosophy

INSTITUTE OF SOUND AND VIBRATION RESEARCH

FLUID DYNAMICS AND ACOUSTICS GROUP

October 2004

Abstract

Most descriptions of the scatter and attenuation of acoustic waves in water by gas bubbles refer to the steady state bubble pulsation, in particular when the concept of the acoustic cross-section of the bubble is applied. However, it is becoming increasingly common for the bubble to be driven by pulses so short that the oscillation may not reach steady state (for example, short pulses are used to overcome reverberation and multipath complications and to obtain range resolution). Hence the option for describing the acoustic effect of the bubbles during the transient period needs to be considered. The specific applications considered in this theory are in the inversion of acoustic attenuation to measure bubble populations, and in exploring the possibility of enhancing sonar performance in bubbly waters.

Consider the concepts of a resonant bubble taking a finite time to reach steady state oscillation and the time-dependent cross-section of a bubble. The potential for using these characteristics for the enhancement of sonar detection in bubbly environments is discussed, and previous studies are reviewed. Previously Akulichev has observed an effect on bubble scatter when the duration of the driving pulse was varied. The theory presented by Akulichev to model this incorporated only the contribution of bubbles at resonance, which is a severe limitation. Attempts to find a pulse length dependence in test tanks in the United States and United Kingdom were subsequently unable to find any, and the attempt to extrapolate Akulichev's theory to incorporate off-resonance effects was flawed. Hence a major goal of this thesis is to explain these apparently conflicting observations and in so doing improve upon the theory.

In order to investigate the potential for sonar enhancement, a theory for the time-dependent cross-section of a bubble using a non-linear bubble model has been developed. The model has then been extended to allow the estimation of the acoustic cross-sections of a 1 m^3 cloud, neglecting propagation effects. A further cloud model, which takes into account propagation effects, has been developed to calculate the attenuation from a finite bubble cloud. The model has also been adapted to allow the input of experimentally measured waveforms.

A laboratory experiment to measure the attenuation is described, and the results (using both pulses and chirped signals) are compared with theory. The experiments

were conducted in an 8 m x 8 m x 5 m deep fresh water tank. The bubble cloud was generated by electrolysis. The attenuation from a series of pulse lengths and chirps, with a fixed bandwidth but variable duration, was measured. Good agreement between theory and experiment is shown but no sonar enhancement was achieved using the current experimental arrangement. Use of the model allowed confirmation that the type of bubble populations that are usually generated in test tanks would not be expected to show such enhancements, but that enhancements might be seen in population distributions found in the ocean environment. This is proposed and tested. It is also an explanation for the conflicting observations in the previous studies mentioned above.

A further series of trials were conducted at a beach on the south coast of the United Kingdom. An air filled buoy was mounted in the surf-zone and a Furgo-UDI Ltd. transmit/receive array was used to test a variety of waveforms. Short pulses were shown to improve target detection at some frequencies. However a combination of short pulses and optimisation of the transmit frequency gave the best results.

Although for decades the emphasis has been on the effects of resonant bubbles, this thesis uses these experimental results to underline the importance of the contribution made by bubbles close to (but not at) resonance when considering short pulse lengths. The response of these bubbles can easily mask the ring-up of resonant bubbles. Furthermore this critical near-resonant bubble response is not included in the simple linear models used in previous studies mentioned above, and is the cause of the discrepancy between the experimental and theoretical results of these previous studies.

Table of Contents

Acknowledgements

Firstly, I would like to thank my Supervisor, Prof Tim Leighton. I could not have imagined having a better advisor and mentor for my PhD, and without his knowledge, patience and perceptiveness I would never have finished. I would also like to thank Dr Gary Heald and Mr Hugh Dumbrell of DERA Bincleaves for scientific input and technical support whilst undertaking this research.

As is often the case with difficult experimental work one pair of hands is never enough. For their patience and understanding and support during long hours of testing and brain storming. I would like to thank Dr Rivan Evans and Dr Lee Culver for additional scientific assistance especially during difficult lab trials. I would also like to thank Mr Steven Meers, Mr Mathew Simpson, Mr Gun Tae Yim for their sense of humour and invaluable assistance during the sea trial. Finally the experimental phases of this work could not have been completed without the technical assistance of Mr A Edgley and Mr J Taylor.

The theoretical and computational modelling undertaken during this work would not have been possible without the teachings and support of Dr Paul White.

Finally, I have to say 'thank-you' to all my friends and family, wherever they are, and most importantly of all to my Mum and Dad; without their unwavering support and patience this thesis would not have been written.

James Clarke

4th October 2004

Symbols List

a	radius of a sphere
A	constant
A_1	constant
A_2	constant
α	acoustic attenuation in dB per unit length
α_{cloud}	acoustic attenuation of a bubble cloud in dB per unit length
α_{th}	the dimensionless multiplicative factor which corrects for the effects of heat flow in the stiffness and resonance frequency of a bubble.
B	constant
b	resistive dissipation constant
b_{VP}	resistive dissipation constant in the velocity-pressure frame
b_{RP}	resistive dissipation constant in the radius-pressure frame
b_{RF}	resistive dissipation constant in the radius-force frame
b_{VP}^{rad}	radiation dissipation constant in the velocity-pressure frame
b_{VP}^{vis}	viscous dissipation constant in the velocity-pressure frame
b_{VP}^{th}	thermal dissipation constant in the velocity-pressure frame
β	resistive constant leading to damping
β_{tot}	total resistive constant leading to damping
c	speed of sound
c_0	speed of sound in water
C_T	complex sound speed in bubbly water
γ	ratio of specific heat of a gas at constant pressure to that at constant volume

DI acoustic source directivity index

DT detection threshold of a target

d_{tot} total dimensionless damping constant

d_{rad} radiation dimensionless damping constant

d_{th} thermal dimensionless damping constant

d_{vis} viscous dimensionless damping constant

d' sonar equation detectability index

ΔIL change in intensity

δ_0 bubble the total dimensionless damping at resonance

δ_{tot} total dimensionless damping constant at resonance

δ_{rad} radiation dimensionless damping constant at resonance

δ_{th} thermal dimensionless damping constant at resonance

δ_{vis} viscous dimensionless damping constant at resonance

E acoustic energy

e exponential constant ≈ 2.718

ε displacement of an oscillatory system

$\dot{\varepsilon}$ velocity of an oscillatory system

$\ddot{\varepsilon}$ acceleration of an oscillatory system

F_0 amplitude of a general driving force of an oscillator

F Faraday's constant (constant $\approx 9.65 \times 10^4$ $Cmol^{-1}$)

Fs *s*cattering amplitude

f linear frequency

f_0 linear resonant frequency

f_1 starting frequency

f_2 ending frequency

f_a scattering amplitude

η shear viscosity

I plane wave intensity

I_{inc} incident plane wave intensity

i imaginary number ($i^2 = -1$)

K wavenumber (= $2\pi/\lambda$)

K_{eff} effective wavenumber of a bubbly medium

k stiffness

k_{RP} stiffness in the radius-pressure frame

k_{VP} stiffness in the velocity-pressure frame

κ polytropic index

L length

L_D width of thermal boundary layer

λ wavelength

M number of moles of gas

m mass

m_{RP} radiation mass in the radius-pressure frame

NL background acoustic noise level

n number of bubbles per m^3 per μm increment in radius

n_e number of electrons liberated to produce a gas molecule in electrolysis

P acoustic pressure

P_A acoustic pressure amplitude

P_{bl} acoustic pressure radiated by a bubble

P_i incident driving pressure amplitude

p_0 hydrostatic liquid pressure outside of the bubble

$p_{i,e}$ pressure within the bubble at equilibrium

p_∞ pressure in the liquid far from the bubble

p_B pressure immediately outside the bubble wall

ρ density (generally of the fluid surrounding a bubble)

Q the quality factor

Q_c electrical charge

σ surface tension of a liquid

R range from the transmit/receive array to centre of bubble cloud in the range dependent cloud model

R_x distance in x-plane of a bubble from the receive array in the range dependent cloud model

R_y distance in y-plane of a bubble from the receive array in the range dependent cloud model

R_z distance in z-plane of a bubble from the receive array in the range dependent cloud model

R_0 bubble equilibrium radius

R_ε displacement of bubble radius from equilibrium

$R_{\varepsilon 0}$ radial displacement amplitude of the wall of a spherical bubble

$\dot{R}$ velocity of the bubble wall

$\ddot{R}$ acceleration of the bubble wall

r range

r_o reference range

S cross-section of a bubble cloud

S_{ext} extinction cross-section of a bubble cloud

S_a surface area

S_n time dependent scattering cross-section defined by V A Akulichev

SL acoustic source level

t time

T sonar equation processing time

T_p period

T_{60} reverberation time

TL acoustic transmission loss

TS target strength

τ_0 characteristic relaxation time to steady state of an oscillator. The time taken for an oscillator to reach $\left(1-e^{-1}\right)$ or 63% of its maximum amplitude.

τ acoustic pulse duration

Φ energy loss

ϕ phase constant determined by initial conditions

V volume

x a distance

Ω_{scat} scattering cross-section of a bubble

Ω_{ext} extinction cross-section of a bubble

$\Omega_{Rayleigh}$ Rayleigh scattering cross-section

$\Omega_{Geometric}$ geometric scattering cross-section

Ω_r resonant cross-section

Ω_{nr} non resonant cross-section

ω angular frequency (= $2\pi f$)

ω_0 resonant angular frequency (= $2\pi f_0$)

ω_d angular frequency of a damped system

ω_M estimate of bubble angular resonance frequency calculated by Minnaert equation

W sonar equation system bandwidth

CHAPTER 1

INTRODUCTION

1 Introduction

Historically the application of active sonar for target detection has been limited in bubbly environments such as the surf-zone, or the subsurface ocean layer[1] when wind speeds exceed 7 m/s. This is a direct consequence of the excess attenuation from the oscillation of bubbles in a sound field, through scattering and absorption losses. These losses[2] can be as great[3] as 30 dB/m between 50 and 100 kHz, significantly reducing the operational range of sonar. If a means could be developed to reduce these losses, it may facilitate target detection and underwater communication in bubbly environments.

One possibility of enhancing sonar performance in bubbly waters is through the use of very short duration or broadband signals. However, most descriptions of the scatter and attenuation of acoustic waves in water by gas bubbles refer to the steady state bubble pulsation, in particular when the concept of the acoustic cross-section of the bubble is applied. When a bubble is driven by very short duration signals the bubble response may not reach steady state, hence the option for describing the acoustic effect of the bubbles during the transient period needs to be considered.

This thesis presents theoretical and experimental work exploring the potential for short duration and broadband signals to investigate their potential for sonar enhancement in bubbly environments. It has been divided into six chapters. In addition, an important collaborative study that arose from the measurements taken to design the tank experiment is bound at the back of the thesis as Appendix G (because the investigation grew beyond the main topic of the thesis).

The first chapter introduces bubble dynamics in an acoustic field by reviewing linear models for the bubble damping terms and for calculating the response of bubble wall to an acoustic field. The concept of bubble acoustic cross-sections is also introduced

and the implications of the presence of bubbles for sonar detection are discussed. Previous work on sonar enhancement is reviewed, and a hypothesis for progressing this work is proposed. Chapter 2 develops new bubble models that can be used to explore sonar enhancement, including novel time-dependent models for calculating scattering and attenuation of single bubbles and bubble clouds. Time-dependency is vital if the propagation of short pulses through bubble clouds of finite size is to be modelled, if reverberation is ever to be incorporated into such models, and if the effect of bubble 'ring-up' is to be included. Chapter 3 describes the experimental arrangement, and analysis techniques developed for investigating sonar enhancement experimentally in the tank including the development of a bubble cloud generator using electrolysis. Such a generator was required because the models described in Chapter 2 indicated that the large proportion of big bubbles generated by the method of producing bubbles in one of the two laboratory studies conducted prior to this thesis, may be responsible for their failure to observe a 'ring-up' effect experimentally. The new electrolysis method was an attempt to generate a bubble cloud with proportionally few large bubbles, i.e. a population more representative of oceanic populations in which Akulichev has observed ring-up.

The results of both the theoretical modelling of the tank experiments, and the tank experimental work itself, are described in chapter 4. The techniques and models investigated in the tank (chapters 3 and 4) were then tested in the surf-zone during a beach-based trial at Milford on Sea, Hampshire, England. Surf-zone bubble populations were measured acoustically. Various methods of sonar enhancement were tested experimentally and the results compared with the theoretical models. The details of the surf-zone trial and the results of both the experiment and theoretical modelling are presented in chapter 5. In the last chapter conclusions and a summary of this work are presented.

1.1 The acoustics of gas bubbles in liquids

In order to understand why air bubbles are an important consideration for target detection using active sonar in the sea, it is necessary to investigate the nature of air bubbles in liquids and then explain how they interact with a sound field.

Section 1.1.1 explains how air bubbles are formed in the ocean, and gives examples from the ranges of populations of bubbles that are likely to be encountered. The interactions between bubbles and a sound field are then introduced in the following two sections, by modelling a bubble as a linear oscillator and introducing a forcing term. Such linear models have been shown to be good first order approximations of bubble response. The exposition starts with Minnaert's[4] calculation of the resonance frequency of a spherical gas bubble, and concludes with Devin's[5] and Eller's[6] calculations of damping terms for spherical oscillations of air bubbles.

The concept of acoustic cross-sections of bubbles is then covered, as this is a common method of characterising the impact of single and multiple bubbles on a sound field. Finally the concept of a bubble as a non-linear oscillator, and the limitations of linear bubble theory, are discussed.

1.1.1 Introduction to air bubbles in the oceanic environment

A wide variety of near-surface air bubble populations have been measured in the ocean under a range of conditions.[1,7,8] The bubbles can be generated by many physical, biological and chemical actions. Measurements to date have demonstrated a dependence of bubble population on water depth, bubble depth, time of day or night, wind speed, rainfall, cloud cover, season of year and presence of sea slicks[2]. Geography can also significantly impact bubble populations. Some results obtained in coastal waters[9,10], for instance, show a) increased bubbles caused by increased breaking waves at higher wind speeds; b) seasonal dependence of increased biological activity in coastal waters; c) increased numbers of smaller bubbles in daylight due to photosynthesis; d) increased numbers of larger bubbles at night, possibly due to offshore winds ('sea breeze') dropping continental aerosols, which trap bubbles when they fall into the sea, or biological activity on the sea floor[2].

Additional factors affecting bubble populations are dissolution, hydrostatic and buoyancy forces acting on the bubbles once they have been formed. The higher buoyancy forces acting on large bubbles, and the removal of small bubbles by dissolution, results in a characteristic peak in the bubble population[11]. This is so particularly in deep water at high wind speeds, where entrainment due to breaking waves generates a persistent bubble layer just below the ocean surface[12].

These processes lead to the formation of bubble layers and clouds with measured bubble radii of just a few microns up to several hundred micrometers or more.[11] Void fractions (or percentage of gas per unit volume) have been estimated[13] at between 0.01-0.02% and[14] 0.1-0.2%. This decreases[13] to 10^{-4}% to 10^{-5}% under more stable conditions where the bubbles penetrate to a greater depth.

1.1.2 The bubble as a linear oscillator

When a gas bubble in a liquid experiences a change in pressure over its whole surface (i.e. the acoustic wavelength is much greater then the bubble radius) it will compress or expand to a new equilibrium radius. If such pressure changes were a low frequency oscillation, as is often the case with acoustic signals, the bubble will attempt to expand and contract in sympathy with that signal and will itself oscillate about its equilibrium radius.

Consider further the scenario of a bubble encountering, or being insonified by, a pressure fluctuation. The gas inside the bubble will act as a restoring force owing to pressure fluctuations as the gas expands and contracts. The system also has inertia dominated by the mass of the surrounding liquid. Damping results from the acoustic emission by the bubble, and thermal and viscous losses associated with the motion of the bubble wall.

For small amplitudes of oscillation, the system that has just been described is analogous to a bob on a spring. Both have mass, a restoring force and damping and, when driven harmonically, will respond with simple harmonic motion. This analogy leads to a simple equation of motion for the bubble [1-1]. This equation of motion is a first order approximation of the bubble response only. The limitations of the model will be highlighted in a later section.

$$m\ddot{\varepsilon} + b\dot{\varepsilon} + k\varepsilon = 0 \qquad [1\text{-}1]$$

Here ε is a displacement, k is the stiffness, m is the mass, b is the dissipation constant and $\dot{\varepsilon}$ and $\ddot{\varepsilon}$ are the velocity and acceleration respectively.

The damping term represented by b, the dissipation constant, requires further explanation. To conform with the standard papers on bubble damping by Devin[5] and Eller[6], the damping term will be considered in the volume-pressure frame (denoted by

the subscript VP)[15]. From this dissipation constant the dimensionless damping constant *d*, which is applicable to all frames of reference, can be determined.

$$d = \frac{\omega b_{VP}}{k_{VP}} \qquad [1\text{-}2]$$

where ω is the pulsation frequency in radians per second.

Energy losses from a bubble can occur through three distinct mechanisms[16]:

- Energy is radiated away from the bubble as acoustic waves *(radiation damping)*.
- Energy is lost through thermal conduction between the gas and the surrounding liquid (*thermal damping*).
- Work is done against viscous forces at the bubble wall (*viscous damping*).

A damping constant can be associated with each of these three mechanisms with the total damping equalling their sum. The total damping can also be related to the bubble quality factor, *Q*, at the resonance frequency by the well-known equation:

$$Q = \frac{1}{\delta_0} \approx \frac{\omega_0}{2\beta} \quad (\text{when } \beta \langle\langle \omega_0) \qquad [1\text{-}3]$$

where δ_0 is the total dimensionless damping at resonance, ω_0 is the resonance frequency of the bubble in radians, and β is the resistive constant leading to damping.

The radiation damping in the radius-force frame can be determined by considering the radiation impedance. This is defined as the ratio of the applied force to the particle velocity. Since it is defined in the radius-force frame, it is numerically equal to the product of the specific acoustic impedance and the surface area. The specific acoustic impedance can in turn be defined as the ratio of driving pressure to particle velocity. It is this impedance that characterises the coupling between the acoustic source, in this case the bubble, and the radiated waves. The real and imaginary parts of this impedance give rise to the resistive and inertial properties of the source.

Under the condition of $KR_0 << 1$ (K is the wavenumber and R_0 is the equilibrium bubble radius) the radiation damping term is:

$$b_{VP}^{rad} = \frac{\rho\omega^2}{4\pi c} \qquad [1\text{-}4]$$

where ρ is the density of water and c is the speed of sound in water.

In the same limit the stiffness of the bubble, k_{VP}, is given by[17]:

$$k_{vp} = \frac{\gamma}{\alpha_{th}} \frac{p_o}{V_o} \qquad [1\text{-}5]$$

where α_{th} is the dimensionless multiplicative factor, which corrects for the effects of heat flow in the stiffness and resonance frequency of a bubble.

Thus the dimensionless radiation damping constant is:

$$d_{rad} = \frac{\omega b_{VP}^{rad}}{k_{VP}} = \frac{\rho R_0^3 \omega^3}{3\kappa p_0 c} \qquad [1\text{-}6]$$

where p_0 is the hydrostatic pressure outside of the bubble and κ is the polytropic index ($1 \le \kappa \le \gamma$; κ is equal to unity in isothermal conditions, and γ in adiabatic conditions, where γ is the ratio of specific heat of a gas at constant pressure to that at constant volume). For a real gas bubble the value of κ normally takes some intermediate value between γ and unity, and can be calculated analytically[6]. The use of κ is not fundamental but is a useful approximation[26].

It can be shown, by application of the Stokes assumption to the Navier-Stokes equation for fluid of a constant viscosity[16], that there are no net forces acting in the body of an incompressible viscous liquid around a pulsating bubble[12]. However, net viscous forces can occur at the liquid surface of the bubble wall, where they result in excess pressure. Mallock[18] described how these viscous forces could cause the distortion of the spherical shell volume elements concentric with a bubble, resulting

in a net energy loss in compression in an incompressible liquid. Eller[6] derived the viscous damping term to be:

$$b_{VP}^{vis} = \frac{\eta}{\pi R_0^3} \qquad [1\text{-}7]$$

and its dimensionless equivalent to be:

$$d_{vis} = \frac{\omega b_{VP}^{vis}}{k_{VP}} = \frac{4\omega\eta}{3\kappa p_0} \qquad [1\text{-}8]$$

where η is the shear viscosity of the liquid.

The thermal damping term is the most complicated to formulate. The damping mechanism occurs as a result of a hysteresis effect[5,19]. The driving pressure does more work compressing the bubble than the gas inside the bubble does in moving the liquid on expansion. The reason for this is that, in an air bubble in water, the gas in contact with the liquid can be considered isothermal, (where heat conducts freely) owing to the liquid's large specific heat and thermal conductivity. Conversely, the gas in the centre of the bubble is insulated from any substance having a high specific heat and thus behaves almost adiabatically (where conduction is inhibited). Therefore the heat transfer through the bubble wall into the liquid during compression is more than the heat flow from the liquid into the bubble during expansion. This gives rise to the hysteresis effect described above, with a net heat flow from the bubble into the liquid. Thus a net loss of energy from the bubble. Eller[6] derived the thermal damping in the volume-pressure frame in terms of L_D, the width of the thermal boundary layer, to give:

$$b_{VP}^{th} = \frac{9(\gamma-1)\kappa p_o}{4\pi R_0^3}\left[\frac{(R_0/L_D)\{\sinh(R_0/L_D)+\sin(R_0/L_D)\}-2\{\cosh(R_0/L_D)-\cos(R_0/L_D)\}}{(R_0/L_D)^2\{\cosh(R_0/L_D)-\cos(R_0/L_D)\}+3(\gamma-1)(R_0/L_D)\{\sinh(R_0/L_D)-\sin(R_0/L_D)\}}\right] \qquad [1\text{-}9]$$

Hence from [1-8]

$$d_{\text{th}} = \frac{\omega b_{VP}^{th}}{k_{VP}} = \frac{3(\gamma-1)(R_0/L_D)\{\sinh(R_0/L_D)+\sin(R_0/L_D)\}-2\{\cosh(R_0/L_D)-\cos(R_0/L_D)\}}{(R_0/L_D)^2\{\cosh(R_0/L_D)-\cos(R_0/L_D)\}+3(\gamma-1)(R_0/L_D)\{\sinh(R_0/L_D)-\sin(R_0/L_D)\}} \qquad [1\text{-}10]$$

The total dimensionless damping constant is given by the summation of the damping mechanisms: $d_{tot} = d_{rad} + d_{th} + d_{vis}$. Figure 1-1 shows the various damping terms for a bubble of equilibrium radius 100 μm plotted against the frequency of the driving sound field.

A freely oscillating bubble has therefore been described in terms of a linear equation of motion and the damping mechanisms defined. In the next section a harmonic forcing term will be applied and the equation solved.

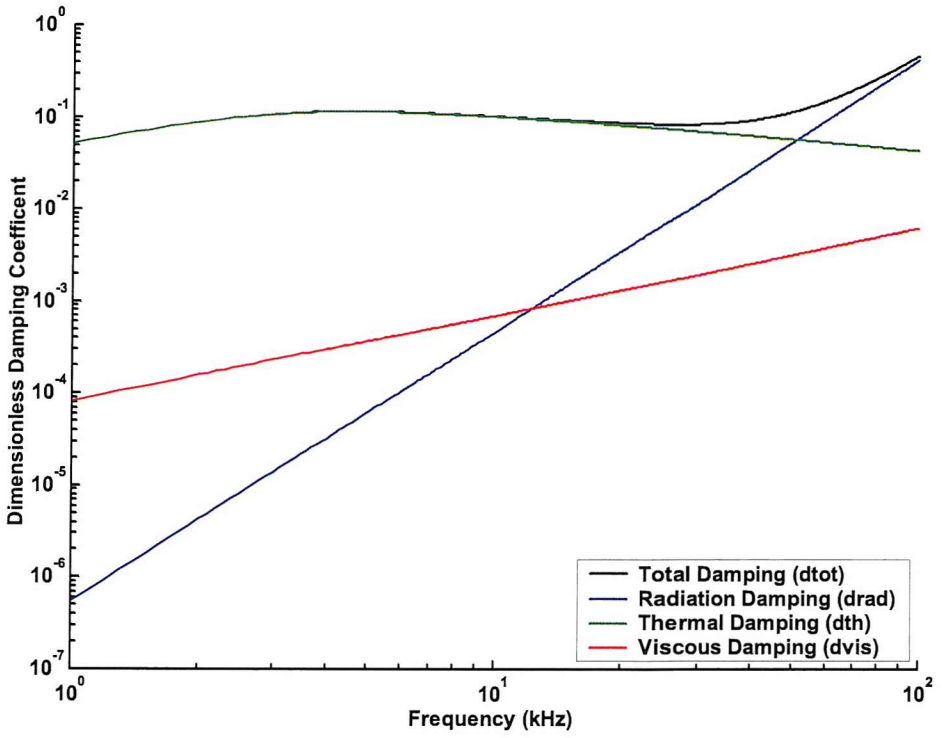

Figure 1-1 Dimensionless damping constant (d) of a 100 μm radius air bubble in water, plotted as a function of driving frequency under 1 atm. static pressure. The solid line indicates the total dimensionless damping coefficient whilst the dashed lines show the contributions of the different damping mechanisms as indicated by the legend.

1.1.3 The bubble as a harmonically forced oscillator

As has already been mentioned, the response of a spherical gas bubble in a low amplitude sound field can be modelled as a bob on a spring driven harmonically. The equation of motion is given in [1-1]. The system has an associated mass m, stiffness k, and damping b and when driven harmonically by a force of angular frequency ω, has the equation of motion[20]:

$$m\ddot{\varepsilon} + b\dot{\varepsilon} + k\varepsilon = F_0 \sin(\omega t) \qquad [1\text{-}11]$$

The solution of this non-homogeneous differential equation can be found by adding the general solution of the homogeneous to the particular solution of [1-11]. The homogenous equation is:

$$m\ddot{\varepsilon} + b\dot{\varepsilon} + k\varepsilon = 0 \qquad [1\text{-}12]$$

This is the equation for damped free vibration and has the solution:

$$\varepsilon = e^{-\beta t}\left(A_1 e^{i\omega_d t} + A_2 e^{-i\omega_d t}\right) \qquad [1\text{-}13]$$

where $i = \sqrt{-1}$, the damped frequency $\omega_d = \sqrt{\omega_0^2 - \beta^2}$ and A_1 and A_2 are constants determined by the initial conditions. Equation [1-13] can be written in the more recognisable form:

$$\varepsilon = Ae^{-\beta t}\cos(\omega_d t + \phi_1) \qquad [1\text{-}14]$$

Here the initial amplitude A and the phase ϕ_1 are constants determined by the initial conditions.

The particular solution can be found by writing [1-11] in complex form:

$$m\ddot{\varepsilon} + b\dot{\varepsilon} + k\varepsilon = F_0 e^{i\omega t} \qquad [1\text{-}15]$$

and assuming a solution of the form:

$$\varepsilon = \varepsilon_0 e^{i\omega t} \qquad [1\text{-}16]$$

Differentiating and substituting into [1-15] gives:

$$\left(-m\omega^2 + i\omega b + k\right)\varepsilon_0 e^{i\omega t} = F_0 e^{i\omega t} \qquad [1\text{-}17]$$

Hence

$$\varepsilon = \frac{F_0 e^{i\omega t}}{-m\omega^2 + i\omega b + k} = \frac{F_0 \cos(\omega t)}{-m\omega^2 + i\omega b + k} + \frac{iF_0 \sin(\omega t)}{-m\omega^2 + i\omega b + k} \qquad [1\text{-}18]$$

Taking the real part of [1-18]:

$$\varepsilon = \frac{F_0 \left\{\cos(\omega t).\left(k - \omega^2 m\right) + \sin(\omega t).b\omega\right\}}{b^2\omega^2 + \left(-\omega^2 m + k\right)^2} \qquad [1\text{-}19]$$

which again can be rewritten in a similar form to [1-14]:

$$\varepsilon = \frac{F_0 \cos(\omega t - \phi_2)}{\sqrt{b^2\omega^2 + \left(-\omega^2 m + k\right)^2}} \qquad [1\text{-}20]$$

Here ϕ_2 is a constant determined by the initial conditions.

The total solution to [1-11] can be found by adding [1-14] to [1-20]:

$$\varepsilon = Ae^{-\beta t}\cos(\omega_d t + \phi_1) + \frac{F_0 \cos(\omega t - \phi_2)}{\sqrt{b^2\omega^2 + \left(-\omega^2 m + k\right)^2}} \qquad [1\text{-}21]$$

Physically this represents the summation of a damped free vibration with a forced vibration.

This formulation can be applied to a bubble by rewriting [1-11] in terms of a bubble in the radius-pressure frame. This frame of reference is chosen to be consistent with other models used in this work and because it is the most useful for real-world applications.

The radiation mass of a bubble in the radius-pressure frame m_{RP} is given by[21]:

$$m_{RP} = \rho R_0 \qquad [1\text{-}22]$$

The stiffness, k, or spring constant (which is the ratio of the force a spring exerts to the extension which produces that force) when written in the radius-pressure frame is given by[21]:

$$k_{RP} = \frac{3\kappa}{R_0} p_{i,e} \qquad [1\text{-}23]$$

where $p_{i,e}$ is the pressure within the bubble at equilibrium:

$$p_{i,e} = p_\infty + \frac{2\sigma}{R_0} \qquad [1\text{-}24]$$

Here p_∞ is the pressure in the liquid far from the bubble and σ is the surface tension of the liquid.

The dissipation term can be written in terms of a bubble dimensionless damping constant by rearranging [1-2] and utilising the relationship[21]:

$$\frac{b_{RP}}{b_{VP}} = 4\pi R_0^{\,2} \qquad [1\text{-}25]$$

to give

$$b_{RP} = \frac{d_{tot} k_{RP}}{\omega}\left(4\pi R_0^{\,2}\right) \qquad [1\text{-}26]$$

Finally [1-11] can be written in the radius-pressure frame to give:

$$m_{RP}\ddot{R} + b_{RP}\dot{R} + k_{RP}R_\varepsilon = P_A \sin(\omega t) \qquad [1\text{-}27]$$

Here P_A is the amplitude of the driving pressure field, and R_ε is the bubble wall displacement from the equilibrium bubble radius R_0, $\dot{R}$ and $\ddot{R}$ are the velocity and acceleration terms respectively and a sine term is used for the driving field for simplicity in determining the constants.

Thus [1-21] can also be rewritten to given the bubble wall response to a driving sound pressure field:

$$R_\varepsilon(t) = Ae^{-\beta t}\cos(\omega_d t + \phi_1) + \frac{-P_A \sin(\omega t - \phi_2)}{\sqrt{{b_{RP}}^2\omega^2 + \left(-\omega^2 m_{RP} + k_{RP}\right)^2}} \qquad [1\text{-}28]$$

The first part of [1-28], representing a damped free vibration, can be further simplified for calculation purposes by noting that the Quality factor (Q) of a bubble can be related to β using [1-3]. Furthermore under conditions of very light damping when $\beta << \omega_0$ the resonance frequency of oscillation, then $\omega_d \approx \omega_0$ and [1-28] becomes:

$$R_\varepsilon(t) = Ae^{-\left(\frac{\delta_{tot}\omega_0}{2}\right)t}\cos(\omega_0 t + \phi_1) + \frac{-P_A \sin(\omega t - \phi_2)}{\sqrt{{b_{RP}}^2\omega^2 + \left(-\omega^2 m_{RP} + k_{RP}\right)^2}} \qquad [1\text{-}29]$$

The constants A, ϕ_1 and ϕ_2 can now be determined using the initial conditions of a bubble of equilibrium radius $R_\varepsilon = 0$ at rest, at time t=0 and differentiating with respect to time. The resulting simultaneous equation can then be solved to give:

$$\phi_2 = \tan^{-1}\left(\frac{\omega k_{RP}}{\omega_0\left(\omega m_{RP} - k_{RP}/\omega\right)}\right) \quad , \quad \phi_2 = \tan^{-1}\left(\frac{\omega m_{RP} - k_{RP}/\omega}{b_{RP}}\right)$$
$$A = \frac{-P_A \sin(\phi)}{\sqrt{{b_{RP}}^2\omega^2 + \left(-\omega^2 m_{RP} + k_{RP}\right)^2}} \qquad [1\text{-}30]$$

As will be shown in the next section, this linear model can be applied to determine the time dependent bubble response to a driving sound field.

1.1.4 Linear bubble response

In this section the response of a 100 μm radius bubble to various driving sound fields is calculated using the linear model developed in the preceding section. The results and the limitations of the model are discussed, including the special case where $\omega = \omega_0$

The linear model shown in [1-29] consists of two parts. The first is damped free vibration at the resonance frequency of the bubble ω_0 and a decay term $e^{-\left(\frac{\delta_{tot}\omega_0}{2}\right)t}$ that results in the oscillation reducing from its initial amplitude (determined by the constant A) as time t increases. The rate of decay is dependent on the Q and resonance frequency of the bubble. The second part of [1-29] is also an oscillation but at the frequency of the driving sound field. It has amplitude proportional to that of the driving sound field and a starting phase determined from the driving source. As t becomes large, the solution is dominated by the second term and is said to be in steady state (although strictly this is only attained as $t \to \infty$). In steady state the response is become periodic for as long as the driving sound field remains unchanged. Hereafter the first part of the solution is termed the transient and the second part the steady-state.

The summation of these two oscillations will thus give the complete bubble response. Consider a bubble at rest at its equilibrium radius and insonified by a continuous driving sound field of frequency ω and amplitude P_A. In this case it is the difference between the driving and resonance frequencies that will determine the form of the bubble response and the magnitude of the damping that will determine the time to reach steady state. The effect of the difference between the resonance and driving frequencies will be considered first.

The resonance frequency is[22]:

$$\omega_0 = \frac{1}{R_0}\sqrt{\frac{3\kappa p_0}{\rho}\left(1+\frac{2\sigma}{p_o R_o}\right)-\frac{2\sigma}{\rho R_o}} \qquad [1\text{-}31]$$

For a 100 μm radius air bubble in water under one atmosphere of pressure, the resonance frequency is ~ 33 kHz.

First consider the response of the 100 μm air bubble when driven by a 100 kHz sound field (of zero amplitude for $t < 0$; and 100 Pa amplitude for $t \geq 0$). The bubble is at

rest at $t < 0$. The results of the model[i] are shown in Figure 1-2. It can be seen that a steady-state response is reached within ~0.5 ms of the onset of insonification, with a tiny displacement of ~0.003 μm, but that the bubble wall displacement is initially transient and that the amplitude of oscillation can exceed the amplitude at steady state. This is as a result of the constructive and destructive interference when the different frequency oscillations of the transient and steady state parts of the solution are summed.

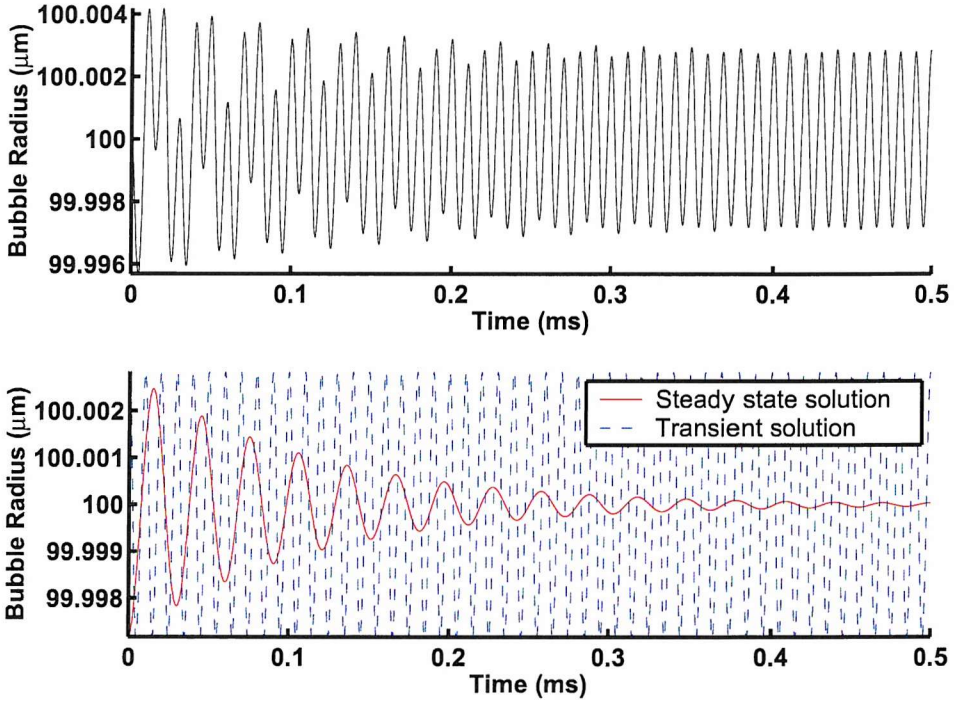

Figure 1-2 The solution of the linear model for a 100 μm radius air bubble in water driven by a 100 kHz, 100 Pa amplitude sound field, sampled at 10 MHz. The top plot shows the response of the bubble wall relative to the equilibrium radius and the bottom plot shows the transient part of the solution in black and steady state part in grey.

---

[i] In Figure 1-2 through Figure 1-5 the bubble motion is calculated from equation [1-27] and [1-28]. The damping b_{RP} is calculated from Eller[6]. Since this formulation requires a single frequency input the driving frequency is used in each case. However, it is recognised that this is an approximation since in the period prior to steady state the pulsation motion of the bubble contains other frequencies.

Next consider the same bubble driven from rest at $t = 0$ closer to its resonance frequency by a 40 kHz, 100 Pa amplitude sound field. The results are shown in Figure 1-3. The smaller difference between the frequencies of the transient and steady state oscillations produces a very different response when summed. The response is again steady state after ~0.5 ms of insonification, but this time has a larger amplitude of ~0.04 μm. Again the amplitude of oscillation during the transient phase can exceed that of the steady state.

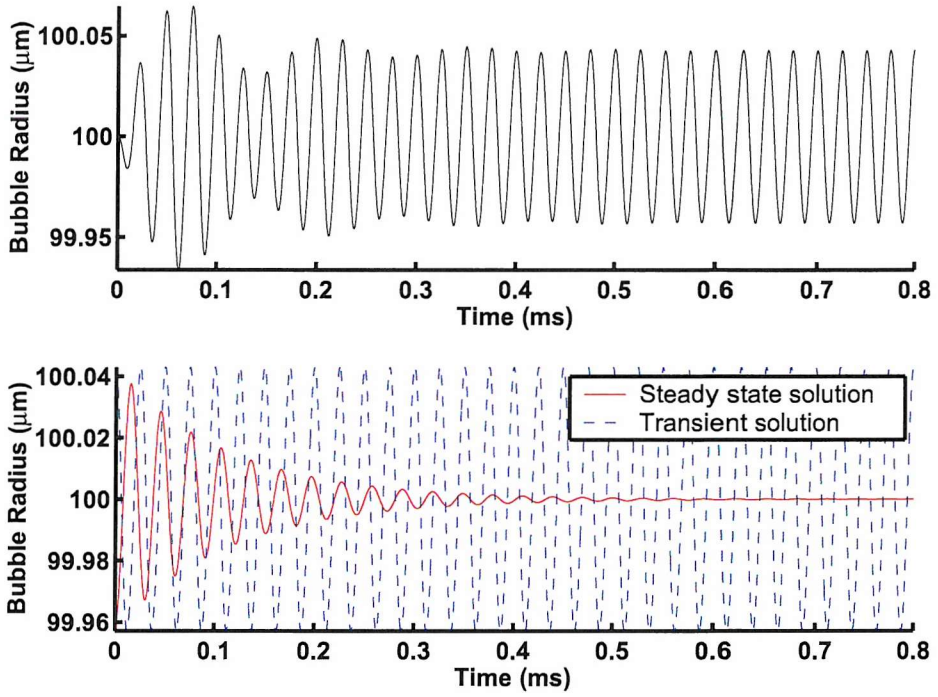

Figure 1-3 The solution of the linear model for a 100 μm radius air bubble in water driven by a 40 kHz, 100 Pa amplitude sound field, sampled at 10 MHz. The top plot shows the response of the bubble wall relative to the equilibrium radius and the bottom plot shows the transient part of the solution in black and steady state part in grey.

Finally consider the special case where $\omega = \omega_0$. Since the bubble is being driven at resonance, the frequency of the transient and steady state solutions are equal but the oscillations are in anti-phase, resulting in destructive interference. The bubble response is thus a steady rise or 'ring-up' to steady state and, unlike the previous examples, at no point does the transient response exceed the steady state response. In addition the amplitude of the response has increased by an order of magnitude over the previous examples to ~0.3 μm. The results of this case are shown in Figure 1-4.

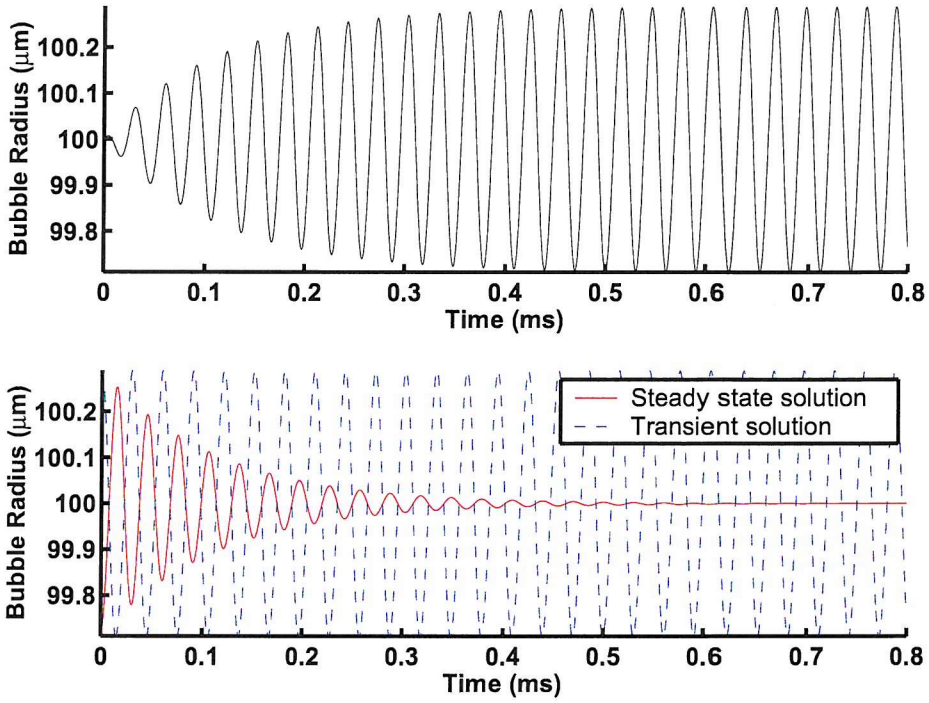

Figure 1-4 The solution of the linear model for a resonant 100 μm radius air bubble in water driven by a 33 kHz, 100 Pa amplitude sound field, sampled at 10 MHz. The top plot shows the response of the bubble wall relative to the equilibrium radius and the bottom plot shows the transient part of the solution in black and steady state part in grey.

In all the above examples, including the resonance case, the time to reach steady state is determined by the rate of decay of the transient part of [1-29]. This in turn is a function of the exponential term $e^{-\left(\frac{\delta_{tot}\omega_0}{2}\right)t}$. This expression can be rewritten in terms of the bubble Q and resonance frequency f_0:

$$e^{-\left(\frac{\delta_{tot}\omega_0}{2}\right)t} = e^{-\left(\frac{\pi f_0}{Q}\right)t} \qquad [1\text{-}32]$$

Thus the time taken to reach steady state is a function of the bubble Q and the resonance frequency f_0. Since the decay is exponential it will never reach zero but instead will become infinitesimally small. One method of quantifying the time to reach steady state is termed the characteristic relaxation time to steady state[40] τ_0 or the time to reach $(1/e)$ of the steady state value. It can be calculated from the bubble quality factor and resonance frequency:

$$\tau_0 = \frac{Q}{\pi f_0} \qquad [1\text{-}33]$$

Whilst at resonance this can be related to the time taken for the amplitude to grow to $(1-e^{-1})$ or 63% of the steady state amplitude. Off resonance we do not see the monatomic 'ring-up' to steady state illustrated in Figure 1-4 and hence such a simple criterion cannot be applied. This issue is further discussed in section 1.3.1.

A final facet of the linear model, and its biggest limitation, is the scaling of the response in proportion to the amplitude of the driving signal. It is apparent from the steady state solution that, as the driving amplitude doubles, so does the amplitude of the response (equation [1-29]). Eventually this will exceed the equilibrium radius of the bubble were this model to hold true at such high amplitudes. This is obviously impossible and occurs because the linear model does not take into account the amplitude-dependence of the stiffness of the gas inside the bubble when it is compressed. This leads to increasing inaccuracies in the linear model as the driving sound pressure level grows. Non-linear models have been formulated to include this factor. Figure 1-5 compares results from one such model, the Rayleigh-Plesset[26], with the linear model at different driving amplitude for a resonant 100 μm radius bubble.

The bubble resonance frequency is 33 kHz for the linear model and 32 kHz for the non-linear model owing to the different damping models used[i]. The non-linear model is discussed further in section 1.1.6, although the cost has been that not all damping mechanisms are included. The figure clearly shows that for very small amplitude, the models are in close agreement, but as the sound pressure increases the linear model overestimates the wall response. Furthermore, the Rayleigh-Plesset model predicts a deviation from the ring-up to steady state indicated by the linear model in this plot and by both models for lower driving sound field.

The linear model derived in the preceding sections is a useful tool in predicting the response of air bubbles in water to a sound field, but is limited by increasing inaccuracies as the driving sound pressure rises. Non-linear models that overcome this problem are discussed in section 1.1.6. In the next section a further facet of the linear bubble model is discussed. Specifically, it discusses acoustic cross-sections that can be derived from the linear model. These cross-sections are widely used in acoustics to predict the effect of both single bubbles and clouds of bubbles on acoustic signals.

---

[i] The Rayleigh Plesset model incorporates neither radiation nor thermal damping, but does describe nonlinearities in, for example, the gas stiffness. Therefore even at low amplitudes its results will not agree exactly with those of the linear model (which includes thermal, viscous and radiation damping). However the differences seen in Figure 1-5a result from nonlinearities, as could be demonstrated through the presence of harmonies (see the power spectral density plots in Figure 1-5b) of the driving signal in the steady-state response

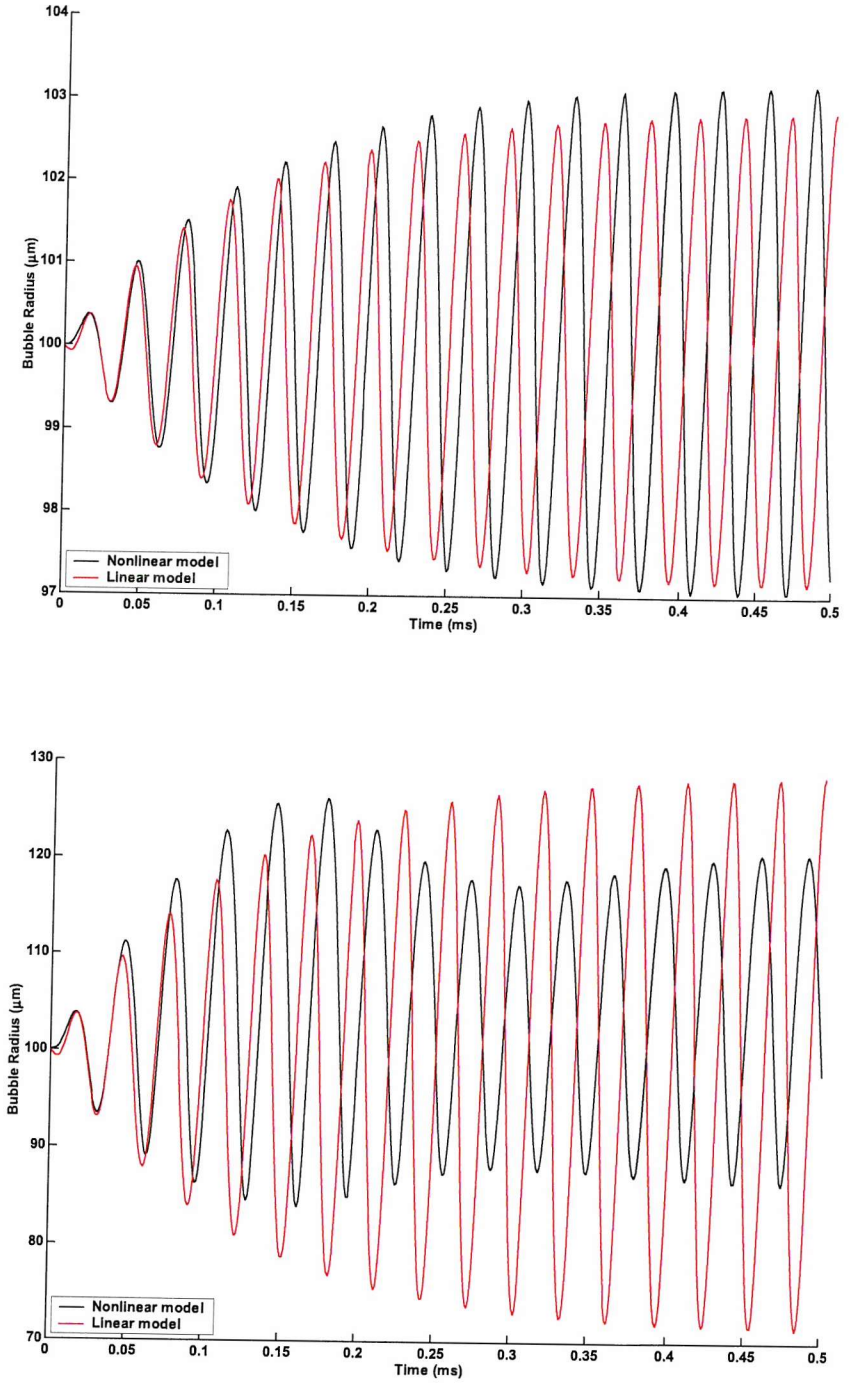

Figure 1-5a The response of a 100 μm radius resonant bubble using the linear model (dashed line) and the Rayleigh-Plesset non-linear bubble model (solid line) driven by a 1 kPa amplitude sound field in top plot and a 10 kPa amplitude sound field in the bottom plot.

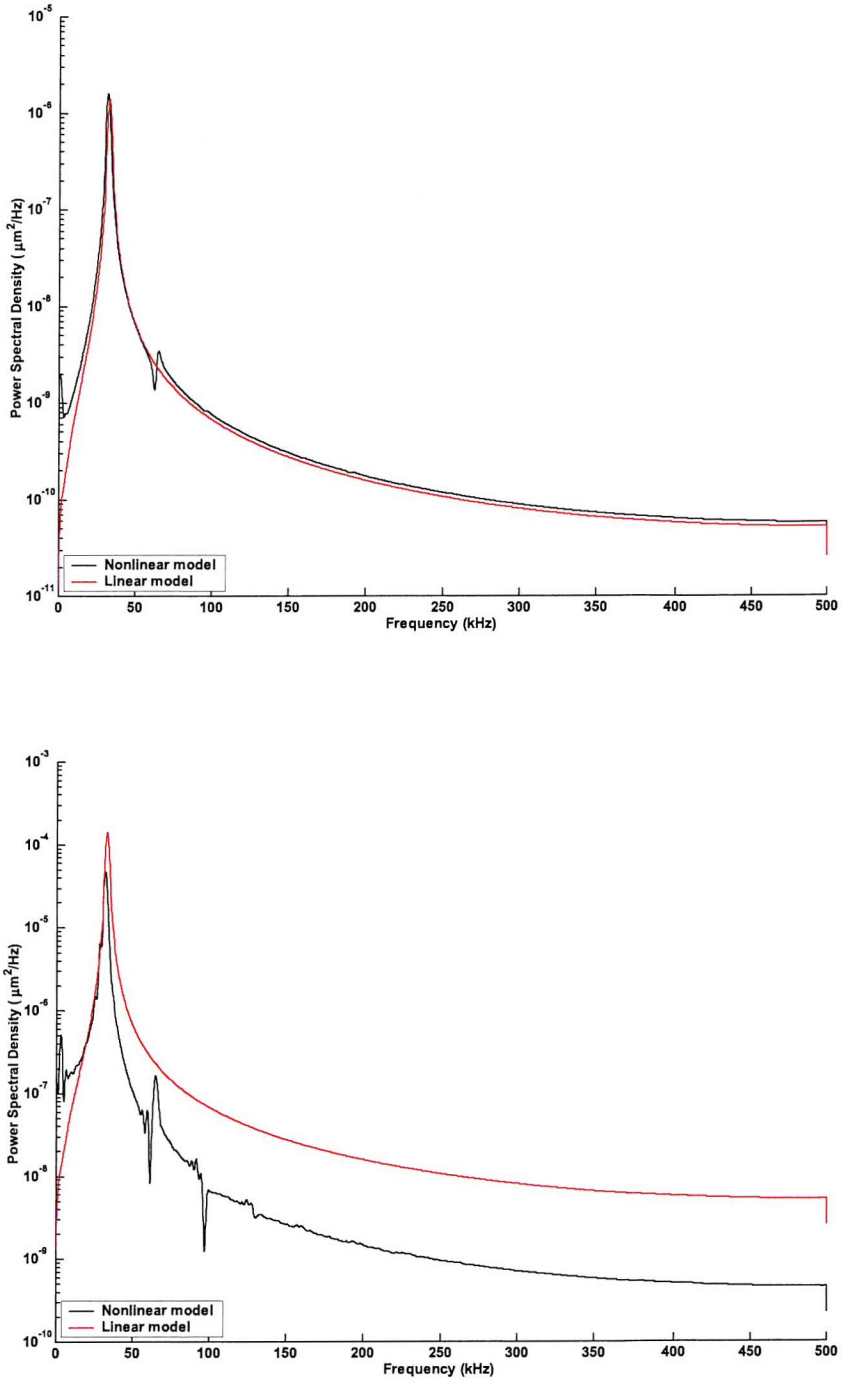

Figure 1-5b The power spectral density of the time series shown in Figure 1-5a i.e. a 100 μm radius resonant bubble using the linear model (dashed line) and the Rayleigh-Plesset non-linear bubble model (solid line) driven by a 1 kPa amplitude sound field in top plot and a 10 kPa amplitude sound field in the bottom plot

1.1.5 Acoustic cross-section of a bubble

The acoustic cross-section is a method of characterising the steady state scattering or attenuation of a bubble in terms of an effective target strength with dimension m^2. This is very useful since it can be applied quickly and easily to clouds of bubbles to give the steady state cloud target strength in both m^2 and decibels for use in sonar equations. The basic extinction and scattering cross-sections are derived here and applied to bubble clouds in section 1.2.1. As will be shown, prior to this thesis cross-sections have been derived from the steady-state solution of the linear mode [1-29] and are thus subject to the limitations of that model.

The linear scattering cross-section, Ω_{scat}, is defined by the ratio of the time averaged energy loss to incident energy[23]:

$$\Omega_{scat} = \frac{\text{Time Averaged Energy Loss}}{\text{Incident Energy}} = \frac{\lim_{t\to\infty}\left|R_{\varepsilon_o}\right|^2 \omega^2 b_{RP}^{rad} \Big/ 2}{P_A^2/2\rho c} \qquad [1\text{-}34]$$

where $R_{\varepsilon o}$ is the amplitude of the bubble wall response. Using [1-29] and the relationships in [1-6] and [1-26], the scattering cross-section becomes:

$$\Omega_{scat} = \frac{4\pi k_{RP}\left(\omega^4 R_0^3/3\kappa p_0\right)}{\left(\omega_0^2-\omega^2\right)^2+(2\beta\omega)^2} \qquad [1\text{-}35]$$

The expression can be further simplified by using [1-3] and [1-23] and noting that $\frac{p_{i,e}}{p_0} \approx 1$ and $\beta \langle\langle \omega_0$:

$$\Omega_{scat} = \frac{4\pi R_0^2}{\left(\frac{\omega_0^2}{\omega^2}-1\right)^2+\delta_{tot}^2\left(\frac{\omega_0}{\omega}\right)^2} \qquad [1\text{-}36]$$

The scattering cross-section is the ratio of the intensity of the scattered acoustic field to the intensity of the incident acoustic field, and hence is a measure of the energy dissipated by re-radiation having units of area. Similarly the extinction cross-section,

Ω_{ext} represents the energy dissipated by all mechanisms and thus is related to the scattering cross-section by[23]:

$$\Omega_{ext} = \frac{d_{tot}}{d_{rad}} \Omega_{scat} \qquad [1\text{-}37]$$

The model described by [1-36] and [1-37] is here after referred to as the Medwin model[2] to differentiate it from time-dependent cross-section models described in later sections.

The scattering cross-section of bubbles with radii from 1 μm to 1500 μm in a 30 kHz sound field and one atmosphere static pressure is shown in Figure 1-6 and Figure 1-7. The resonant bubble radius is ~110 μm, indicated by the local maxima in the scattering cross-section. For radii much less than the resonant bubble radius $\omega \langle\langle \omega_0$ and the scattering cross-section simplifies to give the Rayleigh law of scattering[16]:

$$\Omega_{Rayleigh} = 4\pi R_0^2 \left(\frac{\omega}{\omega_0} \right)^4 \qquad [1\text{-}38]$$

Conversely, as the bubble radii becomes much greater than the resonant radius $\omega \rangle\rangle \omega_0$ and the scattering cross-section simplifies to give the geometric scattering law whilst $KR_0 << 1$:

$$\Omega_{Geometric} = 4\pi R_0^2 \qquad [1\text{-}39]$$

The geometric scattering law is plotted in Figure 1-6 and Figure 1-7 for comparison. It is clear that, in the limit $KR_o << 1$, large off-resonant bubbles follow the geometric scattering regime and thus, for a given insonification frequency, there is always in principle a critical bubble size, such that all single bubbles larger than this size scatter more than the single resonant bubble. Thus, resonant scattering is only a local maxima when the cross-section is plotted as a function of radius for a given driving frequency; and despite having a scattering cross-section orders of magnitude larger than geometric scattering from a bubble of a similar radius, the scattering from a resonant bubble can be exceeded and thus masked by large off-resonant bubbles.

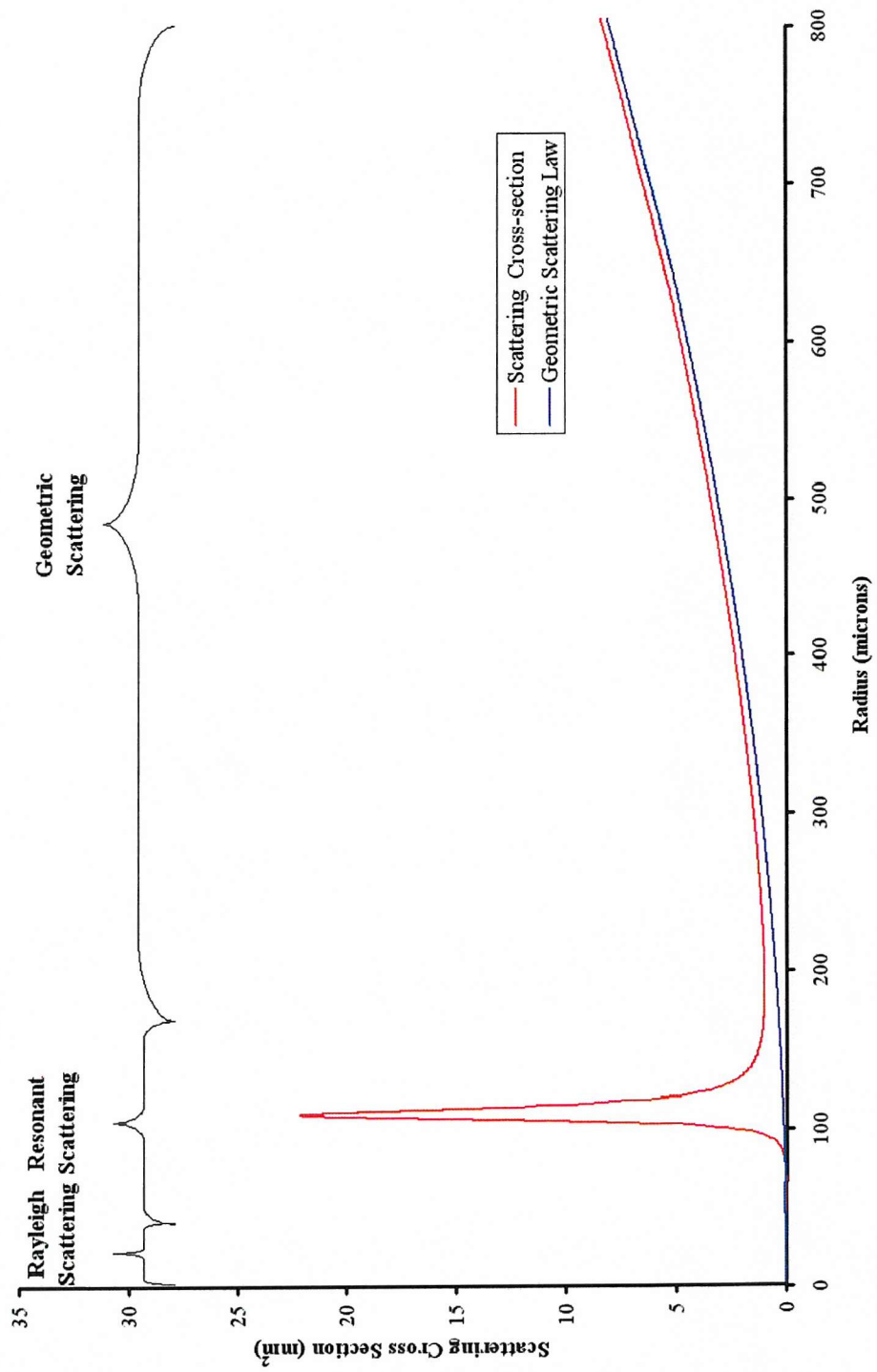

Figure 1-6 Scattering cross-section as a function of bubble radius in a 30 kHz sound field under 1 atmosphere static pressure. Note the local maxima corresponding to resonance at 110 μm. The data has been resolved down to 0.01 μm to reduce aliasing around the 110 μm radius local maxima. The brackets at the top of the graph indicate the approximate scattering regime. The geometric scattering is only valid when $KR_0 << 1$. *For 800 μm radius at 30 kHz* $KR_0 = 0.1$.

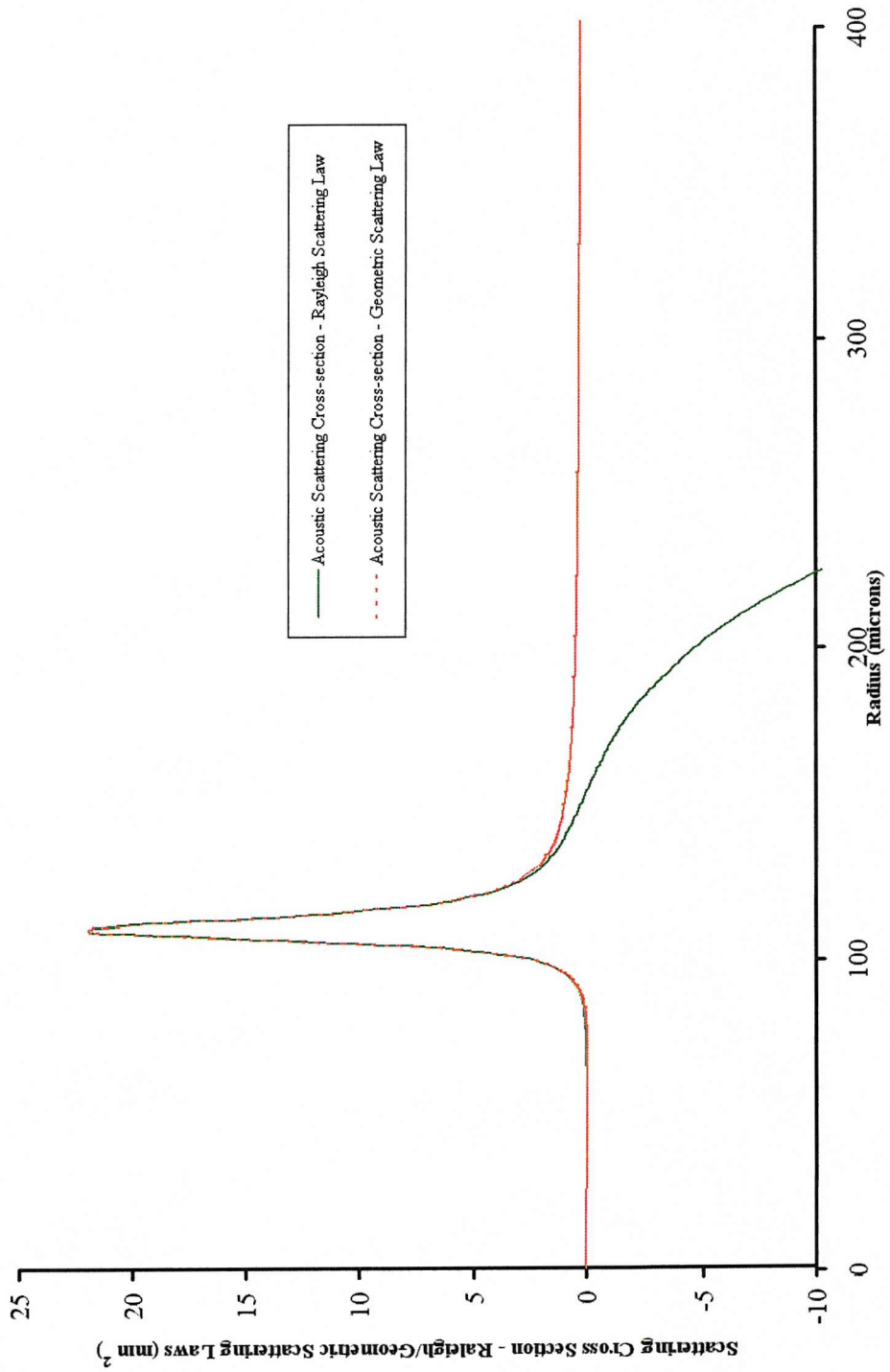

Figure 1-7. A plot of the difference between the scattering cross-section and non-resonant scattering laws. The orange line represents the quantity calculated by the acoustic scattering cross-section minus the geometric scattering law. The green line represents the quantity calculated by the acoustic scattering cross-section minus the Rayleigh scattering law.

The next section discusses modelling a bubble as a non-linear oscillator to overcome the amplitude constraints of the linear models, as illustrated in Figure 1-5.

1.1.6 The bubble as a non-linear oscillator

In the preceding sections the bubble is considered to be analogous to a mass-on-a-spring linear system, where the response of the system is directly proportional to the driving force[24]. In reality, however, a bubble can be expected to oscillate non-linearly at finite amplitudes, since expansion and compression are not symmetrical. Whilst the bubble could, in theory, expand without limit, upon compression, the radial displacement cannot exceed the value of the equilibrium radius[25]. Thus it is apparent that when the motion of the bubble wall becomes large (as occurs when the bubble is driven at high amplitudes), the bubble will no longer be accurately modelled as a simple linear system (see Figure 1-5).

There are three families of equations modelling bubbles as non-linear oscillators[26]. The simplest of these groups is the Rayleigh-Plesset equation. It is described here in order to illustrate the form and assumptions that govern existing non-linear bubble models. It also illustrates whether important aspects of the linear theory (such as the damping mechanisms) are incorporated; and if so, how this is done. More advanced models are considered in chapter 2, such as the Keller-Miksis equation[27], which is a member of the second (i.e. Keller-Miksis) family of bubble models.

The Rayleigh-Plesset equation is of the form:

$$R(t)\ddot{R}(t)+\frac{3\dot{R}(t)^2}{2}=\frac{1}{\rho}(p_B(t)-p_0-P(t)) \qquad [1\text{-}40]$$

Here $R(t)$ is the bubble radius, $p_B(t)$ represents the pressure immediately outside the bubble wall, at some time t and $P(t)$ is the driving pressure field at time t. This is the term that incorporates the force exerted on the liquid by the bubble, which the hydrostatic and acoustic pressures have to overcome. The $p_B(t)$ term in full is:

$$p_B(t)=\left(p_o+\frac{2\sigma}{R_0}\right)\left(\frac{R_o}{R(t)}\right)^{3\kappa}-\frac{2\sigma}{R(t)}-\frac{4\eta\dot{R}}{R(t)} \qquad [1\text{-}41]$$

This equation has several fundamental assumptions. These are:[25]

- The bubble exists in an infinite medium.
- The bubble stays spherical at all times during pulsation.
- Spatially uniform conditions exist within the bubble.
- The bubble radius is much smaller than the wavelength of the driving sound field.
- There are no body forces acting (e.g. gravity).
- Bulk viscous effects can be ignored.
- The density of the surrounding fluid is much greater than that of the internal gas.
- The gas content is constant.
- The speed of sound in the fluid is infinite (i.e. the liquid is incompressible).

The fundamental problem with the Rayleigh-Plesset equation is inherent in the last assumption. Since it assumes that the fluid is incompressible, no account is taken of the energy radiated into the fluid. Whilst rudimentary correction factors may be applied,[28] as the amplitude increases proper account needs to be taken of the liquid compressibility. Thus in the absence of correction factors, radiation damping is neglected in the standard Rayleigh-Plesset formulation. Viscous damping appears through the $4\eta\dot{R}/R$ term. Net thermal losses are not taken into account through the use of the polytropic index κ; it merely adjusts the gas stiffness to take into account heat transfer across the bubble wall. Thus, in this model, as much heat flows out of the bubble during the compression half cycle as returns into the bubble during expansion. Hence the only mechanism by which there is net energy loss from the bubble is through viscous effects.

As introduced above, the lack of a radiation damping term in the Rayleigh-Plesset equation can be partially overcome by adding an approximate additional term[i] similar to the viscous damping term[29]. It is of the form:

$$\frac{R(t)}{\rho c}\left(1-\frac{\dot{R}(t)}{c}\right)\frac{dp_B}{dt} \qquad [1\text{-}42]$$

where c is the speed of sound in water.

Thus the Rayleigh-Plesset equation becomes:

$$R(t)\ddot{R}(t)+\frac{3\dot{R}^2}{2}=\frac{1}{\rho}\left\{p_B(t)-p_0-P(t)+\frac{R(t)}{c}\left(1-\frac{\dot{R}(t)}{c}\right)\frac{dp_B}{dt}\right\} \qquad [1\text{-}43]$$

This form of bubble model can in general only be solved numerically, although with small amplitude assumptions the Rayleigh-Plesset can be solved analytically. Since the Rayleigh-Plesset model is included here for illustrative purposes only, numerical methods for solving these non-linear models will be discussed in Section 2.

1.2 Bubble constraints on sonar detection

The frequencies available for sonar detection in the ocean are limited at low frequencies by the target dimension and, at high frequencies by attenuation of the medium itself. These constraints are discussed below.

Consider the constraint of the target dimension. Assume for the moment that the absorption of sound by the water itself can be neglected. In order to maximise the return signal from a non-resonant target, the scattering must be geometric in nature [1-39], i.e. the wavelength of the sound must be very much less than the target dimension[30]. Thus in order to maximise the potential for detecting a target sphere of,

---

[i] Such a term includes no physics beyond that of the linear model, and hence to obtain a true nonlinear representation of radiation damping, it is necessary to employ one of the equations from the Herring-Keller family.

say, 0.1 m radius, the insonifying frequency would have to be much greater than 15 kHz.

However the acoustic absorption of the water itself is usually too large to neglect. The attenuation of sound in a bubble-free ocean increases significantly with increasing frequency[38]. At low frequencies (less than 10 kHz) typical values of absorption are less than 0.001 dB/m. However, at higher frequencies of 200 kHz, this increases to greater than 0.04 dB/m. At very high frequencies of 800 kHz, typical values (at one atmosphere) are in excess of 0.2 dB/m. When compared with the expected level of attenuation from bubbles, of order tens of dB per metre at 50 to 100 kHz, it can be seen that the attenuation of the medium is small but significant as the frequency approaches a MHz. Thus the levels of attenuation of the medium at frequencies greater than a few hundred kHz could pose a further constraint on the frequency range available for sonar detection.

Measurements of oceanic bubble populations (see section 1.1.1) have detected bubbles in the size range 5 – 500 μm. This is not to say that there are no bubbles outside this size range. Rather that the equipment used was not capable of detecting them. The resonance frequency for bubbles of this radius range can be estimated using the Minnaert frequency[4]:

$$\omega_M = \frac{1}{R_0}\sqrt{\frac{3\kappa p_0}{\rho}} \qquad [1\text{-}44]$$

(for the smallest bubbles i.e < 5μm radius, the effect of surface tension becomes important and equation [1-31] must be used in place of [1-44]).

The resonance frequency of bubbles in the range of 5 – 500 μm radius for air bubbles in water at a depth of 5 m would be between 8 kHz and 800 kHz, with the smaller bubbles having the higher resonance frequency. For propagation through oceanic clouds, resonant bubbles are thus potentially present at all frequencies of interest and, therefore, bubble-mediated attenuation cannot be completely avoided by changing the frequency without a priori knowledge of the bubble population and a predictive capability of the type this thesis aims to provide. The bubble-mediated attenuation is, however, a function of frequency and the population distribution. This relationship

will be investigated further in later sections with respect to enhancement of target detection.

When ocean bubbles are present, their contribution to the absorption of sound by bubbles is not easily avoided by choosing a certain frequency range. Once known, their contribution to attenuation can be used to quantify the effect of bubbles on a typical target detection scenario and the potential gains from sonar enhancement. In the next section the linear acoustic cross-sections previously derived will be revisited and applied to bubble clouds to give attenuation per unit length. In section 1.2.2 the sonar equation for active sonar will then be defined, and an example given to illustrate the impact of bubble clouds on detection ranges.

1.2.1 Acoustic cross-sections of bubble clouds

The extinction cross-sections of single bubbles defined in section 1.1.5 can be applied to clouds of many bubbles in order to formulate an attenuation rate in dB per unit distance[31]. This is because extinction cross-sections are proportional to the power dissipated. Hence they are additive for all bubbles which are subjected to the same incident intensity if their radiation is incoherent. As has already been stated in section 1.1.5, calculations based on linear acoustic cross-sections are steady-state time-independent models only and are limited to low sound pressure levels. Furthermore, the application of scattering cross-sections below is range independent since, to add the cross-section all bubbles must be exposed to identical incident intensities.

In order to apply the extinction cross-section to a bubble cloud, the population distribution must be known. It is convenient to define this in terms of the number of bubbles per unit volume (typically 1 m^3) per radius increment (typically 1 μm) or mathematically:

$$n(R_0) = \frac{\text{number of bubbles per radius increment}}{\text{volume}} \qquad [1\text{-}45]$$

Here n represents the number of bubbles per unit radius increment (defined by the bubble equilibrium radius R_0) per unit volume. Hence the number of bubbles per unit volume with a radius between R_0 and $R_0 + dR$ is $n(R_0)dR$.

The extinction cross-section, Ω_{ext} for each radius increment can then be calculated and scaled by the number of bubbles, effectively integrating the cross-section across the bubble distribution provided the restrictions described above are adhered to:

$$S_{ext} = \int_0^\infty \Omega_{ext} n(R_0) dR_0 \qquad [1\text{-}46]$$

Here S_{ext} is the extinction cross-section of a bubble cloud. Assuming that the bubbles are separated enough that there are no bubble-bubble interactions (Appendix B) the cloud extinction cross-section can be used to calculate an attenuation rate.

Clearly not all bubbles can be exposed to the same incident intensity. The above calculation can nevertheless be used by applying it in turn to volume elements in which the incident field has uniform intensity. For example if a plane wave propagates through a uniform bubble cloud, these elements are thin planes perpendicular to the direction of propagation. In such a case the total power (both absorbed and scattered) by each bubble in a given incident sound field in a given volume element is found by multiplying the incident plane wave intensity I_{inc} by the bubble extinction cross-section. In this way the spatial rate of change of intensity for a cloud is:

$$\frac{dI_{inc}}{dx} = -I_{inc} S_{ext} \qquad [1\text{-}47]$$

Integrating gives:

$$I(x) = I_{inc} \exp(-S_{ext} x) \qquad [1\text{-}48]$$

After travelling a distance x, the change in intensity level (ΔIL) will be:

$$\Delta IL(dB) = 10 \log_{10}\left(\frac{I(x)}{I_{inc}}\right) = -10 S_{ext} x \log_{10} e \qquad [1\text{-}49]$$

This equates to the spatial attenuation (α_{cloud}) of a bubble cloud in dB per unit distance by dividing through by x:

$$\alpha_{cloud}(\text{dB/distance}) = \frac{\Delta IL}{x} = 4.34 S_{ext} \qquad [1\text{-}50]$$

This equation will be applied in the following section, where the active sonar equation is used to investigate the impact bubbles have on target detection.

1.2.2 Bubbles and the sonar equation

The active (monostatic) sonar equation in a noise-limited environment (as apposed to reverberation limited)[32] is:

$$SL - 2TL + TS = NL - DI + DT \qquad [1\text{-}51]$$

where SL is the source level; TL the transmission loss; TS the target strength; NL the noise level; DI the directivity index and DT is the detection threshold. All values are in dB ref. 1 μPa @ 1 m.

Consider an example calculation of the source level required for target detection at range r from the source at a driving frequency of 20 kHz. The directivity index for a continuous line transducer[32] of length L and wavelength λ is:

$$DI = \left(\frac{2L}{\lambda}\right) \qquad [1\text{-}52]$$

Thus, 20 kHz with a transducer length of 0.1 m the directivity index is approximately 3 dB.

Measurements of ambient noise levels in coastal waters (such as bays and harbours) have shown that they are subject to wide variations both temporal and spatial. Sources include shipping and industrial noise, wind noise and biological noise. Measurements of ambient noise in harbours and bays[33] during World War II indicate an average ambient noise level of 100 dB (ref. 1μPa @ 1m) at 10 Hz decreasing to 40 dB (ref. 1μPa @ 1m) at 20 kHz. Further studies of five US ports[34] took measurements at 30 kHz, 90 kHz and 150 kHz. Respective average ambient sound pressure levels of approximately -42 dB, -50 dB and -55 dB (ref. 1μPa @ 1m) were measured.

There is a significant discontinuity between the results of the two studies jumping from a noise level of 40 dB at 20 kHz in the first study to –42 dB at 30 kHz for the

second study. Since a driving frequency of 20 kHz is used in this example a noise level of -50 dB is used.

The detection threshold is a function of the signal to noise ratio (SNR) and the detectability of a signal. If the detection signal is know exactly then cross-correlation can be used to search for the detection signal in the received signal with noise. The detection threshold is thus a function of the system bandwidth and processing time and the detectability index. This is a measure of the statistical probability of detecting a signal and the false alarm rate. Assuming a 50% probability of detection and a 2% probability of false alarm the detectivity index (d') is two[35]. The detection threshold is given by:

$$DT = 10\log[(d')^2/(2WT)] \qquad [1\text{-}53]$$

For a detectbility index of 2, a system bandwidth of 1 kHz and a processing time of 0.05s the detection threshold is –14 dB.

Assuming a target sphere of radius a the target strength is given by:

$$TS = 10\log_{10}\left(\frac{a^2}{4}\right) \qquad [1\text{-}54]$$

which gives an approximate target strength of -22 dB for a 0.15 m radius target sphere.

The final term to be defined, the transmission loss, is also the most involved. In this example three mechanisms must be considered; geometric spreading, absorption loss of sound in bubble-free water and attenuation by gas bubbles. In shallow water or in the presence of a mixed bubbly layer geometric spreading is confined to a horizontal wave guide for most frequencies[36,37]. Assuming negligible losses at the boundaries the geometric loss follows a simple cylindrical spreading model:

$$\text{Cylindrical Spreading Loss} = 10\log_{10}(r/r_0) \qquad [1\text{-}55]$$

The absorption of sound in the sea per metre range is small but for completeness is included here. At the two example frequency of 20 kHz the absorption losses are approximately[38] $1x10^{-3}$ dB/m.

The transmission loss owing to the attenuation and scattering of a bubble cloud, α_{cloud}, is determined for this first order calculation using the method defined in the previous section. The model, as has already been stated, assumes linear bubble pulsation at steady state and is range and time independent. A population distribution based on oceanic measurements by Farmer and Vagle[72] is described by the following equation, where R_0 is the bubble equilibrium radius in metres and n is the number of bubbles per cubic metre per μm increment:

$$n(R_0) = 69410e^{-0.0426(R_0 x 10^6)} \qquad [1\text{-}56]$$

The resulting attenuations for this population distribution, under one atmosphere of static pressure, at the example frequency is ~3.0 dB/m. The source level required for target detection is plotted against range in Figure 1-8 for a driving frequency of 20 kHz.

The graph clearly shows that the presence of bubbles can significantly increase the source levels required to detect a target. Typical shipboard sonar systems have output powers ranging from a few hundred watts to tens of kilowatts. This translates to an effective source level of between 210 and 240 dB (ref. 1μPa @ 1m)[39] effectively limiting target detection ranges to ~50 m in the bubble case and approximately 1 km in the no-bubble case for the example shown in Figure 1-8.

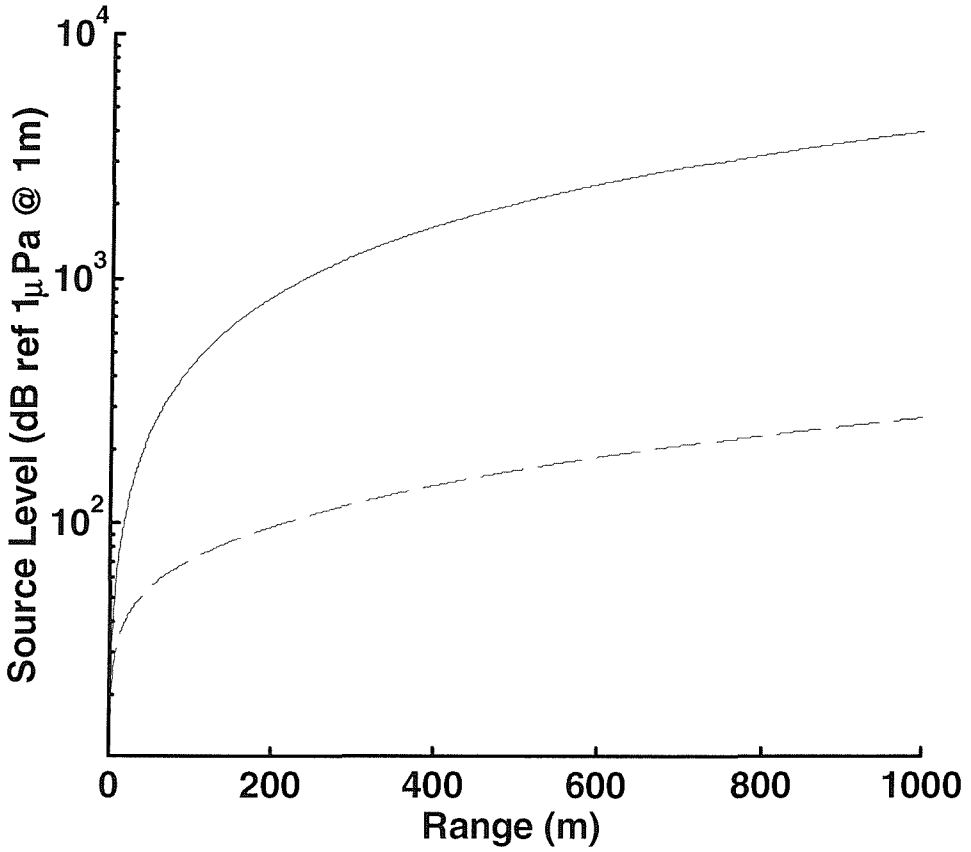

Figure 1-8 The required source level for target detection in coastal waters is plotted versus range at 20 kHz. Source levels as high 1000 dB re 1μPa @ 1m are plotted merely to allow the required source levels with and with out bubbles present to be compared on the same axis; it is of course recognised that such a source level is in practice impossible to generate. The solid line is the source level required with bubbles present and the dashed line indicates the required source level without any bubbles present for comparison.

1.3 A Review of sonar enhancement work

Previous work on methods for enhancing active sonar detection in bubbly environments are reviewed in the following sections. This comprises of three separate studies. For convenience the work reviewed has been separated into those studies that have measured backscatter and those that have measured attenuation. The backscatter section reviews the results of a single sea trial undertaken by Akulichev *et al.*[40] and the attenuation section reviews two sets of data taken in test tanks made by Suiter et al.[42] and Pace et al.[43]. All three sets of published data include some theoretical work that is also discussed.

1.3.1 A Review of pulse dependence in acoustic backscatter from bubble clouds

Prior to this thesis only a single experimental study of the pulse dependence of acoustic backscatter from air bubbles has been published. The work undertaken by Akulichev *et al.*[40] in the early 1980's investigated the backscatter from micro-inhomogeneities in the form of bubbles, solid particles, plankton etc. The backscatter at various frequencies and pulse lengths was investigated experimentally and a simple model was developed for the time-dependent scattering cross-section (the effective target strength in m^2 of the scattering bodies).

A time-dependent cross-section can be derived in a similar fashion to the steady-state cross-section derived in section 1.1.5 by including the transient part of [1-29].

Consider a bubble that is insonified by a pulse with zero amplitude for all times $t<0$; amplitude P_a for $0 \le t \le t_1$; and zero amplitude for $t > t_1$. The cross-section can only be defined for the interval $0 \le t \le t_1$, and in this period it equals the following (from [1-33]):

$$\Omega_{scat}(t) = \left|R_{\varepsilon_o}(t)\right|^2 \frac{\omega^2 b_{RP}^{rad}/2}{P_A^2/2\rho c} \qquad [1\text{-}57]$$

Here the wall displacement $R_{\infty}(t)$ follows some time-varying envelope, comprising (if the pulse is sufficiently large) transient and steady-state periods (as illustrated in Figure 1-2 -Figure 1-5, for example).

If the insonification frequency equals the bubble resonance, the envelope follows a particularly simple form growing monotonically (as $1-e^{-\frac{t}{\tau_0}}$) to steady state (Figure 1-5). This is readily shown as follows.

Equation [1-29], after the initial conditions shown in [1-30] have been included becomes

$$R_{\varepsilon}(t)=\frac{-P_A}{\sqrt{b_{RP}^2\omega^2+\left(-\omega^2 m_{RP}+k_{RP}\right)^2}}e^{-\left(\frac{\delta_{tot}\omega_0}{2}\right)t}\cos(\omega_0 t)+\frac{-P_A\sin(\omega t-\pi/2)}{\sqrt{{b_{RP}}^2\omega^2+\left(-\omega^2 m_{RP}+k_{RP}\right)^2}} \qquad [1\text{-}58]$$

By considering the resonant condition only i.e. $\omega=\omega_o$ and by noting that $\sin(\theta-\pi/2)=-\cos(\theta)$ equation [1-58] becomes:

$$R_{\varepsilon}(t)=\frac{-P_A}{\sqrt{b_{RP}^2\omega^2+\left(-\omega^2 m_{RP}+k_{RP}\right)^2}}e^{-\left(\frac{\delta_{tot}\omega_0}{2}\right)t}\cos(\omega_0 t)+\frac{P_A\cos(\omega_o t)}{\sqrt{{b_{RP}}^2\omega^2+\left(-\omega^2 m_{RP}+k_{RP}\right)^2}}$$

$$R_{\varepsilon}(t)=\frac{P_A}{\sqrt{b_{RP}^2\omega^2+\left(-\omega^2 m_{RP}+k_{RP}\right)^2}}\left(1-e^{-\left(\frac{\delta_{tot}\omega_0}{2}\right)t}\right)\cos(\omega_0 t) \qquad [1\text{-}59]$$

And by using [1-33] to simplify the exponential term and taking the non-oscillatory part of equation [1-58] the envelope of the bubble response is:

$$\left|R_{\varepsilon}(t)\right|=\frac{P_A\left(1-e^{-\frac{t}{\tau_0}}\right)}{\sqrt{b_{RP}^2\omega^2+\left(-\omega^2 m_{RP}+k_{RP}\right)^2}} \qquad [1\text{-}60]$$

This assumes that [1-29] is evaluated at resonance. This limitation will be discussed once the derivation has been completed.

Applying the same simplifications as in section 1.1.5 and taking the square of $|R_\varepsilon(t)|$, equation [1-60] becomes:

$$|R_\varepsilon(t)|^2 = \frac{P_A^2\left(1-e^{-\frac{t}{\tau_0}}\right)^2}{\rho^2 R_0^2\left(\left(\omega_0^2-\omega^2\right)^2+(2\beta_{tot}\omega)^2\right)} \qquad [1\text{-}61]$$

This expression can then be substituted back into [1-57], with further simplification as per section 1.1.5, to give

$$\begin{aligned}\Omega_{scat} &= \frac{4\pi k_{RP}\left(\frac{\omega^4 R_0^3}{3\kappa P_0}\right)\left(1-e^{-\frac{t}{\tau_0}}\right)^2}{\left(\omega_0^2-\omega^2\right)^2+(2\beta_{tot}\omega)^2} \\ &= \frac{4\pi R_0^2\left(1-e^{-\frac{t}{\tau_0}}\right)^2}{\left(\left(\frac{\omega_0}{\omega}\right)^2-1\right)^2+\delta_{tot}^2\left(\frac{\omega_0}{\omega}\right)^2}\end{aligned} \qquad [1\text{-}62]$$

As a final check it can be shown that this is equal to the steady state scattering cross-section ([1-36]) as time $t \to \infty$ since $e^{-\frac{t}{\tau_0}} \to 0$.

In his paper Akulichev defined the time dependent scattering cross-section as[40]

$$|S_n(t)|^2 = \frac{R_0^2\left(1-e^{-t/\tau_0}\right)^2}{\left(\left(\omega_0^2/\omega^2-1\right)^2+\delta_{tot}^2\right)} \qquad [1\text{-}63]$$

where $|S_n(t)|^2$ is Akulichev's notation for the time-dependent scattering cross-section and is used here for clarity.

A comparison of [1-62] and [1-63] shows two discrepancies. The first is that the $\left(\delta_{tot}^2\,\omega_o/\omega\right)^2$ in [1-62] differs from the δ_{tot}^2 in Akulichev's formulation. The reason for

this is that, in deriving [1-59] from [1-29], conditions very close to resonance have been assumed. If $\omega \approx \omega_o$, then of course $\left(\delta_{tot}^2\, \omega_o/\omega\right)^2 \approx \delta_{tot}^2$. Note however, that the same approximation cannot be applied to the $\left(\omega_0^2/\omega^2 - 1\right)^2$ term without the term becoming zero. The second discrepancy is that Akulichev's formulation must be multiplied by a factor of 4π to agree with [1-62] and the steady state cross-section in [1-36] as time $t \to \infty$. This is the result of a difference in the definition of cross-section[41] (back scatter = $\Omega_{scat}/4\pi$), though this is not explicit in Akulichev's paper; however, since the theory in Akulichev's paper is only used to predict the time taken to reach steady-state, it is an omission which has no bearing on their.

Prior to discussing the experimental measurements presented in Akulichev's paper, the limitations of the time-dependent scattering cross-section derived above need to be highlighted. The model is based on linear theory and thus is subject to the limitations of such a theory as previously discussed, i.e. it overestimates the bubble response at higher driving pressures. Additionally, the formulation is valid only very close to resonance. Akulichev acknowledges this limitation by stating in his paper that the time-dependent scattering cross-section is for "near-resonant" gas bubbles only. By this he means bubbles which follow a $1 - e^{-\frac{t}{\tau_0}}$ ring-up. Within the perspective of this thesis it would be better to term these "resonant", and restrict the term "near-resonant" to an important class of bubbles which are sufficiently close to resonance to pulsate at large amplitude, but not so close as to ring-up as $1 - e^{-\frac{t}{\tau_0}}$.

Akulichev *et al.* also measured, experimentally, the instantaneous sound pressure scattered from an oceanic bubble cloud, after insonification by a pulse of length τ and at several different frequencies (5 kHz, 15 kHz and 35 kHz). The experiment was conducted at sea and used a parametric source to produce very short pulse lengths without distortion. The results published in the paper are duplicated in Figure 1-9. Equation [1-32] suggests that the characteristic relaxation time to steady state oscillation, τ_0, should decrease with increasing frequency since it is proportional to $1/f_0$. The value of τ_0 (calculated using Equation [1-32] and Eller's damping theory) is plotted over a range of resonant frequencies in Figure 1-10 where τ_0 decreases from ~6 cycles at 5 kHz to ~3 cycles at 35 kHz. There is a small reduction, of order 1-

2 cycles, in the experimentally measured values of τ_0 in Figure 1-9 (indicated by the light circles in the plot) but it is smaller than predicted by theory. This may be due to the increasing numbers of large off-resonant bubbles scattering inertly as the insonification frequency is increased. The increase in the amplitude of the back-scatter may also be a result of this as well as an increase in the number of resonant bubbles being insonified. These propositions are explored further in subsequent sections.

The Akulichev *et al.* paper predicts theoretically the pulse length dependence in the back-scatter from resonant bubbles and has experimentally measured the back-scatter from an oceanic bubble cloud for varying pulse lengths. However, many questions remain unanswered. The theory presented (equation [1-32]) is linear and, as has already been shown, the bubble is a non-linear oscillator. Since the sound pressure level used is not stated, it is impossible to assess the importance of bubble non-linearity. The contributions to the acoustic response of the population, made by off-resonant bubbles, have also not been considered. The presence of large off-resonant bubbles can account for a significant portion of the sound scattering and may be important when considering the pulse length effects in the bubble response. These issues will be considered further before attempting to enhance transmission through a bubble cloud.

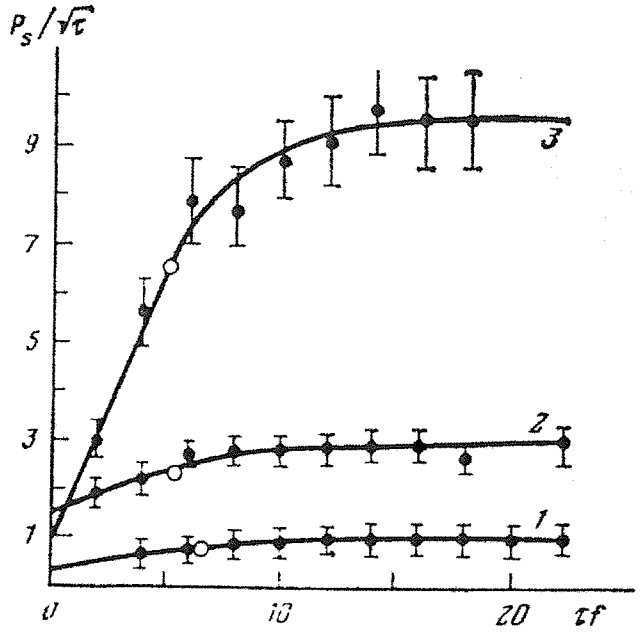

Figure 1-9 Ratio $P_s/\sqrt{\tau}$ (where P_s is the amplitude of the scattered sound) vs. acoustic pulse duration τ at various carrier frequencies f. 1) f = 5 kHz; 2) 15kHz; 3) 35 kHz. The dark circles represent the results of experimental measurements (the data scatter is also indicated), and the light circles represent the values of $P_s/\sqrt{\tau}$ at $\tau = \tau_0$. The parameter τf is the length in cycles of the insonifying pulse. After Akulichev et al.[40]

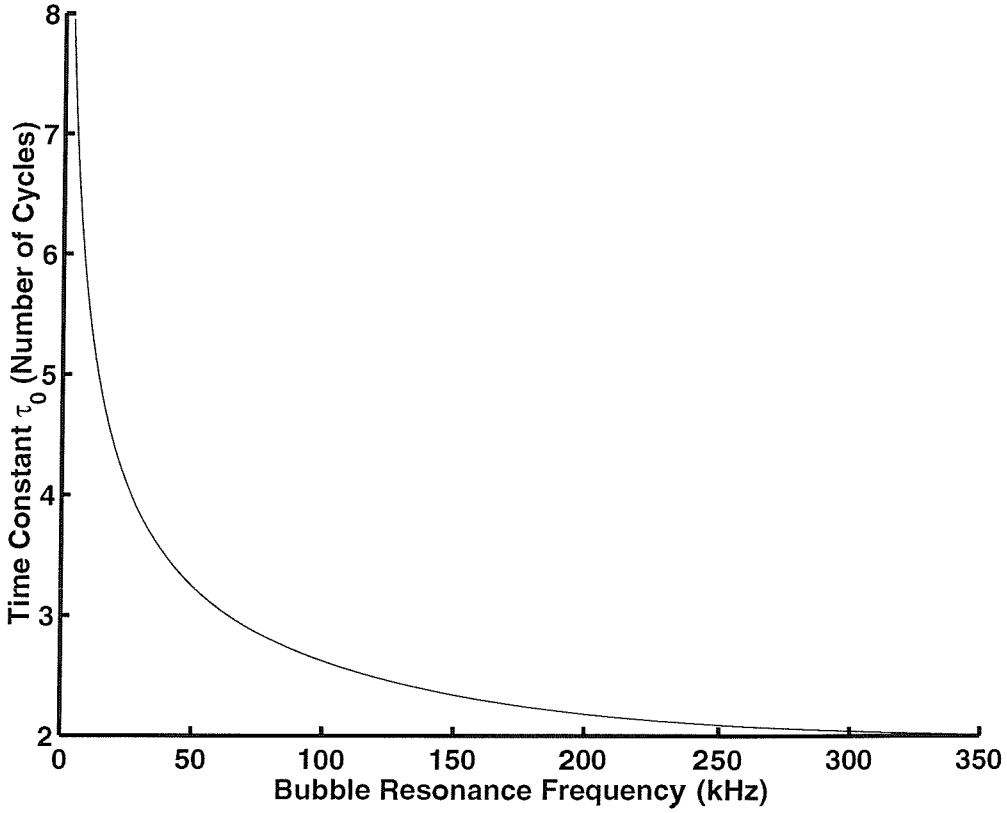

Figure 1-10 Theoretical values of the characteristic relaxation time to steady state oscillation, τ_0, in cycles for a range of bubble resonance frequencies. τ_0 is calculated using equation [1-32].

1.3.2 A review of pulse dependence in attenuation in bubbly water

Two further studies of pulse length dependence have concentrated on the attenuation through bubble clouds for various pulse lengths. The papers were published in the early 1990's, one by Suiter[42] and the other by Pace *et al.*[43] Both studies took place in laboratory tanks with artificially produced bubble clouds. No pulse length dependence was measured.

In both papers the following equation for the time-dependent extinction cross-section for a single bubble is presented.

$$\Omega_{ext}(t) = \Omega_{nr} + \left(1 - e^{-t/\tau_0}\right)\Omega_r \qquad [1\text{-}64]$$

Where Ω_{ext} is the extinction cross-section, Ω_{nr} is the off-resonant extinction-cross section and Ω_r is the resonant extinction cross-section.

Thus, Suiter and Pace *et al.* present identical theories, similar to that of Akulichev's but scaled to give the extinction cross-section (a measure of the total energy loss, not just the loss due to scattering, in m^2) rather than the scattering cross section. The scattering cross-section can be multiplied by $\frac{d_{tot}}{d_{rad}}$ to give the extinction cross-section[23]. However, since the time-dependent cross-section used by Akulichev (and on which Suiter and Pace base their work) is only valid at resonance Suiter and Pace simplify this relationship using Devin's theory of damping at resonance[5] to give:

$$\frac{\delta_{tot}}{\delta_{rad}} = \delta_{tot} \Big/ \frac{\omega_0 R_0}{c} = \frac{\delta_{tot}}{R_0 K} \qquad [1\text{-}65]$$

where K is the wavenumber.

The time dependence modelled by [1-64] is very far removed from that exhibited by real bubbles off resonance. Figure 1-2 and Figure 1-3 suggest the off-resonance response can be complicated (a proposition which will be validated when accurate time-dependent cross-sections are calculated in, for example, Figure 2-6 and Appendix F), but with a cross-section which starts growing from zero at time $t = 0$ (a fact required by arguments of continuity).

In contrast the cross-section of [1-64] is finite at $t = 0$, and takes the value given by the Rayleigh limit [1-38] if $\omega < \omega_o$, or by the geometrical limit [1-39] if $\omega > \omega_o$. It subsequently grows in a smooth $\left(1 - e^{-t/\tau_0}\right)$ fashion (after the fashion of Akulichev's cross-section for a resonant bubble [1-62]), but with a time-dependency far removed from that exhibited by real off-resonant bubbles (Figure 1-2 and Figure 1-3) eventually to reach the steady-state value predicted by the long standing formulation [1-36] (corrected to give the extinction rather then scattering cross-section by multiplying by $\frac{d_{tot}}{d_{rad}}$, as described above). Hence the term Ω_r which Suiter and Pace *et al.* call the resonant cross-section, is a misnomer. It really is the difference indicated by the orange line in Figure 1-7.

Hence there is no physical basis for the time-dependent model described by [1-64], and it is contradicted by time-dependent behaviour of off-resonant bubble predicted by even the linear models.

These assumptions mean that the contribution of near resonant bubbles and especially the time-dependency of the near resonant response is neglected.

In addition, Suiter and Pace *et al.* also apply the resonant damping approximation stated in [1-65] above to the off-resonant contributions. This leads to significant inaccuracies in their estimations of the off-resonant contributions. Figure 1-11 recalculates what their theory would have predicted had they used the off-resonant damping coefficients of Eller[6], which would have been a more accurate implementation of their theory then the resonant damping of Devin[5] which they actually employed.

Experimental measurements of attenuation were made by Suiter in a fresh water test tank with a 120 kHz source and an estimated sound pressure level of 190dB ref. 1 μPa at the face of the bubble cloud. The cloud was generated by electrolysis. The electrical current used was between 0.1 A and 0.2 A. No attempt was made to remove the hydrogen bubbles from the water column (which this thesis found to be critical see section 3.1). The main consideration with this method of generating bubbles, which has to be taken into account when considering the results, is that the hydrogen gas bubbles are likely to behave differently from air bubbles. This is because hydrogen gas has a significantly different density, molar mass, thermal conductivity and specific heat (see Appendix A). If, as is indicated in the paper, similar sized hydrogen and oxygen bubbles exist in the population, then from Prosperetti's[44] damping analysis (which incorporates the thermal effects of the gas; see section 2), the damping of hydrogen is significantly greater. For example the total dimensionless damping of a 25 μm radius bubble in a 120 kHz sound field is ~ 0.07 for Oxygen and 0.87 for Hydrogen. Since the bubble resonance frequency ω_0 is proportional to $\sqrt{\kappa}$ and κ in the above example is 1.04 for air and 1.0005 for hydrogen, the resonance frequency for hydrogen bubbles will have to be lower. The presence of hydrogen bubbles will increase the proportion of off-resonant bubbles and thus may mask any pulse length dependence in the attenuation.

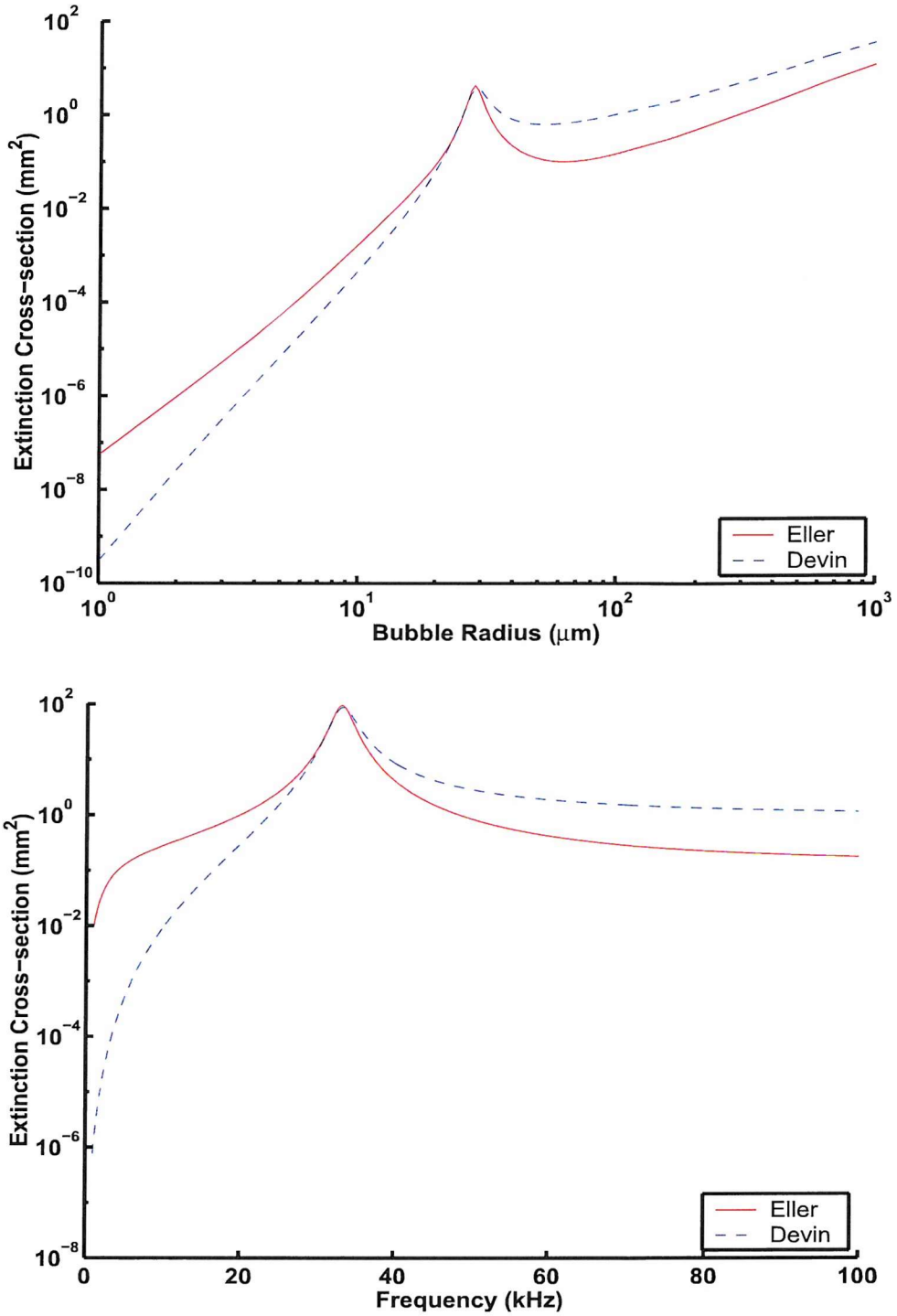

Figure 1-11 A comparison of extinction cross-section calculated using the ratio of the total damping to the radiation damping with Devin's damping at resonance and Eller's damping. The top figure plots the extinction cross-section of a 100 μm air bubble at various frequencies and the bottom figure plots the extinction cross-section of air bubbles of different equilibrium radii in a 120 kHz sound field. Both calculations assume a hydrostatic pressure of one atmosphere.

This may explain why no pulse length dependence was observed when attenuation spectra for short and long pulses were compared in the paper. It should be noted that the potential masking effect of large off-resonant bubbles applies equally to oxygen bubbles as hydrogen bubbles. If there were enough large off-resonance oxygen bubbles present their contribution, due to geometric scattering (section 1.1.1), could again be significant. Although this does not appear to be the case in Suiter's study, it is a consideration for future attempts to measure pulse length dependence. The effect of the contribution of large off-resonant bubbles is considered further in subsequent sections.

As already mentioned, the Pace *et al.* paper uses the same model as Suiter used. Fortunately the experimental results do not rely on the model for interpretation, as is the case for much of the data presented in the Suiter paper discussed above.

Experimentally the work of Pace *et al.* differs from Suiter's in that attenuation is measured at multiple frequencies between 20 kHz and 200 kHz for varying pulse lengths, and a compressed air system is used to generate the bubble cloud. The compressed air was mixed with water and then passed through an orifice. This method of bubble generation[58] generally leads to large numbers of bubbles with a radius in excess of 100 μm. Again no pulse length dependence was detected. This may be due to masking by large off-resonant bubbles as previously described. Unfortunately attempts to measure the bubble distribution optically failed and the only measurement of the bubble population was by inversion of acoustic propagation measurements. This gives no indication of the bubble population above a maximum size of ~120-140 μm radius. If the transient response is important when considering the pulse length dependence, the difference between a non-oscillating bubble and a bubble oscillating at its resonance frequency, even at small amplitudes, may be significant.

In conclusion, there has not yet been a rigorous theoretical study of pulse length dependence in single bubbles and bubble clouds that satisfactorily includes bubble non-linearity, off-resonance contributions, pulse propagation through a cloud and the decay of the bubbles after insonification. Experimental measurements have been more extensive, but again there was, by the start of this project, no systematic investigation of pulse length dependence in attenuation and scattering from bubble clouds under suitable controlled, and monitored, conditions.

1.4 Hypothesis

The following section describes the proposed methodology by which the enhancement of sonar detection in bubbly environments may be achieved. Previous methods of enhancing sonar detection are discussed and the method by which potential enhancement will be investigated is described.

1.4.1 Methods of sonar enhancement in bubbly environments

In total three separate methods of sonar enhancement have been identified. The following paragraphs identify each of these methods and identify potential ways of exploiting them.

Previous measurements[42-44] have indicated that the use of acoustic pulses which have durations that are less than the time taken for a bubble to reach the characteristic relaxation time, τ_o (see [1-33]) may result in a reduction in the attenuation from resonant bubbles. This is clearly illustrated in Figure 1-4 where the amplitude of the bubble response increases with increasing time. However the amplitude of the driving sound field cannot be ignored as it can adversely effect the bubble 'ring-up' (Figure 1-5).

The reason for this pulse length dependence is founded in the non-zero time it takes a resonant bubble to reach steady-state oscillation. For this reason the potential benefits to sonar enhancement are dependent on the population distribution and insonifying frequency. This is because the contribution of the off-resonant bubbles may not exhibit a favourable pulse length dependence, and may swamp the contribution of the resonant bubbles.

One method of exploiting this pulse length dependence for sonar enhancement is to use very short pulses of duration $t << \tau_o$. This method of sonar enhancement will be referred to as Type I enhancement.

Other methods of exploiting the pulse length dependence for sonar enhancement include the use of novel waveforms such as a swept waveform, or chirp, and psuedo-random signals. It is hypothesized that the rapid change in the frequency of insonification may have the same benefit for pulse enhancement (by significantly reducing scattering and attenuation) as a very short pulse, whilst retaining a

reasonable signal to noise ratio. This method of sonar enhancement will be referred to as Type II enhancement.

The final method of sonar enhancement that will be investigated utilises the variability with frequency of the attenuation through a bubble cloud to determine the frequency of minimum attenuation. This method will be referred to as Type III enhancement.

1.4.2 Proposed investigation of enhancement methods

To determine the optimum parameters for sonar enhancement, a series of theoretical and experimental measurements of the response of single bubbles and bubble clouds (with population distributions typical of the oceanic environment) to various waveforms will be conducted.

Existing models of the time-dependent bubble and bubble cloud response are limited in their application by the assumption listed in Table 1-1.

The Medwin model described in section 1.1.5 is a linear steady-state model only and does not include the transient bubble response. It is thus of limited use in investigating time-dependent methods of sonar enhancement. The remaining two models, although time dependent, are limited by the fact that they only include the transient response of resonant bubbles: only the model used by Pace *et al.* and Suiter includes any off-resonant contribution, and this is for steady-state only, and that contribution is itself unphysical. Finally, with the exception of Akulichev's model, the ring-down of the bubble after the driving pressure field has ceased is not included, and again the Akulichev model only considers this at resonance. The effect of bubble ring-down will be considered further in the next chapter.

These assumptions seriously limit the ability of existing models to investigate the potential of novel waveforms. To overcome this, new theoretical models for the response of a single bubble and for bubble clouds will be developed.

In addition this project will seek to develop a method of producing a bubble cloud in a laboratory tank, with a population that more closely mimics that of clouds typically found in the ocean. This bubble cloud generator will then be used in tank experiments to measure the attenuation of a range of signals. The results will then be used to

validate the new theoretical models and to investigate, in conjunction with the models, the potential for sonar enhancement of different driving signals.

A surf-zone based sea trial will be conducted to test methods of sonar enhancement and obtain information on surf-zone bubble populations for further theoretical modelling. These results, in conjunction with further use of the models introduced in this thesis, will be used to determine the relative merits of the different methods of sonar enhancement tested.

	Assumption						
Model	Linear	Time Indepen-dent	Resonance Only	No Off Resonance Contribution	Ring Down not Included	Resonant Damping Model Only	No Off-Resonant Transient Response
Medwin	√	√	X	X	√	X	√
Akulichev	√	X	√	√	X	√	√
Pace & Suiter	√	X	X	X	√	√	√

Table 1-1 List of assumption made by the acoustic cross-section models reviewed in this chapter

CHAPTER 2

THEORETICAL MODELLING

2 Theoretical Modelling

This chapter discusses the development of models for predicting the time-dependent response of a single bubble and bubble clouds. Non-linear models will be introduced to overcome the limitations of the linear models discussed in the preceding chapter. The first limitation is the inaccuracy of the linear model at increasing driving pressures. This can be easily overcome by using numerical solutions to existing non-linear bubble models, such as the Rayleigh-Plesset equation, to give a time-dependent bubble wall response. A more fundamental problem highlighted in the previous chapter is the lack of a fully developed theory to investigate the time-dependent acoustic cross-section of a bubble cloud, including the resonant and off-resonant contributions.

A numerical solution of a non-linear bubble model will be used to determine the time-dependent radiated acoustic pressure. Furthermore this will be used to derive time-dependent scattering and extinction cross-sections. This can then be used to give a first order cloud response in terms of the time-dependent acoustic cross-section.

This model of a bubble cloud using acoustic cross-sections is termed first order because it is range independent. Such effects as attenuation of the signal as it passes through the cloud, and the distribution of the bubbles within the cloud, itself are not accounted for.

The first order cloud model is therefore expanded to include range effects. This is achieved by modelling a cylindrical bubble cloud with an arbitrary population distribution assuming no bubble-bubble interactions. The range-dependent model will be configured to output time series in terms of radiated sound pressure, and to

calculate the time dependent attenuation for an arbitrary driving signal. This will be used to investigate the potential of the different methods of sonar enhancement.

2.1 The single bubble model

In this section a non-linear bubble model and its numerical solution are introduced. The model determines the bubble wall motion as a function of time. It is exploited in this thesis to derive the time-dependent extinction and scattering cross-sections and radiated acoustic pressure. Example outputs are shown for single resonant and off-resonant bubbles.

2.1.1 The Keller-Miksis non-linear bubble model

The Keller-Miksis[27] bubble model (equation 2.1) is an advanced form of the Rayleigh-Plesset equation already introduced. It is used here instead of the Rayleigh-Plesset as it accounts for the finite sound speed in the liquid. This is a significant improvement over the Rayleigh-Plesset equation, but is no more difficult to implement. The correction for the finite sound speed was first introduced by Herring[45] and was derived through the consideration of the effect of underwater explosions. The Keller-Miksis form of the model is:

$$\left(1-\frac{\dot{R}}{c_0}\right)R\ddot{R}+\frac{3\dot{R}^2}{2}\left(1-\frac{\dot{R}}{3c_0}\right)=\left(1+\frac{\dot{R}}{c_0}\right)\frac{1}{\rho}\left\{p_B(t)-p_o-P\left(t+\frac{R}{c_0}\right)\right\}+\frac{R}{\rho c_0}\frac{dp_B(t)}{dt} \qquad [2\text{-}1]$$

$$p_B(t)=\left(p_0+\frac{2\sigma}{R_0}\right)\left(\frac{R_0}{R}\right)^{3\kappa}-\frac{2\sigma}{R}-\frac{4\eta\dot{R}}{R} \qquad [2\text{-}2]$$

Comparison with the Rayleigh-Plesset model [1-43] shows that each of the terms is expanded to account for the finite Mach number of the bubble wall. In addition, there is an extra term dependent on the rate of change of the pressure at the bubble wall. This allows the inclusion of energy storage within the liquid medium around the bubble. As the speed of sound in water $c_0 \to \infty$, the Rayleigh-Plesset equation is recovered from [2-1].

It should be recalled that, whilst the Keller-Miksis equation includes viscous damping (as does the Rayleigh-Plesset), and radiation damping up to first order in $\frac{\dot{R}}{c_0}$, it does not include any net thermal losses. Hence if, for a given bubble size and driving frequency, Eller were to predict $d_{th} << d_{tot}$, then the radius-time plots predicted by the Keller-Miksis equation can be assumed to be accurate. But if d_{th} is not much less then d_{tot}, the radius-time plots will underestimate the losses. To introduce a good practice, in this thesis the ratio d_{th} / d_{tot} will be quoted in figure captions.

This second order differential equation can be solved numerically by using the Runge-Kutta method[46] and rewriting [2-1] as two first order equations as follows:

$$\dot{x}_1 = \frac{\left\{\left(1+\frac{x_1}{c_0}\right)\frac{1}{\rho}\left[p_B(t) - p_0 - P\left(t+\frac{x_2}{c_0}\right)\right] + \frac{x_2}{\rho c_0}\frac{dp_B(t)}{dt} - \frac{3}{2}x_1^2\left(1-\frac{x_1}{3c_0}\right)\right\}}{x_2\left(1-\frac{x_1}{c_0}\right)} \qquad [2\text{-}3]$$

and

$$\dot{x}_2 = x_1 \qquad [2\text{-}4]$$

where $x_1 = \dot{R}$ and $x_2 = R$.

Thus the bubble's wall displacement R, velocity $\dot{R}$, and acceleration $\ddot{R}$ can be determined as a function of time. An example of the output is shown in Figure 2-1 for a 30.8 μm resonant Nitrogen bubble in a 100 kHz, 500 Pa continuous wave sound field for the condition at $t = 0$, $R = R_0 = 30.8\,\mu m$ and $\dot{R} = 0$. This figure clearly shows the amplitude of oscillation increasing monotonically for the first 0.1 ms after the onset of the driving pressure (this is as expected after Figure 1-2 to Figure 1-4, as this bubble is being driven very close to its linear resonance). Thus during this period the bubble is 'ringing-up' but, as the driving force continues beyond this time, the amplitude of response levels off. As already discussed in reference to Figure 1-4 this mode of response is termed steady-state since the amplitude of oscillation is constant with time.

For a resonant bubble the d_{th}/d_{tot} ratio is typically of order 0.78±0.02 for bubbles in the range 10 μm to 200 μm. Introduction of nonlinear thermal damping would be a very major undertaking. The decision has been made to proceed without it, and explore the main characteristics of the time-dependent nonlinear cross-sections that will be developed. Once this pioneering development has been completed in this thesis, incorporation of thermal damping by existing formulations[47,48] could be undertaken as future work.

In the next section the numerical solution to the Keller-Miksis equation is used in the derivation of a time-dependent acoustic cross-section.

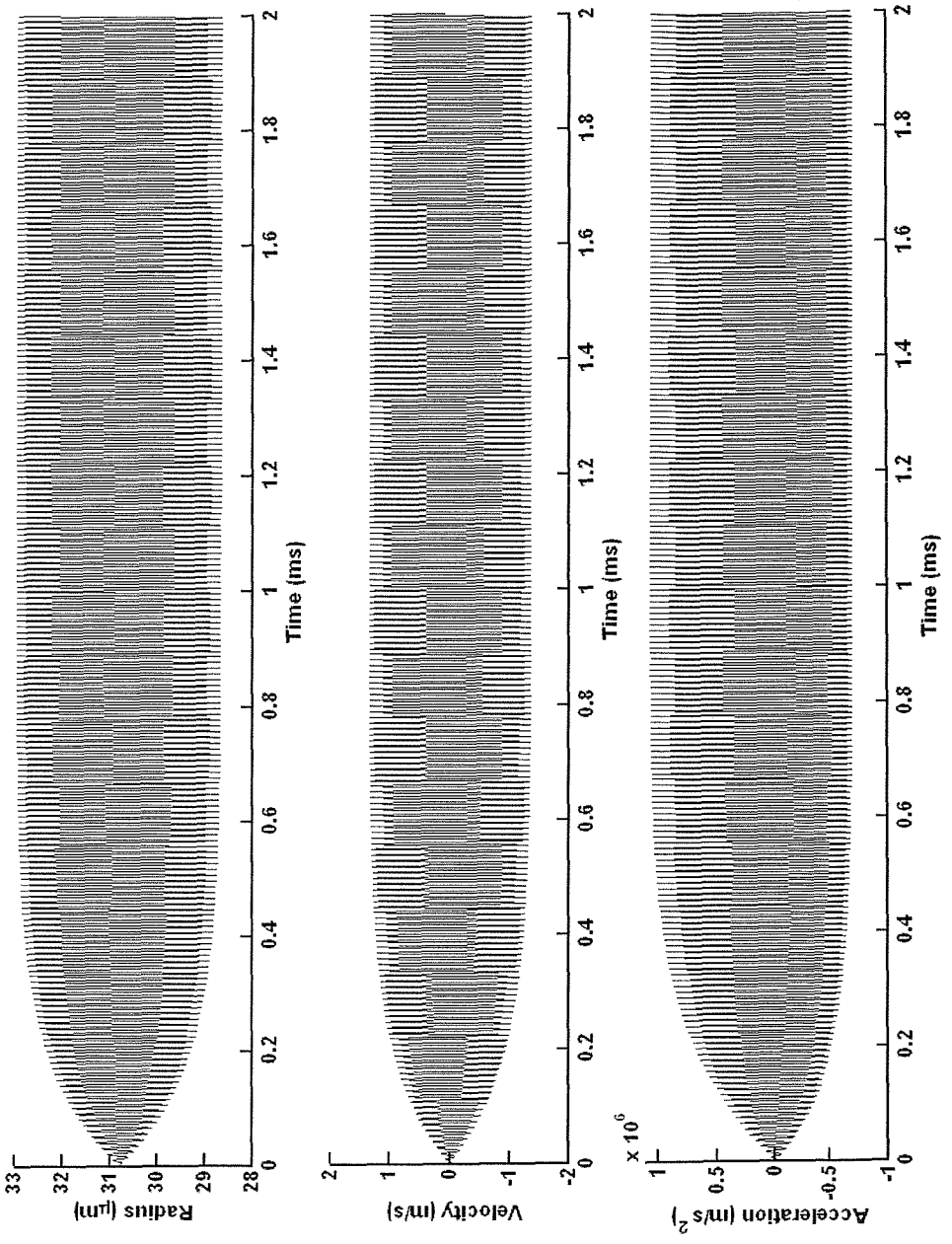

Figure 2-1 Time series showing the response of a 30.8 μm resonant bubble in a 100 kHz, 500 Pa amplitude sound field. Calculated numerically from the Keller-Miksis equation. Plots from left to right: bubble wall radius, wall velocity and wall acceleration plots. The d_{th}/d_{tot} ratio for this plot is 0.80

2.1.2 Time-dependent bubble cross-section and radiated response

In order to derive the scattering cross-section from the analytical solution of the Keller-Miksis, it is first necessary to calculate the radiated sound field. The pressure radiated from a spherically oscillating bubble can be calculated at distances far from the bubble using[49]

$$P_{bl}(t) = \frac{\rho R}{r}\left(\ddot{R}R + 2\dot{R}^2\right) \qquad [2\text{-}5]$$

where r is the distance from the centre of the bubble.

An example of the radiated acoustic pressure 1 m from the bubble centre (using the same parameters as for Figure 2-1) is shown in Figure 2-2.

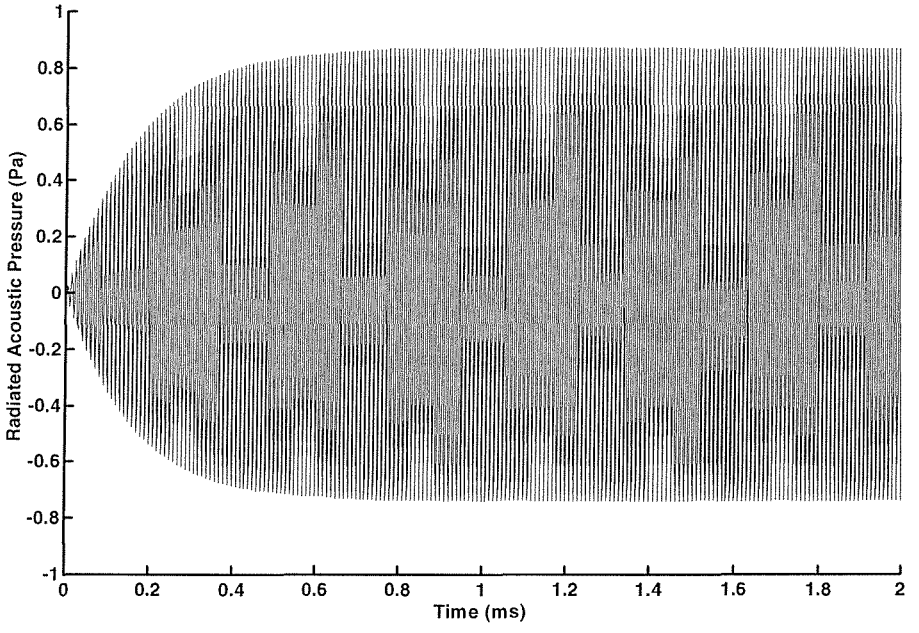

Figure 2-2 Radiated acoustic pressure 1m from a 30.8 μm radius bubble in a 100 kHz, 500 Pa amplitude sound field. The d_{th}/d_{tot} ratio for this plot is 0.80

Similarly the bubble cross-sections, or effective target strength of an oscillating bubble in m^2, can also be calculated. Two cross-sections will be considered, the scattering cross-section, which is a measure of the energy re-radiated by the bubble; and the extinction cross-section, which is a measure of the total energy lost from the system due to scattering and absorption.

In both cases the cross-section can be defined as:

$$\Omega = \frac{\text{Time Averaged Energy Loss}}{\text{Incident Energy}} \qquad [2\text{-}6]$$

For spherical oscillation the power loss is given by:

$$\text{Power} = b_{RF}\dot{R}^2 \qquad [2\text{-}7]$$

where b_{RF} is the damping in the radius-force frame[15]. In the case of the extinction cross-section the total damping should be used, whereas the radiation damping only is used to determine the scattering cross-section.

In order to investigate the effect of changing the insonifying pulse length, using different time-dependent driving signals, it is necessary to measure the time dependent scattering cross-section. Thus [2-7] can be rewritten in terms of the time dependent energy loss required for the acoustic cross-section by integrating over the time period of interest:

$$\Phi = \int_{t_n}^{t_{n+1}} b_{RF}\dot{R}^2 dt \qquad [2\text{-}8]$$

The time dependent cross-section is given by the ratio of the energy loss to the incident energy over the time period of interest. Thus [2-6] becomes:

$$\Omega = \frac{\Phi}{I(t_{n+1} - t_n)} = \frac{\int_{t_n}^{t_{n+1}} b_{RF}\dot{R}^2 dt}{\frac{P_i^2}{2\rho c_0}(t_{n+1} - t_n)} \qquad [2\text{-}9]$$

where P_i is the driving amplitude.

To evaluate [2-9] it is necessary to calculate the damping coefficient b_{RF}. The linear damping theory of Eller[6] can be used to calculate the damping coefficient in the volume-pressure frame (though it should be noted that these coefficients assume small amplitude uniform pulsations).

It should be noted that the above formulation for the time dependent cross-section combines a non-linear bubble model with a linear steady-state damping theory. There is an implied approximation in this technique, which will become increasingly inaccurate for higher sound pressure levels as bubble motion becomes increasingly non-linear. It is possible to develop a fully non-linear theory for the scattering cross-section that can be used as a check on the combined formulation described above. The fully non-linear calculation relies, not on the linearised steady-state damping, but on the non-linear expression of the radiated acoustic pressure from an oscillating bubble given in [2-5] above. The radiated power loss becomes:

$$\Phi_{rad} = \frac{4\pi r^2 \int_{t_1}^{t_{n+1}} \frac{P_{bl}^2}{2\rho c_0} dt}{(t_{n+1} - t_n)} \qquad [2\text{-}10]$$

Thus the new scattering cross-section is:

$$\Omega = \frac{\Phi_{rad}}{I(t_{n+1} - t_n)} == \frac{4\pi r^2 \int_{t_1}^{t_{n+1}} \frac{P_{bl}^2}{2\rho c_0} dt}{\frac{P_i^2}{2\rho c_0}(t_{n+1} - t_n)} \qquad [2\text{-}11]$$

This in turn can be used to calculate the extinction cross-section by multiplying the scattering cross-section by d_{tot}/d_{rad} as per [1-37].

The major advantage of [2-11] over previous methods of calculating cross-sections is in its ability to show time dependence which reflects the various envelopes a bubbles is capable of following off resonance (as show in Figure 1-2 and Figure 1-3). It should be recalled that all previous time-dependent theories could only incorporate time-dependency of the $\left(1 - e^{-t/\tau_0}\right)$ form shown at resonance (Akulichev[40], Suiter[42], Pace *et al.*[43], see Table 1-1). Before exploiting this advance in section 2.1.3 however, it is prudent to compare how the cross-sections predicted by the non-linear theory as $t \to \infty$ compare with the values predicted by the steady-state linear model. It should again be recalled that the previous time-dependent models were scaled to match the predictions of the linear steady-state model as $t \to \infty$, as equation [1-64] showed.

Figure 2-3 compares the different acoustic cross-sections with the linear time independent cross-section derived in chapter 1. The results shown are for a 30 μm bubble driven by a sound field of sound pressure level 1 Pa. The time dependent cross-sections are calculated after two hundred cycles of the driving sound field when the bubble has reached steady state.

The figures indicate a significant difference between the non-linear and linear cross-sections particularly around resonance and must be considered carefully. The non-linear and linear cross-sections shows completely different resonance responses (i.e. resonance frequency and quality factor) and thus differences in the bubble damping. Since as previously mention the Keller-Miksis model does not include thermal damping we would not expect the results of the linear and non-linear models to agree exactly even at this low sound pressure level. However, because of the lack of thermal damping the Keller-Miksis has less damping then the linear model and we thus expect the peak to be narrower and the resonance frequency to be higher[50]. In Figure 2-3 the non-linear peaks do appear narrower (with a Quality Factor of 28 for the non-linear model as compared to 8 for the linear model) but the resonance frequency is less, because the nonlinearity also introduces a frequency shift. To confirm this trend the results are re-plotted in Figure 2-4 but with two different bubble radii to give coincident resonance peaks. The linear model results in Figure 2-4 are now for a 33 μm bubble. The figure shows that the non-linear results do have a narrower peak with a Quality Factor of 30 for the non-linear model compared to 8 for the linear model.

The damping incorporated into the linear and nonlinear models has been shown to be intrinsically different. However, the non-linear model must be used in preference to the linear model owing to its ability to account for non-linear effects at increasing sound pressure levels and because (as has been shown in section 1.3) existing linear models do not accurately describe the time dependence in the bubble response at frequencies away from resonance. It should be noted that at even very low sound pressure levels used to obtain the results in Figure 2-3 (1 Pa) non-linearities are manifest in the results as a second harmonic.

Given the differences between the linear and non-linear cross-sections the different non-linear cross-sections need to be compared. The two different methods of calculating the acoustic cross-sections are consistently offset by a small margin. In

the case of the extinction cross-section both derivations include a linear approximation. However, the comparison plot of the extinction cross-section in Figure 2-3 is very similar to the scattering cross-section with an almost identical offset between the two non-linear calculations. Furthermore, the introduction of the linear approximation into the extinction cross-section calculation occurs at a later stage in the derivation, when using the dimensionless damping ratio. In effect the fully non-linear scattering cross-section is being scaled by the linear approximation. In this way the non-linear velocity and acceleration of the bubble are still retained in the radiated pressure term rather than being discarded, as is the case when the damping coefficient b is used. It is thus reasonable to consider the formulation that uses the dimensionless damping ratio to be the more favourable approximation of the non-linear extinction cross-section.

Although the results using the damping coefficient, b, agree better with the linear cross-section (as expected as this partially corrects for the differences in the damping models) Figure 2-3 and Figure 2-4 show that the linear and non-linear results cannot be compared directly. Thus it is more desirable to maintain a consistent approach using the radiated pressure term than to use the linear damping coefficient simply because it agrees slightly better with linear theory away from resonance.

The following section discusses the implication of these findings for sonar enhancement. The theory is then used to calculate the non-linear cross-sections and the scattering and attenuation of a bubble cloud.

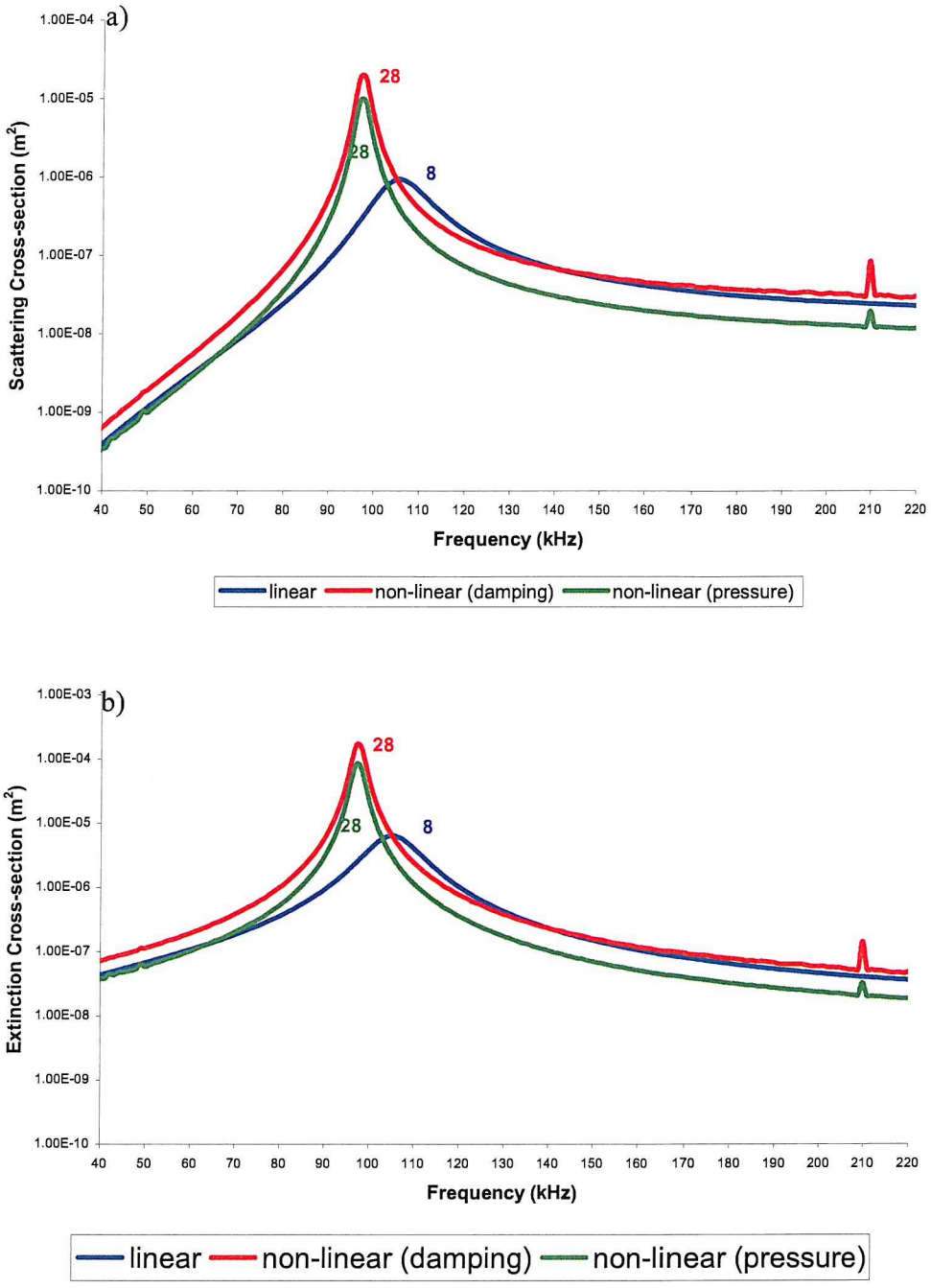

Figure 2-3 Comparison of linear and the different non-linear methods of calculating the acoustic cross-section at 1 Pa sound pressure level for a 30 μm radius bubble. Plot a) shows the various scattering cross-sections and plot b) the extinction cross-sections. In both plots the blue line indicates the linear cross-section whilst the red line uses the damping term, b, and the green line use the radiated pressure term from the Keller-Miksis model. In all cases the dimensionless damping ratio is used to get the extinction cross-section. Note the harmonic in the non-linear model at twice the resonance frequency.

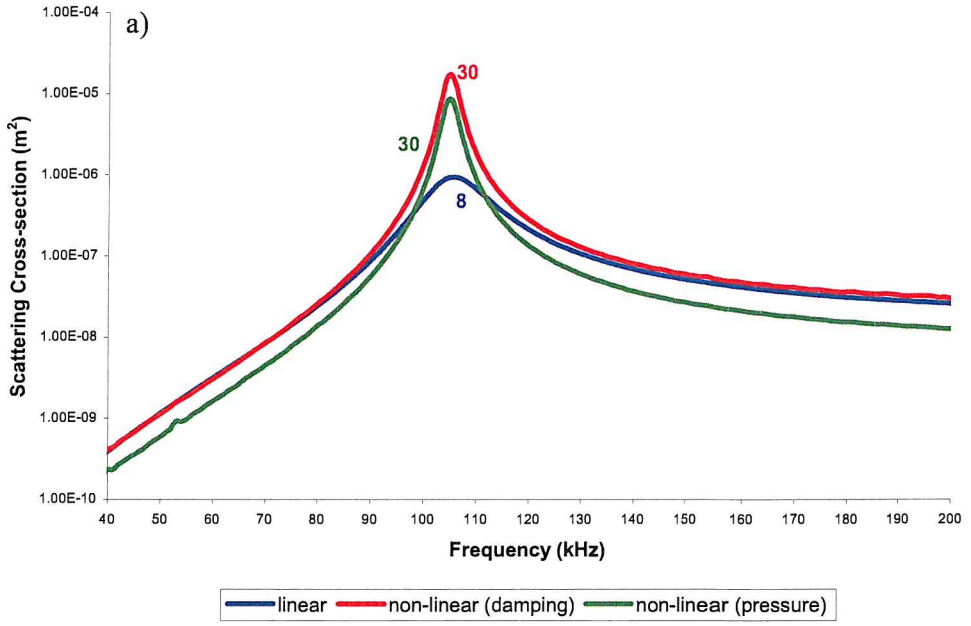

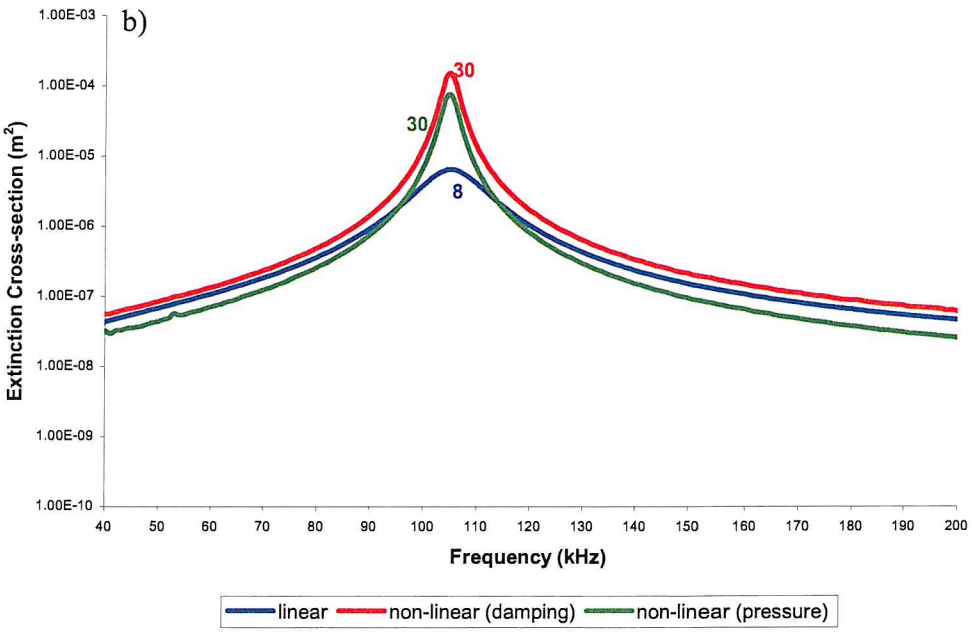

Figure 2-4 Comparison of linear and the different non-linear methods of calculating the acoustic cross-section at 1 Pa sound pressure level for a 30 μm and 33 μm radius bubble for the linear and non-linear models respectively. Plot a) shows the various scattering cross-sections and plot b) the extinction cross-sections. In both plots the blue line indicates the linear cross-section whilst the red line uses the damping term, b, and the green line use the radiated pressure term from the Keller-Miksis model. In all cases the dimensionless damping ratio is used to get the extinction cross-section. Note the harmonic in the non-linear model at twice the resonance frequency.

2.1.3 Implications for sonar enhancement

The time-dependent bubble wall response and the scattering cross-section [2-11] of a single bubble have been calculated (using the preferred formulations of the non-linear cross-section described in the previous section) for a sound pressure level of 1 Pa, 1 kPa and 10 kPa. The results for a bubble near resonance are given in Figure 2-5 and Figure 2-6 showing respectively the time-dependencies of bubble radii and the scattering cross-section of the bubble in response to a semi-infinite duration pulse which starts at t=0. Since it is a ratio of energy loss over incident energy the scattering cross-section must be calculated over a finite period of time. In this case it is calculated for each cycle of the insonifying sound field to give the cycle-by-cycle variation in the cross-section.

The results show that as the driving pressure becomes large, despite the increase in amplitude of bubble wall oscillation (Figure 2-5), the scattering cross-section decreases (Figure 2-6). This is because the definition of the scattering cross-section normalises the power scattered by the bubble to the intensity of the incident plane wave and, unlike in linear theory, the bubble response no longer scales linearly with driving pressure. The reduction in the time taken to reach steady-state as the driving amplitude increases (Figure 2-6) also indicates that the likelihood of detecting 'ring-up' effects decreases as the driving pressure is increased.

Note that the $\left(1-e^{-t/\tau_0}\right)$ 'ring-up' envelope which (as Figure 1-2 to Figure 1-5 showed) is a characteristic of the linear resonance condition, is present only at the lower driving amplitudes. A major strength of this approach is its ability to describe time-dependencies other than $\left(1-e^{-t/\tau_0}\right)$ which has been shown to only occur very close to resonance at small driving amplitudes. As will be seen, it is this behaviour that is key to understanding why the findings of Suiter and Pace *et al.* appear to contradict those of Akulichev, and to explain how sonar enhancement might be achieved.

To illustrate the ability of this method to describe time-dependencies that depart from $\left(1-e^{-t/\tau_0}\right)$ ring-up the bubble response when driven off resonance is shown in Figure 2-7 and Figure 2-8.

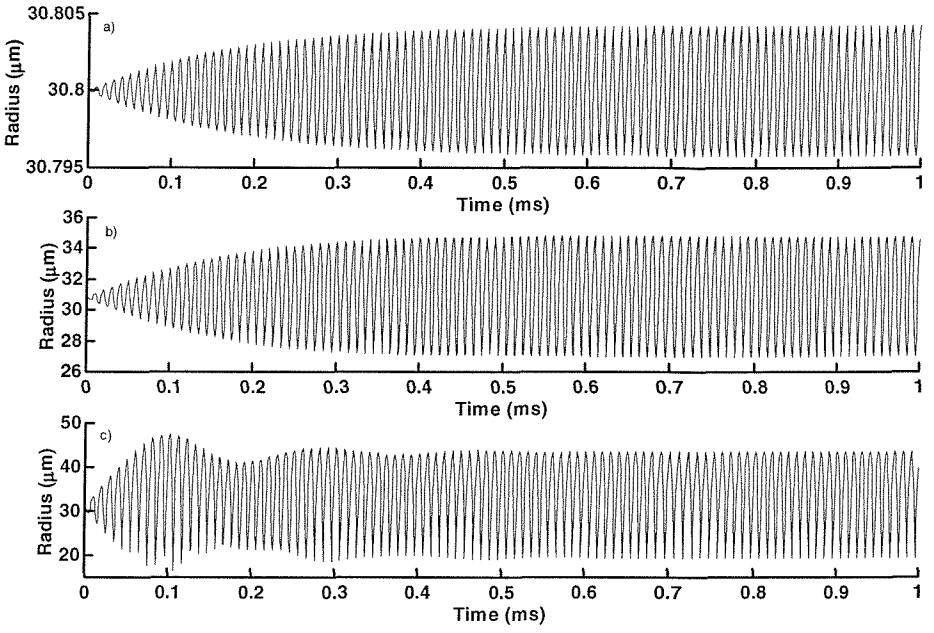

Figure 2-5 Bubble wall radius time series for a resonant bubble (R_0=30.8 μm) in a 100 kHz sound field of sound pressure amplitude a) 1 Pa, b) 1 kPa and c) 10 kPa.

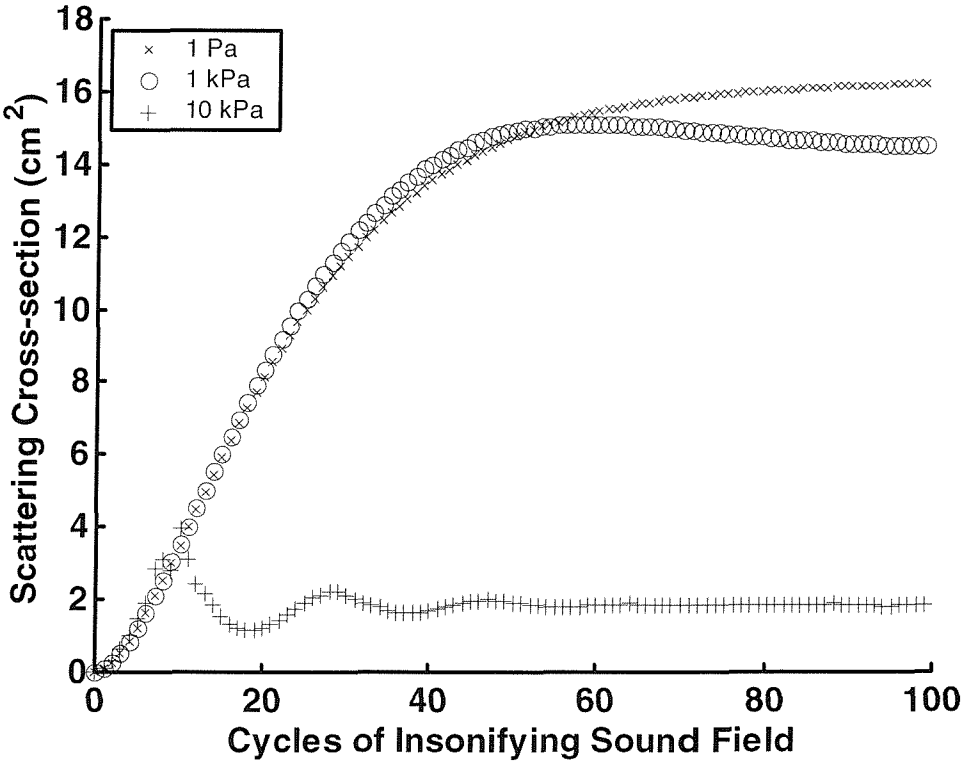

Figure 2-6 Predictions of the scattering cross-section for driving amplitudes of 1 Pa (+), 1 kPa (x) and 10 kPa (O) for a 30.8 μm resonant bubble in a 100 kHz sound field. The preferred non-linear bubble cross-sections are used.

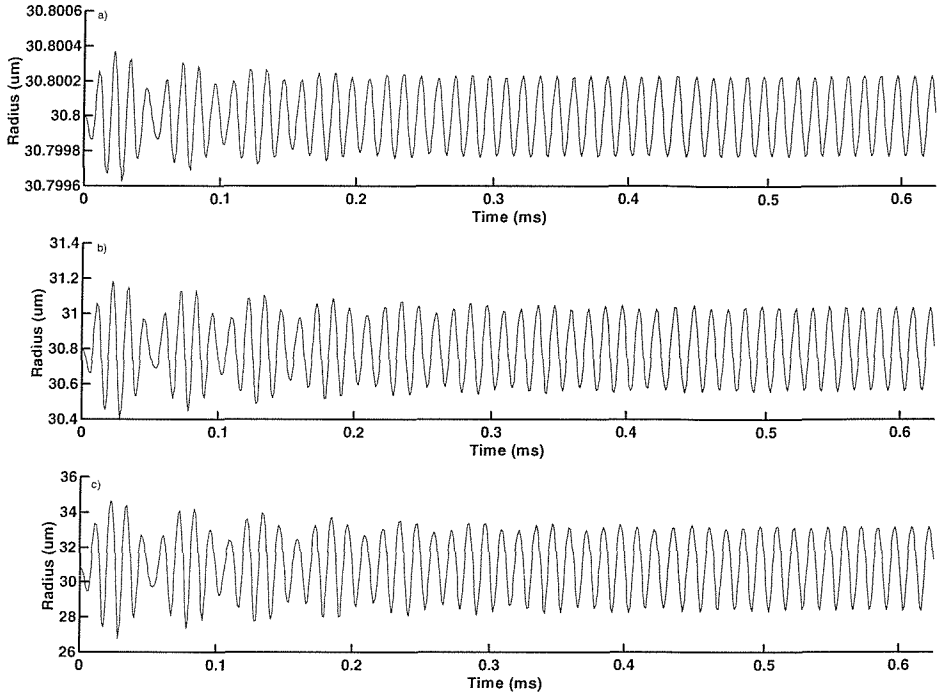

Figure 2-7 Bubble wall radius time series for an off-resonant bubble (R_0=30.8 μm) in a 80 kHz sound field of sound pressure amplitude a) 1 Pa, b) 1 kPa and c) 10 kPa.

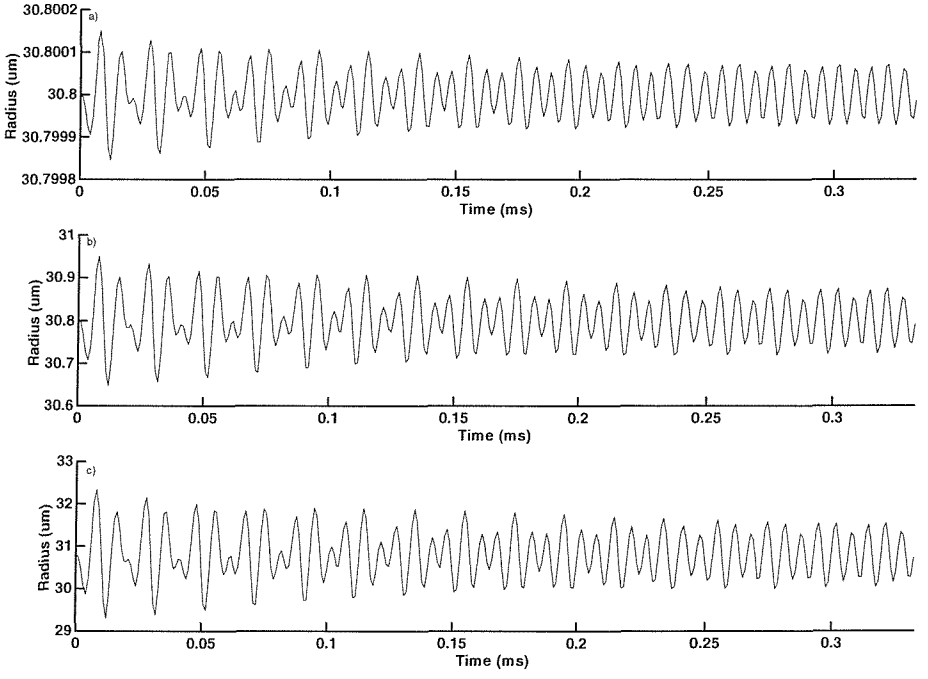

Figure 2-8 Bubble wall radius time series for an off-resonant bubble (R_0=30.8 μm) in a 150 kHz sound field of sound pressure amplitude a) 1 Pa, b) 1 kPa and c) 10 kPa.

2.2 Range independent bubble cloud models

The formulation for the time-dependent cross-section and the radiated acoustic pressure of an oscillating bubble (described above), can be used as the basis for modelling the response of a bubble cloud. Two types of cloud model have been developed. The first type (called subsequently the range independent model) is a simple model for estimating the scattering cross-section for a given population of incoherently scattering bubbles. This model assumes all the bubbles are excited simultaneously and so ignores propagation through the cloud.

The second model type (called subsequently the range dependent model) simulates the response from a cylindrical bubble cloud of finite dimension, including propagation through the cloud. A cylindrical cloud has been chosen as it closely mimics the sort of cloud that can easily be generated artificially in the laboratory. However, as will be shown, the model reduces the position of each bubble to a time delay corresponding to the onset of insonification. Thus an arbitrary cloud shape can be created if necessary.

Here, however, the cloud is modelled as a number of randomly distributed bubbles within a cylindrical cloud. The response of the cloud is then calculated by incoherently summing the response of each bubble. The cloud response to an arbitrary incident sound field is then easily determined. In all cases the effect of multiple bubble interactions is assumed to be negligible. The criteria for this assumption to be valid are reviewed in Appendix B.

The assumption of coherent or incoherent scattering in the cloud models also requires further clarification. In the case of the simple cloud model all the bubbles are assumed to be insonified simultaneously, and the scattering or extinction cross-section is used to calculate the cloud response. This assumes that the bubble response is coherent since adding cross-sections is equivalent to a summation of the respective power losses from the incident wave as a result of each bubble.

2.2.1 Simple cloud model for an infinite duration pulse

The analysis of the acoustic cross-section of a bubble cloud in chapter 1 can be combined with the non-linear time-dependent acoustic cross-section derived above to give a first-order estimation of the time dependent cross-section of a bubble cloud

insonified by an infinitely long driving pulse (a journal paper by Clarke and Leighton investigating this is included in Appendix F). It is assumed that the bubble population density is sufficiently small that bubble-bubble interactions can be neglected, as is the reduction in intensity of the incident wave as it propagates through the cloud. By calculating the cross-sectional areas of single bubbles of varying radii, and incoherently summing the results, the cycle-by-cycle response of a bubble layer with a population size distribution can be calculated. The density of the population is then simply a scaling quantity given the limitations discussed above. Thus [1-46] becomes:

$$S(t) = \int_0^\infty \Omega(t) n(R_0) dR_0 \qquad [2\text{-}12]$$

and the time-dependent scattering or attenuation of the cloud in dB per unit distance is given by (from [1-50]):

$$\alpha_{cloud}(\mathrm{t}) = 4.34 S(t) \qquad [2\text{-}13]$$

Figure 2-9 and Figure 2-10 summarises the time dependent cross-section of a range of bubble sizes in a continuous 1 kPa and 10 kPa sound field respectively. For any given fixed time, the plot of cross-section as a function of radius exhibits the familiar characteristics of resonance scattering dividing the Rayleigh and the Geometric scattering regimes, (as defined in section 1.1.5 and Figure 1-6). A ring-up time is also evident at resonance.

Therefore, the response of a bubble distribution can be investigated by applying [2-12], which scales the individual bubble response by the population distribution. When the population distribution is described in the conventional fashion of numbers of bubbles per μm increment per metre cubed the time dependent total response of a bubble cloud of volume 1 m^3 can be ascertained using this equation.

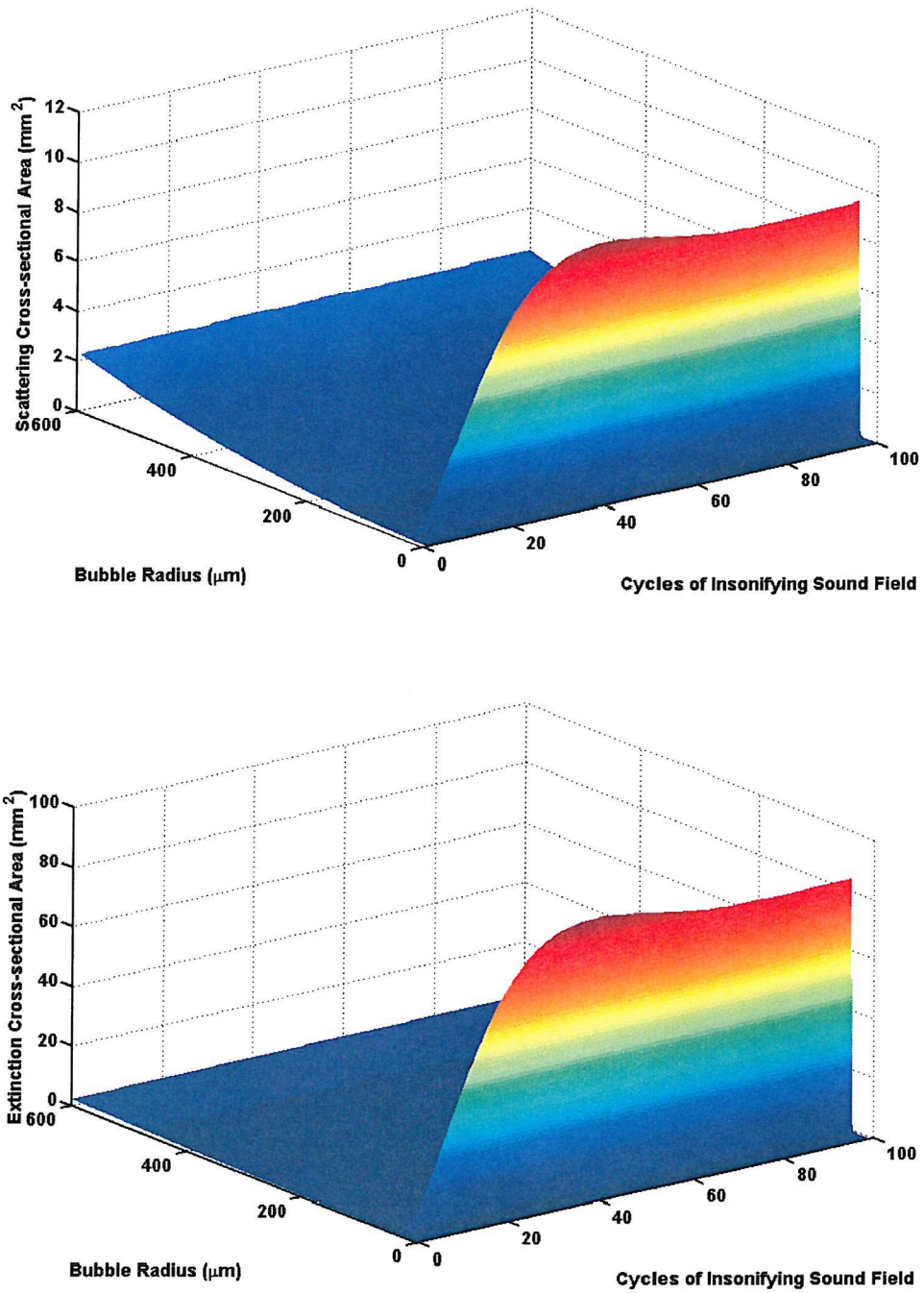

Figure 2-9 Scattering (top) and extinction (bottom) cross-sectional area of a single air bubble in water of equilibrium radius up to 600 μm in a 100 kHz sound field of amplitude, 1 kPa under 1 atmosphere of hydrostatic pressure.

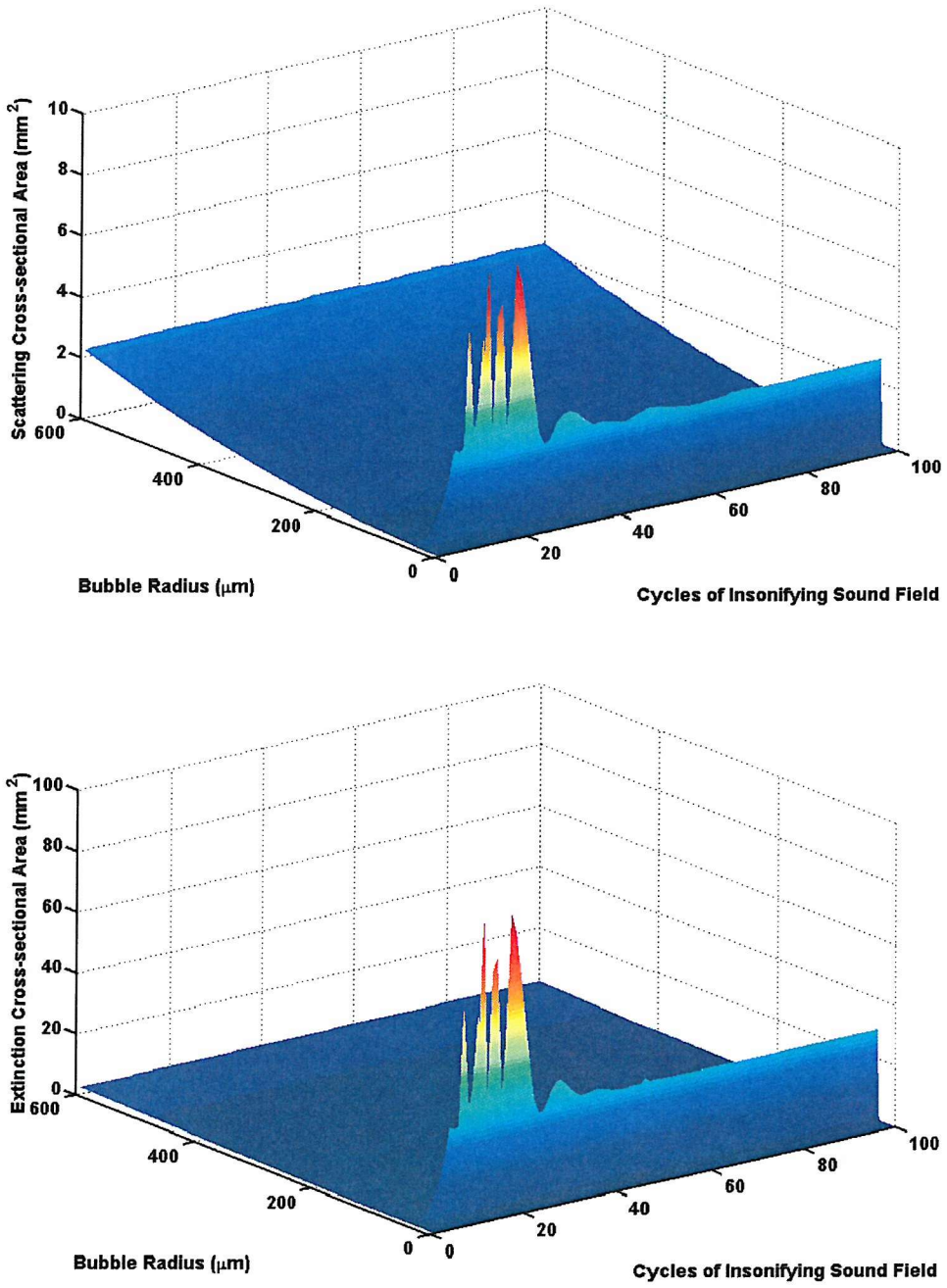

Figure 2-10 Scattering (top) and extinction (bottom) cross-sectional area of a single air bubble in water of equilibrium radius up to 600 μm in a 100 kHz sound field of amplitude, 10 kPa under 1 atmosphere of hydrostatic pressure.

Throughout this section the Farmer and Vagle[72] measurements of oceanic bubble populations are used as an example of a typical bubble distribution. For computational purposes a curve ([2-14]) has been fitted to the data and the population extrapolated over the required radius range.

$$n(R_o) = 69410e^{-0.0426R_o} \qquad [2\text{-}14]$$

where R_0 is in μm. A logarithmic plot of equation [2-14] is shown in Figure 2-11.

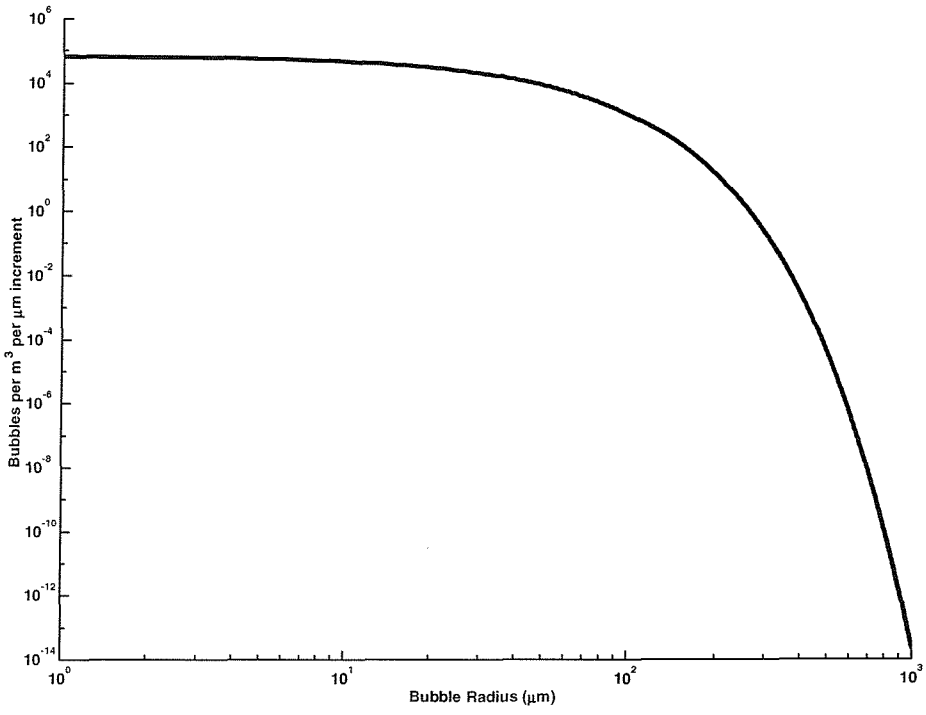

Figure 2-11 Logarithmic plot of the Farmer and Vagle[72] population distribution using equation [2-14].

The time-dependent cross-section and attenuation for a 1 m^3 cloud using the Farmer and Vagle[72] bubble distribution in a 100 kHz sound field of amplitude 1 kPa and 10 kPa, is shown in Figure 2-12 and Figure 2-13. The cross-section is calculated discretely for pulse lengths of 1 to 100 cycles and the bubbles are under one atmosphere of hydrostatic pressure. The top row of plots in Figure 2-12 and Figure 2-13 indicate the extinction cross-section of the cloud as a function of radius and

time. The top plots are an intermediate step and represent the function $S(t)$ from [2-12] prior to integration where each bubble size has been multiplied by the number of bubbles of that size in a 1 m^3 cloud.

The next step is to apply the integral from [2-12] to give the time-dependent cross-section of the cloud $S(t)$. The middle line of plots in Figure 2-12 and Figure 2-13 show the cloud response as a function of time after integrating with respect to the bubble radius.

Finally equation [2-13] can be applied to determine the time dependent attenuation of the cloud in dB per unit distance. The result of applying [2-13] is shown in the bottom plots of Figure 2-12 and Figure 2-13. Since the population distribution used ([2-14]) is for a 1 m^3 cloud the attenuation calculated from [2-13] has unit dB/m.

The plots of Figure 2-12 and Figure 2-13 reinforce the importance of using a non-linear time-dependent bubble model in this investigation. The resonant bubble response for the 10 kPa sound pressure level in particular widely deviates from the $\left(1-e^{-t/\tau_0}\right)$ 'ring-up' predicted by the linear model. It should also be noted that the models of Suiter assume a time invariant off resonant contribution added to a $\left(1-e^{-t/\tau_0}\right)$ resonant contribution ([1-64]). We have already seen that the $\left(1-e^{-t/\tau_0}\right)$ assumption is only valid under at low amplitudes for bubbles at resonance. Close examination of the results shown in Figure 2-12 and Figure 2-13 indicate that the bottom attenuation plots do not exactly follow the resonant response apparent in the top most plots. This is not unexpected as we have already seen the complex nature of the bubble off resonant response predicted by the non-linear model in Figure 2-7. However this conclusion is not immediately apparent from Figure 2-12 and Figure 2-13. It is also impossible to ascertain the relative importance of the contribution of resonant bubbles, bubbles near to resonance but not at resonance, and bubbles off resonance. To investigate these issues further the results shown in the bottom plots of Figure 2-12 and Figure 2-13 are broken down into these regions and the results plotted in Figure 2-14. For the purposes of this plot the off-resonant bubbles are considered to be those bubbles that do not exhibit a ring up or transient behaviour. The resonant bubbles are those that exhibit a monotonic ring up. The near resonant bubbles are the remaining bubbles defined by the limits of the resonant and off resonant regions. In Figure 2-14 these regions are defined as follows. The resonant

contribution includes all bubbles in the 31 μm radius bin. The off-resonant contribution includes all bubbles in the 1 to 15 μm and 50 to 300 μm radius bins. The near resonant contribution includes all bubbles in the 16 to 30 μm and 32 to 49 μm radius bins.

It is clear from Figure 2-14 that for this population distribution the bubbles at, and near to, resonance dominate the cloud cross-section. For the first 20 cycles of the 1 kPa plot the near-resonant bubbles are proportionally more important than the resonant bubble contribution. Furthermore, by increasing the amplitude, the relative importance of the near resonant bubbles increases for all pulse lengths. The off-resonant bubbles contribute little to the cloud response for both the 1 kPa and 10 kPa sound pressure levels.

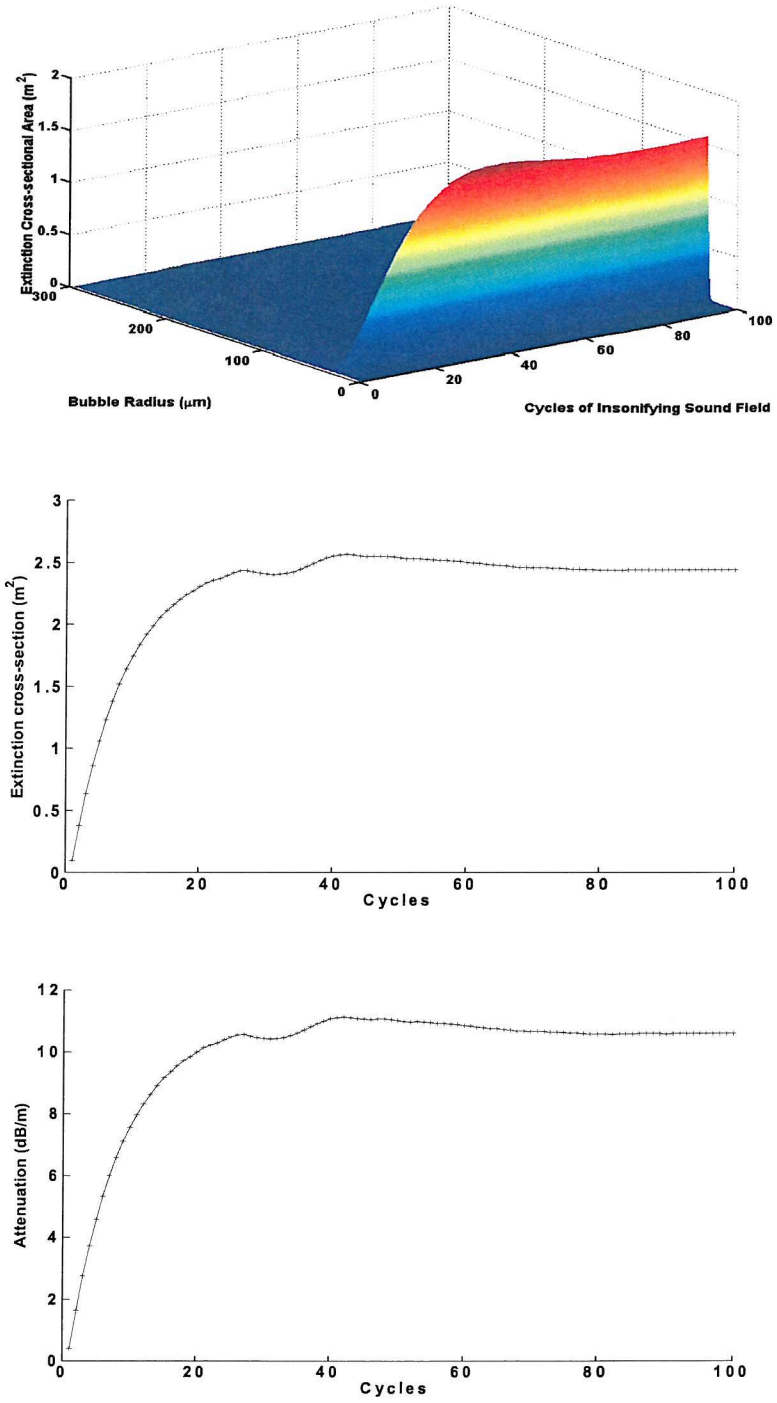

Figure 2-12 The attenuation of a 1 m^3 bubble cloud using the non-linear range independent cloud model. The population distribution is that of Farmer and Vagle[72]. All plots are for a 100 kHz sound field of amplitude 1 kPa. The top plot shows the extinction cross-section as a function of bubble radius and cycles of the insonifying sound field scaled by the population distribution. The middle plot shows the extinction cross-section of the cloud as a function of cycles of the insonifying sound field. Finally the bottom plot is the attenuation of the cloud in dB/m, again as a function of cycles of the insonifying sound field.

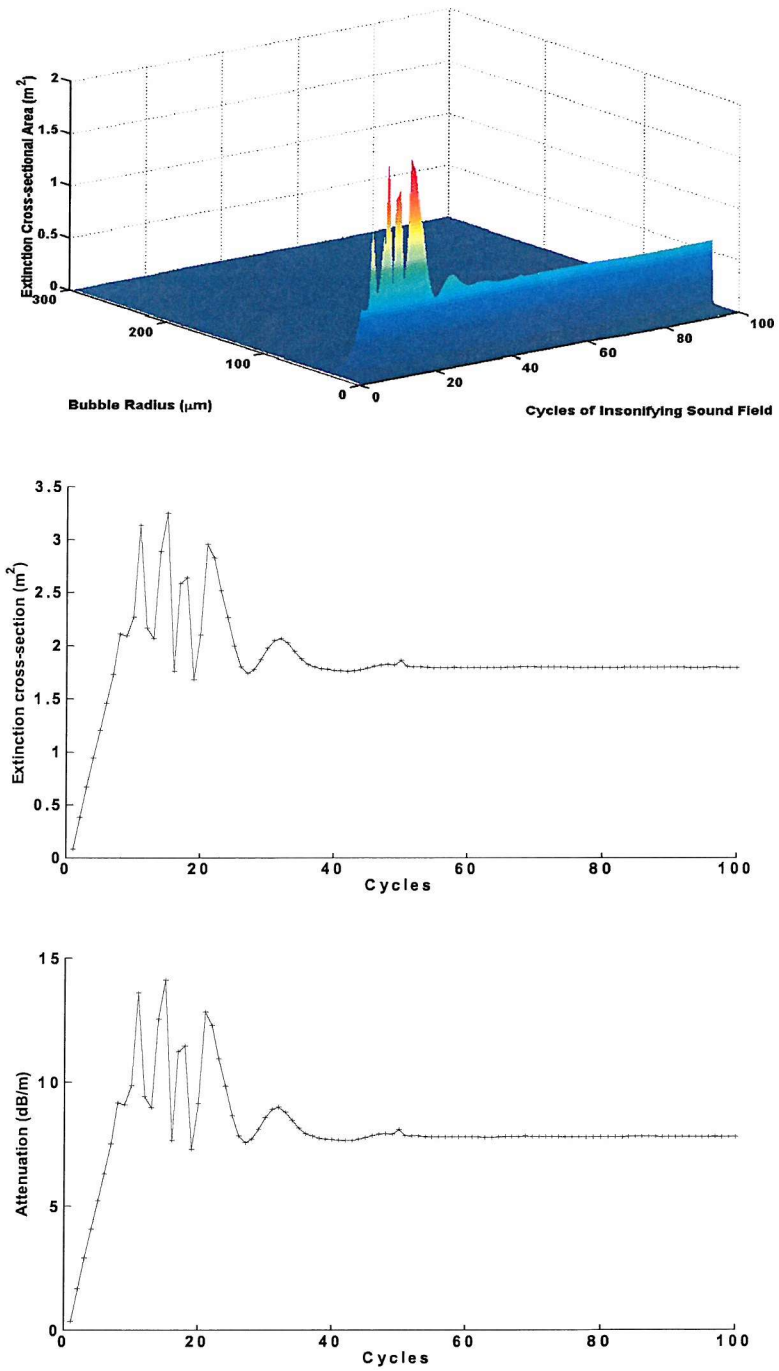

Figure 2-13 The attenuation of a 1 m^3 bubble cloud using the non-linear range independent cloud model. The population distribution is that of Farmer and Vagle[72]. All plots are for a 100 kHz sound field of amplitude 10 kPa. The top plot shows the extinction cross-section as a function of bubble radius and cycles of the insonifying sound field scaled by the population distribution. The middle plot shows the extinction cross-section of the cloud as a function of cycles of the insonifying sound field. Finally the bottom plot is the attenuation of the cloud in dB/m, again as a function of cycles of the insonifying sound field. This is a discrete calculation for the data points plotted. Line between data points are included to aide in interpretation.

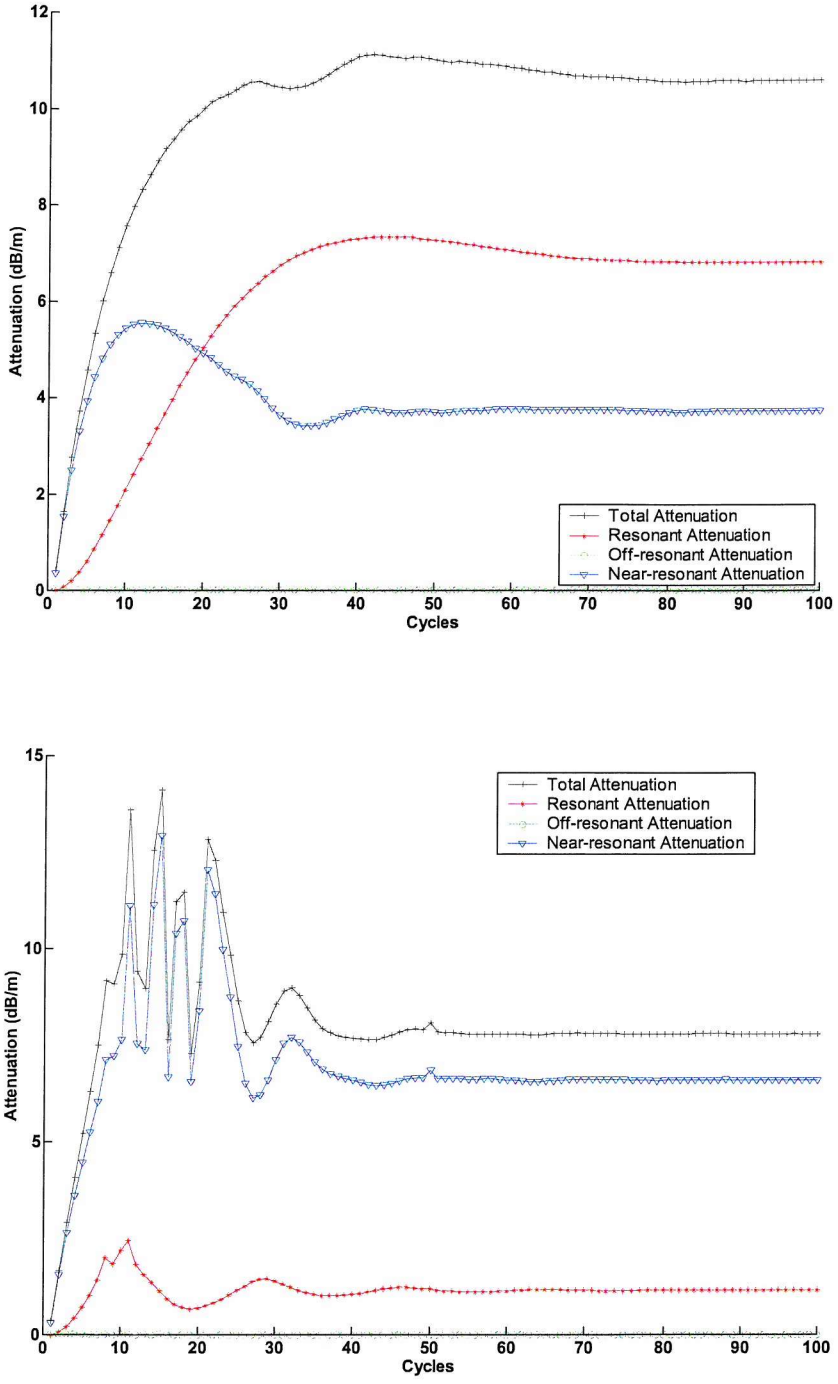

Figure 2-14 The attenuation of a 1 m^3 bubble cloud using the non-linear range independent cloud model. The population distribution is that of Farmer and Vagle[72]. All plots are for a 100 kHz sound field of amplitude 1 kPa (top) and 10 kPa (bottom). Each plot shows the attenuation of the entire cloud (+) the contribution of the resonant bubble (♦), the contribution of the off-resonant bubbles (o) and the contribution of the near resonant bubbles (▽). This is a discrete calculation for the data points plotted. Lines between data points are included to aide in interpretation.

2.2.2 Simple cloud model for a finite duration driving pulse

Unlike the formulation used in previous studies by Pace *et al.*[43] and Suiter[42], the technique used here employs a non-linear bubble model to overcome the limitations of the linear model (section 2.1.2). In addition, the time-dependency has a physical basis. In all the previous calculations of the acoustic cross-section in this chapter the limits of the integrations to calculate the energy loss have corresponded to the length of the driving pulse. This method of calculating the cross-section is suitable for investigating how the bubble cross-section changes as the length of the driving pulse increases, but it assumes the bubble is being driven by a pulse of infinite length. It can thus be considered to be a measure of the cycle-to-cycle variation in acoustic cross-section and not the cross-section of a cloud in response to an insonifying waveform. This is because when the driving pulse ceases the bubble will continue to oscillate at its resonance frequency. These oscillations will decay away as a function of the damping at resonance and represent additional energy loss from the insonifying sound field. This 'ring-down' of a bubble must be included in the non-linear formulation of the acoustic cross-sections or the cloud model will underestimate the energy loss and thus the cloud attenuation when driven by a finite length pulse.

To investigate this problem the calculations of the extinction cross-section of a 1 m^3 bubble cloud using the Farmer and Vagle[72] population are recalculated for pulses of finite length. To investigate the effect of different pulse lengths the limits of the integral in [2-9] now represent the full extent of the driving pulse and the bubble response from $t = 0$ to the time when the bubble returns to rest.

Cross-sections have been calculated for a driving frequency of 100 kHz and pulse durations of 1 to 100 cycles in 5 cycle steps to reduce processing time.

The results are shown in Figure 2-15 and Figure 2-16 for a 100 kHz 1 kPa and 10 kPa sound pressure level driving pulse respectively. The top plot shows the extinction cross-section of a 1 m^3 cloud with the Farmer and Vagle[72] population distribution and the bottom plot shows the attenuation in dB/m of the same cloud. Figure 2-17 shows the contribution of resonant bubbles, bubbles near to resonance but not at resonance, and bubbles off resonance for both the 1 kPa and 10 kPa sound fields. As with Figure 2-14, these regions are again defined as follows. The resonant contribution includes all bubbles in the 31 μm radius bin. The off-resonant contribution includes all bubbles

in the 1 to 15 μm and 50 to 300 μm radius bins. The near resonant contribution includes all bubbles in the 16 to 30 μm and 32 to 49 μm radius bins

The modification of the cloud model to calculate cross-sections of pulses of finite duration has changed the predictions of the cloud cross-section and attenuation. The results of the 1 kPa amplitude sound field will be considered first. Although the shape of the results has remained similar (i.e. a ring-up to steady state) the attenuation at the shortest pulse lengths has increased and the near resonant bubbles are even more dominant for the shorter pulse durations. Conversely, the attenuation of the longer pulses as steady state is reached has changed little. The net result of this is a much smaller change in attenuation as the pulse length increases. The 10 kPa amplitude sound field results show a similar trend. The near resonant bubbles are still dominant and the attenuation at the shortest pulse lengths has increased. In this case any ring-up to steady state has been entirely masked.

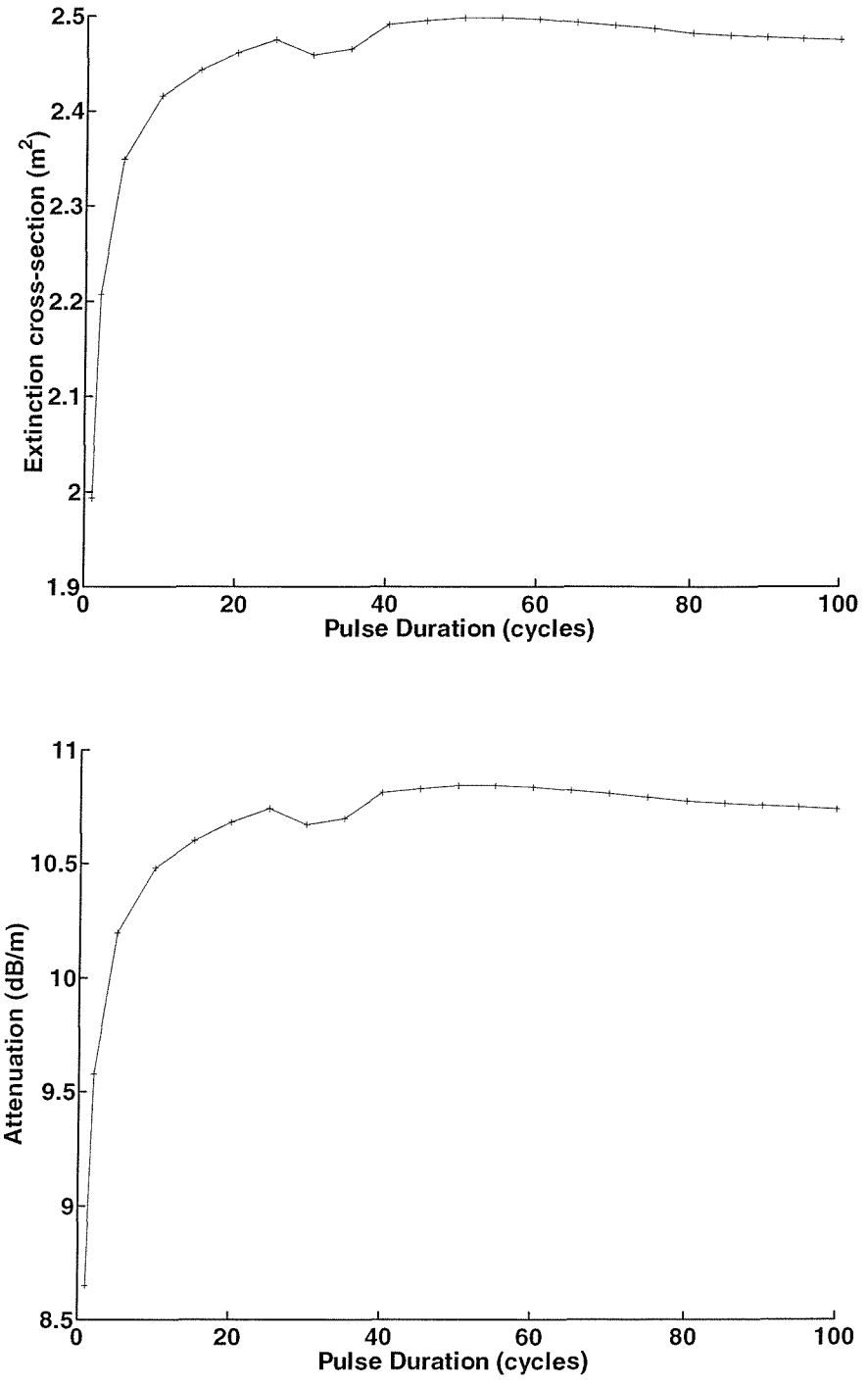

Figure 2-15 The attenuation of a 1 m^3 bubble cloud using the non-linear range independent cloud model including bubble ring-down. The population distribution is that of Farmer and Vagle[72]. All plots are for a 100 kHz sound field of amplitude 1 kPa. The top plot shows the extinction cross-section of the cloud as a function of pulse duration in cycles. The bottom plot is the attenuation of the cloud in dB/m again as a function of pulse duration in cycles. This is a discrete calculation for the data points plotted. Lines between data points are included to aide in interpretation.

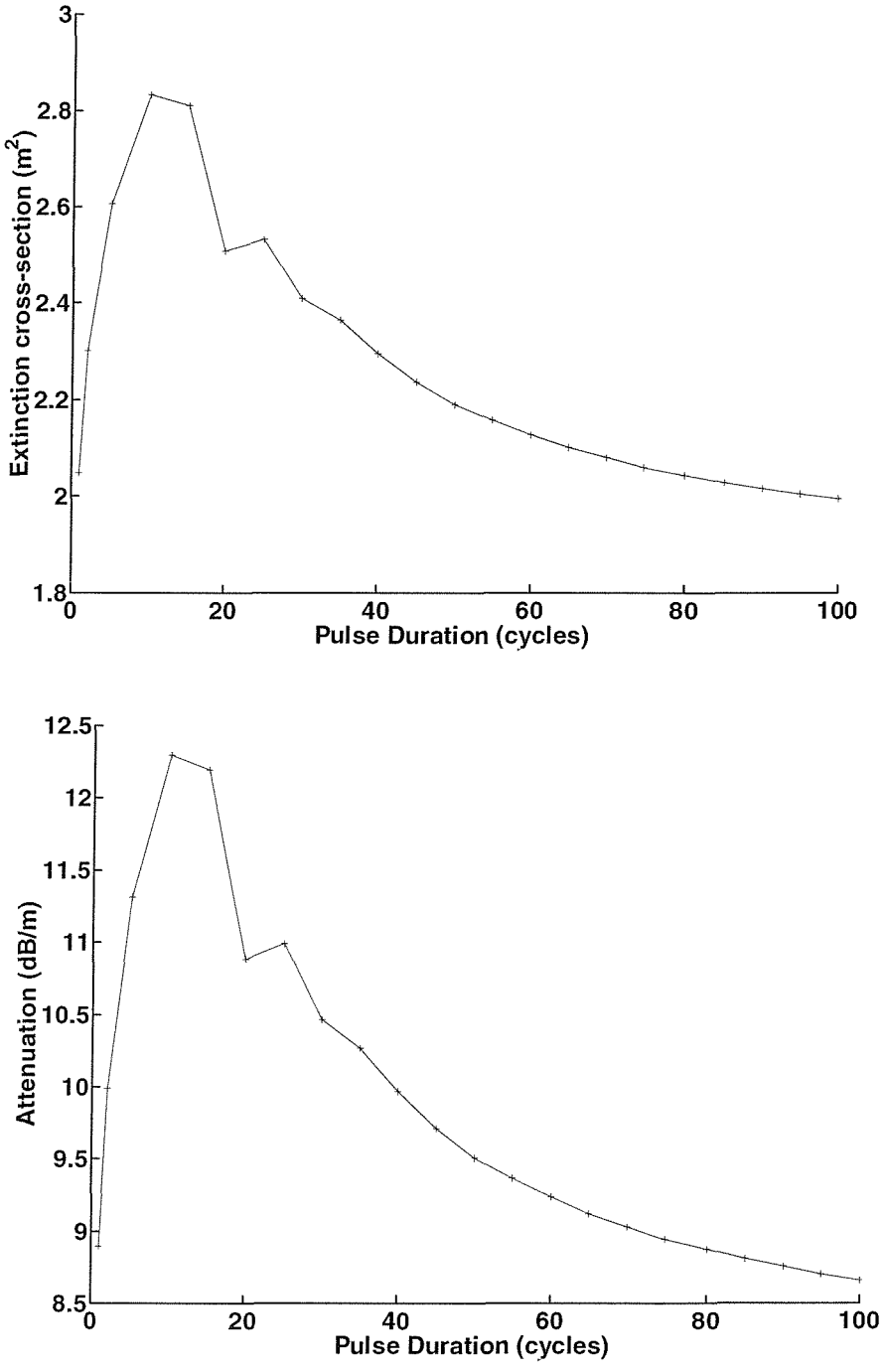

Figure 2-16 The attenuation of a1 m^3 bubble cloud using the non-linear range independent cloud model including bubble ring-down. The population distribution is that of Farmer and Vagle[72]. All plots are for a 100 kHz sound field of amplitude 10 kPa. The top plot shows the extinction cross-section of the cloud as a function of pulse duration in cycles. The bottom plot is the attenuation of the cloud in dB/m again as a function of pulse duration in cycles. This is a discrete calculation for the data points plotted. Lines between data points are included to aide in interpretation.

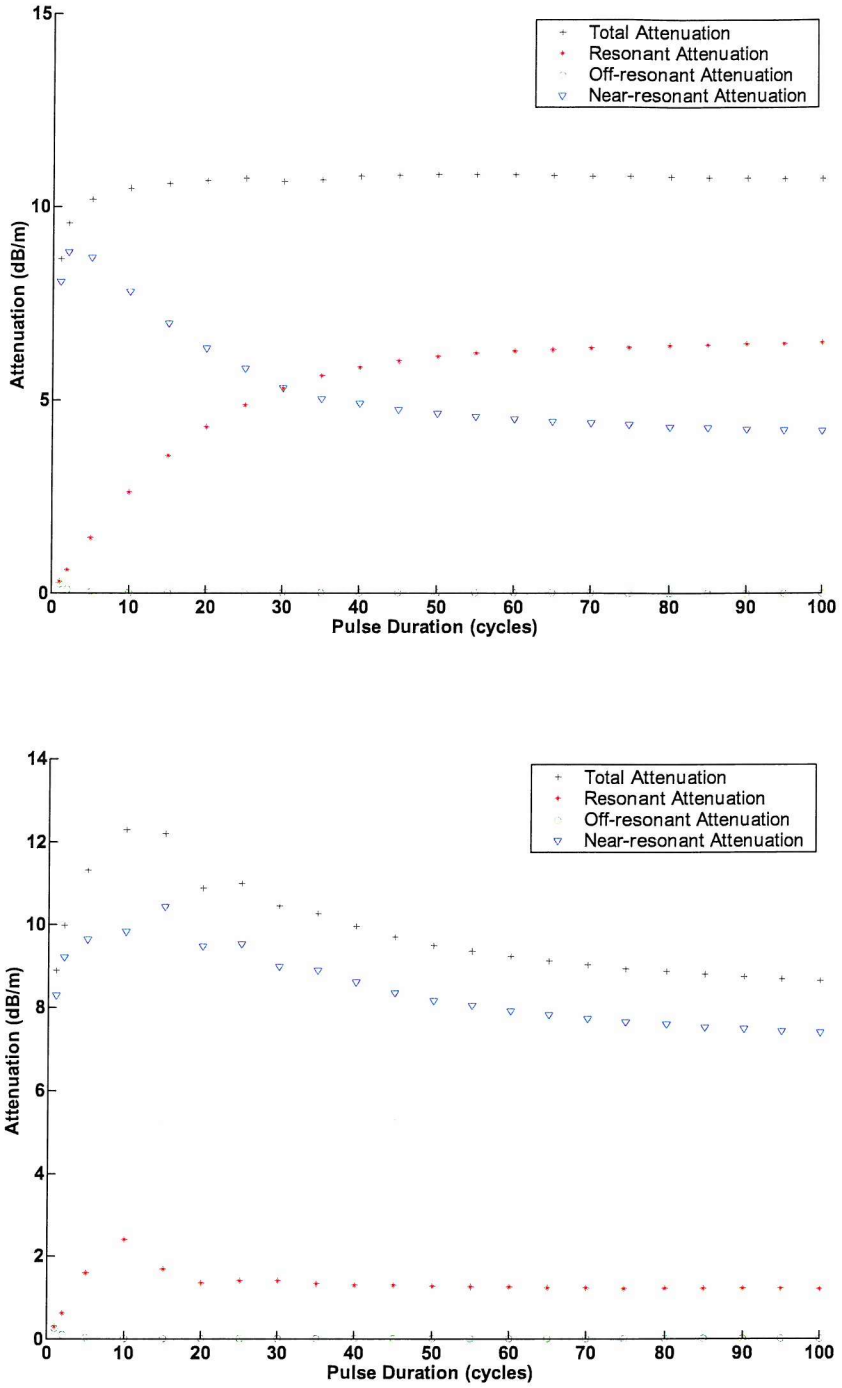

Figure 2-17 The attenuation of a 1 m^3 bubble cloud using the non-linear range independent cloud model for finite pulse lengths. The population distribution is that of Farmer and Vagle[72]. All plots are for a 100 kHz sound field of amplitude 1 kPa (top) and 10 kPa (bottom). Each plot shows the attenuation of the entire cloud (+) the contribution of the resonant bubble (♦), the contribution of the off-resonant bubbles (o) and the contribution of the near resonant bubbles (▽).

To investigate the effects of different pulse durations and sound pressure levels further the sonar equation for detection of a 0.15 m radius sphere introduced in chapter 1 will be applied. All values will be as indicated in chapter 1, except that the attenuation will be calculated using the time-dependent non-linear cross-section in a 100 kHz sound field at 1 kPa amplitude (90 dB ref 1 μm Pa at 1 m) and 10 kPa amplitude (100 dB ref 1 μm Pa at 1 m) for a finite duration pulse. The noise level is also assumed to be –50 dB as in chapter 1.

In order to compare the relative performance of different pulse lengths and sound pressure levels, the sonar equation is solved numerically to give the detection range as a function of pulse duration. The results are shown in Figure 2-18 along with the cloud attenuation also as a function of pulse length. The results predict that short pulse can result in a small enhancement of detection ranges in bubbly environments for low sound pressure levels. The increase in sound pressure levels quickly masks this benefit providing less enhancement than might be expected. A slight improvement is indicated, however, during the steady state part of the cloud response. Conversely the transient behaviour leads to a very slight degradation of target detection ranges for the 10 kPa results for pulse durations of approximately 10 cycles in length. Although this is not an important effect in these plots, it should not be neglected since transient response will be an important factor in population distributions, where resonant bubbles are not dominant.

The results of the range independent cloud model for finite pulse length indicates significantly less potential for sonar enhancement than the previous version of the model for infinite driving pulses. This is because of the increase in the attenuation for short pulse lengths predicted by the model. This is because, as the bubble approaches steady state, the energy loss owing to bubble ring-down is progressively less important. The plots in Figure 2-19 and the accompanying Table 2-1 demonstrate this. The table shows the percentage energy loss of an acoustic wave owing to a resonant bubble for: 1) the period the bubble is being driven and 2) the period that the bubble is ringing down after insonification has ceased. The results show that the contribution of the bubble ring down is proportionally more important for short pulses.

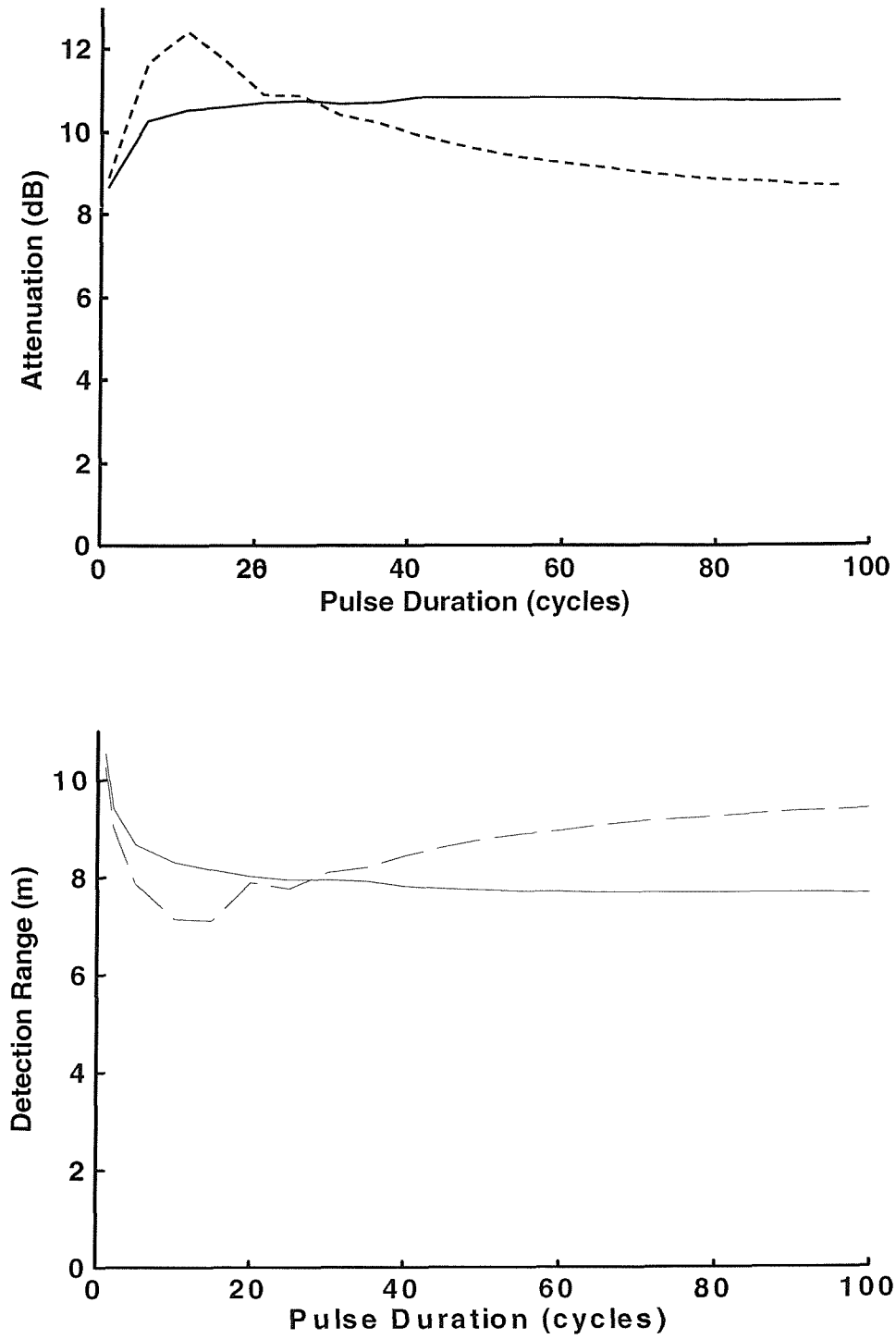

Figure 2-18 Attenuation (top) and target detection ranges (bottom) using the sonar equation and the time dependent extinction cross-section, including bubble ring-down, for a $1m^3$ cloud under one atmosphere hydrostatic pressure in a 1 kPa (solid line) and 10 kPa (dashed line) sound field. Note the linear theory indicates a detection range of ~14 m.

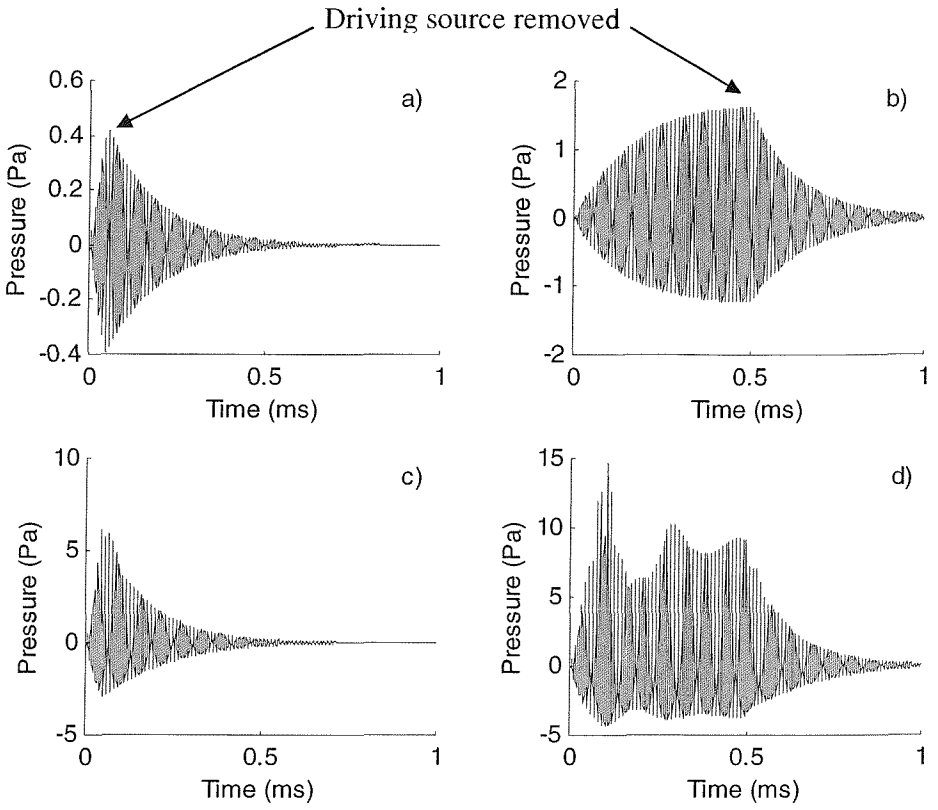

Figure 2-19 Four plots of the radiated pressure time series for a 30.8 μm bubble in a resonant 100 kHz sound field a) 5 cycle pulse of amplitude 1 Pa b) 50 cycle pulse of amplitude 1 Pa c) 5 cycle pulse of amplitude 10 kPa d) 50 cycle pulse of amplitude 10 kPa.

Energy Percentage		Driven	Ring Down
Pulse	5 cycles 1 kPa	17.8	82.2
	50 cycles 1 kPa	79.8	20.2
	5 cycles 10 kPa	18.2	81.8
	50 cycles 10 kPa	87.7	12.3

Table 2-1 Percentage of energy radiated for the bubble responses shown in Figure 2-19 when the bubble is being driven and during the ring down of the bubble after insonification has ceased.

The results of the simple cloud model for finite pulse lengths shows that short pulses can in fact be detrimental to sonar enhancement. When infinite pulses are used the opposite conclusion is erroneously indicated. Examination of the bubble response for each bubble radii in Figure 2-17 indicates that the resonant bubble still shows a reduction in the cross-section for short pulses over steady state. It is the increase in the scattering cross-section of the near resonant bubbles when insonified by short pulses that has masked the ring-up evident in the resonant bubbles. The following section expands the simple cloud model to incorporate range dependent effects.

2.3 Range dependent cloud models

In the preceding section a simple model to estimate the attenuation and cross-sections of a bubble cloud has been described. However this simple model does not take into account the geometry of the cloud. The different ranges of the bubbles from the source and receiver and the attenuation of acoustic signals as they pass through the cloud are not considered. This section expands on the simple cloud model to include the cloud geometry and range effect, and incorporates the attenuation of the driving acoustic signal.

2.3.1 Range dependent cloud model without driving pulse attenuation

One method of simulating the range dependent aspects of a bubble cloud is to distribute a representative proportion of the bubble population randomly within the cloud volume. The distance of each bubble from the source is then calculated and this can be related to a time delay of that bubbles response at the receiver. Each individual bubble response can then be determined using the Keller-Miksis bubble model, and the cloud response found by summing each response with the appropriate delay.

The bubble radius response as given by the Keller-Miksis can be used to calculate the scattering or attenuation from each bubble. The radiated sound pressure level is obtained using [2-5] and the attenuation by calculating the power over the bubble response in the same way, as for the acoustic cross-sections discussed previously (section 1.1.5). The energy loss owing to attenuation or scattering from the cloud can

be calculated by integrating with respect to time the power loss for a given driving sound field.

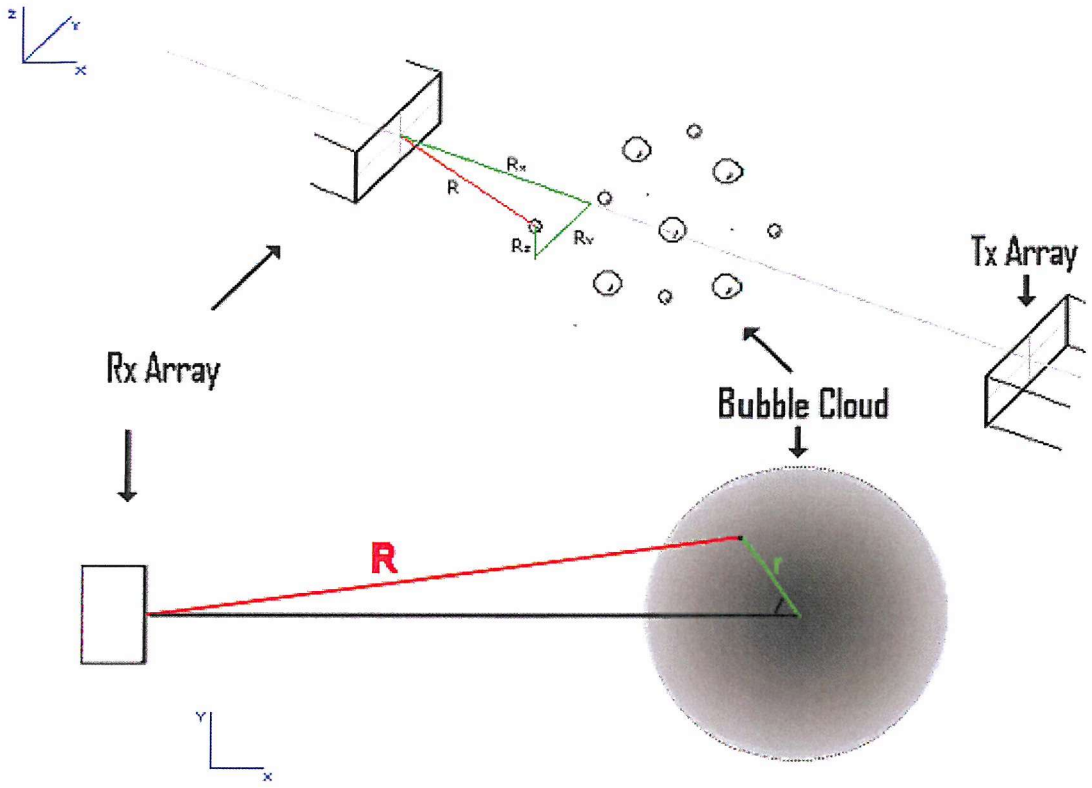

Figure 2-20. Asymmetric view and schematic showing how the cloud is modelled by randomly generating the position of the bubbles (radius, angle and depth from cloud center) within the cloud volume and calculating the path length to the receiver. The shaded region indicates the cloud boundary and bubble density, a darker shade indicating a higher bubble density.

In the formulation of the previous cloud model it has been shown that the time taken for the bubble to ring-down must be included in the limits of integration. Also in the case of the range dependent model, the pulse will take a finite time to propagate through a cloud; thus the bubbles will not be oscillating with the same phase. Furthermore, the cloud has finite dimensions and will respond differently depending on whether the pulse train is longer or shorter than the time taken to propagate through the cloud. Consider when the pulse train is much shorter. Only a part of the cloud is insonified at a given time; thus not all the bubbles will reach steady-state oscillation at the same time. If the pulse train is sufficiently longer than the cloud, then at some point the entire cloud will be oscillating at steady state. As in the case of

the modified simple cloud model, this model will determine the response of a bubble cloud to arbitrary waveforms of finite length, including the bubble ring-down.

The model has been implemented using Mathworks Matlab^{TM}. The methodology of the model is described here with the aid of an example. In this case a 1 m^3 volume cylindrical cloud with a population distribution taken from Farmer and Vagle[72] ([2-14]) to allow comparison with previous model results. In this case a cylindrical cloud insonified mono-statically is modelled. The bubbles are uniformly distributed over the depth insonified by the transmit array but are distributed in the horizontal plane such that the density reduces towards the edges of the cloud but is radially uniform.

This geometry is generated by randomly determining an angular component and distance, as well as the vertical distance, from the centre of the cloud for each bubble. The cloud is 0.5 m in radius and 1.27 m in depth (giving a cloud volume of 1 m^3) with the centre of the cloud on axis with the transmit/receive array. A plane wave is assumed with the receive array 2 m from the centre of the cloud

The distance of each bubble from the receive array is then calculated by resolving along the axis of the source and cloud origin and applying basic trigonometry (Figure 2-20). It is then a simple matter to calculate the time at which the signals are received for each individual bubble using the distance and the speed of sound in water (assumed to be bubble-free to speed up the calculation). The bubble population is then ordered in terms of this time delay.

The scattering or attenuation of each bubble radius increment is then calculated for the incident pulse using the Keller-Miksis model as described previously. The increment is normally one micrometre as defined by the population formula. This is fine enough to resolve the bubble resonance and avoids the need to integrate the bubble population to give the number of bubbles per radius increment. The cloud response is then constructed by stepping through the bubble population, in order of increasing delay, and adding the response for the appropriate bubble size.

The model is able to produce a time-series response for the sound pressure scattered from a cloud of a given population and cylindrical radius for any incident plane wave signal. Furthermore, the time-dependent scattering and attenuation in decibels can be calculated using the energy loss owing to the bubble cloud and the calculated energy

of the incident pulse. A further benefit of this model is that it can use a formula or a driving pressure time series in Pascals to define the incident signal. The use of a time series requires that pressure time series be sampled at the same (or greater) frequency as the model output. This is normally set to 1 MHz.

Although a cylindrical cloud has been used in this case, as it is easy to model and can be produced artificially in a tank, a variety of cloud shapes could be implemented by changing the algorithm for calculating the distance of the bubbles from the source.

The results of the range dependent model based on the example described above are shown in Figure 2-21. To obtain these results the bubble population has been scaled down to reduce processing time. Several repeat tests were conducted to ensure that enough bubbles were modelled such that the standard deviation of the cloud response (scaled up to the desired population density) varied by less than 1% for different randomisations of the bubble locations.

The results of the range dependent model shown in Figure 2-21 differ slightly from the cloud model results shown in Figure 2-18. The results from each of these figures are overlaid in Figure 2-22 for comparison. Although the peak attenuation of the 1 kPa traces is similar the results calculated using the range independent model generally shows a greater attenuation than the results for the range dependent model as pulse length increases. Both models, however, show an increase in attenuation between one and fifteen cycles after which the attenuation of 1 kPa continues to increase slowly with increased pulse duration and the 10 kPa attenuation reduces rapidly with increasing pulse length. In addition the maximum target detection range of ~5.6 m is somewhat less then the ~7.5 m predicted by the range independent theory. It is also significantly less then the 12.8 m predicted by the steady-state linear theory.

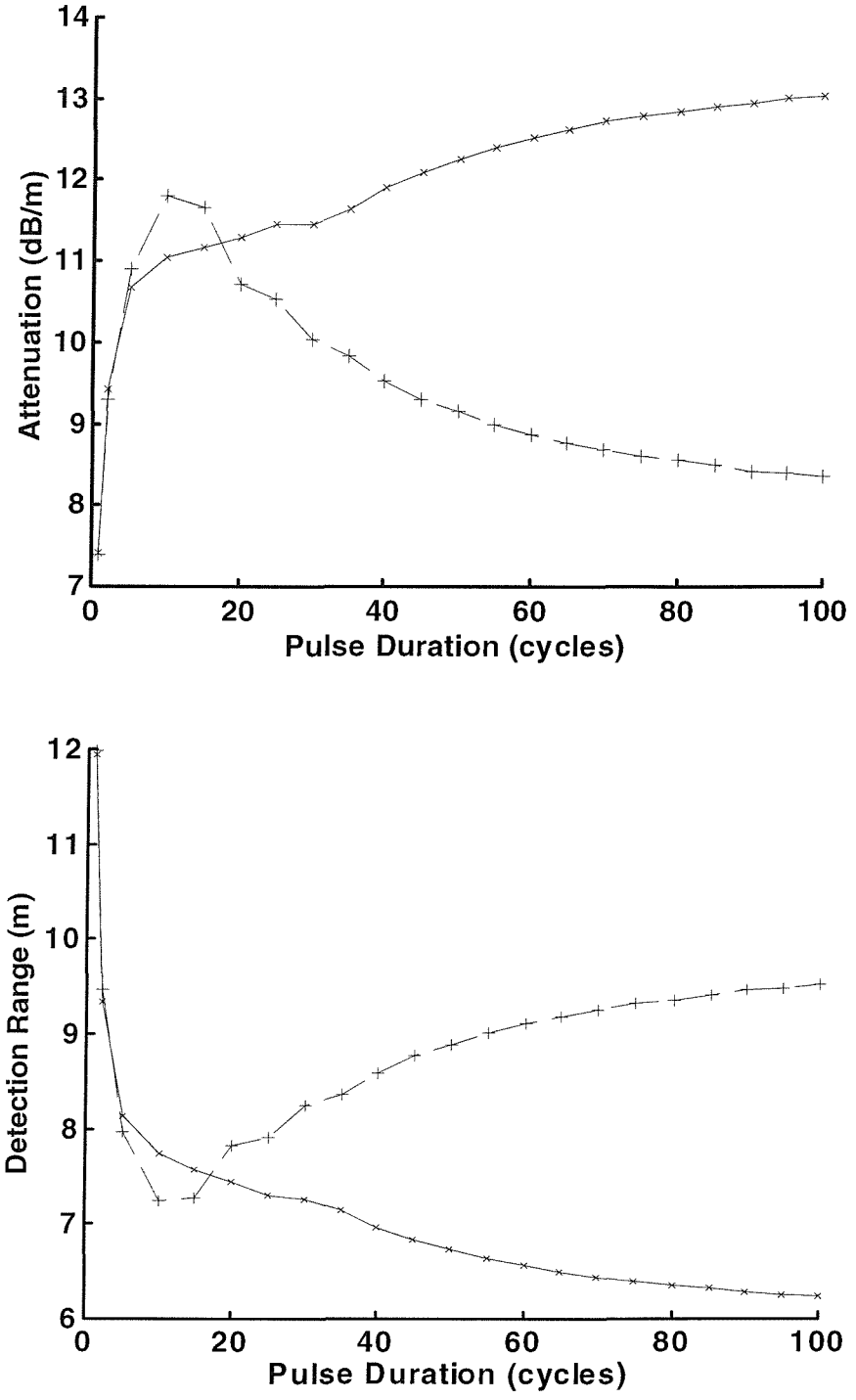

Figure 2-21 Attenuation (top) and target detection ranges (bottom) using the sonar equation and the range dependent bubble model for a 1 m^3 cloud (Farmer and Vagle[72] distribution) under one atmosphere hydrostatic pressure in a 1 kPa (x) and 10 kPa (+) sound field. The insonification frequency is 100 kHz. Note the linear theory indicates a detection range of ~14 m. This is a discrete calculation for the data points plotted. Lines between data points are included to aide in interpretation.

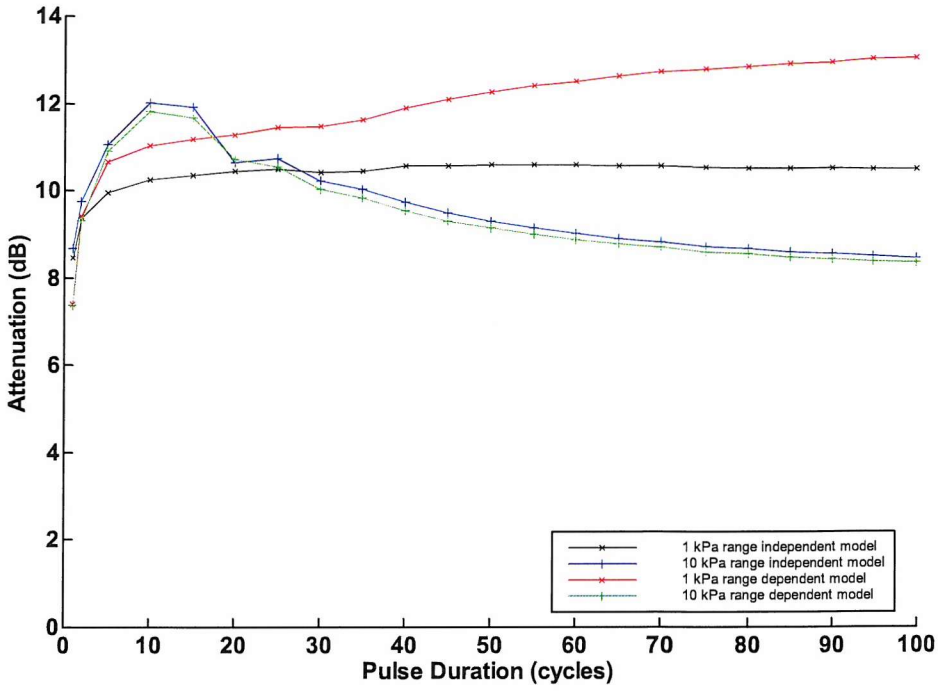

Figure 2-22 Attenuation for a 1 m^3 cloud (Farmer and Vagle[72] distribution) under one atmosphere hydrostatic pressure in a 1 kPa(x) and 10 kPa (+) sound field for the range independnt cloud model (solid line) and the range dependent cloud model (dashed line). The insonification frequency is 100 kHz.

2.3.2 Range dependent cloud model including driving pulse attenuation

One of the assumptions in the range dependent cloud model described above is that the sound pressure level of the signal does not change as it passes through the cloud. This assumption could be a significant source of error because the model assumes bubbles furthest from the source are being insonified by a greater sound pressure level than should be the case and could lead to an error in the estimation of the cloud attenuation.

To overcome this problem the theoretical cloud is segmented into an arbitrary number of layers (determined by the number of bubbles and the level of attenuation). The attenuation owing to the first layer is calculated in the same way as described above and the reduction in the incident signal determined. The driving signal is then scaled by this amount. This new reduced signal is then applied to the following layer. To reduce processing time the response of the succeeding layers is calculated by linearly

scaling the individual bubble responses used to determine the first layer response, in line with the reduction in the incident signal.

The effect is cumulative over the layers and the total cloud response is determined by adding each layer response with the appropriate delays. This is implemented by adding an extra function to the Matlab model that segments the population delay vector into uniform length 'layers'. The response from each layer, with the appropriate reduction in bubble response owing to the attenuation, is then calculated and summed in the manner described above. The attenuation in dB/m is shown in Figure 2-23.

The inclusion of pulse attenuation into the range dependent model has resulted in a small reduction in attenuation of approximately 1-2 dB for both the 1 kPa and 10 kPa sound pressure levels.

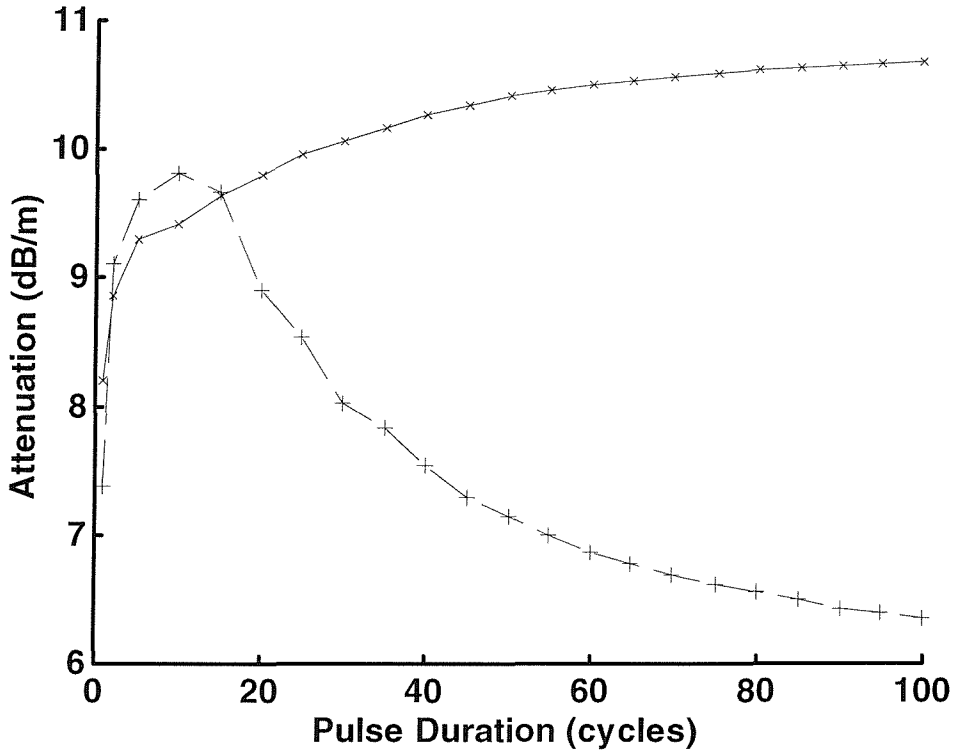

Figure 2-23 Attenuation from the range dependent bubble model including pulse attenuation for a 1 m^3 cloud (Farmer and Vagle[72] distribution) under one atmosphere hydrostatic pressure in a 1 kPa (x) and 10 kPa (+) sound field. This is a discrete calculation for the data points plotted. Lines between data points are included to aide in interpretation.

The importance of the range independent cloud model (owing to cloud geometry) when trying to predict the effect of changing the pulse duration on scattering and attenuation of bubble clouds has thus been established. Although the range independent model is a useful first approximation (owing to its simplicity) care should be taken when interpreting the results especially when considering bubble clouds of finite dimension.

A method of incorporating the attenuation of an acoustic driving pulse as it passes through a bubbly medium has also been introduced. In this case the results are only slightly changed from those that do not include the driving signal attenuation. However in circumstances where the bubble cloud is larger and/or the attenuation greater than in this example case it will be important to incorporate driving pulse attenuation.

In the following section the bubble cloud models are reviewed and methods of sonar enhancement discussed.

2.4 Review of cloud models and methods of sonar enhancement

2.4.1 Classes of model developed

Two distinct classes of model have been derived and discussed in this chapter. The first is the range independent cloud model. This model uses the time dependent extinction cross-section of individual bubbles, scaled by the population distribution, to determine the bubble cloud attenuation. The model can be used for any given driving signal and, once the matrix of bubble responses has been calculated over a suitable radius range, it can be easily applied to any bubble population. The model also incorporates the bubble ring down. The main advantage of this model is that bubble responses can be calculated and stored for typical driving signals. It is then a simple matter to determine the time-dependent cloud attenuation by applying [2-12]. The disadvantage of the model is that it fails to take into account cloud geometry and attenuation of a pulse propagating through a cloud potentially underestimating the attenuation at higher bubble void fractions.

The second type of model is the range dependent cloud model. This model includes the geometry of the bubble cloud and can incorporate the attenuation of the driving signal as it passes through a bubble cloud. The inclusion of pulse attenuation is expected to be very important in the surf-zone where high levels of attenuation are expected[51] and thus high amplitude driving pulses will need to be used. This in turn suggests the capability of including bubble non-linearity will be important as the amplitude dependence shown in Figure 2-18 indicates. The main disadvantage of this model is the long processing time and the need to rerun the model for each new bubble population and driving signal. It is, however, possible to minimise the model processing time by calculating and storing the individual bubble response to typical driving waveforms for use in later iterations of the model. A facility of this model is that a time series of the scattering from the cloud can be calculated.

2.4.2 Characteristics of the models developed

A time dependent non-linear bubble cloud model has been derived. The model can be used to calculate the scattering and attenuation of an arbitrary driving signal through an arbitrary bubble cloud. The models have been expanded to include such effects as bubble ring-down and attenuation of the driving pulse. For each version of the model the attenuation of a 100 kHz pulse of varying length and amplitude 1 kPa and 10 kPa has been calculated for the Farmer and Vagle bubble population[72].

The simple cloud models demonstrate how acoustic cross-sections and attenuation can be calculated for a bubble cloud using a non-linear time dependent single bubble model such as the Keller-Miksis. The importance of the bubble ring down has also been shown when determining the cloud response to a finite driving pulse. This is a consideration neglected in previous time-dependent cloud models reviewed in chapter 1 and the Clarke and Leighton journal paper in Appendix F, all of which assume an infinitely long driving signal.

The model has also shown, through the use of plots such as Figure 2-17, that although resonant bubbles apparently dominate and exhibit the characteristic ring up to steady state, the bubbles close to resonance are also important and do not ring-up in the manner of resonant bubbles. The transient response of the large off resonant bubbles can also be an important contributor to the cloud response. It is the combined effect

of near resonant and large off resonant bubbles that can mask the ring-up of the resonant bubbles.

In section 2.3 the geometry of the cloud was modelled, thus incorporating the attenuation of the driving pulse as it passes through the cloud. This does however increase the processing time by a significant amount. The test results for the Farmer and Vagle bubble population show a reduction in attenuation as a pulse propagates through the cloud of approximately 0.5 dB when pulse attenuation is included. Furthermore the shape of the attenuation versus time curve has changed very little. Thus the full range-dependent model is likely to be a benefit over the simple non-linear cloud model only when attenuation levels are high. This is because it is the relative differences in attenuation of different signals that is important for determining sonar enhancement. The importance of driving signal attenuation will be investigated further in chapter 5.

2.4.3 Methods of sonar enhancement

The time dependent cloud models discussed in this chapter give insights into possible methods of sonar enhancement. Three possible approaches have been identified and are described in detail below.

The first and simplest approach relies on two characteristics of the resonant bubbles indicated by the time dependent models derived in this chapter. The first characteristic is that the resonant bubbles dominate the response of a cloud and thus contribute a significant proportion of the attenuation of an acoustic pulse. This can be expected in most natural bubble populations where, above about 30 μm radius, the numbers of bubbles per μm increment decrease with increasing radius[52-55]. The second characteristic is that resonant bubbles take time to ring-up, and the attenuation due to these bubbles can be reduced if the bubbles do not reach steady state oscillation. These characteristics can be exploited by using pulse of the order of a few cycles with sound pressure amplitudes typically less than 10 kPa. As introduced in section 1.4.1, this method of enhancement will be referred to as Type I enhancement.

A second approach is a derivative of the first. A potential problem with using short low amplitude pulses is that the energy contained in the pulse is low and can result in a poor signal to noise ratio that prevents target detection. This could negate the

potential benefits of using short pulses. A possible solution is to increase the bandwidth of the driving pulse, whilst maintaining the low amplitude and short duration at the resonance frequency of any given bubble. This would allow increased energy in the driving signal whilst attempting to minimise the contribution of the resonant bubbles. The main drawback of this method is that more bubbles will be driven at their resonance frequencies i.e. all those bubbles with resonance frequencies that fall within the bandwidth of the driving signal. As introduced in section 1.4.1, this method of enhancement will be referred to as Type II enhancement.

A third approach utilises a different property of bubble clouds. The cloud model outputs shown in this chapter have all been from a 100 kHz driving frequency. However if the driving frequency were changed, the numbers of resonant bubbles would change depending on the bubble cloud population distribution. Furthermore, the extinction cross-section of the resonant bubbles also changes with bubble size as illustrated in Figure 2-24. Thus the attenuation of a bubble cloud changes with frequency and is a characteristic of the population distribution.

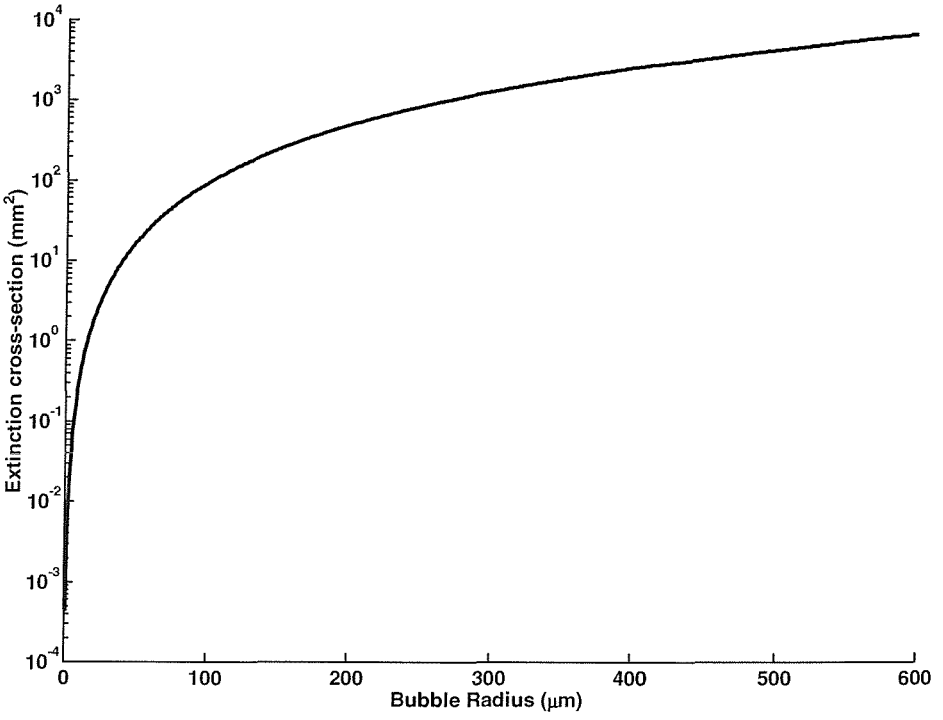

Figure 2-24 Extinction Cross-section of resonant bubbles versus equilibrium radius under one atmosphere of hydrostatic pressure.

A good example, for illustrative purposes, of the frequency dependence of attenuation is shown in Pace *et al*[43] a study of pulse length dependence in bubble clouds that was reviewed in the previous chapter (section 1.3.2). In this paper several measurements of cloud attenuation versus frequency were made and are repeated here in Figure 2-25. The figure shows large changes of attenuation as frequency increases. The levels of attenuation increase from 0 to 20 dB and returns to zero again as the frequency approaches 200 kHz. Although this data are not necessarily representative of oceanic conditions, it clearly shows that selecting the correct insonification frequency is an important consideration for target detection in bubbly environments. This last method of enhancement, which is not mentioned as a possibility in the paper by Pace *et al.* (though Figure 2-25 shows that their data points to it) will be referred to as Type III enhancement, following the convention of section 1.4.1.

The three methods of sonar enhancement are summarised in Table 2-2.

Type	Methodology	Signal Types Used
I	Resonant bubble ring-up	Short pulses
II	Broadband excitation	Chirps and Pseudorandom
II	Attenuation minima	Tuned long pulses

Table 2-2 Summary of the three proposed methods of sonar enhancement

2.4.4 Initial cloud model validation

Finally the results of the Pace *et al*[43], paper can be used to test the simple cloud model described in section 2.2.1. The range dependent cloud model is not tested since the geometry of the cloud in the Pace *et al.* experiment is unclear. The population distribution published in the Pace *et al.* paper was tested with an idealised 20 cycle pulse. Pace *et al.* do not publish the amplitude of their driving signals thus a 10 kPa amplitude has been assumed. The results are shown in Figure 2-25. Excellent agreement is shown between the theoretical results and the experimental measurements with the theoretical data points in most cases lying within the range of experimental variability indicated by the three separate 20 cycle tests plotted.

In the next section the model will be used to investigate which bubble population distributions are most likely to show Type I sonar enhancement.

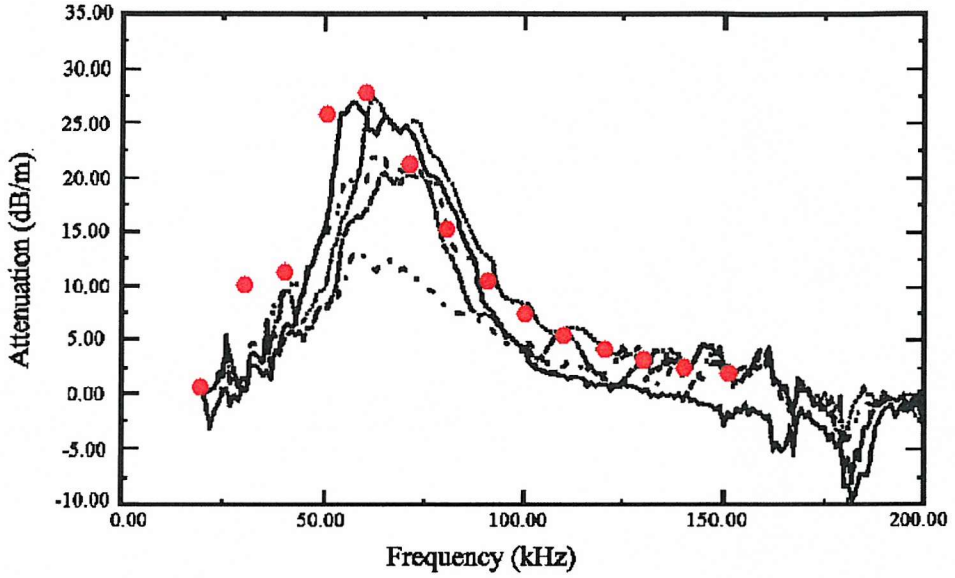

Figure 2-25 Attenuation versus frequency of an artificially generated bubble cloud measured by Pace et al.[43](black lines). The dashed lines represent short 6 cycle pulses and the thick lines long 20 cycle pulses. The dots, added here, are the results of the range independent non-linear cloud model (in section 2.2.2) for a 20 cycle pulse of amplitude 10 kPa.

2.5 Bubble cloud population distribution and sonar enhancement

The range independent cloud model (section 2.2.2) has passed a preliminary verification by comparing the model results with data collected by Pace *et al*[43]. Three types of enhancement methods have been identified from the response of the linear model to a monodisperse population. The verification of the range independent cloud model allows Type I enhancement to be tested with several types of bubble cloud populations to determine the conditions under which a pulse length dependence can occur.

Measurements of oceanic bubble populations in the field have shown that they can be described in one of three distinct ways. The first is known as a 'peaked distribution' because of the presence of a maxima in the population. Farmer *et al*[72] and Phelps, Ramble and Leighton[28] have both measured an example of this type of population.

The peak in the Farmer *et al.* population distribution occurs at 21 μm, and this corresponds to a resonance frequency of 145 kHz for air bubbles in water under one atmosphere hydrostatic pressure. The second type of population can be described by an exponential equation of the form:

$$n(R_o) = Ae^{BR_0} \qquad [2\text{-}15]$$

where n is the number of bubbles per μm increment per m^3, A and B are constants and R_o is the equilibrium bubble radius.

An example of this population type is a second population measurement by Farmer *et al*[72] was used in section 2.2.1.

The third and final type of population can be described by a power-law equation of the form:

$$n(R_o) = AR_o^B \qquad [2\text{-}16]$$

where n is the number of bubbles per μm increment per m^3, A and B are constants. An example of this third type is the population distribution measured by Akulichev[40]. In both equations [2-15] and [2-16], the constant A is a simple scaling factor and the constant B determines the shape of the population. Thus A will scale the attenuation, but B determines the gradient of the population and the relative number of resonant and off-resonant bubbles. The constant B is thus the important factor for sonar enhancement.

The three types of populations will be referred to as peaked, exponential and power-law populations.

The range independent cloud model (section 2.2.2) has been used to calculate the percentage change in attenuation between a single cycle and 20 cycle pulse with a driving frequency of between 50 kHz and 300 kHz and an amplitude of 600 Pa for each of the populations described above. In addition a measurement of a bubble population measured in the surf-zone made by Phelps *et al*[28] is also tested. This population is also described by [2-17] and is of the form of equation [2-16].

$$n(R_o) = 7x10^{12} R_o^{-3.82} \qquad [2\text{-}17]$$

The results are shown in Table 2-3.

		Population (Type)			
	% (dB/m)	Farmer 1 (Peaked)	Farmer 2 (Exponential *B*=-0.04)	Akulichev (Power *B*=-3.7)	Phelps *et al.* (Power *B*=-3.8)
Frequency (kHz)	300	*-124 (-3.5)*	11 (0.5)	33 (1.7)	31 (1.6)
	250	*-61 (-2.1)*	12 (0.6)	25 (1.2)	23 (1.1)
	200	*-3 (-0.1)*	11 (0.5)	14 (0.7)	12 (0.6)
	150	53 (3.3)	15 (0.7)	*-3 (-0.1)*	*-6 (-0.3)*
	100	*-7 (-0.3)*	18 (0.8)	*-21 (-0.8)*	*-25 (-1.0)*
	50	*-105 (-3.1)*	9 (0.4)	*-55 (-1.9)*	*-65 (-2.2)*

Table 2-3 Percentage and dB/m change in bubble cloud attenuation (in brackets) between a 1 and 20 cycle pulse of 600 Pa amplitude. The population name is shown at the top of the plot with the type of population and the value of the constant B for that population shown in brackets below. The negative numbers (highlighted in red italics) indicate a decrease in attenuation between 1 and 20 cycles indicating Type I suppression.

The results in Table 2-3 show that the Farmer 1 population would give optimum Type I enhancement (53%) if the driving frequency is tuned to the resonance frequency of bubble radius at the peak of the distribution. Away from this peak the opposite of Type I enhancement occurs. The power-law type distributions of Phelps *et al.* and Akulichev both show enhancement at the higher frequencies (31% and 33% respectively at 300 kHz). The exponential type population measured by Farmer shows the poorest enhancement (an average of 13%) but enhancement is effective over the widest frequency range. The values are however generally small (< 3dB) compared to the types of enhancement required for sonar operation.

The power-law and exponential type populations can be investigated further by varying the *B* parameter to determine the effect on Type I enhancement. The results are shown in *Table 2-4* and *Table 2-5*.

		Population (Power-law)				
	%	B = -1	B = -2	B = -3	B = -4	B = -5
Frequency (kHz)	300	11	34	37	29	*-2*
	250	8	28	30	20	*-11*
	200	3	20	21	9	*-29*
	150	1	14	10	*-12*	*-110*
	100	*-1*	8	*-2*	*-33*	*-129*
	50	*-2*	*0*	*-20*	*-82*	*-353*

Table 2-4 Percentage change in bubble cloud attenuation between a 1 and 20 cycle pulse of 600 Pa amplitude for a bubble population with a power-law distribution. The constant B from equation [2-16] is shown at the top of the table. The negative numbers (highlighted in italics) indicate a decrease in attenuation between 1 and 20 cycles indicating no Type I enhancement.

		Population (Exponential)				
	%	B = 0.02	B = 0.04	B = 0.06	B = 0.08	B = 0.1
Frequency (kHz)	300	*-5*	10	21	28	33
	250	*-6*	10	21	27	32
	200	*-8*	9	19	25	28
	150	*-2*	13	21	24	26
	100	5	17	20	18	14
	50	13	11	*-6*	*-37*	*-89*

Table 2-5 Percentage change in bubble cloud attenuation between a 1 and 20 cycle pulse of 600 Pa amplitude for a bubble population with an exponential distribution. The constant B from equation [2-15] is shown at the top of the table. The negative numbers (highlighted in italics) indicate a decrease in attenuation between 1 and 20 cycles indicating no Type I enhancement.

The results clearly show that a power-law distribution with a value of B between 2 and 4 is best suited to Type I enhancement, and that an exponential distribution show enhancement for values of B in excess of 0.02. The tables also indicate that in general a higher frequency is better unless the off resonant contribution is significant.

2.6 Summary

In this chapter non-linear models of bubble cloud attenuation for arbitrary waveforms and population distributions have been developed. The models have been used to identify three possible methods of sonar enhancement and the types of cloud where Type I enhancement can be expected to work for certain populations and at certain frequencies though enhancement of less than 3 dB are generally produced. It is now necessary to compare the performance of these models with experimental results and investigate the potential of each of the sonar enhancement techniques. To achieve this a series of tank tests will be conducted in an 8 m x 8 m x 5 m deep test tank using an artificially generated bubble cloud. The implementation and results of these tests are described in the next two chapters (chapter 3 and 4), respectively. The knowledge gained in the tank will then be applied to target detection trials in the surf-zone. This is necessary to obtain knowledge of surf-zone bubble populations and conditions. It also allows the models and the different methods of sonar enhancement to be tested under realistic conditions. These trials are discussed in chapter 5.

CHAPTER 3

EXPERIMENTAL METHODS FOR TANK TESTS

3 Experimental Methods for Tank Tests

This chapter considers the experimental arrangements for measuring the benefits of different signals for sonar enhancement and validation of the theoretical models. The development of a bubble cloud generator, experimental arrangement, methods of analysing the data and the criterion for sonar enhancement are all discussed. As shown in the previous chapter, the ring-up and ring-down characteristics of the bubbles are an important consideration in this study. These depend on the bubble damping, and since the tank measurements described here were to be used in the design of an oceanic experiment, it was necessary to undertake a study of the effect of tank reverberation on bubble damping.

This study expanded significantly beyond the original needs, and would not fit within the scope of this thesis. Hence the resulting publication is bound into the back of this thesis as Appendix G.

3.1 Artificial generation of an oceanic type bubble cloud

The development of an artificial bubble cloud generator that can produce bubble clouds in a test tank that mimic (as far as is reasonably achievable) those found in the ocean is described below. The reason for choosing electrolysis over other generating techniques is discussed first before a technical description of the generator and its operating principles is given. Finally the bubble cloud population distribution is characterised.

3.1.1 The development of an electrolysis type bubble cloud generator

As discussed in section 1.3, out of the three studies on the pulse length dependence of acoustic attenuation or scatter by bubble clouds, only the oceanic studies showed a positive result. Clarke and Leighton[56] (Appendix F) suggested that one of the main reasons why the other two tank studies (by Suiter[60] and Pace *et al.*[43]) failed to show an effect was that these authors used techniques for generating bubble populations in tanks which produced too many large bubbles. As section 2 showed, such large bubbles do not display the smooth ring-up characteristic of resonant bubbles.

To prevent the possible masking of the pulse length dependence by large off-resonant bubbles, it was necessary to generate a repeatable artificial bubble cloud that produced predominantly small bubbles, of the order 10 – 100 μm radius, similar to oceanic bubble distributions[55]. Experiments have shown that it is difficult to produce large quantities of bubbles this size by injection of compressed air through a needle[57], which is a common method for bubble generation[58,59]. One alternative bubble generation method is by electrolysis[60,61]. Laboratory tests using platinum and copper electrodes have shown that oxygen bubbles form on the surface of the anode, and will grow in size until there is sufficient buoyancy force to overcome surface tension and they detach. If a flow is induced over the anode, the bubbles detach sooner and thus the bubble population has, on average, a smaller radius. In addition the quantity of bubbles produced can be controlled by two methods: First by increasing the current; and second, by moving the anode closer to the cathode. This increases the proportion of the current utilised for electrolysis and thus bubble production. These criteria are not entirely compatible and thus a compromise must be sought. A further method of increasing the void fraction within the cloud is to reduce the size of the cathode, reducing the volume of the cloud.

The volume of gas produced by electrolysis can be calculated, from the current passing between the two electrodes, by Faraday's Law.[62]

$$Q_c = n_e MF \qquad [3\text{-}1]$$

where Q_c is the charge in coulombs, n_e is the number of electrons liberated to produce a gas molecule, M is the number of moles of gas and F is Faraday's constant 9.65 $\times 10^4$ $Cmol^{-1}$. For the electrolytic generation of O_2 from water, four electrons are liberated to produce each gas molecule and each mole of gas has a volume of 24×10^{-3}

m^3, at standard temperature and pressure. It should be noted that the actual volume of gas produced is dependent on the pressure and thus the depth of the cloud.

Another design issue is the production of hydrogen gas at the anode. The potential problems of hydrogen bubbles contaminating the cloud, owing to their different level of damping, was discussed in Chapter 1, where the potential problems of not considering such contamination in Suiter's[60] study were discussed. It would thus be desirable if the bubble cloud generator could be designed with a system for preventing this.

With these design considerations in mind, a large scale electrolysis-type bubble cloud generator was developed for use in a fresh water[i] 8 m x 8 m x 5 m tank. A novel approach to the placement of the anode and cathode was taken, to ensure maximum bubble production as well as a reproducible small bubble population. The generator consists of a dexion™ lifting frame incorporating a waterproof housing containing a motor and electrolysis circuitry. On top of this is mounted a baseboard with four copper plates wired together as the anode. This is in turn covered in a fine mesh filter to prevent the hydrogen bubbles from contaminating the cloud. Through the middle is a drive shaft from the motor to a turntable on which is mounted a fifth copper plate acting as the cathode. The anode and the cathode are both wired into the waterproof housing, in the former case by slip rings. Power to drive the motor and electrolysis is supplied from the surface via three cables. In addition the rpm of the turntable is measured and monitored via a digital display on the surface control box, where the rpm of the motor can also be adjusted. Mounting the anode on a turntable to induce a flow over the generating surface has a two-fold advantage. Firstly it minimises the numbers of large bubbles produced and, secondly, it generates (as far as possible) a spatially uniform cloud with a diameter of approximately 0.5 m. A photograph of the completed generator is shown in Figure 3-1.

Early experimentation used a cathode design, consisting of a wire mesh grid to minimise the distance between the electrodes at all points, whilst minimising the area of the cathode. These cathode designs were unsuccessful since the manufacturing of

---

[i] Although one author[63] has suggested that the damping of bubbles in salt water may differ from the damping in fresh water, no evidence for this has been found by others, and Appendix G shows how the effect observed may have been an artefact of the test tank.

the copper wire used in the cathode appears to have led to pitting of the wire, significantly increasing the surface area. The solution to the problem was to use a single copper plate. This both increased the density of the cloud and improved the efficiency allowing a higher current per unit voltage compared to the mesh electrode.

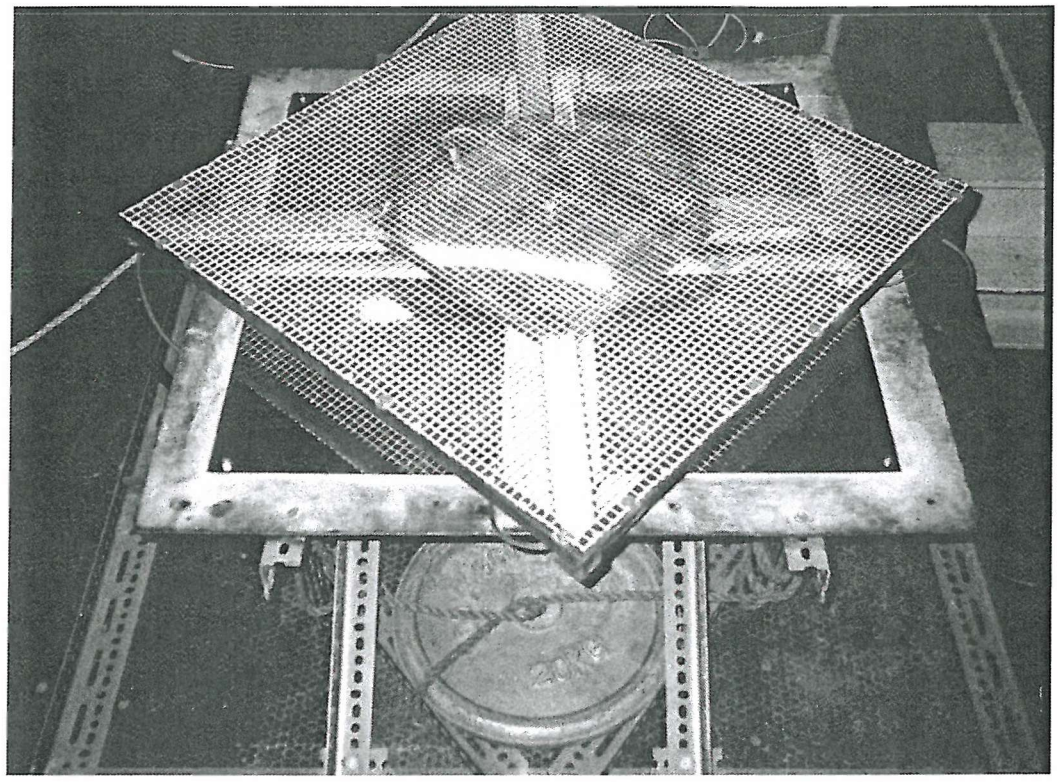

Figure 3-1 Photograph of the electrolysis bubble cloud generator. This photographs shows the wire mesh cathode before it was replaced with a smaller copper plate.

3.2 Experimental arrangement

The experimental arrangement, data acquisition and control systems for the generation of arbitrary waveforms, and the measurement of their attenuation, are described in section 3.2.2. In addition, schematics of the experimental arrangement and equipment are given, and experimental procedures described, in sections 3.2.3 and 3.2.4. Firstly the measurement and characterisation of the artificial bubble cloud is discussed in section 3.2.1.

The measurement of the bubble population via the inversion of attenuation required the measurement of the frequency dependent attenuation. A plot of these measurements is shown in Figure 3-2. The figure shows a maximum attenuation of approximately 5 dB/m at 20 kHz with the attenuation then decreasing with increasing frequency. This information is important when considering the experimental arrangement for several reasons. Firstly, in order to determine the relative benefits of different driving signals, it will be necessary to compare the attenuation levels of the different signals. Higher attenuation levels are desirable to improve the accuracy of these measurements. Secondly, the theoretical models have indicated that too high a sound pressure level will limit the potential for pulse enhancement. The combination of high attenuation and low sound pressure levels can result in poor signal to noise at the receiver, or failure of the driving signal to penetrate the cloud. Thirdly, it is necessary to time gate the received signal to negate tank wall reflections, thus limiting the length the pulse that can be tested. A higher frequency pulse would allow a greater number of cycles during the time gate. Conversely, too low a frequency pulse would restrict the pulse length and prevent the investigation of pulse length dependence in the cloud response.

These constraints were considered along with the available sources and receivers and the reverberation levels of the tank (see Appendix C) when determining the experimental arrangement discussed below and the test signal characteristics described in this chapter.

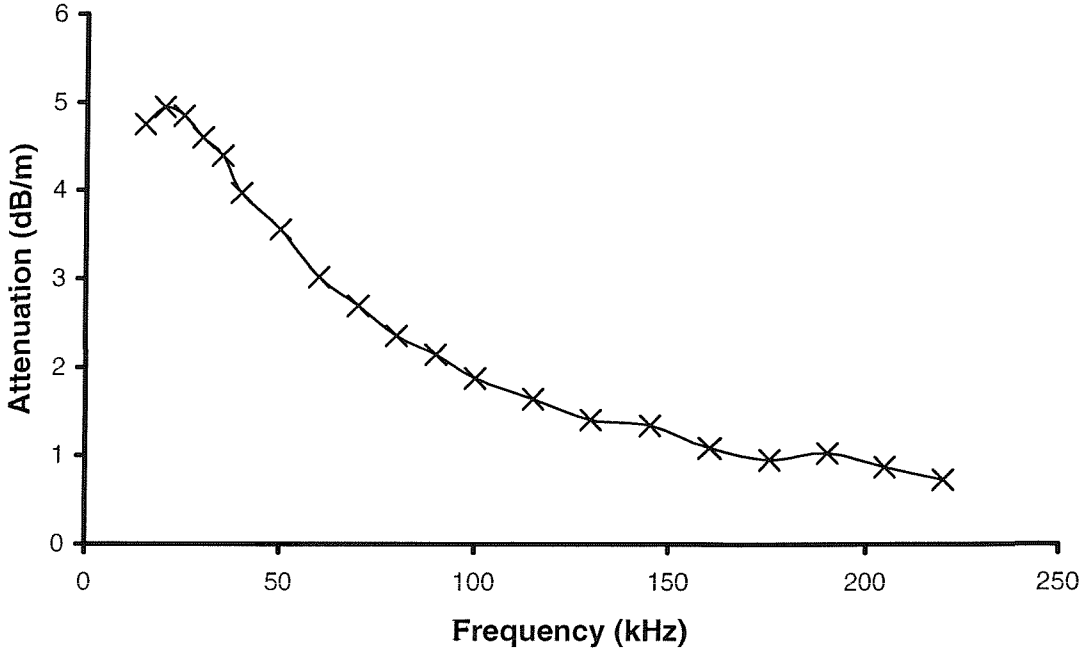

Figure 3-2 Plot of attenuation versus frequency for the bubble cloud generated by electrolysis using pulses of 1 ms duration. The crosses represent data points and the line is an interpolation of the data. This data was used to invert for the bubble population distribution shown in Figure 3-4.

3.2.1 Measurement of the bubble cloud population

Preliminary characterisation of the bubble cloud was achieved by measuring the size of bubbles with a graduated microscope. A sampling dish was passed through the cloud just below the surface to collect the bubbles for examination by the microscope. The gas flux was also measured by collecting the gas bubbles in a reservoir at the surface. All measurements were made with the turntable set to 10 rpm and a current of 10 amps. The void fraction was measured to be approximately 0.0067%±0.00034%, assuming an average rise speed of 1 cms^{-1}. The normalised optically measured bubble distribution is shown in Figure 3-3. This is a preliminary measure only, and does not give the exact population distribution encountered by the acoustic pulse. This is because larger bubbles have greater rise speed and so in a given time interval a glass plate samples over a greater vertical distance in the cloud for larger bubbles then it does for small. In addition, the reduced hydrostatic pressure at the glass plate compared to that at the acoustic propagation path will distort the population.

Further measurements of the bubble population have used inversion of the attenuation[64] of pulses transmitted between two hydrophones within the bubble cloud and spaced 0.25 m apart over a frequencies range of 15 to 220 kHz. Pulse durations of 1ms were used in all cases corresponding to durations of between 15 and 220 cycles as the frequency increased. The void fraction measured by this technique, 1.1 x 10^{-3} % and the resulting population distribution is shown in Figure 3-4. The normalised optical measurements shown in Figure 3-3 are scaled (to give a void fraction of 1. 1 x 10^{-3} %) and added to this plot (as triangles) for comparison.

The grey line in the plot is an extrapolation of the inverted measurements and is described as follows:

$$n(R_o) = 1.84x10^6 e^{-1.44182R_o^{0.3}} \qquad [3\text{-}2]$$

where n is the number of bubbles per m^3 per μm increment in bubble radius in the usual fashion.

The measurement of attenuation (owing to the bubbles), from which the bubble populations are inverted, is shown in Figure 3-2.

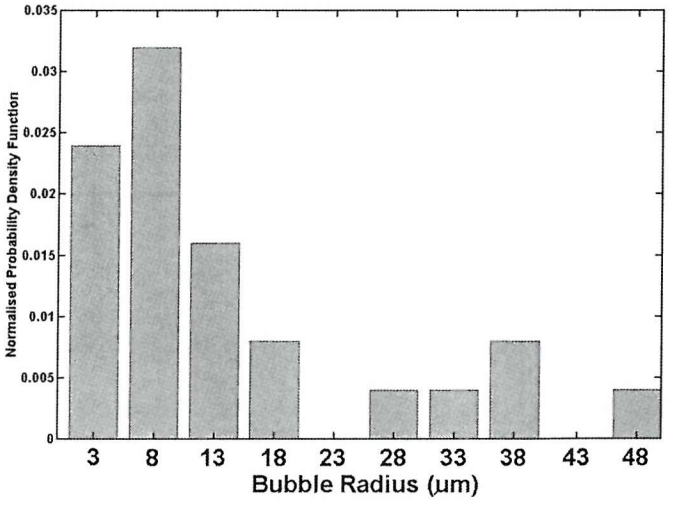

Figure 3-3 Optically measured bubble size distribution from the electrolysis bubble cloud generator drawing a current of 10 amps and the turntable rotating at 10 rpm.

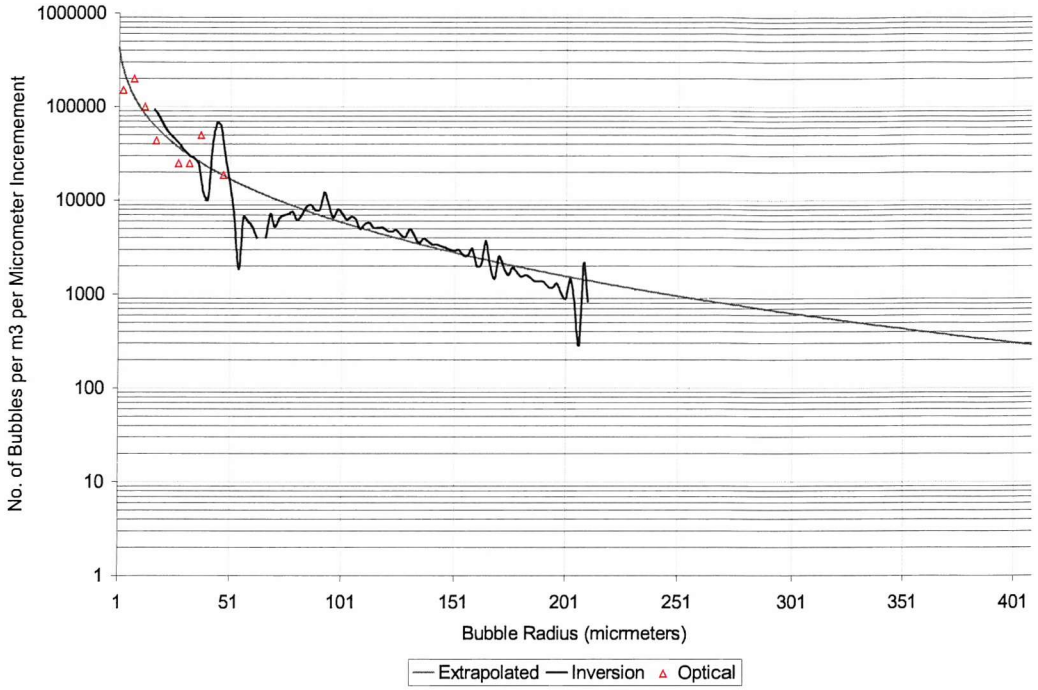

Figure 3-4 Bubble cloud population distribution of the electrolysis type bubble cloud running at 10 amps and a turntable rpm of 10. The measurements were made at a depth of approximately 3 m. The graph shows experimental data (black line) and a best-fit curve (grey line) to the population obtained by inversion of the attenuation through the bubble cloud. The equation of the extrapolated best fit curve is given by [3-2] The opticals measurement from the previous plot are also show as triangles.

3.2.2 Tank arrangement

The attenuation measurements were conducted in an 8 m x 8 m x 5 m deep fresh water tank. The tank is not anechoic and special care was taken when positioning the bubble cloud generator, the source and the receiver, to avoid spurious signals from bottom and wall reflections. Figure 3-5 shows the relative positions of the cloud, source and receiver.

The bubble cloud generator was bottom-mounted in the centre of the tank floor. The generator was lowered into the water with a rope and pulley system. The rope had to remain attached to the rig for retrieval, but was allowed to go slack so that it ran along the tank bottom, before returning to the surface. This ensured it remained outside of the direct path between the source and the receiver.

The acoustic source for the tank experiment consisted of a calibrated Bruel & Kjaer 8105 hydrophone with an optimum transmit frequency of 120 kHz (Appendix D

Figure D-3). The source was suspended approximately 2.30 m from the cloud, at a depth of 2.43 m. Two Bruel & Kjaer 8103 hydrophones were used as receivers. The first was suspended 1 m from the source on axis with the bubble cloud as a reference hydrophone and the second was suspended on the far side of the bubble cloud 2.46 m from the source. Both hydrophones were suspended at a depth of 2.43 m in line with the source and bubble cloud generator.

The theory models developed in the preceding chapters assume that the bubbles are insonified by a plane wave, i.e. the bubble is insonified by a uniform sound field. Thus, in order to make a valid comparison between theory and experiment it is necessary to ensure that this is also the case for the experimental bubble cloud. The 8105 hydrophone is uniform (± 1dB) source and receiver over 360° in the x-y horizontal plane and 270° in the x-z vertical plane with the output reducing by approximately 20 dB in the region of the hydrophone cable (see Appendix D Figure D-4) [65]. The nearest part of the cloud is approximately 2 m from the source. It is assumed that the cloud is insonified by the direct path from the source. This will be ensured by time gating the receiver, the details of which will be discussed in the data acquisition section below. At the test frequency of 80 kHz (see section 4.1) a spreading loss of $r^{1.45}$ was measured with the curvature in the wave front across the face of the cloud corresponding to approximately one wavelength. Care was taken to ensure that all the Bruel & Kjaer hydrophones were vertical in the water column for this reason (see Appendix D Figure D-4)[66].

The receive frequency response of the B&K 8103 hydrophone is nominally flat below 100 kHz (± 2 dB, see Appendix D Figure D-5). The B&K 2635 charge amplifiers used in conjunction with the B&K 8103, as conditioning amplifiers, also have a response[67] which is flat to within ±1 dB up to 100 kHz.

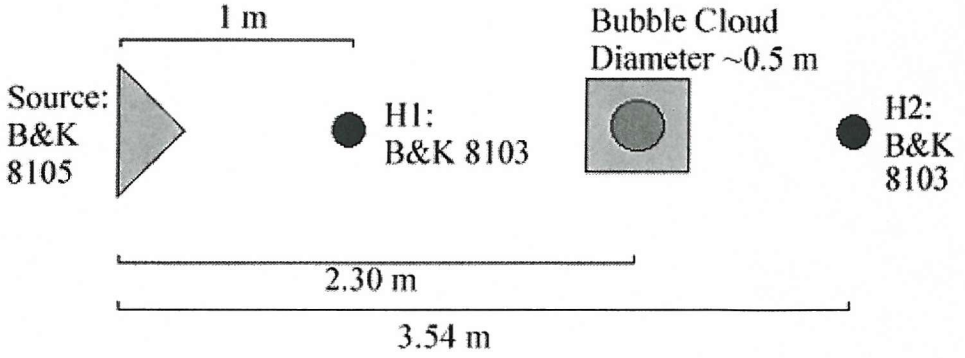

Figure 3-5 Schematic of the tank layout for measurements of attenuation from an artificially generated bubble cloud in an 8 m x 8 m x 5 m deep fresh water tank. Here the reference hydrophone is labelled H1 and the second hydrophone is labelled H2 for future reference.

3.2.3 Signal generation

The source was powered through a Bruel & Kjaer 2713 power amplifier and the signals generated by a Thurlby Thandar TG1304 signal generator and an AWG2021 Arbitrary Waveform Generator manufactured by Sony Tektronix. The former was used to generate pulses of varying length in cycles. The latter arbitrary waveform generator was used to produce linear frequency swept chirps. These were produced using the AWG's internal equation editor to define the signal. The following equation was used:

$$x = \sin(2\pi f_1 t + \pi t^2 (f_2 - f_1)/Tp) \qquad [3\text{-}3]$$

where T_p is the sweep period, f_1 the starting frequency and f_2 the ending frequency.

In all cases the Thurlby-Thandar was used to trigger signal generation at predetermined intervals, normally every half-second. The repeat time was chosen to optimise data acquisition whilst allowing unwanted returns from the tank walls to decay away (see Appendix C for tank reverberation times).

3.2.4 Data acquisition and control

The signals from the 8103 hydrophones were passed through a Bruel & Kjaer 2635 charge amplifier before inputting into a LeCroy 9314 CL four-channel digital oscilloscope for data acquisition. Control of the signal generator and the oscilloscope and acquisition of data to a PC was via GPIB interface and National Instruments LabView software. A schematic of the apparatus arrangement and software control layer is shown in Figure 3-7. The LeCroy was set up to acquire the signals from both 8103 hydrophones simultaneously. Spurious returns from the tank surfaces were time gated out during processing of the data. The nearest tank boundary is the water surface. Figure 3-6 indicates the shortest possible path length using the tank surface. The difference between the direct path length and the shortest indirect path length, assuming a speed of sound in the tank of 1480 m/s, yields a useable time window of approximately 1.7 ms.

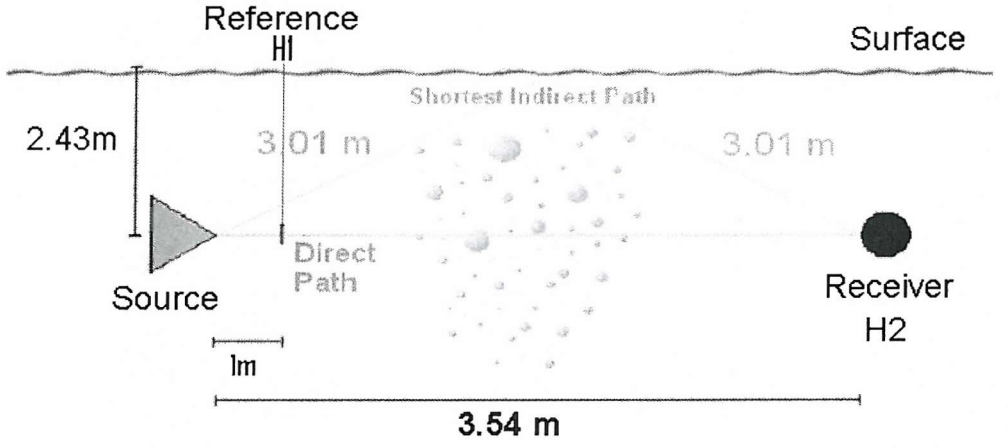

Figure 3-6 schematic showing the length of the direct path and the shortest indirect path. The difference in path lengths yields the available time window between the arrival of the direct path signal and the first surface return.

Control of the experiment was via the PC using a LabView virtual instrument to control each of these instruments shown in Figure 3-7. This allows the signal to be configured by the PC and the resulting signal acquired by the digital oscilloscope to be uploaded and stored on the PC's hard drive. The parameters (amplitude and delay) of the triggering pulse could also be configured via a LabView virtual instrument. An

integrated control program, also written in LabView, controlled each of these virtual instruments. This program used a 'Make Control File', essentially a script file, to control the experiment. This file included the type of waveform to be generated and the name of the file the data would be stored to. The Make Control File was written automatically using the Mathworks Matlab programming language. The hardware acquisition was triggered by the software through the use of a common TTL trigger generated by the Thurlby Thandar function generator. In this way a series of waveforms could be generated without user intervention. For example a series of pulses could be generated with lengths of between 1 and 10 cycles in single cycle steps and each pulse type repeated numerous times. Since the script file was computer-generated, the order could also be randomised to eliminate any potential bias caused by sequentially increasing the pulse length.

A large number of waveforms could be analysed without user intervention using this system. It is also possible with this system to conduct tests over a period of several hours requiring no user intervention. For this reason an Internet Email virtual instrument was created so that users could be notified of completion of an experiment via the Internet. The controlling computers hard drive and a DVD RAM device were used for storing and backing up the acquired waveforms.

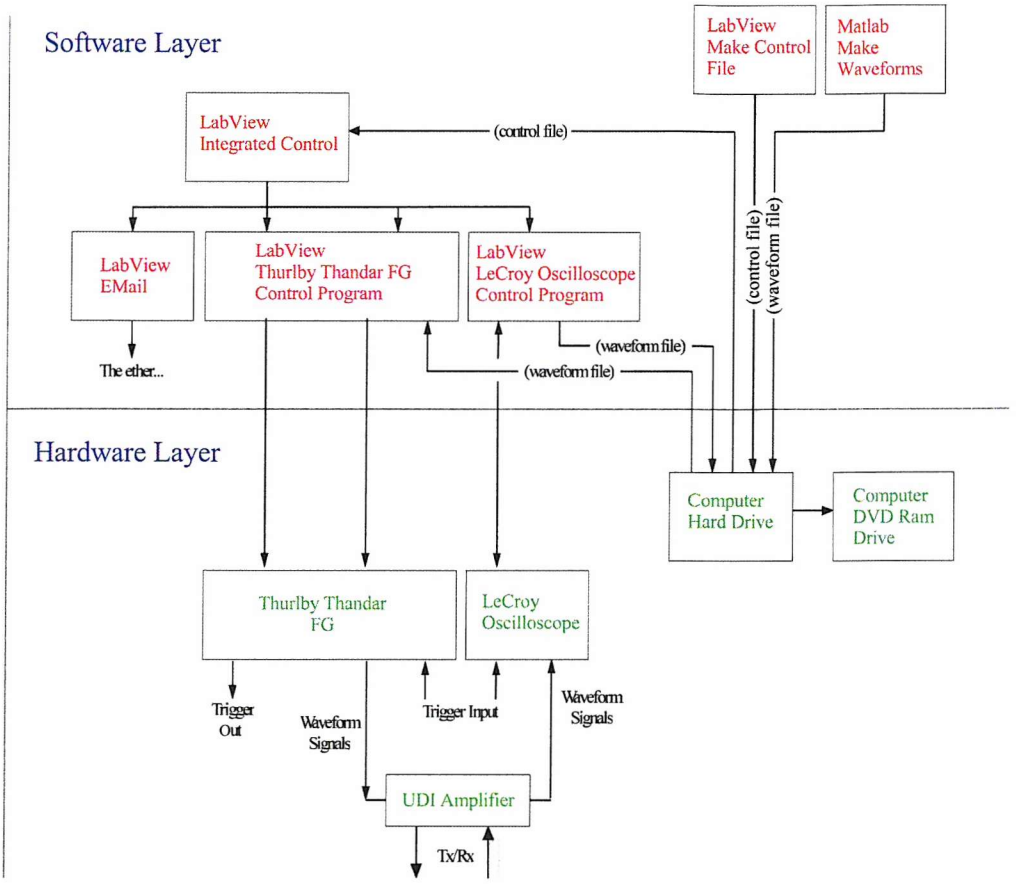

Figure 3-7 Software/Hardware schematic for experimental measurement of attenuation from an artificially generated bubble cloud in an 8 m x 8 m x 5 m deep fresh water tank. The top half of the schematic, or 'Software Layer' shows the various software modules written in Mathworks Matlab and LabView programming Languages to control the hardware signal generation and acquisition. The bottom half of the schematic or 'Hardware Layer' show the hardware components and their interconnectivity.

3.3 Method for determining sonar enhancement

An experimental arrangement for measuring the attenuation of sound through an artificially generated bubble cloud for a range of pulse lengths has been developed. In order to investigate the effect of sonar enhancement, attenuation through the bubble cloud must be measured in such a way that different waveforms can be compared. This will be achieved by calculating energy loss as a percentage of the incident energy.

3.3.1 Criterion for sonar enhancement

Prior to any experimental measurements, a suitable criterion must be developed for determining the relative ability of signals to penetrate a bubble cloud. Three methods of sonar enhancement are summarised in Table 2-2 with each using a different type of signal. In order to be able to compare the benefits of each of these methods, the criterion must be independent of, but not biased by, changes in sound pressure levels, signal duration and frequency spectrum, as well as the characteristics of the source and receivers.

In order to compare the relative benefits of different signals, the attenuation of the driving signals owing to the bubble cloud is calculated. This calculation is based on the energy transmitted and received at all frequencies (limited by the frequency response of the hydrophones). This is an important consideration because the resonant bubbles themselves will reradiate energy at harmonics of their resonance frequency if driven at high enough sound pressure levels, as predicted by the non-linear model (Figure 1-5b). For this reason, signals were acquired without additional filtering other than by the frequency response of the receiving hydrophone and an anti-aliasing filter. The error in the results, owing to temporal variability in the cloud, can be ascertained by repeating experiments in quick succession and looking at the ping-to-ping variability. The average attenuation for each signal type can then be calculated along with the experimental error. This allowed the significance in any trend to be ascertained.

A method of calculating attenuation that meets these criteria, for tone-burst and broadband signals, is described in the following section.

3.3.2 Signal energy and transmission efficiency

The waveforms measured using hydrophones H1 and H2 were acquired to a PC and analysed using the Mathworks Matlab programming language. The energy levels at each of the hydrophones can then be calculated by squaring and integrating the acquired waveform with respect to time, after converting the signal from volts to Pascals and correcting for any amplification in the acquisition stage. The signal at hydrophone H2 is time gated to ensure direct path transmission only. Then the energy levels with and without bubbles present are calculated. Equivalent time gating is used

on all channels to allow a comparison. The bubble-free results can then be subtracted from the results with bubbles present for each waveform. The resulting difference is the energy lost, and thus can be used to determine the attenuation owing to the cloud. Throughout the results from hydrophone H1 are a record of the sound field incident on the bubble cloud and can be used to calculate the sound pressure level at the cloud.

Thus, a direct measurement of the signal attenuation can be made on a waveform-by-waveform basis whilst factoring out attenuation owing to spreading losses, the propagating medium, and the receiver characteristics, such as the frequency response. Although accounted for here the attenuation owing to the passage of sound in the water itself is insignificant over the short path length at the frequencies used, being of the order[68] 1×10^{-2} dB/m at 100 kHz.

The methodology described above will be used to test a variety of driving signals to establish their potential benefits to sonar enhancement. The characteristics of the driving signals and the results are presented in the next chapter. The results will also be used to compare the range dependent theoretical model from chapter 2 with the experimental data.

CHAPTER 4

RESULTS OF THE EXPERIMENTAL AND THEORETICAL INVESTIGATION INTO PULSE LENGTH DEPENDENCE

4 Results of the Experimental and Theoretical Investigation into Sonar Enhancement

This chapter describes the results of theoretical and experimental tests conducted using the tools and methods introduced in the preceding chapters. The aim of the tests is to compare the range dependent cloud model with experimental data, and to investigate the three different mechanisms for sonar enhancement. The driving signals used in the tests are first introduced, and then the theoretical and experimental data are analysed in terms of propagation efficiency. Finally, the experimental and theoretical results are compared and some initial conclusions drawn.

4.1 Signals tested for sonar enhancement

Initial theoretical modelling described in section 2.1.2 has suggested that minimising the time the bubble is driven at or near resonance can reduce the acoustic cross-section of a bubble and, thus, the attenuation of the driving signal resulting from its motion. Two methods of achieving this are by driving the bubbles with short pulses, and by chirping a signal across a range of frequencies. These signals limit the time during which a bubble of a given radius will be driven at resonance. If the duration of the period that the bubble is driven at resonance is less than its ring-up time, then a pulse enhancement will be observed, assuming the off-resonant contribution does not mask the resonant response. The models described in section 2.2 are capable of

testing this assumption and predicting the magnitude of the off-resonant contribution using the test show in Figure 2-17. The following two sections discuss the signals used in the experimental and theoretical tests.

4.1.1 Pulsed signals

The pulse signals used were of centre frequency 80 kHz and of pulse lengths between one and ten cycles. The sound pressure level was approximately 600 Pa at 1 m. The frequency of the pulse was chosen for three reasons. Firstly, in order to limit the contribution of off-resonant bubbles, it was important to minimise the number of large off-resonant bubbles. This criterion suggests a lower frequency is more desirable given the measured bubble population (Figure 3-4). Secondly, the Bruel & Kjaer 8105 hydrophone response[69] rapidly drops off below 100 kHz (when used as a source). Thus the centre frequency was chosen as it was the lowest frequency at which a good signal-to-noise ratio could be achieved.

Theoretical and experimental tests were conducted for pulses of centre frequency 80 kHz with a Thurlby Thandar signal generator producing pulse lengths of one to ten cycles in steps of one cycle.

The actual waveforms transmitted are shown in Figure 4-1. The actual number of cycles transmitted varied from the number produced by the signal generator. This is because the damping of the source resulted in a ring-down and further acoustic generation after the driving voltage from the signal generator had ceased. To correct for this, the energy of each waveform calculated from the experimental data collected using the reference hydrophone H1 will be used to characterise each waveform. The method of analysing the data is described in more detail in section 4.2.1 below.

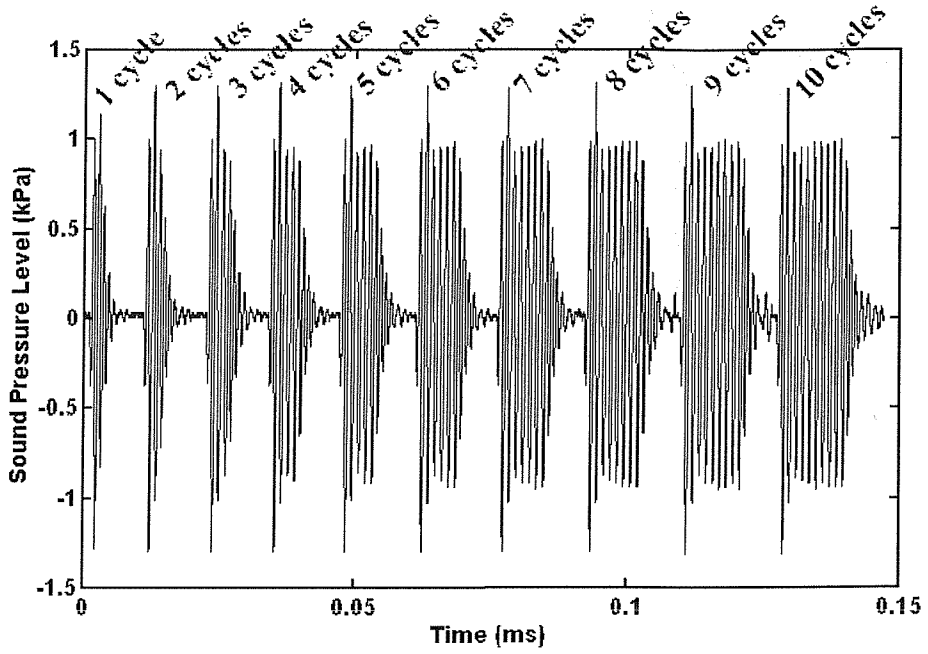

*Figure 4-1 A concatenated plot of the driving pressure time series used in the tank test. The traces are from hydrophone H1 1 m from the source (*Figure 3-5*) and are sampled at 25 MHz. The number of 1 V cycles that the source is driven by is indicated by the text at the top of the plot.*

In order to assist in analysing the data, a further set of control measurements were taken. These measurements used ten-cycle pulses, but the amplitude of the pulse was progressively reduced. This allowed the energy in the pulse to be reduced by a mechanism other than the one associated with reducing the number of cycles. If sonar enhancement owing to a reduction in pulse length occurs, it would be apparent from a divergence between the pulse length and control data sets. To differentiate between the different pulse signals used these data sets are referred to as "duration-varying" and "amplitude-varying" pulses.

4.1.2 Chirped signals

One feature in interpreting the pulsed signals is that the bandwidth of the signal increases as the pulse length decreases. This is an added complication because if the bandwidth of the driving signal were to change significantly, (i.e. by more than the bandwidth of the resonant bubbles), then a change in the number of bubbles being driven at resonance may result. This could affect the apparent efficiency of the signal

attenuation. Another drawback of pulsed signals (already discussed in section 2.4) is the low signal-to-noise ratio.

An alternative method of exploiting bubble ring-up that can overcome these drawbacks is to use broadband signals. Here chirped signals are used, as the bandwidth is easy to specify and the sweep rate of the chirp can be varied. This changes the dwell time at any given frequency, and thus the time for which a bubble is driven at resonance. If the dwell time is short enough, the bubble will not attain its steady-state response. As a result the attenuation of the resonant bubbles is reduced.

The chirp signals investigated are linear swept chirps between 60 and 120 kHz. The bandwidth was the widest that the Bruel & Kjaer 8105 hydrophone, used as the source, could emit whilst maintaining satisfactory signal amplitude at all frequencies. The sound pressure level of the chirp peaked at over 600 Pa at 1 m. The duration of the chirps was varied between 100 μs and 1 ms. The chirp was generated using a constant voltage signal. This of course resulted in an amplitude modulation owing to the frequency response of the 8105 hydrophone. Note that the 8103 hydrophones (when used in receive mode) are nominally flat over the frequency range tested. The minimum length of signal that could be generated whilst maintaining the desired bandwidth was 100 μs. A further consideration was the time window for gathering data at hydrophone H2 (Figure 3-6). This was limited by the time taken for the pulse to travel to the hydrophone along the direct path and the arrival time of the first reflection (Figure 3-6). The time window was approximately 1.5 ms in length, and the cloud response from the chirp was received prior to the first wall return. Figure 4-2 shows an example of the 1 ms chirp as received at hydrophone H2, without a bubble cloud being generated, illustrating the amplitude and time windowing constraints.

In the following section the results of the tests are presented and discussed.

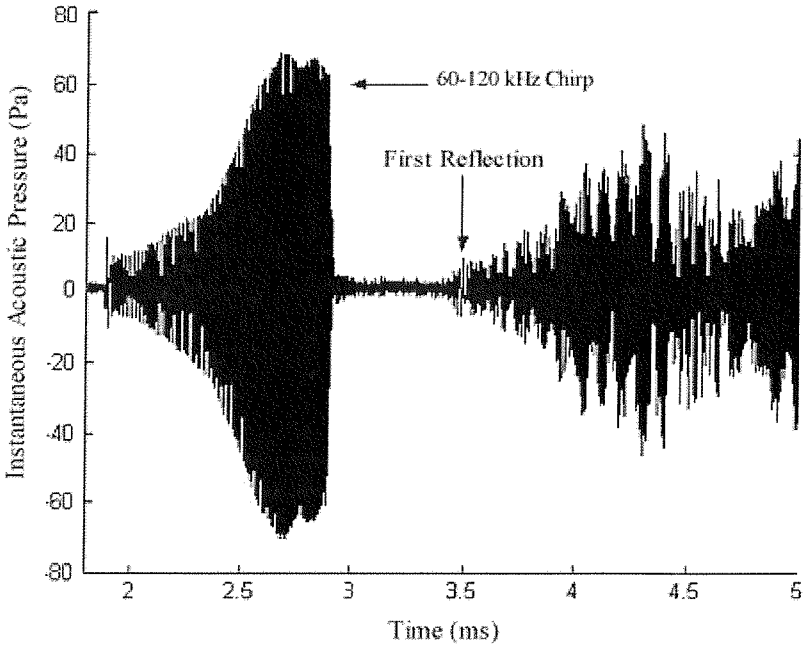

Figure 4-2 1 ms linearly swept chirp signal of bandwidth 60 - 120 kHz as received by Hydrophone H2 with no intervening bubble cloud. The amplitude modulation and first wall return can be clearly seen. The y-axis indicates time in seconds after the signal was generated.

4.2 Results

The theoretical and experimental results obtained using the pulses described above are presented and discussed in the following section. The experimental results are described first in section 4.2.1 and a method of interpreting the data introduced. In section 4.2.2 the range-dependent cloud model is applied using the pulse data and the results compared with the experimental pulse data. The implications of the theoretical and experimental investigation of the effect of pulse duration on the electrolysis bubble cloud are discussed in 4.2.3. The model is then applied using the chirped waveforms and the results compared with the experimental data. This is discussed in section 4.2.5. Finally the potential for Type III enhancement is discussed in section 4.2.6.

4.2.1 Experimental measurement of pulsed signals

In order to explore the effect of changing the pulse length, four separate tests were carried out. As described in section 4.1.1, the first two tests involved changing the pulse length while maintaining a constant centre frequency and amplitude with and without a bubble cloud present. The test data was validated by repeating the above two tests using the longest pulse length, but systematically reducing the amplitude as described above. Owing to the low sound pressure levels used, the bubble response will vary almost linearly with pressure. This mimics the reduction in attenuation without incurring any of the effects owing to ring-up. This allows the length varying and amplitude varying data to be overlaid when plotting the energy measured (see section 3.3.2 for method) at hydrophone H1 versus the energy measured at hydrophone H2. Any divergence between the data sets can then be interpreted as a change in the attenuation efficiency and thus, sonar enhancement.

Figure 4-3 shows a sketch indicating how the data will be presented to aid in interpretation. In order to understand this method of plotting the data consider three scenarios. First, if there is no bubble cloud both data sets will increase linearly with increasing pulse length and amplitude starting from the origin. The gradient of the line is a function of the spreading loss and attenuation of water at the driving frequency. In this case both the "amplitude-varying" and "pulse-varying" data sets should overlay each other. This is represented in Figure 4-3 by the dotted line. Any deviations will be as a result of experimental error. Second, if the bubble cloud is present and there is no pulse length dependence, then again both sets of data will increase linearly with increasing pulse length and amplitude starting from the origin. The gradient will have changed however, owing to the increase in attenuation, because of the presence of the bubble cloud. This is represented on the plots by the dashed line. Thus the plots of the bubble cloud and no bubble cloud data sets will diverge from the origin, but again the pulse varying and amplitude varying data sets will overlay each other. This is shown on the plot by the divergence of the dashed and dotted lines. Thirdly, consider the case where the bubble cloud is present and there is a pulse length dependence. This is the scenario that is expected. In this case the amplitude varying and pulse varying data sets taken when no bubble cloud is present will linearly increasing from the origin (dashed line) as before. The amplitude varying bubble cloud data with a bubble cloud present will also increase linearly with a

different gradient (dotted line). This is the same as scenario two. In the case of the pulse length varying data, however, it is expected that the gradient will change with changing pulse length. This will result in a divergence from the amplitude varying data, until steady-state is reached. Once steady-state has been reached, the data will again increase linearly with increasing pulse length, and should overlay the "amplitude-varying" data set. If this is the case, the "pulse-varying" data curves towards the no-bubble data sets, as shown by the solid line in Figure 4-3. This therefore would indicate a reduction in attenuation, and an enhancement in sonar detection over steady-state. Conversely, if the "pulse-varying" data curves away from the no-bubble data sets, then attenuation has increased compared to steady state, resulting in a degradation of sonar performance. In both cases, the plot will return to zero as the driving energy tends to zero.

The energy levels at each of the hydrophones were calculated following the method described in section 3.3.2. It should also be noted that the method of calculating attenuation described in section 3.3.2 (by using the difference in energy at hydrophone H2 with and without a bubble cloud present) is implicit in this analysis. The magnitude of the gap between the lines labelled 'no bubbles' and 'with bubbles' in Figure 4-3 is the equivalent energy loss.

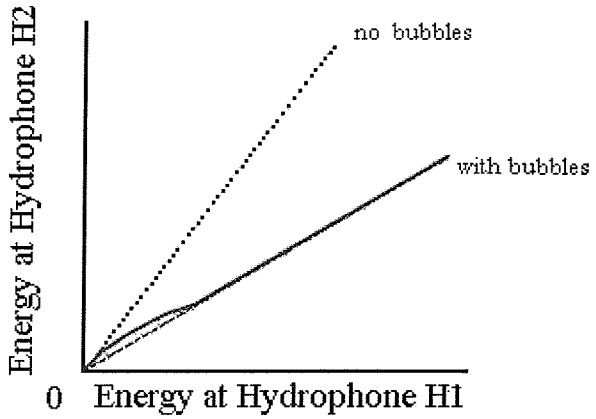

Figure 4-3 A sketch showing how the data will be interpreted. The amplitude varying and pulse length tests are expected to vary linearly and should overly (dotted line). The tests with the bubble cloud present are expected to show a reduction in the energy measured at H2 owing to the cloud attenuation. The amplitude varying tests should still vary linearly with the energy at H1 (dashed line). However if using short pulses reduces the attenuation the resulting plot will shift from the dashed line to the dotted line (indicated by the thick black line).

Thirty traces were taken from the hydrophones for each of the driving signals tested and the results averaged and plotted in Figure 4-4. This figure follows the format sketched in Figure 4-3. The two uppermost lines labelled 'no bubble cloud data' represent the data taken in the absence of any bubble cloud. As expected, the "amplitude-varying" (dashed line) and "pulse-varying" (solid line) data overlay. The error bars indicate scatter in the data equal to one standard deviation. The fact that the no-bubble data sets are in close agreement suggests that the experimental technique and level of averaging are sufficient to be able to detect any pulse length dependence in the bubble cloud data. Furthermore, it confirms, up to this point, the sketch and analysis of the data interpretation discussed above.

The lower pair of lines, labelled bubble cloud data, shown in Figure 4-4 are the measurements taken with the bubble cloud generator switched on. Again as expected the gradient of these lines is less than the gradient of the bubble-free data, owing to the increased levels of attenuation. The amplitude varying data (dashed line) is expected to vary linearly with increasing amplitude, and thus energy, at the reference hydrophone. It can be seen in Figure 4-4 that this is not quite the case. The small

scatter in the data that causes this is consistent with fluctuations in the bubble cloud over time resulting in changes in the levels of attenuation measured.

The pulse length varying data (solid line) is plotted with error bars showing scatter in the data equal to one standard deviation. For almost all the tested pulse lengths the data is within one standard deviation of the amplitude varying data set. The exceptions to this are one data point at approximately 45 Pa^2 measured at hydrophone H1 and the two data points below 20 Pa^2 measured at hydrophone H1. The first data points and last two data points where a deviation was measured will be considered separately.

The deviation indicated at approximately 45 Pa^2 measured at H1 falls within the pulse lengths where the cloud is apparently at steady-state since data points with energy levels both above and below agree with the amplitude varying data set to within one standard deviation. One possible reason for this deviation lies in the fact that the cloud as a whole deviates from a $\left(1-e^{-t/\tau}\right)$ ring-up. This will be tested in section 4.2.3. The second two data points showing deviation between pulse length and amplitude varying data sets represent the two shortest pulse lengths tested, and indicate increasing deviation with decreasing pulse length. This is the type of trend described in scenario three of the analysis of data interpretation discussed above. These two data points lie between the bubble cloud and no-bubble data, and are indicative of a reduction in attenuation as pulse lengths become very small (of the order 1 to 2 cycles).

To summarise, the experimental data, when compared with a control experiment, appears to indicate Type I pulse enhancement. This will now be compared with the quantative predictions of Type I enhancement predicted for this cloud by the range-dependent theory described in chapter 2.

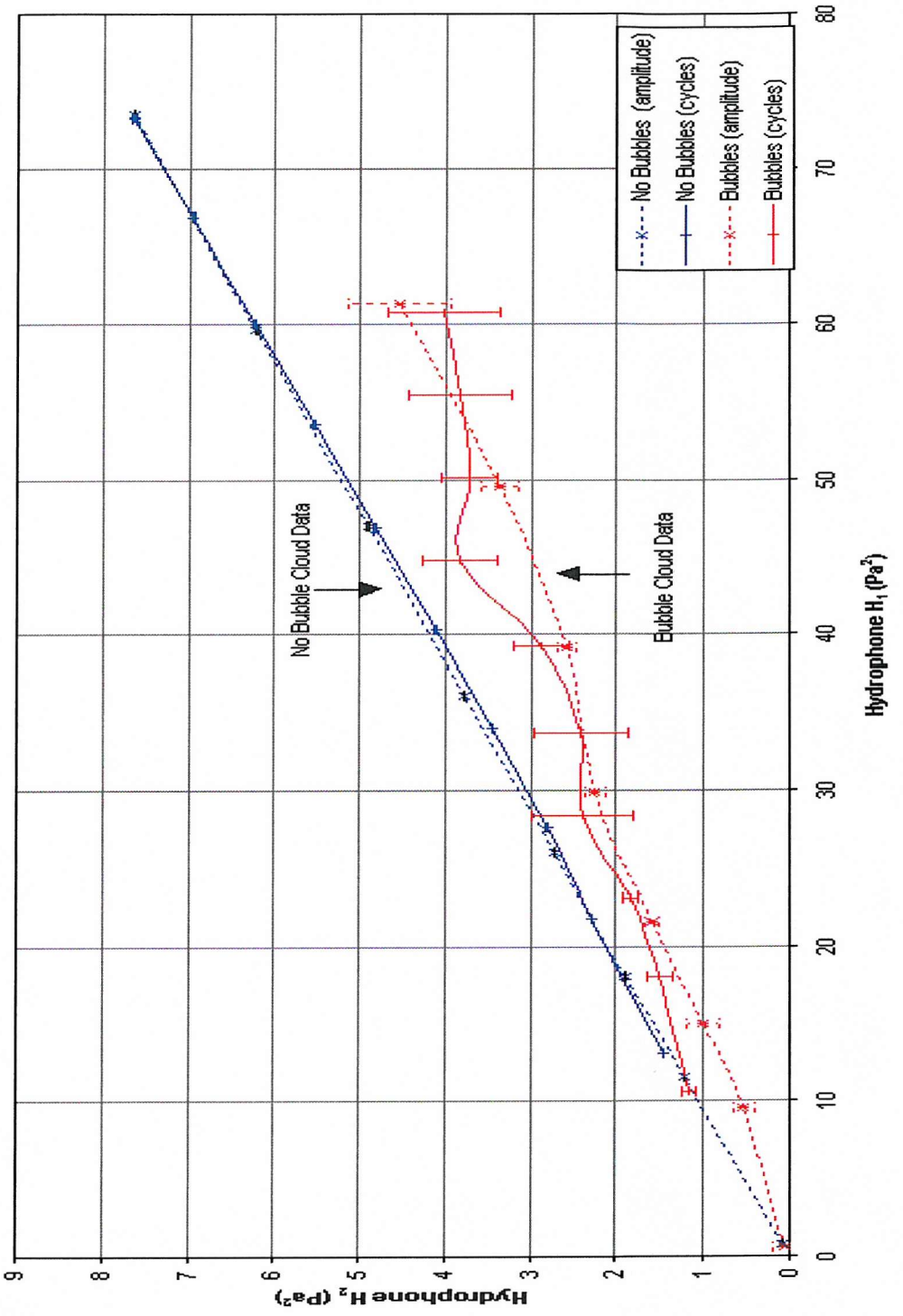

Figure 4-4 Experimental results showing the relationship between transmitted and received energy with and without a bubble cloud. Results are for pulse lengths between 1 and 10 cycles (x solid line) and a 10 cycle pulse at different amplitudes (x dashed line). The data taken with and without the bubble cloud present is labelled and error bars indicating one standard deviation in the results are shown for the variable pulse length data.

4.2.2 Theoretical model of pulsed signals

In this section the experimental results of Figure 4-4 are compared to theoretical models. The range-dependent cloud model described in chapter two, section 2.3, was used to calculate the attenuation of the signal by the cloud, using pulses of the same time series and amplitude (at the cloud) as were employed in the experiment. This was calculated by determining the spreading loss between the two hydrophones and inferring the sound pressure level at the leading edge of the cloud from the energy recorded at hydrophone H1.

The spreading loss was calculated using the following equation:

$$\frac{P_1}{P_2} = \frac{E(H1)}{E(H2)} = \left(\frac{r_1}{r_2}\right)^y \qquad [4\text{-}1]$$

Here P_1 and P_2 are the acoustic pressure amplitudes at hydrophones H1 and H2 respectively. The energy levels at hydrophones H1 and H2 are *E(H1)* and *E(H2)* respectively and r_1 and r_2 are the ranges of the hydrophones from the source. The spreading loss is a function of the power y. For example, for spherical spreading $y = 2$ and for cylindrical spreading $y = 1$. The spreading loss in the tank differed from the spherical spreading expected with the actual spreading loss exponent (y in the above equation) calculated to be 1.45 from measurements made in the bubble-free-tank. This measured exponent was used in conjunction with [4-1] and the range of the bubble cloud from the source to infer the sound pressure level at the cloud.

In order to plot theory and experiment on the same graph, it is necessary to relate the attenuation, as calculated by the model, with the attenuation shown in Figure 4-4. This is indicated by the difference in the energy levels measured at hydrophone H2 with and without a bubble cloud present for each test waveform. Theory can thus be compared to the pulse length varying experiment by subtracting the theoretical energy loss from the experimental data taken without a bubble cloud (the uppermost data labelled no-bubble data in Figure 4-4). The resulting theoretical data set, plotted against the experimental data, is shown in Figure 4-5. This figure is identical to Figure 4-4 but with circles to show the discrete values of the theoretical model for different pulse lengths with a thick solid line interpolated through these points.

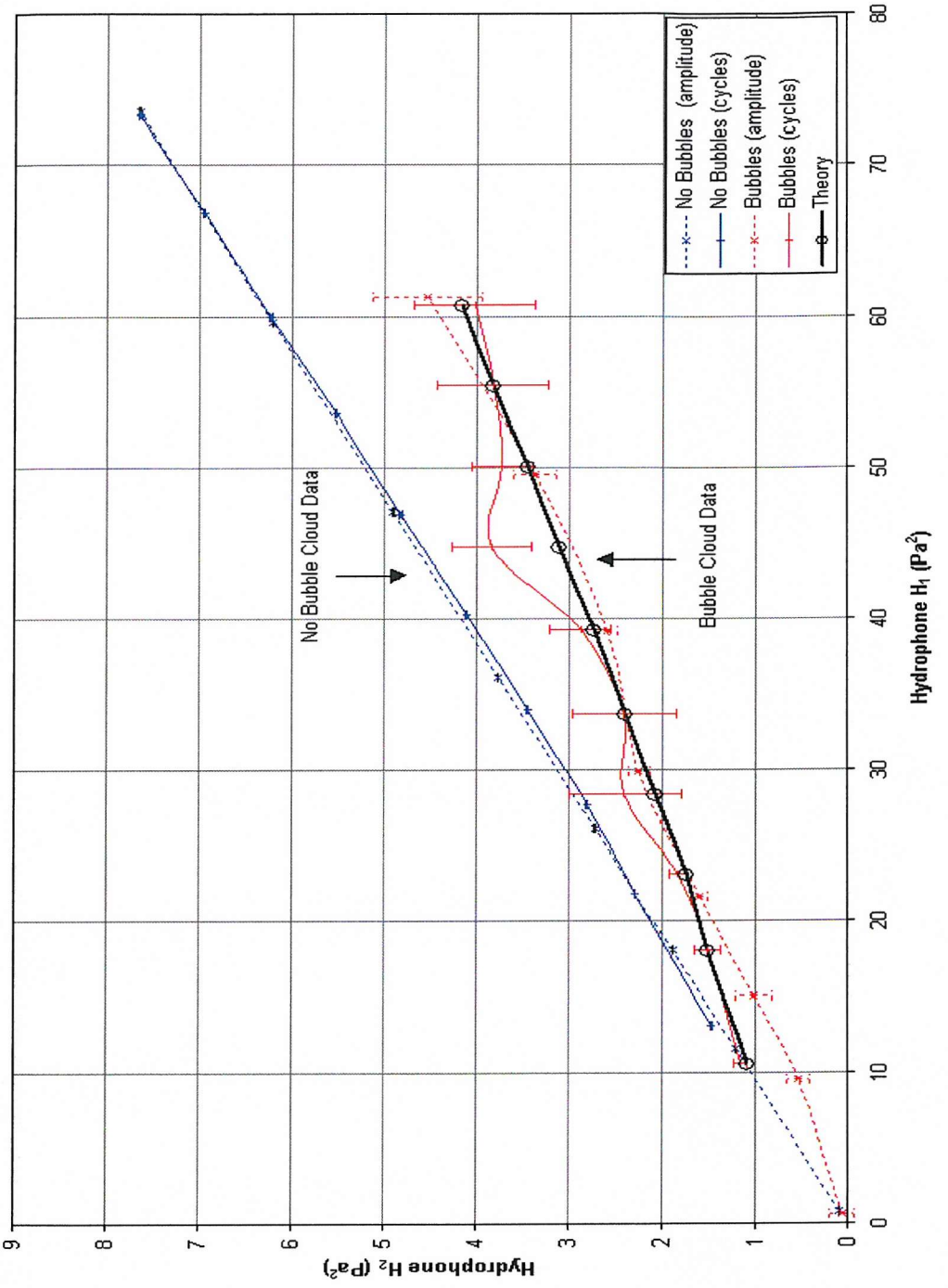

Figure 4-5 Comparison of theoretical and experimental results using measured pulses in the model. Results are for pulse lengths between 1 and 10 cycles (x solid line) and a 10 cycle pulse at different amplitudes (x dashed line). Theoretical data for varying pulse lengths is indicated by a circle (o) and thick solid line. The data taken with and without the bubble cloud present is labelled and error bars indicating one standard deviation in the experimental results are also shown for the variable pulse length data.

The figure shows excellent agreement between theory and pulse varying experimental data. The theoretical data points lie within one standard deviation of the experimental data. The only exception is an anomalous data point at 45 Pa^2 at H1.

However to understand the implication of this figure, it is vital to appreciate that the driving sound field used as input to the theory came from the measured incident pulses, and not from idealised pulses at the frequency of the signal generator used in the experiment (80 kHz). This key point will now be further explored in section 4.2.3 in order to understand precisely which mechanism is causing the enhancement seen in Figure 4-5.

4.2.3 Discussion of experimental and theoretical pulse data

Good agreement between theory and pulse varying experimental data has been shown when using the time series recorded by hydrophone H1 as the driving signal for the model. The data also shows a divergence similar to that sketched in Figure 4-3 prior to undertaking the experiment. This is indicative of Type I enhancement. However, as can be seen from Figure 4-1, the transmitted pulse in the experiment is filtered by the characteristics of the transmitter. When a single cycle pulse is generated by the function generator, the source produces a time series several cycles in length. This is the reason for using measured time-series of the 80 kHz driving pulse when running the model to produced the data plotted in Figure 4-5.

This artefact was further investigated by analysing the single cycle and ten cycle pulses identified in Figure 4-1 in the frequency domain. Figure 4-6 shows the frequency spectrum of both the pulses on a logarithmic scale. It is clear that the centre frequency of the pulse changes significantly. The centre frequency of the single cycle pulse is approximately 100 kHz, which (as expected) is closer to the resonance of the transducer (120 kHz) than the 80 kHz centre frequency of the longer pulse. As the signal generator inputs to the source a signal that more closely resembles an impulse excitation, so the output of the transducer will be increasingly dominated by its resonance frequency.

Thus care must be taken when interpreting the results shown in Figure 4-5. As already mentioned the trend suggests Type I enhancement, but the introduction of a frequency shift could also produce this trend through Type III enhancement i.e. if the

attenuation reduced with increasing frequency. As the frequency increases, the equilibrium bubble radius that is resonant becomes smaller. Examination of the population distribution of the cloud, shown at the beginning of chapter 4, will show that the numbers of bubbles are increasing with decreasing bubble radius. However, the reduction in their size results in reduced scattering and attenuation by each individual bubble. The range independent cloud model can be used to calculate the extinction cross-section for a single cycle pulse at 80 kHz and 100 kHz respectively. The attenuation for each of these cases, using the tank population, is 0.12 dB/m and 0.7 dB/m respectively. Thus the attenuation outweighs the increase in the number of bubbles, resulting in the trend shown in Figure 4-5.

This experiment clearly indicates that great care is required in interpreting the results of pulse-enhancement experiments. Although the data appeared to indicate Type I enhancement, and agree well with qualitative theoretical predictions that Type I enhancement could occur, careful analysis of the data indicated that the main source of enhancement was Type III. Because the measured incident pulses, and not idealised 80 kHz pulses, were used as input for the theoretical predictions of Figure 4-5, the theory will include any contribution from both the Type I (if it exists) and type III enhancement mechanisms.

Hence interpretation of the experimental data confirms the presence of Type III enhancement but not the looked-for Type I enhancement. It is possible that the Type I enhancement is being masked by the frequency shift in the transmitted signals. Since excellent agreement between the model and experimental data has been shown the model can be used to estimate the Type I enhancement. The range-dependent non-linear cloud model is again used but this time driven by idealised (without ring-up or ring-down) 80 kHz pulses of the same sound pressure level as the experimental data. The results are shown in Figure 4-7. This figure is identical to Figure 4-5 but the theoretical data shows the results of the model using idealised pulses instead of measured time series.

The theoretical results now differ from the measured pulse length data and agree more closely with the amplitude varying data. This suggests no Type I enhancement occurred. The enhancement seen in Figure 4-5 is dominated by a Type III mechanism.

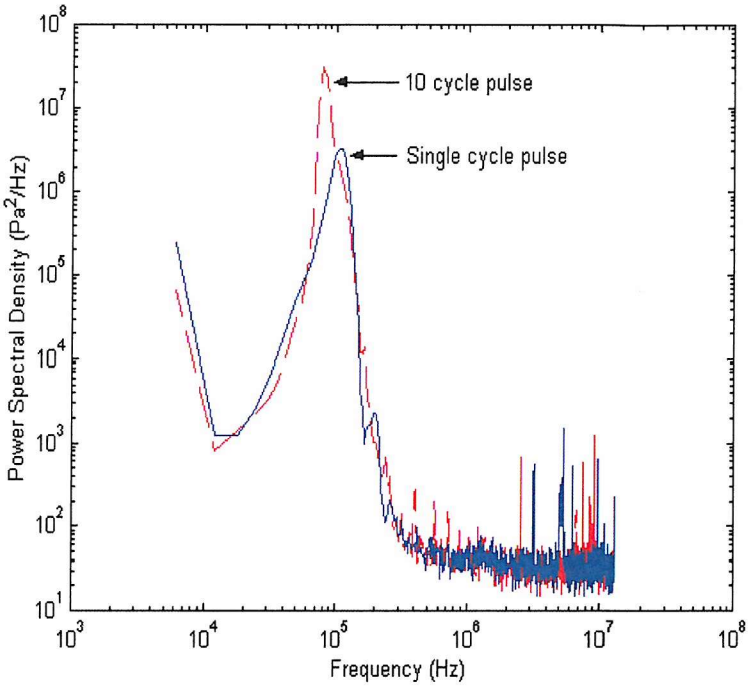

Figure 4-6 Frequency response of the single cycle pulse (solid blue line) and the 10 cycle pulse (dashed red line) generated with a centre frequency of 80 kHz. The effect of the transmitter on the shorter pulse is clearly shown by the shift in the peak in the frequency response to approximately 100 kHz.

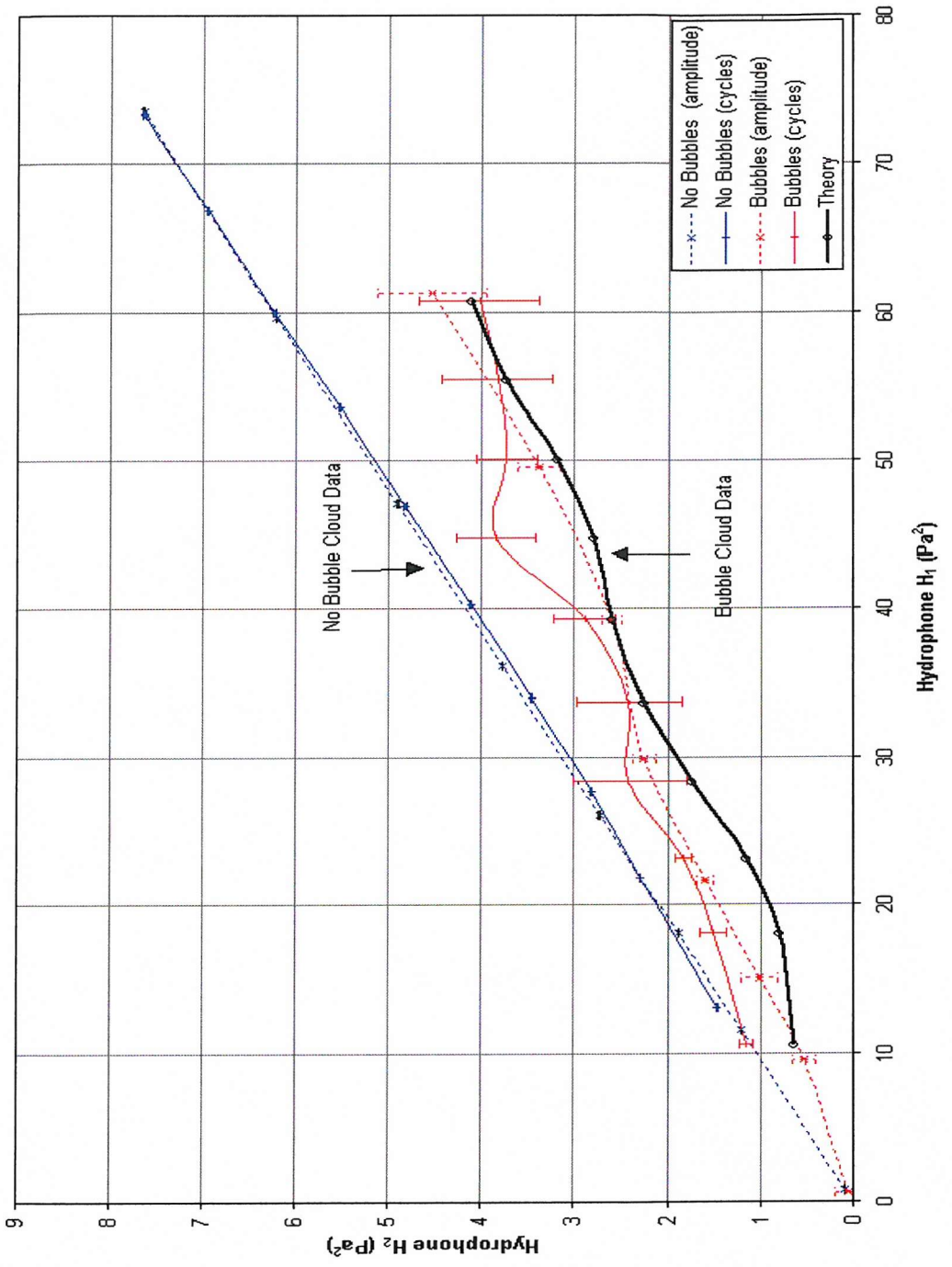

Figure 4-7 Comparison of theoretical and experimental results. Results are for pulse lengths between 1 and 10 cycles (x solid line) and a 10 cycle pulse at different amplitudes (x dashed line). Theoretical data for varying pulse lengths is indicated by a circle (o) and thick solid line. The data taken with and without the bubble cloud present is labelled and error bars indicating one standard deviation in the experimental results are also shown for the variable pulse length data.

4.2.4 Theoretical model of chirped signals

To investigate Type II enhancement, (the use of broadband excitation, section 2.4.3) a series of tests were conducted using chirped signals of fixed bandwidth (60 kHz – 120 kHz). The experimental arrangement described in the previous chapter was used to measure the attenuation of the bubble cloud. The only change was to increase the delay between the generation of successive driving waveforms to 2 s to allow for the increased reverberation at frequencies in excess of 100 kHz (See Appendix D). Chirp lengths of 100 μs, 200 μs, 400 μs, 600 μs, 800 μs and 1 ms were tested. Again thirty traces were taken for each waveform and the energy levels at each of the hydrophones calculated. In this way geometric effects are removed and only the attenuation owing to the cloud is measured.

The average level of attenuation of the driving signal was again calculated in the fashion described in section 3.3.2. The attenuation in dB was determined by dividing this energy loss by the energy at hydrophone H2 when no bubble cloud was present for each of the driving waveforms. The results are plotted as attenuation versus chirp length in Figure 4-8. Error bars indicating one standard deviation of the scatter in the data are also shown.

The method of determining attenuation used in Figure 4-8 normalises the results with respect to the energy received at hydrophone H2 allowing waveforms of different energy levels to be compared directly. In the following section the results of the chirp test are discussed and compared with results of the range dependent theoretical model from chapter 2 for both chirps and long pulses.

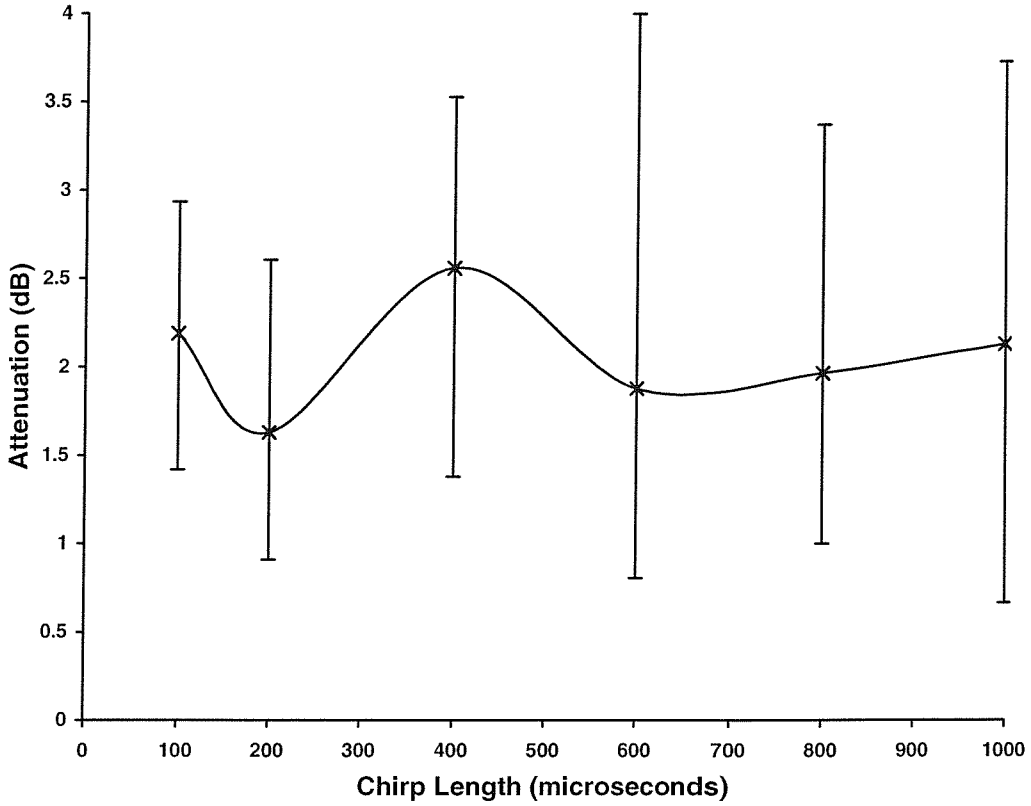

Figure 4-8 Experimental measurements of attenuation of the signal received at hydrophone H2 versus the chirp length. Error bars indicate the extent of the scatter in the results.

4.2.5 Theoretical measurement and analysis of chirped signals

Theoretical predictions of the attenuation of the chirped signals by the bubble cloud were obtained using the range dependent theoretical model developed in chapter 2. Measured signals taken at hydrophone H1 were used as the model input with amplitude corrections to account for spreading losses between the hydrophone and the cloud (as discussed in the preceding section on the experiments with pulses). The theoretical results were processed in the same manner as the experimental signals and the results plotted in Figure 4-9. The experimental results from Figure 4-8 are also plotted in this figure for comparison.

The measurements of attenuation used to invert for the bubble population in section 3.2.1 can be used to investigate whether chirped signals show any sonar enhancement

over pulses whose centre frequencies span the same range. The results for the 1 ms pulses with centre frequencies between 60 kHz and 120 kHz are plotted on the right hand side of Figure 4-9 as hollow circles. A further data set can be plotted using the 80 kHz amplitude varying and pulse varying data sets from the pulse tests in section 4.2.1. This data is plotted on the left hand side of Figure 4-9.

The theoretical model (Figure 4-9b) again shows good agreement with the experimental data with all bar one data point (at 400 μs) within one standard deviation of the experimental results. However, the results vary about a mean attenuation of approximately 2.1 dB with no obvious trend relating to the chirp duration. Since no dependence on the chirp length is indicated by the theoretical or experimental the results suggest no Type 1 enhancement.

The chirp results are also compared to 1 ms pulses of different frequencies to investigate Type II enhancements. The pulses between 60 and 120 kHz show a spread in attenuation from 3 dB to 1.5 dB as frequency increases with an average attenuation of 2.3 dB. This is very close to the average attenuation of the chirped data of 2.1 dB. Hence, given the error bars associated with the data, this comparison does not indicate that the attenuation by the bubble cloud is anything other than simply an average of the attenuation as a function of frequency over the bandwidth of the insonifying waveform. Hence no evidence has been found for Type II enhancement in these tanks tests[i]. This is also confirmed by the comparison with the data sets collected in the previous section.

The final method of enhancement, Type III, is investigated in the following section. This method of enhancement seeks to take advantage of the frequency dependence in the attenuation of the bubble cloud as illustrated by the pulse data in Figure 4-9.

[i] These findings cannot rule out the possibility that it occurred but the effect was not large enough to be apparent given the level of uncertainty indicated by the error bars.

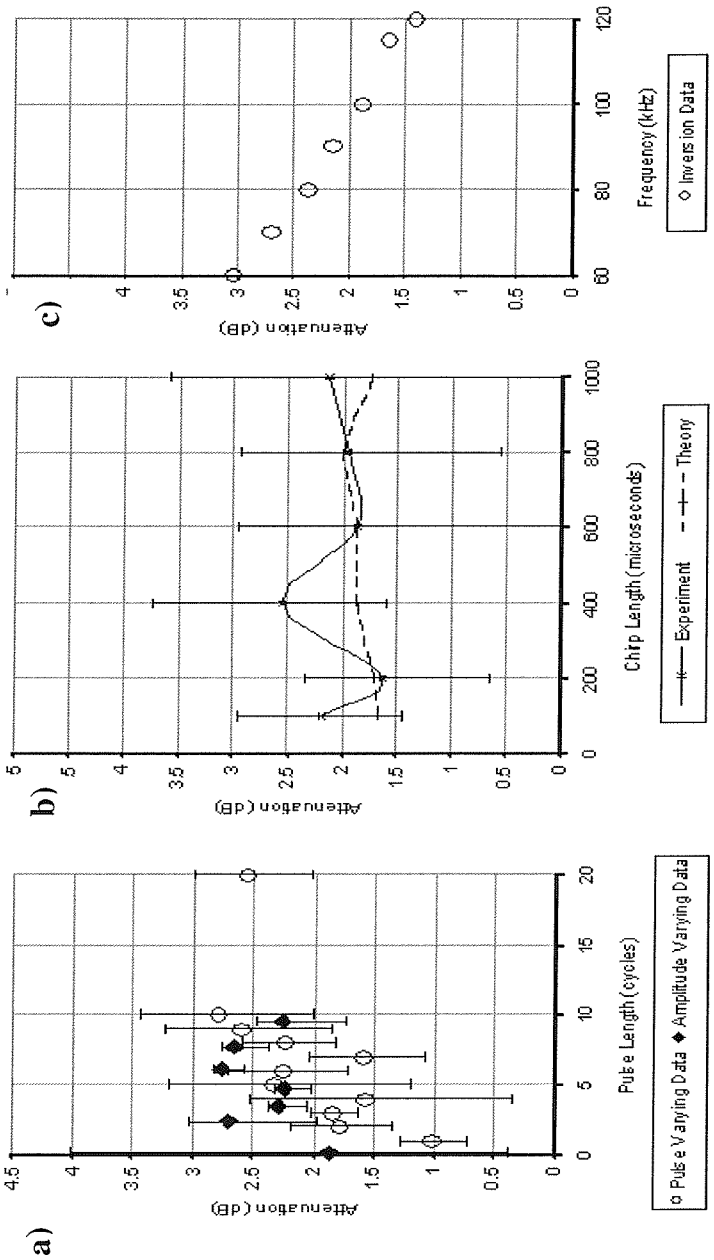

Figure 4-9 Comparison of experimental and theoretical measurements of attenuation of the signal received signal for pulses and chirps. Plot a) is the attenuation of the pulse varying and amplitude varying data (hollow and filled circles respectively) versus pulse length from the previous section (this is the same experimental data as shown in Figure 4-4). The nominal acoustic frequency was 80 kHz though, as discussed in section 4.2.2, for the shorter pulses this tended towards 100 kHz. Plot b) shows the theoretical and experimental attenuation of the chirp data versus the chirp length. Plot c) is the attenuation versus frequency measured to obtain the bubble population by inversion using 1 ms pulses (section 3.2.1). Error bars indicate the extent of the scatter in the experimental results. All plots share a common y-axis.

4.2.6 An investigation of Type III enhancement

It has long been recognised that the attenuation of a bubble population is dependent on frequency. Indeed attenuation information is commonly inverted to measure the bubble population[70]. Thus there is a relationship between the levels of scattering and attenuation of a cloud and the driving frequency. This is a function of the non-linear increase in scattering and attenuation as bubbles increase in size particularly when driven at resonance. This trend is scaled by the cloud distribution. In naturally occurring clouds, generated by breaking waves in the ocean, the number of bubbles typically reduces with increasing bubble radius[71,72] (although there may be a global maxima see section 2.4). It is logical to conclude (given these trends) that for each population distribution, a bubble cloud will have an insonification frequency where the scattering and attenuation is at a minimum. If that frequency is in a useable range, neither too high or too low, (where the signal-to-noise ratio, ambient noise, or diffraction effects become problematic) then Type III enhancement could occur.

The attenuation as a function of frequency has already been measured for the bubble cloud used in the tank experiments. The data was taken for the purpose of inverting for the bubble population distribution (section 3.2.1) and is plotted in Figure 3-2. The plot is referred to here for the purpose of investigating Type III enhancement.

The attenuation of this bubble cloud varies from less than 1 dB at 220 kHz to a peak of 4.9 dB at 20 kHz. The impact of this variation in attenuation on target detection can be determined by applying the sonar equation from section 1.2.2. In this test the parameters of the sonar equation are in most cases identical to those given in section 1.2.2 i.e. a 0.1 m long array with a target strength of –22 dB and source level of 60 dB. The differences are in the attenuation owing to bubbles, which are taken from Figure 3-2, the noise level which is assumed to be 0 dB at all frequencies and the acoustic absorption of sea water which is calculated after Fisher and Simmons[38] for an atmospheric pressure of 1 atm and a water temperature of 10°C (the full absorption calculation is used, which incorporates the effects of Boric acid and Magnesium sulfate). The resulting detection ranges are shown in Figure 4-10.

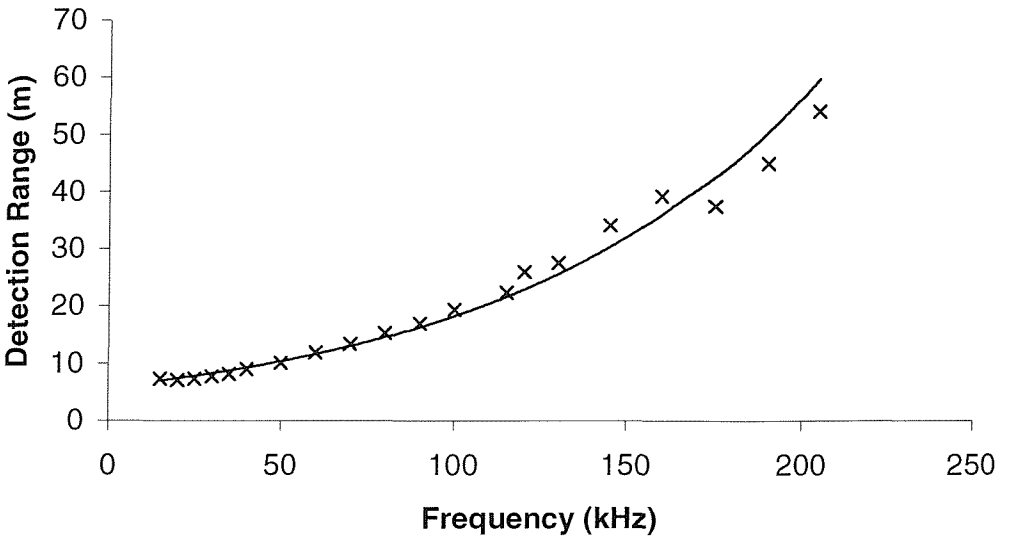

Figure 4-10 Target detection range as a function of frequency for the bubble cloud population used in the tank experiments (the bubble cloud, for this calculation, is assumed to be isotropic, homogenous, and to extend to infinity in all directions).

Since the attenuation owing to the bubble cloud decreases with increasing frequency it is to be expected that target detection ranges should increase with increasing frequency. In the example shown here the range of detection increase from approximately 7 m to 45 m as the frequency increases from 15 kHz to 190 kHz, a seven-fold increase. Thus, as expected, an increase in frequency results in an increase in detection ranges. This is in contradiction to the hypothesis that a lower frequency reduces off-resonant contributions that can mask Type I enhancement. These results clearly show that the frequency of insonification is an important consideration for target detection in bubbly environments.

4.3 Conclusions

In this chapter the three types (Table 2-2) of sonar enhancement have been investigated theoretically and experimentally in a test tank. The bubble cloud used in these experiments was artificially generated using electrolysis. Of the three types of enhancement tested, only Type III, which seeks to optimise the insonifying frequency, resulted in an apparent increase in target detection ranges. However, the comparison of the theoretical and experimental results has shown good agreement

with theoretical results, generally lying within one standard deviation of the experimental results.

There are three possible reasons for the failure to measure any benefit in Type I and Type II enhancement. The first is that large off-resonant bubbles dominated the scattering and thus masked the ring-up of the resonant bubbles despite attempts to minimise this. The second reason is that the transient contribution of bubbles close to, but not at, resonance is significant for this population when compared to the contribution of resonant bubbles. The third and final possibility is that Type I and Type II enhancement is present, but too small to measure experimentally.

To identify which if these possible explanations is valid, the non-linear bubble model was used to calculate the theoretical contribution of each bubble per μm radius bin scaled by the tank bubble population. The results are shown in Figure 4-11. First interpretation of this plot suggests that the resonant bubbles dominate. Closer examination of the plot around resonance (the lower plot in Figure 4-11) shows that near resonant bubbles responses are of a similar magnitude to the resonant bubble. Neither of these features explains why no Type I or Type II enhancement was detected during the tank experiments.

The attenuation of the bubble cloud and the relative contributions of the resonant, near resonant and off resonant bubbles needs to be calculated in order to investigate this further. For the purposes of investigating the masking of Type I and Type II enhancement, off-resonant bubbles are defined as those bubbles that do not exhibit a ring up or transient behaviour in response to an 80 kHz pulse. Resonant bubbles are defined as those bubbles that exhibit a smooth ring-up to resonance. The remaining bubbles, those that do not ring up smoothly to resonant, but do exhibit transient behaviour, are classed as near-resonant bubbles. Typical time series of the radiated sound pressure of a bubble from each of these regimes is shown in Figure 4-12 to illustrate this.

The non-linear range independent finite pulse length cloud model was then used to calculate the attenuation in decibels for all bubbles in the cloud and for the resonant, off resonant and near resonant bubbles. The model was driven with an idealised 80 kHz pulse of between 1 and 10 cycles in length with amplitude of 600 Pa. The results are shown in Figure 4-13.

The plot of attenuation versus pulse length for the entire cloud shows a small increase in attenuation with increasing pulse length. The change is very small, approximately 0.2 dB. The contribution of the resonant bubble shows a smooth ring up as expected with the attenuation increasing five fold for between pulse lengths of 1 and 10 cycles. The contribution of the off-resonant bubbles is small, but of a similar magnitude to the response of the resonant bubble to a one or two cycle pulse. The contribution of the near resonant bubbles is the most significant, contributing 1.7 dB/m of the cloud attenuation for the one cycle pulse (where the initial transient behaviour of the bubble is most significant) reducing to 1.3 dB/m for a 10 cycle pulse.

The model indicates a small amount of Type I enhancement, but it is too small to be detected experimentally owing to cloud variability and signal noise. The results indicate that the reason for this is the contribution of the near-resonant bubbles and as already hypothesized the contribution of the off-resonant bubbles is small.

Thus the original methodology of using an electrolysis type bubble cloud and a pulse frequency of order 80 kHz to minimise the off resonant contribution has been confirmed. However the previously over looked near resonant contribution has masked the majority of the Type I and Type II enhancement.

In conclusion, the theoretical model has been validated by the experimental data. Furthermore, the advantage of being able to use measured time series to drive the theoretical model have been proven. Results of the theoretical model using idealised and measured driving pulses allowed correct interpretation of the experimental results and identification of the correct enhancement mechanism. In addition the range independent cloud model has been used to help identify the presence of Type III enhancement and the reason why Type I and Type II enhancement was not detected. That is to say the relative importance of near resonant bubbles has been identified, and this is all the more significant in that has been overlooked in previous experimental studies and linear steady state models[40,42, 43].

In the next chapter, a surf-zone trial of sonar enhancement is described. The aim of this trial is to gain increased knowledge of the surf-zone bubble population distribution, and to test the three types of sonar enhancement in a realistic population distribution and attenuation levels which cannot be generated in the laboratory. It will also allow the importance of including the attenuation of the driving signal into the range dependent model to be ascertained. The population will be measured using several different acoustic techniques conducted, by a fellow PhD student Steven Meers[i] with the help of Mathew Simpson[i] and Gun Tae Yim[i], two other PhD students and University technicians John Taylor[i] and Anthony Edgely[i]. The trials were undertaken under the supervision of Prof. T G Leighton[i].

[i] Institute of Sound and Vibration Research, University of Southampton

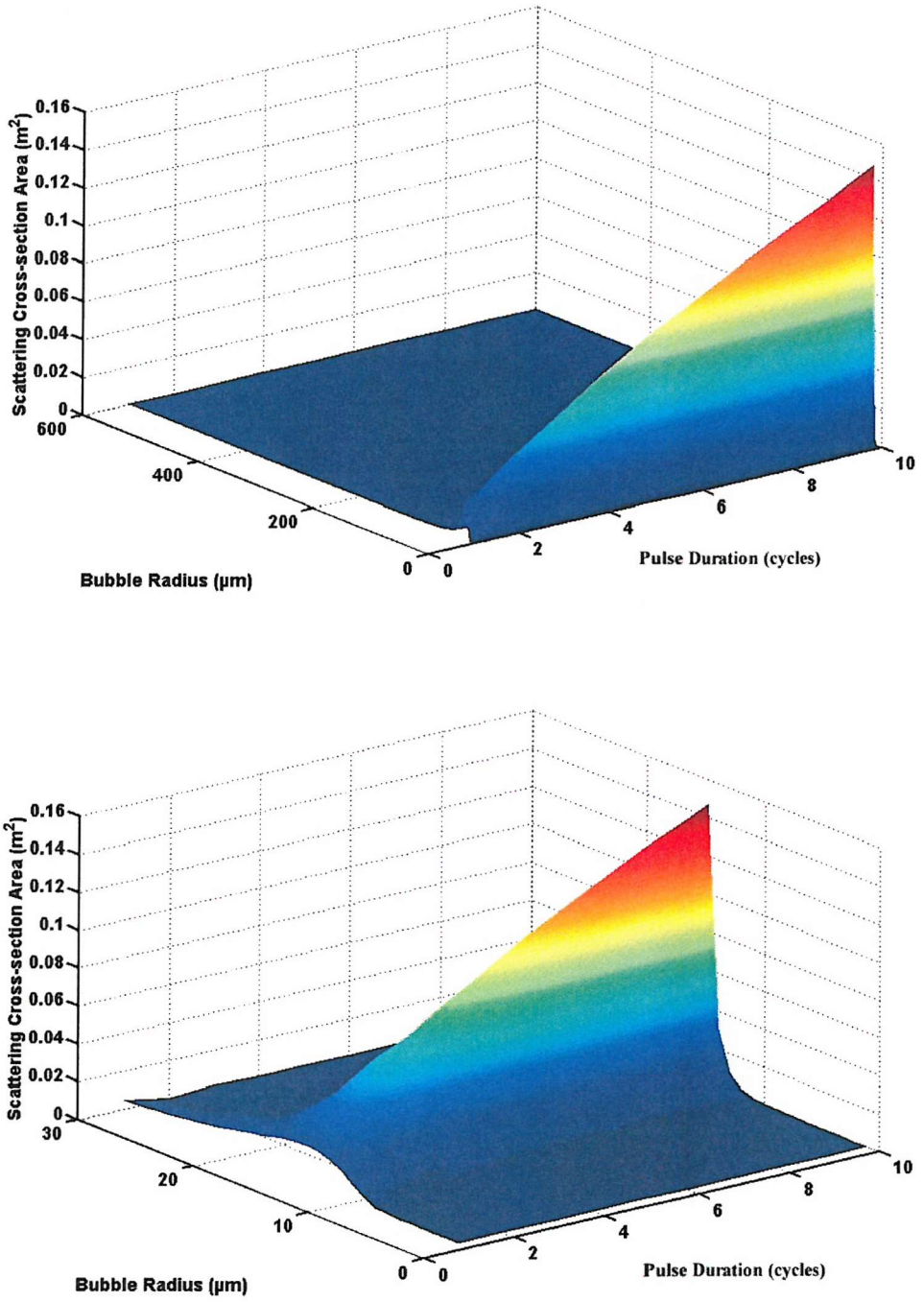

Figure 4-11 Theoretical Scattering Cross-section for different bubble radii and pulse lengths from one to ten cycles in an 80 kHz 600 Pa sound field scaled by the bubble population per μm increment measured during the tank tests. The top plot show all bubble radii up to 600 μm and the bottom plot is the same data but scaled so that only the bubble radii up to 30 μm can be seen to show the contribution of the near resonant bubbles

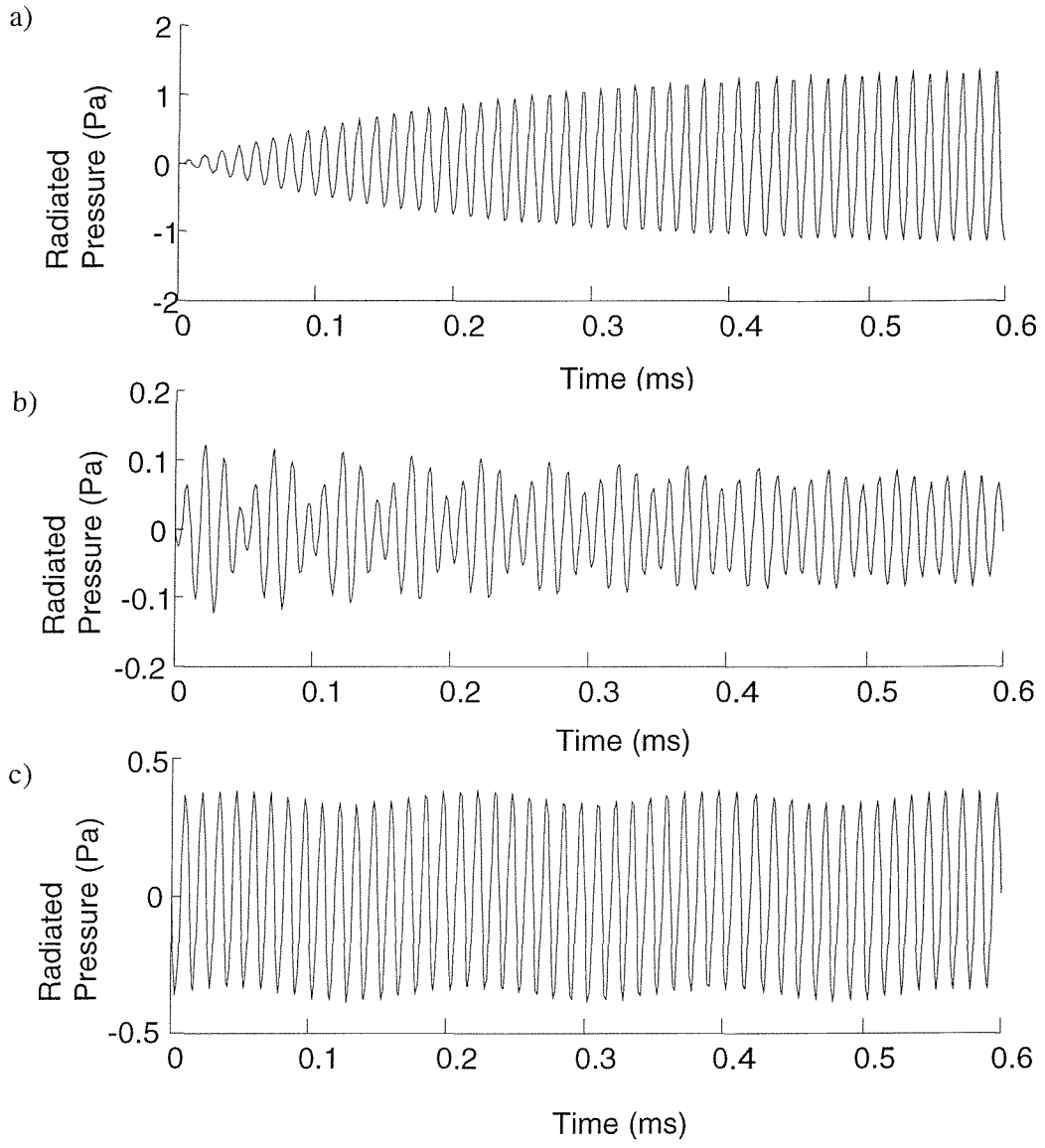

Figure 4-12 Time series of the radiated sound pressure level from a single resonant 40.5 μm radius bubble (a) a near resonant 55 μm radius bubble b) a 600 μm radius off resonant bubble (c) all in a continuous 80 kHz sound field of amplitude 600 Pa.

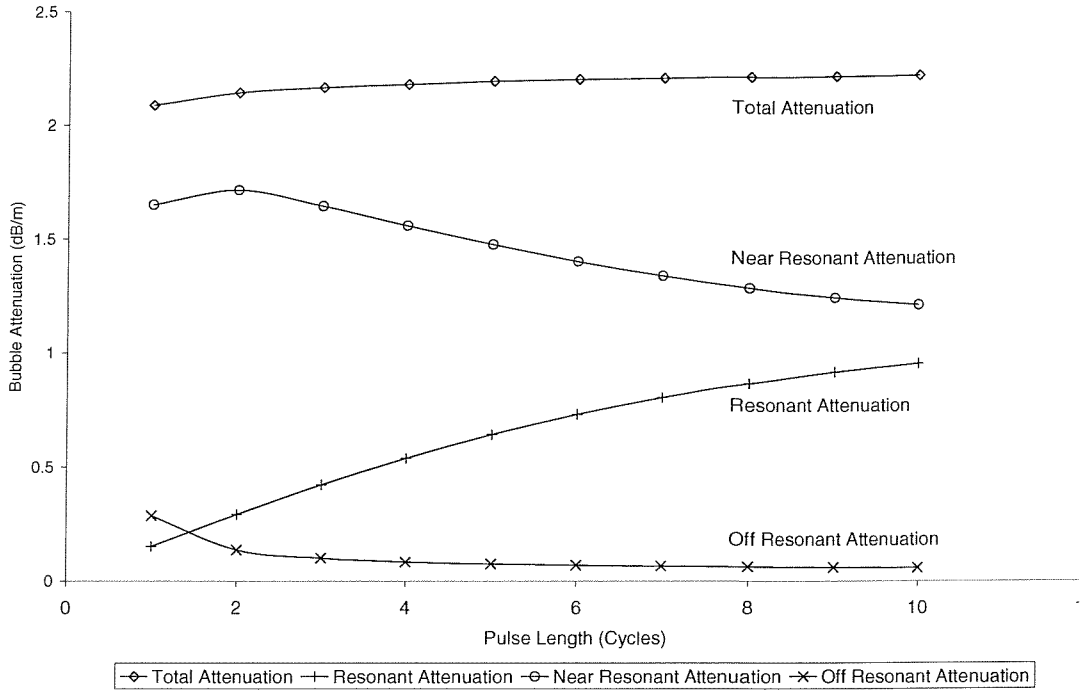

Figure 4-13 The theoretical cloud attenuation for pulse lengths from one to ten cycles in an 80 kHz 600 Pa sound field using the bubble population measured during the tank tests. The contribution of the resonant, near resonant and off resonant bubbles is also plotted. This is a discrete calculation for the data points plotted. Lines between data points are included to aide in interpretation.

CHAPTER 5

SURF-ZONE TRIAL

5 Surf-zone trial

This chapter describes a surf-zone based sea trial to investigate sonar enhancement in the target environment, and to develop a better understanding of the bubble population distributions that occur in the surf-zone. The three methods of sonar enhancement will be tested by comparing the levels of attenuation of the return echo from an air filled buoy suspended in the water column. The theoretical models developed in the proceeding chapters will be used to predict the attenuation levels in the surf-zone with emphasis on establishing the importance of incorporating the driving signal attenuation into the range-dependent model. As was seen in the last chapter, interpretation of any experimental data requires the bubble population to be used as input for the theoretical models (section 2.2). Whilst this information could be obtained for the tank experiments with relative ease (section 3.2.1), measurements of bubble populations in the surf-zone have rarely been accomplished successfully. On this sea trial, measurements of the population were attempted by two other PhD students, who were only successful in covering a very small range of bubble radii (by inversion of attenuation measurements at a range of frequencies). This provides fundamental limits on the input to the theoretical models and on the validity of their predictions and therefore on the interpretation that can be presented here.

5.1 Sea trial arrangement

The surf-zone sea trial was conducted on a beach at Hurst Spit, Milford-on-Sea in Hampshire from the 4th November to the 18th November 2000. The beach is southerly facing with a shingle and sand composition and a significant amount of sediment transport was observed over the two week period of the trials (around the equipment vertical changes in the seabed of approximately 50 cm were observed in a 20 minute

period). After several storm events during the trials, the depth of shingle on the beach changed by several feet and the beach profile changed. The beach profile was stepped, the position of the step changing after a storm event, resulting in a form of reef brake which generated plunging breakers in all but the calmest of conditions. The position of the wave breaking was a function of water depth, owing to the tide and the position of the step in the beach, and was a significant factor in the deployment of the equipment.

Initial attempts to deploy the transducers and targets involved the deployment of a rectangular scaffold array into the surf-zone and the attaching the equipment in-situ. Owing to increasing surf and difficult working conditions (see Figure 5-1) this was not possible before the rig was destroyed during over night storms. The deployment method and the construction of the rig was redesigned (as described below) and then redeployed on the 13th November.

In order to provide a stable and secure platform for mounting equipment on such a dynamic beach, 3" diameter scaffolding poles were attached to large feet, consisting of a 1 m x 1 m square steel plate, using in-line scaffold clips. On these stands would be mounted a UDI transmitter/receiver and pre-amplifiers and a 1.27 m (50") circumference air-filled buoy as a target. The UDI array was selected for its bandwidth and ability to reach high frequencies (360 kHz) since the only previous measurement of surf-zone bubble populations (Phelps *et al.*[28]) indicated a higher frequency would improve the chance of detecting Type I enhancement (section 2.5). The large target was chosen for two reasons. Firstly it increased the target strength in an attempt to limit the potential for the high levels of attenuation expected in the surf-zone[28] to mask the target. Secondly, the large target simplified the alignment of the source and receiver. The system was deployed monostatically with the source and receiver on one stand (consisting of a scaffold pole and base plate) and the target on the second. Further details of the deployment and position are given below.

The equipment was controlled from a portable cabin onshore, and communication with the equipment was via direct cable connection. In a similar fashion to the laboratory experiments previously described, signals were acquired to a PC via a LeCroy 9314 digital oscilloscope and GPIB software. Signals were generated using a Sony AWG 2020 and both the signal acquisition and generation were controlled via PC using National Instruments LabView software.

The two stands, minus the equipment, were positioned at the low-tide mark during a spring low tide and left to allow the feet to be buried. Once the stands were secure, the equipment would be deployed at the next low tide. The feet of the stands were quickly buried by shingle, in excess of 0.3 m, providing the stable base required. However, owing to a low pressure system resulting in high winds, high tides and large surf, a suitable low tide did not occur until the beginning of the second week. The equipment was attached to the stands using 3" exhaust clips.

Care was taken to confirm the alignment of the array and the target. This was achieved by sighting along a straight edge to check the array was pointing at the centre of the sphere and running a rope temporarily between the centre of the array and the buoy. The buoy had a seam joining the two halves running around the circumference, providing an excellent marker of the centre of the buoy in the vertical plane. The height of the buoy was altered with the aid of the rope until the array was pointed at the centre of the buoy. The geometry of the apparatus was carefully measured. A schematic of the experimental layout is shown in Figure 5-2 and a scale drawing in Figure 5-3.

The signals used and the criteria of the tests conducted using this setup are described in the next section.

(a)

(b)

Figure 5-1 Two photographs[73], taken a fraction of a second apart, showing (a) two of Professor Leighton's PhD students (Meers and Simpson) attempting to bolt sensors to a scaffolding rig the team have just deployed at sea; (b) Mr Simpson's feet (Mr Meers is not visible). During the subsequent trial the winds increased from the calm conditions shown here to speeds in excess of 50 mph.

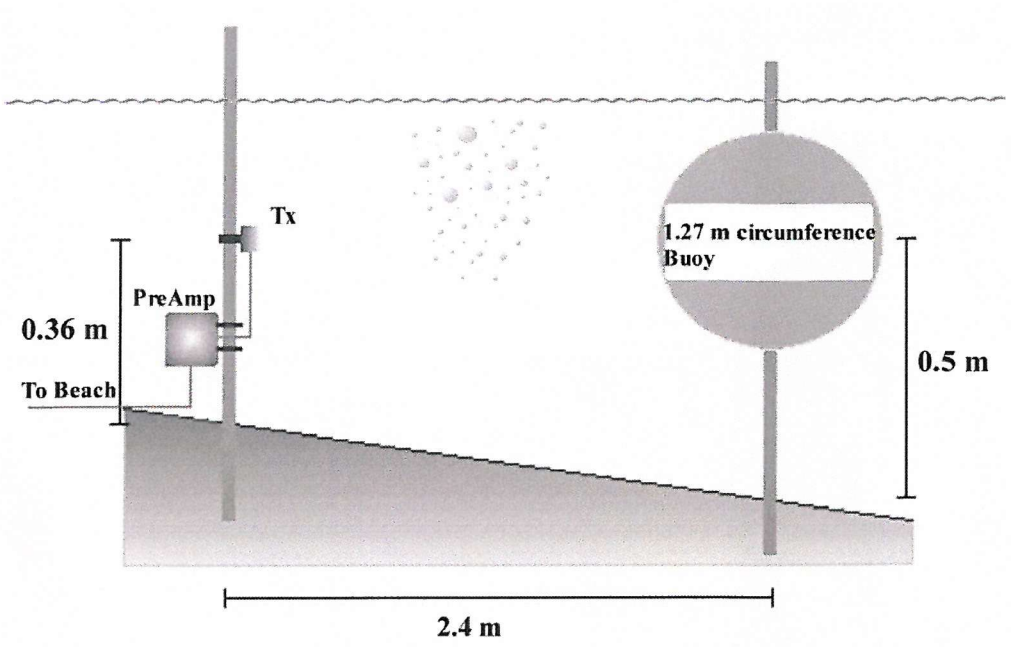

Figure 5-2 Schematic of the apparatus deployed into the surf-zone at Milford-on-Sea

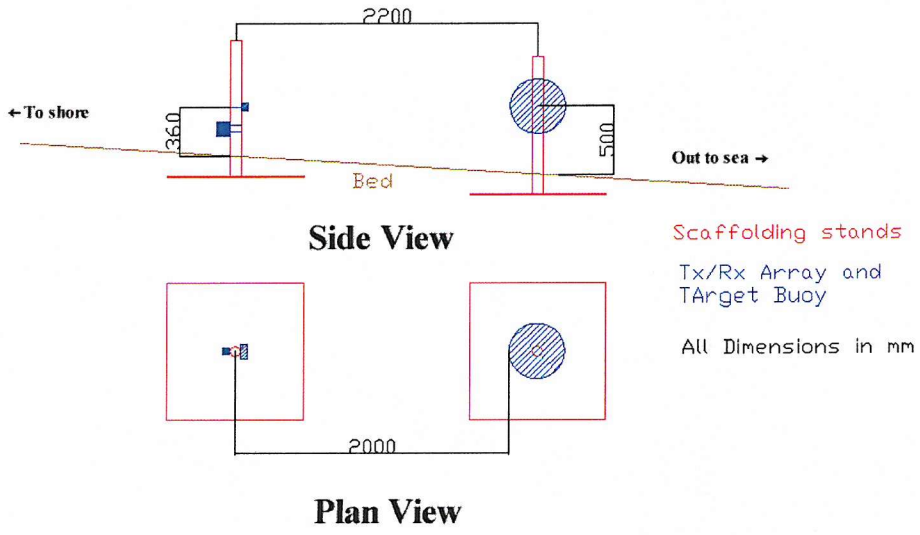

Figure 5-3 Scale drawing of the deployed rig in both plan and side views

5.2 Signals and test criteria

The UDI source and receiver used in the experiment has been calibrated for used between 200 kHz and 360 kHz. Using the full frequency range of the transducer array a series of signals were chosen to test the various types of sonar enhancement. These included pulses of 5 and 20 cycles with centre frequencies from 200 kHz to 360 kHz at 20 kHz intervals. In addition a swept chirp from ~200 – 360 kHz of duration 0.1 ms and 1 ms was generated, as well as a pseudorandom signal of bandwidth ~200-400 kHz and durations of 0.1 ms and 1 ms. The actual spectra of the chirp and psuedo-random signal are shown in Figure 5-4. The sound pressure level varied with frequency (Appendix D) but was approximately 205 dB ref 1μpa @ 1m.

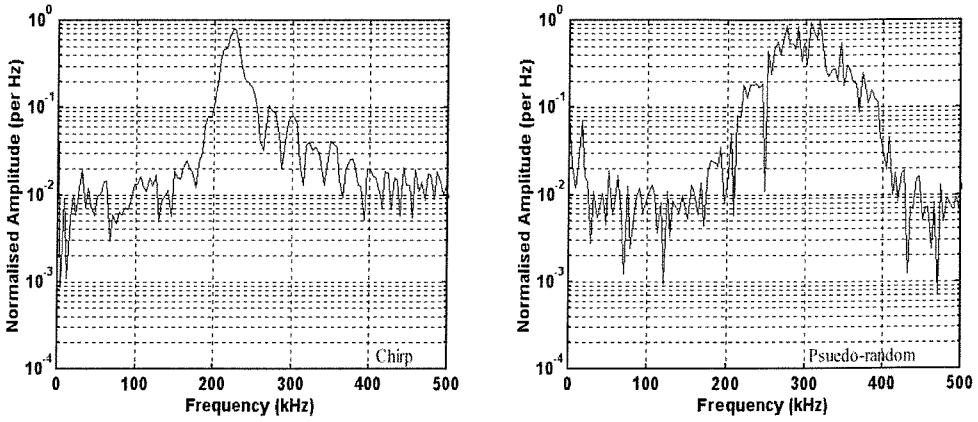

Figure 5-4 The bandwidth of the chirped signal (left hand plot) and pseudorandom signal (right-hand plot) used in the sea trial. The frequency spectrum was calculated using a 256 point FFT and the amplitudes have been normalised.

In order to be able to compare the relative performance of the different signals, it was necessary to concatenate them into a single waveform because the bubble cloud changed on a sub-second time scale. Each component waveform was separated by 10 ms to allow enough time to record the echo from the target buoy before the next waveform component was transmitted. The component waveforms were concatenated in this fashion in the following order: pulses, chirps (short then long) and pseudorandom (short then long). The pulses were concatenated in order of increasing frequency with interleaved 5 and 20 cycle lengths. The resulting signal was approximate 0.22 s in duration.

A further concatenated signal consisting of 20 cycle pulse with centre frequencies corresponding to the resonant frequencies of bubbles of equilibrium radius 9 μm to 15 μm (~208 kHz to 340 kHz) was used for inverting for the attenuation to give the bubble population.

The following experimental method and testing criteria were adopted to investigate the potential sonar enhancement of the signals described above.

In a similar fashion to the laboratory experiments previously described, in order to investigate sonar enhancement of the different signals, it is necessary to measure the attenuation owing to the bubbles between the transducer and the target. The laboratory experiments have shown that a robust way of achieving this is by calculating the energy in the echo from the target buoy i.e. calibrating the return during a bubble-free period and comparing this with measurements made with bubbles present.

The bubble-free condition was established by measuring the energy during a very calm period when few bubbles are present. The energy in the echo from the buoy during this calm period can then be compared with the energy in the echo when wave breaking is occurring, and thus bubbles are present. The attenuation owing to the bubbles can thus be calculated from the difference.

Since the equipment was deployed at low tide in calm conditions, during the subsequent high tide the water around the transducer and buoy was particularly calm. This period of calm conditions was used to obtain a nominally 'bubble-free' data set which could be used to ascertain the levels of attenuation owing to bubbles alone in subsequent tests. Owing to the difficulties of recreating the geometry in a test tank and the eventual loss of the target buoy, during a storm, post trial tank calibrations of the buoy, although undertaken were not used in the data analysis. This was because the scattering from a replacement buoy during the post-trial calibrations was on average 30% less than that measured in the surf-zone. Since an identical target could only produce greater scattering than in the surf-zone (where more inhomogeneities could be present in the water), clearly it was not possible to reproduce the target and its geometry to an accuracy which improves upon the use of the calm surf zone data for calibration.

The data were collected in the following fashion. A batch of ten time series were generated and acquired using the 20 cycle pulses equally spaced in bubble radius for latter inversion to estimate the bubble population. Immediately following this the concatenated signal for sonar enhancement was generated and acquired. Again this was repeated ten times.

A series of data sets were acquired in this fashion over a period of two days, the 14 and 15th November 2000. The first day's data set was taken in calm conditions as described above. The following days data sets were collected during 1-2 foot surf with wind speeds of approximately 15 mph (6.7 m/s) from the SW (onshore). No further data sets could be taken owing to the loss, during the night, of the buoy and buoy stand because of stormy conditions (wind speeds in excess of 50 mph) and the resulting high surf.

Analysis and presentation of the data as well as a comparison of theoretical and experimental results is covered in the next section.

5.3 Sea trial results

5.3.1 Summary of experimental results and theoretical modelling

In the previous section the signals to be tested for sonar enhancement are described. In addition a pulse train with frequencies selected to give regularly spaced resonant bubble radii was also generated. This was used to invert the attenuation to estimate the bubble population as was done for the tank tests in section 3.2.1. This allowed the numbers of bubbles to be estimated for an equilibrium radius of 9 – 15 μm in 1 μm increments. In order to be able to model the cloud it was necessary to extrapolate the results using a power law. The measured and extrapolated populations are shown in Figure 5-5.

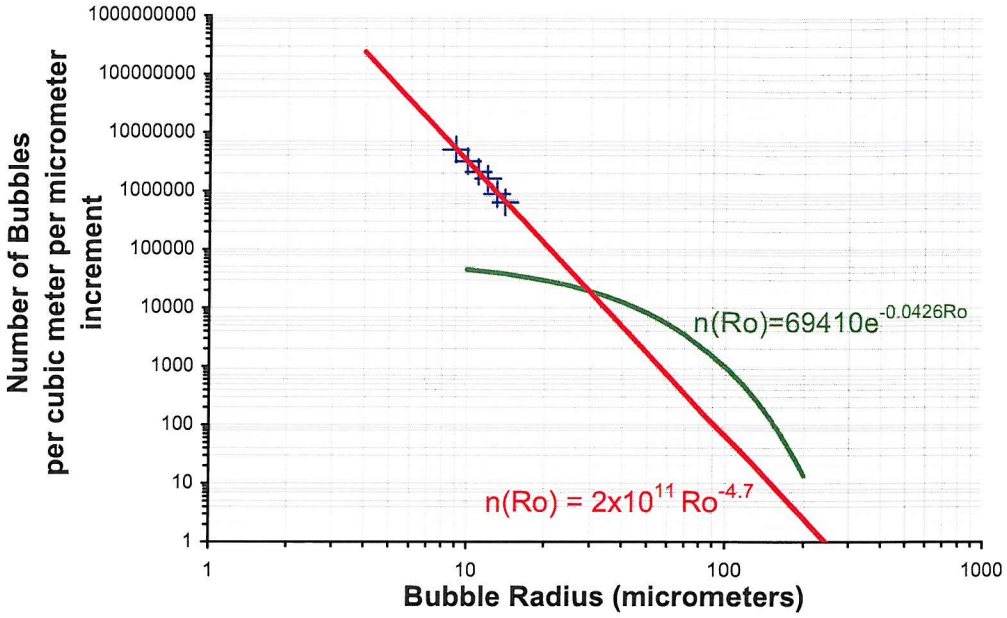

Figure 5-5 Population distribution determined by inversion of attenuation of the target sphere echo. The crosses (x) represent the measured data and the red solid line is an extrapolation of the population, used for modelling the cloud response. The equation describing the extrapolation is shown at the bottom left of the red line. The green line is the Farmer and Vagle[72] population from chapter 2, equation [2-14].

The extrapolation shown in Figure 5-5 is obviously extreme and the uncertainties in the numbers of bubbles become very large as the bubble radius exceeds a few tens of micrometers.

However, theoretical modelling in the preceding chapters has shown that, if the numbers of large off resonant bubbles are small, it is the bubbles that are at or close to resonance which are important i.e. those bubbles that have a time dependent scattering cross-section. The Farmer and Vagle[72] population used in chapter 2 is an example of a population where the large off-resonant contribute little to the cloud cross-section (Figure 2-14). This population is also plotted in Figure 5-5 for comparison.

In order to apply the range dependent model, the number of bubbles must be scaled to keep the processing time manageable. The problem with this is that the contribution of the larger bubbles is lost and assumes the contribution of these bubbles is negligible. In this case only the bubbles of radius 5 μm to 56 μm will be considered.

To test the validity of this assumption, the range independent model will be again be used to access the relative contributions of the bubble cloud. Figure 5-6 shows the contribution of the tested bubble radii (5 μm to 56 μm) and the larger bubble radii up to 600 μm for each of the 5 and 20 cycle pulses tested in the surf-zone. The plot clearly shows that the contribution of bubbles larger than 56 μm is insignificant and thus the assumption is valid.

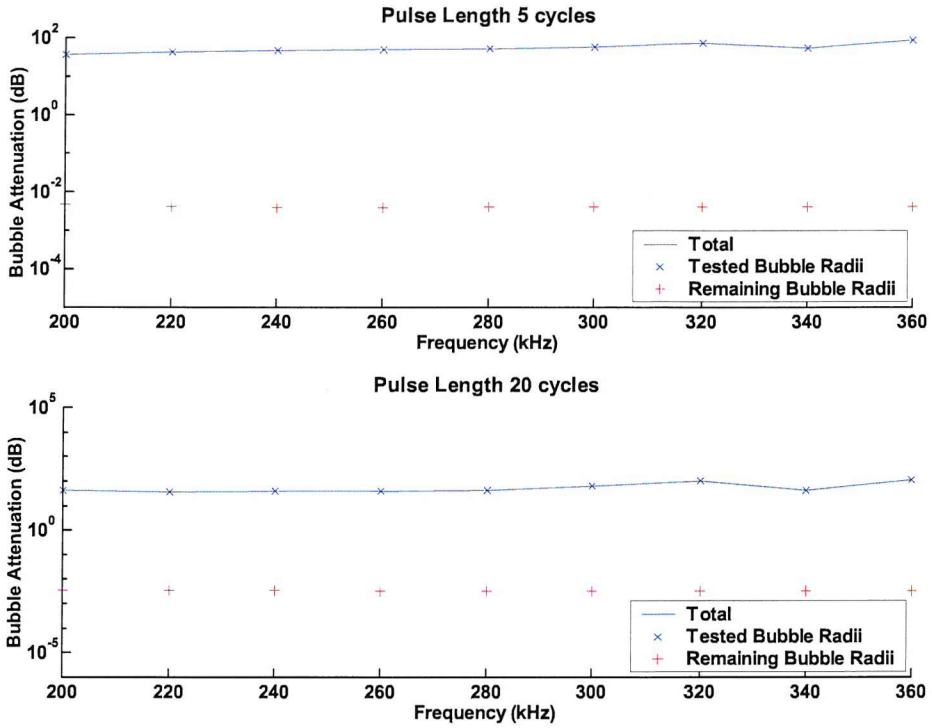

Figure 5-6 Plot showing the relative contributions of the tested bubble radii (5 μm to 56 μm) and the larger bubble radii up to 600 μm for each of the 5 cycle (top plot) and 20 cycle (bottom plot) pulses tested in the surf-zone

The average attenuation of eacg test signals taken on the 15th November 2000 during the period of most intense wave activity are in shown in Figure 5-7. Error bars indicate one standard deviation in the data giving an indication of the variability in the bubble population. Owing to their size it is not possible to interpret this data in terms of the three types of sonar enhancement. Individual tests will have to be examined to minimise the effect of temporal variability in the bubble cloud. However, the average data can be used to test the theory and the extrapolation of the

measured bubble population (since the population used to drive the model is itself an average).

The range-dependent non-linear bubble cloud model (section 2.3) used for comparison during the tank test is again tested here. However, in these trials a much greater attenuation has been measured when compared to the tank tests. This is an opportunity to test the hypothesis, at the end of section 2.3, that the attenuation of the driving pulse as it passes through a cloud should be modelled. For this reason two sets of results are plotted against the experimental data. The first (labelled model 1 in the plots) uses the range dependent model but does not include any attenuation of the driving pulse as it passes through the cloud, whereas the second (labelled model 2 in the plots) uses a modified version of the range-dependent model which does included driving signal attenuation. The results are shown in Figure 5-8 and Figure 5-9. The pulse attenuation model shows the best agreement with the experimental results up to a frequency of 320 kHz and for the chirped and pseudo-random signals. Above this frequency the theoretical and experimental results diverge. The reason for this will be discussed further in the following section. In all cases the model that includes the attenuation of the pulse as it propagates through the cloud is the more accurate generally lying within one standard deviation of the experimental data for all data points but the 340 and 360 kHz pulses.

This would seem to indicate the population measurements when extrapolated from 9 μm to 56 μm are a good representation of the bubble cloud response up to 320 kHz and that the inclusion of the driving pulse attenuation is important. However, the same cannot be said for the smaller bubble radii, because the theory fails to agree with the experimental results for the 340 and 360 kHz pulses.

It has already been mentioned that the extrapolation of the surf-zone population is extreme and the limited range of the population data gives rise to a significant uncertainty in the population distribution. This manifests itself in two ways. Firstly the gradient of the extrapolation shown Figure 5-5 can be varied slightly without significantly affecting the quality of the fit to the data. This is illustrated in Figure 5-10. Secondly, there may be a peak in the population. The existence of such a peak is due to the sorting of the bubble population by buoyancy and dissolution[1,11] but has rarely been measured[51]. This may be because it occurs at such a small bubble radii it is out of the range of most population measurements.

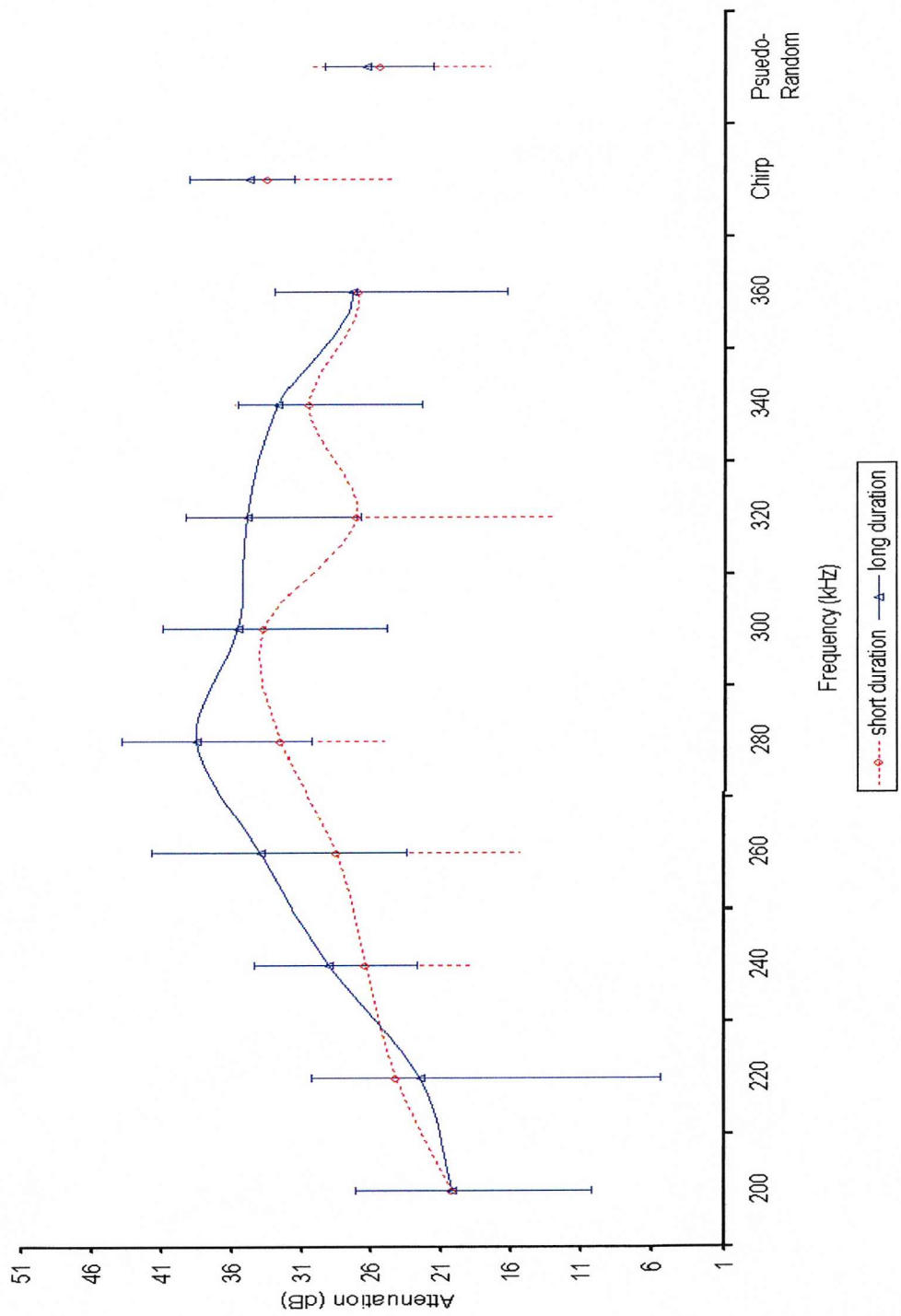

Figure 5-7 A graph showing the average levels of attenuation, in dB, measured in the surf-zone for each of the test signals (denoted on the x-axis). The short duration plot (dashed line) refers to the 5 cycle pulses(for the frequency shown on the x-axis and 0.1 ms chirp and pseudorandom signals and the long duration plot (solid line) refers to the 20 cycle pulses and 1 ms chirp and pseudorandom signals. The error bars represent the extent of scattering in the experimental results.

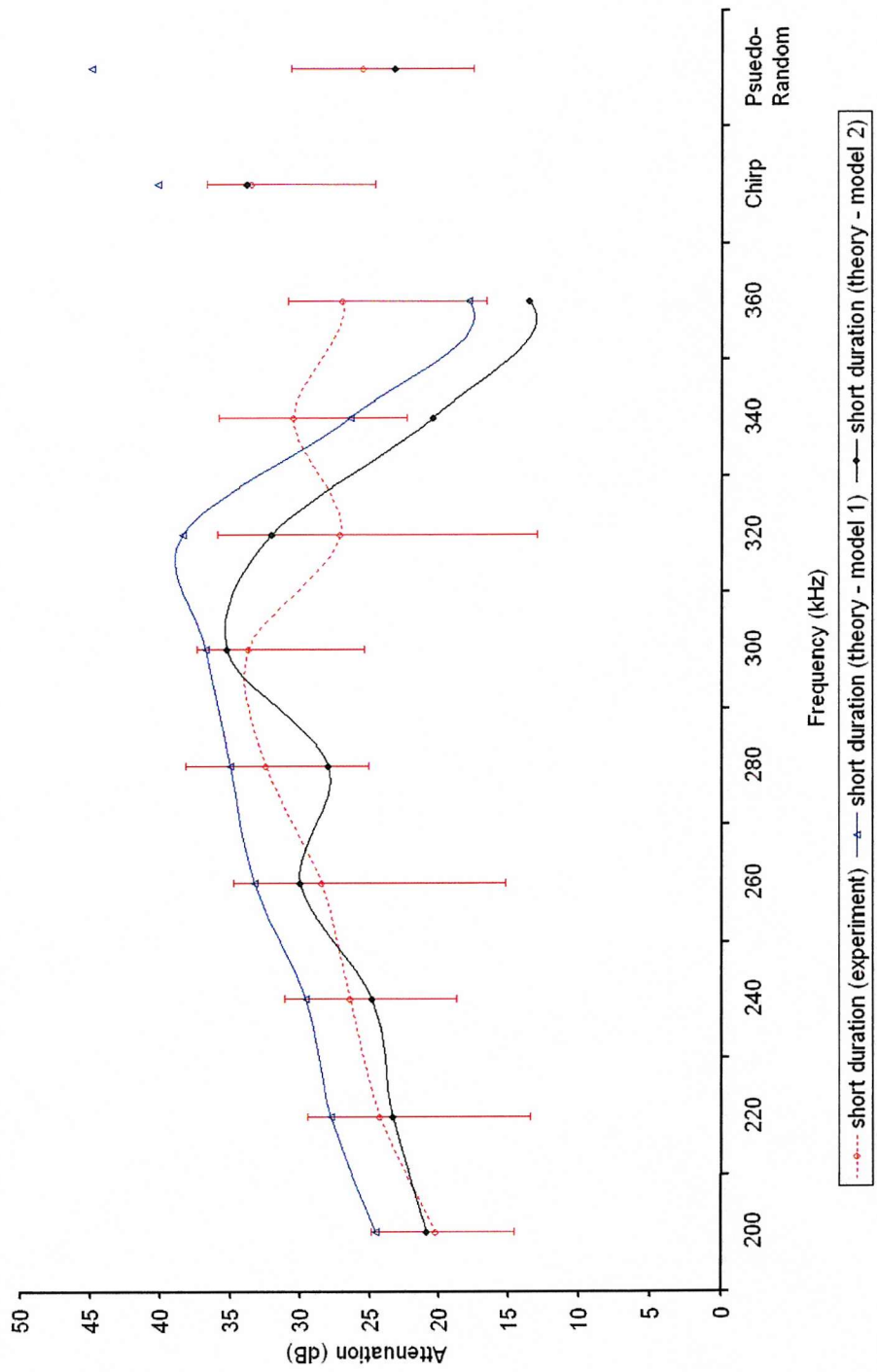

Figure 5-8 A graph comparing theoretical (solid lines) and experimental (dashed line) measurements of the average attenuation in dB for each of the short duration signals used in the surf-zone trial. The blue solid lines show the theoretical predictions of enhancement given the estimated bubble population in the surf-zone but assuming the attenuation of the driving signal as it propagates through the cloud is negligible. The solid black line includes this attenuation. The error bars represent the extent of scattering in the experimental results.

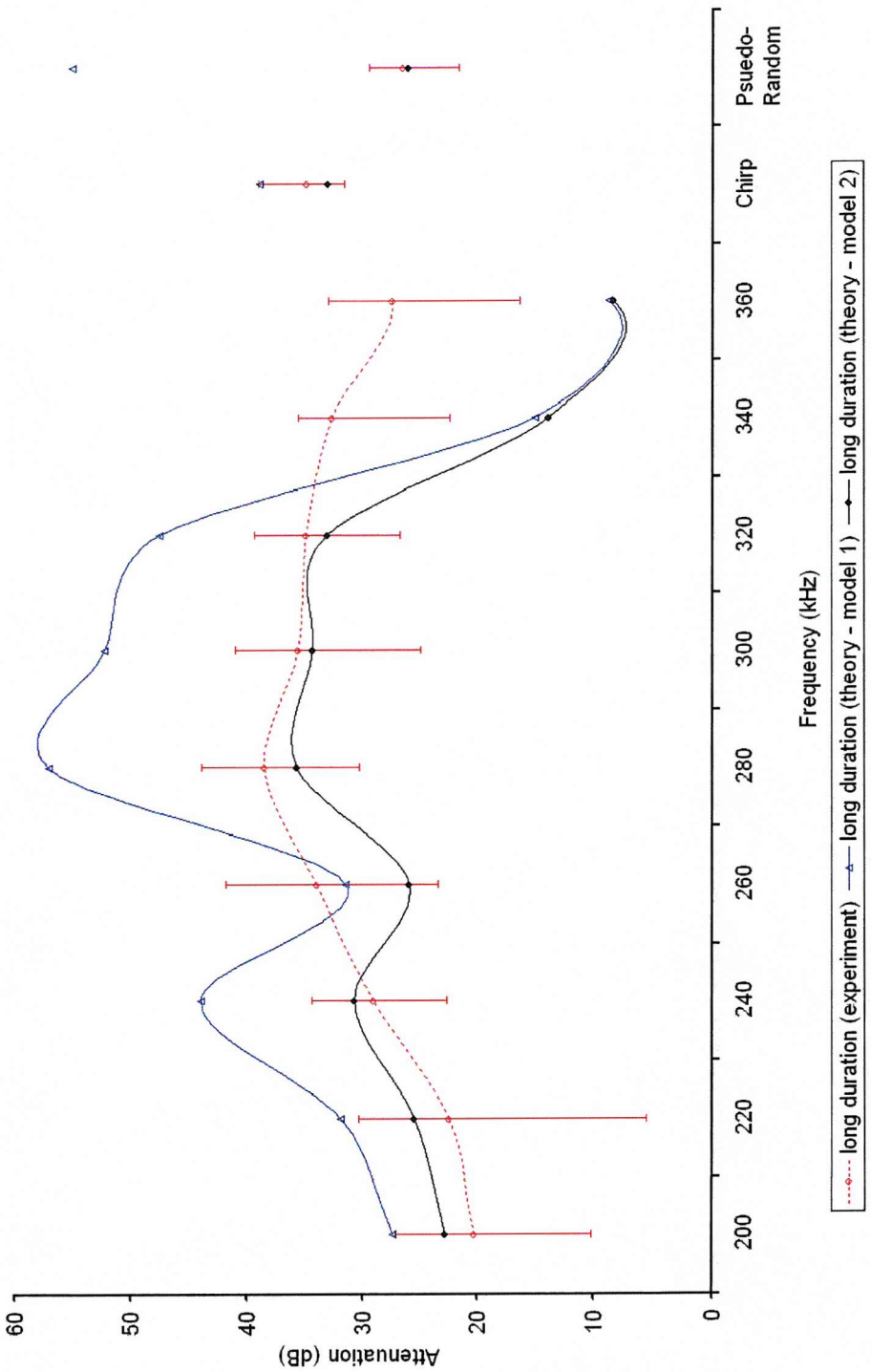

Figure 5-9 A graph comparing theoretical (solid lines) and experimental (dashed line) measurements of the average attenuation in dB for each of the long duration signals used in the surf-zone trial. The blue solid lines show the theoretical predictions of enhancement given the estimated bubble population in the surf-zone neglecting the attenuation of the driving as it propagates through the cloud. The solid black line includes this attenuation. The error bars represent the extent of scattering in the experimental results.

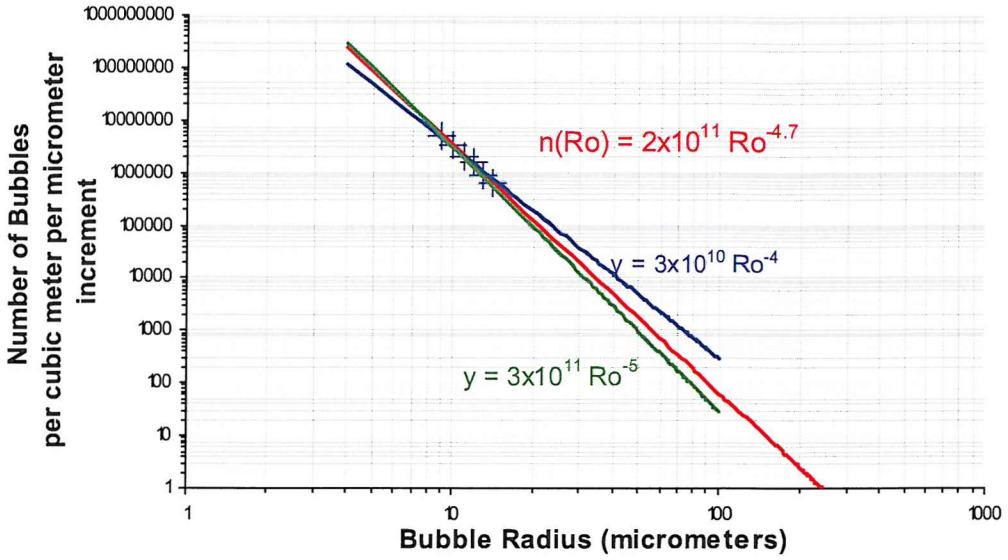

Figure 5-10 Plot showing how by changing the gradient of the extrapolated population (denoted by the blue green and red lines) the quality of fit with the experimental data is not significantly effected.

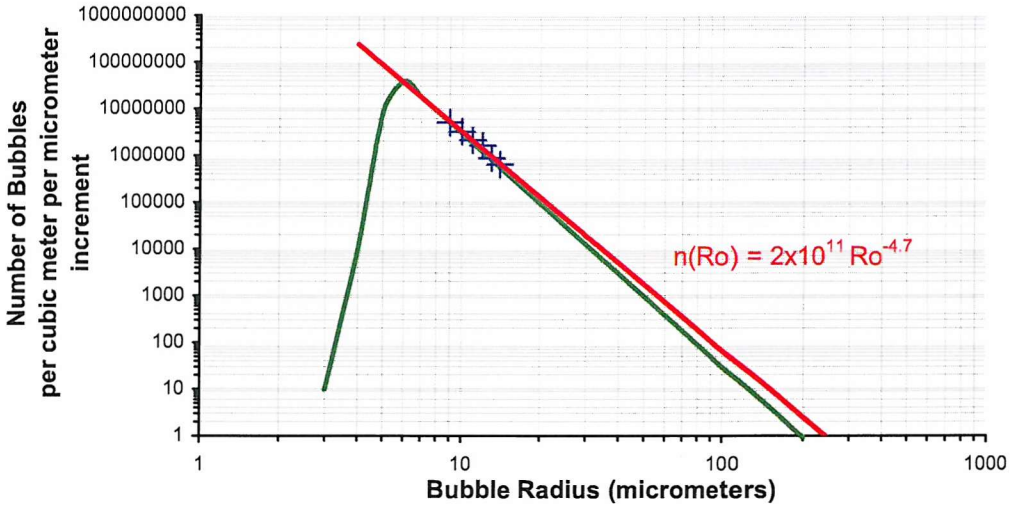

Figure 5-11 A plot showing the tuned population distribution (green line) compared with the measured population (x) and the original extrapolation (red solid line).

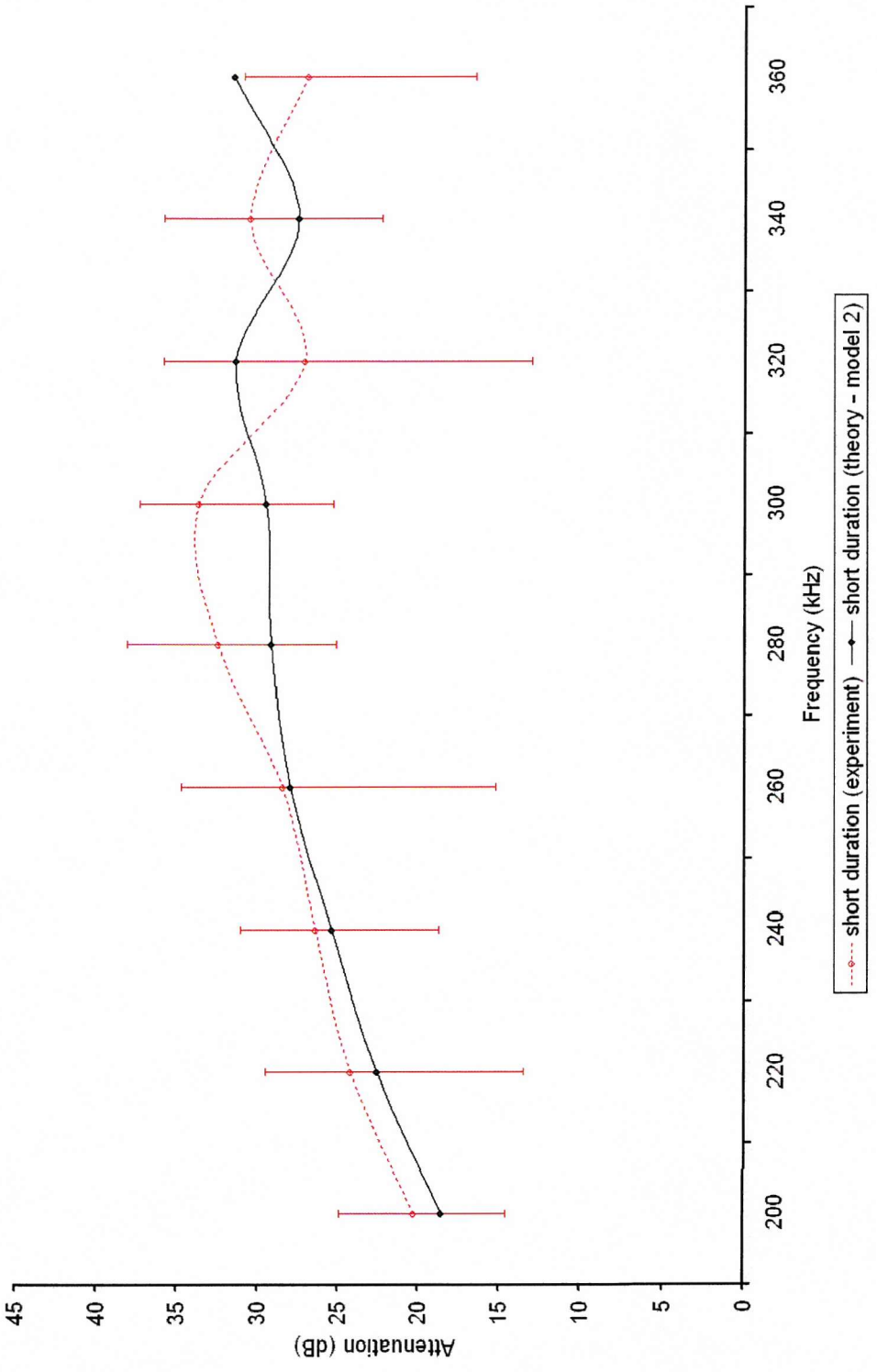

Figure 5-12 A graph comparing theoretical (solid black line) results for a tuned bubble population distribution against experimental (dashed red line) measurements of the average attenuation in dB for each of the 5 cycle pulsed signals used in the surf-zone trial. The error bars represent the extent of scattering in the experimental results.

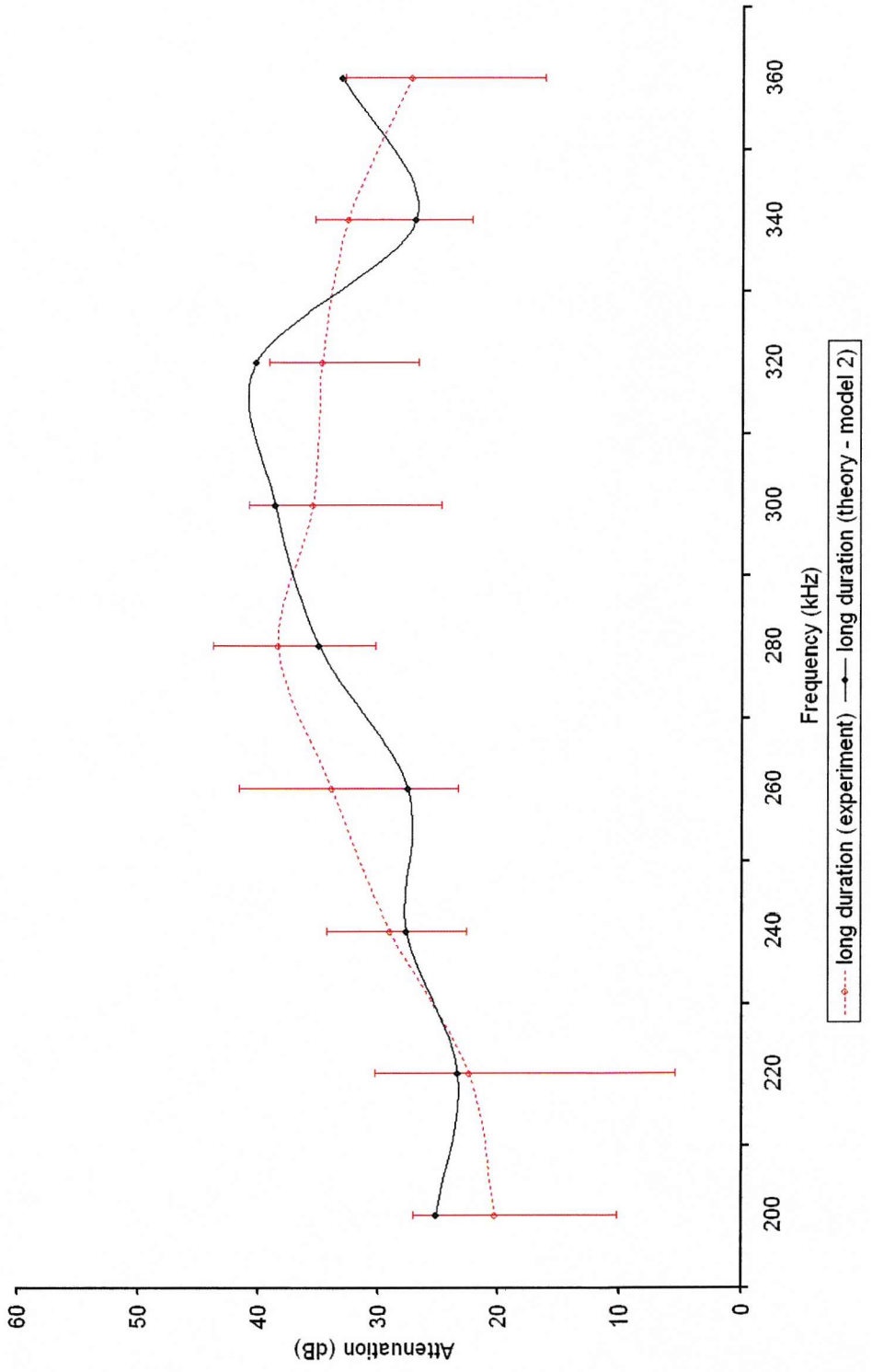

Figure 5-13 A graph comparing theoretical (solid black line) results for a tuned bubble population distribution against experimental (dashed red line) measurements of the average attenuation in dB for each of the 20 cycle pulsed signals used in the surf-zone trial. The error bars represent the extent of scattering in the experimental results.

The results of the range dependent theoretical model can be used to tune the population distribution by taking into account the two issues mentioned in the previous paragraph and adjusting the population iteratively until a better fit is achieved between the theory and experimental results. The tuned population distribution is shown in Figure 5-11, and compared with the measured population distribution and the original extrapolation. The resulting theoretical cloud attenuations using this newly derived population distributions are shown in Figure 5-12 for the 5 cycle pulses and Figure 5-13 for the 20 cycle pulses. The discrepancy between the theory and experimental results for the 340 and 360 kHz pulses shown in Figure 5-8 and Figure 5-9 has been resolved in Figure 5-12 and Figure 5-13.

Thus the inclusion of signal attenuation as it passes through a cloud into the theoretical model has been justified. In addition the model has been used to refine the measurements of the population distribution and overcome the short fall in information regarding the population distribution during the surf-zone trial. This will be invaluable in interpreting the experimental results.

5.3.2 Investigation of sonar enhancement in the experimental results

The ten individual tests used to obtain the average attenuation shown in Figure 5-7 are now plotted individually and analysed to investigate the three types of sonar enhancement that have been identified in chapter 2 (Table 2-2). The attenuation of each of the short and long duration signals for each of the ten tests are plotted in Figure 5-14 through to Figure 5-21. Two graphs representing one test each are plotted for each figure. No error bars are shown in these plots as the background has been measured to be of order –10 dB and is thus too small to be shown on these plots.

As already mentioned, since the bubble population is changing comparisons can only be made between short and long duration signals in a particular test when interpreting the results for sonar enhancement. This is because the short and long duration pulses were interleaved with a 10 ms gap between each signal in an attempt to minimise the effect of temporal variations in the bubble cloud. However, care is still needed when interpreting individual data points. The duration of individual test is just 0.22 s. This is very much less than the typical period of breaking waves (of order a few seconds). Thus comparison between individual data points in a test is acceptable as the primary mechanism for generating and dissipating the bubbles act over a much long time

period. However, each test is separated by several minutes and thus a test-to-test comparison of individual points is not possible as the bubble population may have changed. For this reason the relative enhancement for each of the tests is summarised in *Table 5-1*. The table shows the difference in attenuation (dB) for each of the eleven signals types for each of the ten tests. The attenuation of the long duration signals is subtracted from the attenuation of the short duration signals. Thus, a positive number indicates enhancement and a negative number (shown in red italics in the table) no enhancement. The average of the change in attenuation over the ten tests is shown at the bottom of the table.

The data shown in Table 5-1 is also shown in graphical form in Figure 5-19. In this figure a solid line is plotted at 0 dB indicating no change in attenuation between the short and long duration signals. Data points below this line indicate suppression whilst data points above the line indicate enhancement. The results for the 340 kHz and 360 kHz as well as the chirp and random signals are evenly spread above and below the 0 dB line suggesting no net difference in terms of sonar enhancement between the short and long duration pulses. Conversely the results for the 200 kHz to 320 kHz are generally above the 0 dB line. This is most pronounced for the 280 kHz to 320 kHz pulses. This indicates a reduction in attenuation when using short pulses and thus potential sonar enhancement.

The data has been analysed to look at the relative attenuations for the short and long periods of each of the signals. The results for the 200 kHz to 360 kHz pulses can be interpreted in terms of Type I enhancement. The plots for short and long duration signals are shown in Figure 5-14 through Figure 5-18 indicate a general reduction in attenuation when the shorter pulses are used. This is confirmed by the tabulated results in Table 5-1 by looking at the average attenuation as well as the number of occurrences of negative numbers per test. The results show that the best enhancement occurs for frequencies from 240 kHz to 300 kHz where only one or two negative data points are shown and the change in attenuation is larger then the standard deviation. This distribution can also be seen in Figure 5-19 where the results for the same tests are predominantly above the 0 dB line. Conversely the test at 200 kHz, 220 kHz, 340 kHz and 360 kHz show the opposite trend indicating insignificant or no enhancement.

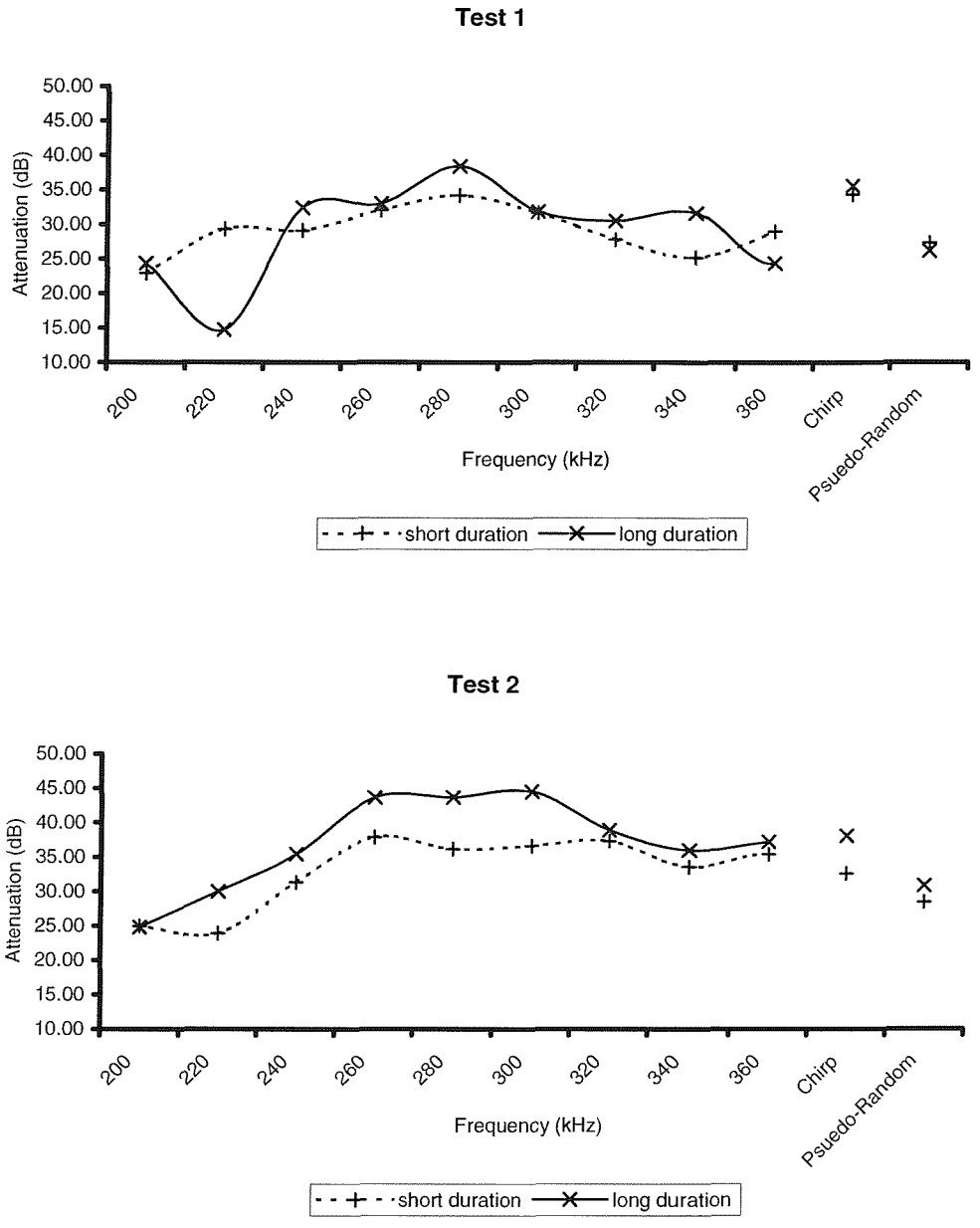

Figure 5-14 Graphs showing the attenuation, in dB, for tests 1 and 2. The short duration plot (dashed line) refers to the 5 cycle pulses and 0.1 ms signals and the long duration plot (solid line) refers to the 20 cycle pulses and 1 ms signals. The test signals are denoted on the x-axis.

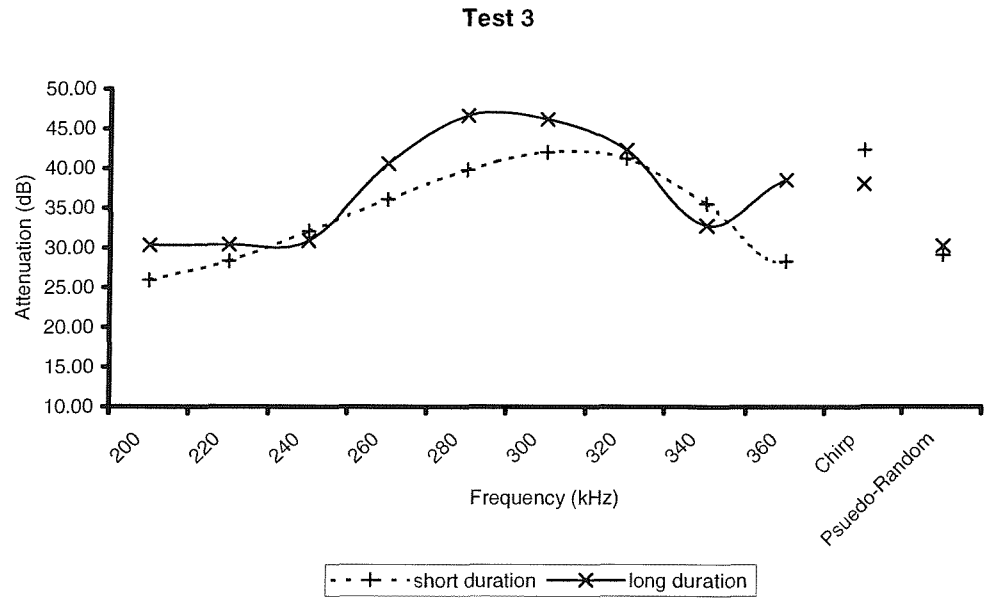

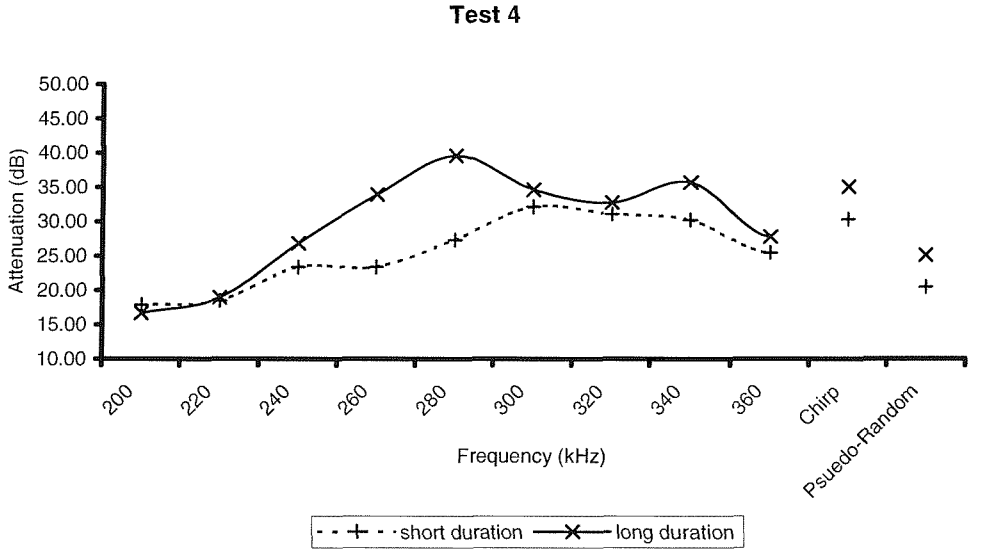

Figure 5-15 Graphs showing the attenuation, in dB, for tests 3 and 4. The short duration plot (dashed line) refers to the 5 cycle pulses and 0.1 ms signals and the long duration plot (solid line) refers to the 20 cycle pulses and 1 ms signals. The test signals are denoted on the x-axis.

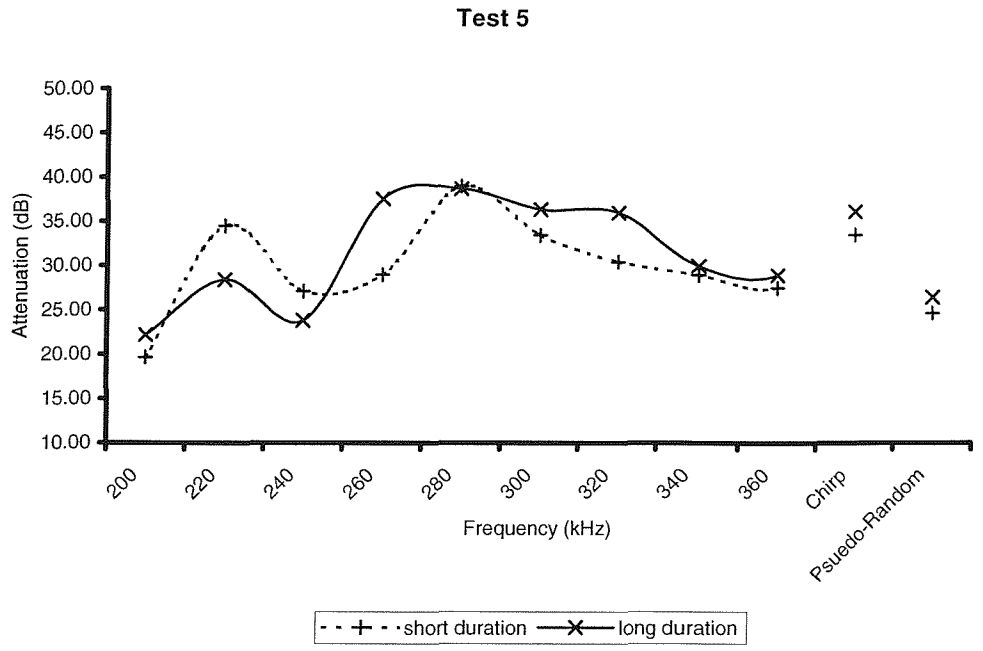

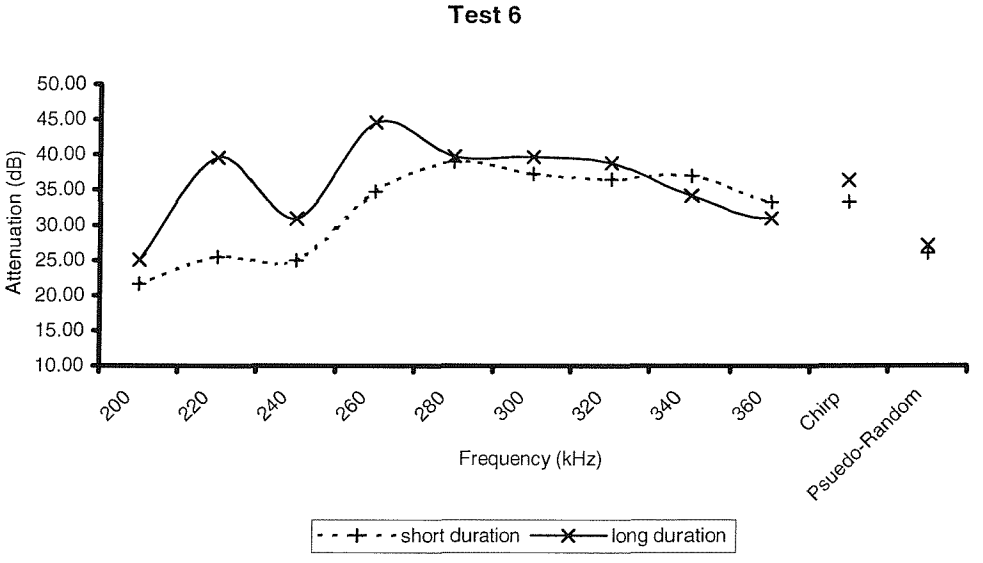

Figure 5-16 Graphs showing the attenuation, in dB, for tests 5 and 6. The short duration plot (dashed line) refers to the 5 cycle pulses and 0.1 ms signals and the long duration plot (solid line) refers to the 20 cycle pulses and 1 ms signals. The test signals are denoted on the x-axis.

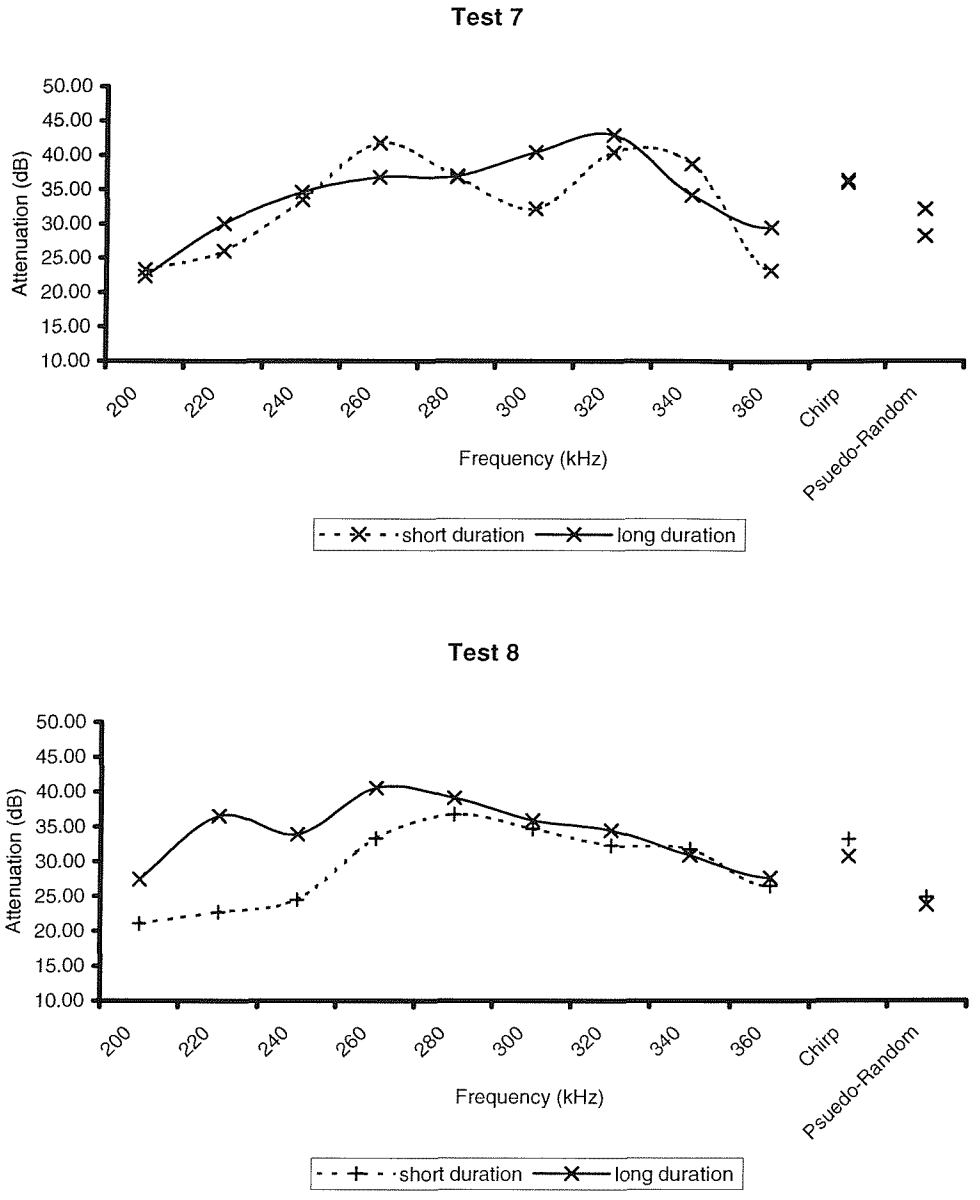

Figure 5-17 Graphs showing the attenuation, in dB, for tests 7 and 8. The short duration plot (dashed line) refers to the 5 cycle pulses and 0.1 ms signals and the long duration plot (solid line) refers to the 20 cycle pulses and 1 ms signals. The test signals are denoted on the x-axis.

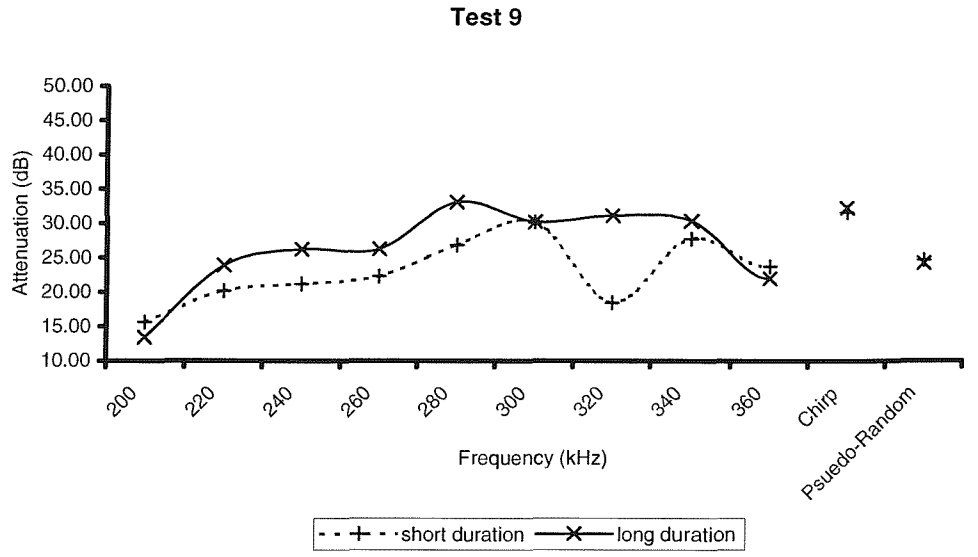

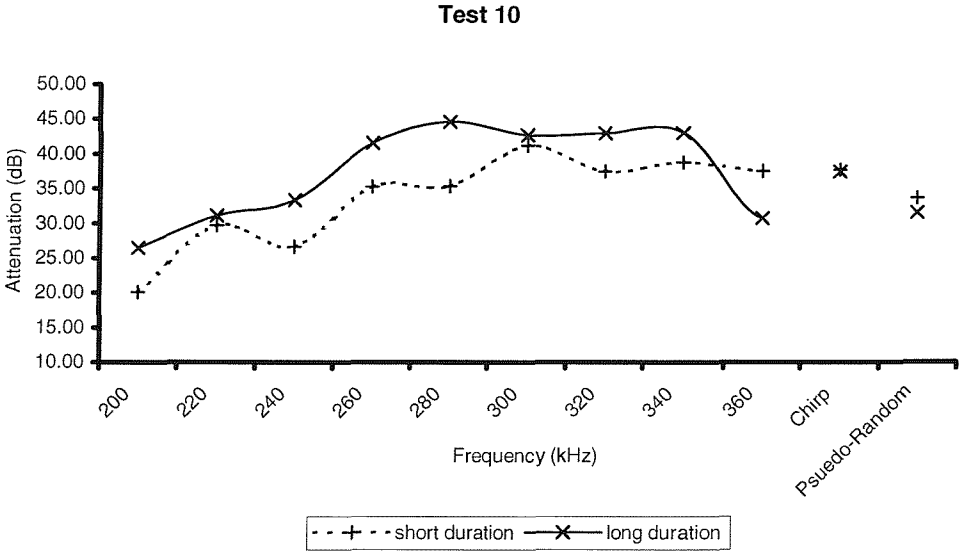

Figure 5-18 Graphs showing the attenuation, in dB, for tests 9 and 10. The short duration plot (dashed line) refers to the 5 cycle pulses and 0.1 ms signals and the long duration plot (solid line) refers to the 20 cycle pulses and 1 ms signals. The test signals are denoted on the x-axis.

Type	Pulse Frequency (kHz)									Broad Band	
	200	220	240	260	280	300	320	340	360	Chirp	Random
1	1.40	*-14.61*	3.32	0.94	4.23	0.21	2.70	6.44	*-4.64*	1.23	*-1.15*
2	*-0.18*	6.11	4.11	5.78	7.50	7.83	1.60	2.38	1.78	5.47	2.39
3	4.41	2.06	*-1.21*	4.53	6.83	4.15	1.07	*-2.79*	10.23	*-4.31*	1.15
4	*-1.22*	0.44	3.45	10.55	12.24	2.48	1.66	5.44	2.31	4.75	4.68
5	2.53	*-6.07*	*-3.29*	8.56	*-0.31*	2.90	5.54	0.99	1.42	2.64	1.77
6	3.46	14.10	5.97	9.76	0.81	2.39	2.36	*-2.83*	*-2.32*	3.07	1.17
7	*-0.99*	3.98	1.10	*-5.01*	0.20	8.23	2.53	*-4.59*	6.29	*-0.36*	*-3.93*
8	6.35	13.82	9.37	7.24	2.35	1.20	2.15	*-0.88*	1.17	*-2.43*	*-1.09*
9	*-2.21*	3.70	5.01	4.00	6.25	0.07	12.70	2.59	*-1.78*	0.66	*-0.46*
10	6.35	1.39	6.69	6.29	9.26	1.42	5.54	4.26	*-6.76*	*-0.25*	*-2.08*
Average	2.50	5.71	4.15	6.18	5.86	3.55	4.58	1.82	2.14	1.52	0.57

Table 5-1 A table summarising the difference in attenuation (dB) between long and short duration signals for each of the ten tests. A negative number (highlighted in red italics) indicates no enhancement. The average difference is shown at the bottom of the table for each signal type.

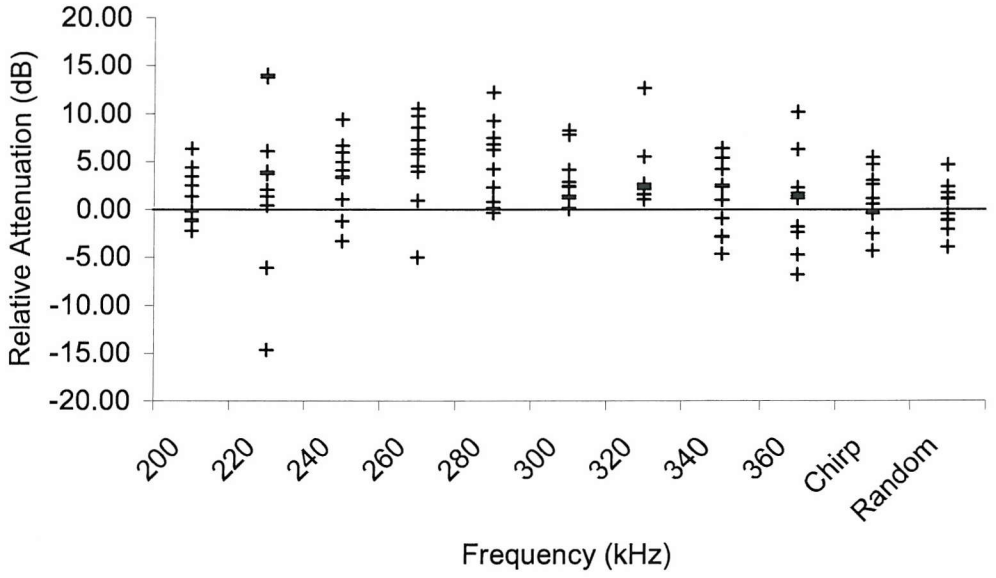

Figure 5-19 Graphical representation of the data shown in Table 5-1 showing the relative attenuation between the short and long duration signals for each of the ten tests. A negative value indicates suppression. A line marking the 0 dB point is also shown to aid in interpretation.

The results for the chirp and pseudorandom signals can be interpreted in a similar way to the pulse data to investigate Type II enhancement. The pseudorandom signal shows no enhancement with the data in Figure 5-19 distributed evenly about the 0 dB line and a mean attenuation difference of 0.57 dB and a spread of ±4 dB indicated in *Table 5-1*. The chirp data also shows no significant enhancement with a mean attenuation difference of 1.52 dB and a spread of ±5 dB.

Finally Type III enhancement must be considered. This is the most difficult type of enhancement to quantify from the results, owing to the variability in the data on a test-by-test basis. In addition the average attenuation data shown in Figure 5-7 indicates that the lowest attenuation was for the 200 kHz pulse, with approximately 15 dB less attenuation of the worst case 280 kHz pulse. This indicates a significant enhancement can be gained by using Type III enhancement. However, the plots in Figure 5-14 through Figure 5-18 show that although in general the long duration 200 kHz pulse gives the minimum attenuation, the test-by-test variation is significant. Table 5-2 shows the summary of the difference in attenuation between the 200 kHz pulses and the 280 kHz pulses for both the short and long duration signals. The table shows that an average reduction of 15.8 dB can be expected.

Test	Long Pulse	Short Pulse	Difference
1	14.09	11.27	2.82
2	18.86	11.19	7.67
3	16.31	13.90	2.41
4	22.95	9.49	13.46
5	16.50	19.34	-2.84
6	14.76	17.42	-2.66
7	14.63	13.44	1.19
8	11.66	15.66	-4.00
9	19.64	11.19	8.45
10	18.07	15.17	2.90
Average	17.31	14.33	2.98

Table 5-2 The difference in attenuation (dB) between the 200 kHz pulse and the 280 kHz pulse for the short and long duration signals. The average results are shown at the bottom of the table.

5.4 Surf-zone trial conclusions

The surf-zone trial has provided additional information for the enhancement of sonar detection in bubbly environments and the population distribution of bubbles in the

surf-zone. Measurements of the bubble population have shown a significant deviation from published measurements in deep water of oceanic bubble clouds, and deviation from population measurements obtained from the artificial cloud generated for the tank tests in chapter 3 (Figure 5-21).

The form of the surf-zone population plotted in Figure 5-5 is of great significance for sonar enhancement. There are relatively few numbers of large bubbles (as compared to the numbers of small bubbles) present in the model surf-zone population provided by extrapolating the 9 – 13 μm data (after tuning by using the range dependent cloud model). The result of this is that the contribution of the large off-resonant bubbles is unimportant. Furthermore, the steepness of the population distribution reduces the contribution of the large near resonant bubbles that masked the ring-up of the resonant bubbles in the tank tests. It can thus be assumed that the optimum frequency for Type I enhancement would coincide with the resonance of bubbles at the peak in a distribution (as predicted in section 2.5). Tuning of the population distribution to optimise the fit between the theoretical and experimental results suggests that such a peak may exist (*Figure 5-11*) but it was not directly detected in the surf-zone trial. Suck a peak has been measured in deep water by Farmer and Vagle[72]. The existence of this peak is due to the sorting of the bubble population by buoyancy and dissolution[1,11]. This peak has only been measured in mature bubble populations with theory predicting delays of order tens of seconds before the peak manifests itself[51].

The use of Type III optimal frequency enhancement has been tested, and has proven to be a significant factor in minimising the attenuation from a bubble cloud. Over the frequency range tested, which covered a relatively small resonant bubble radius of 9 – 15 μm, the attenuation ranged from 4 – 8 dB/m. It is clear that of all the signals tested that the optimal signal for target detection, for the conditions prevalent during the trial, would be a 200 kHz pulse and that the duration of the pulse appears to have a small effect on the level of attenuation measured at this frequency.

It is also important to note that the numbers of bubbles present were linearly scaled for the purposes of modelling the cloud so as to keep processing time within reasonable limits. However, because of the steep gradient of the extrapolated population the large bubbles, above 56 μm in radius, are removed from the calculation. Thus the theory confirms the population distribution used but only up to a

radius of 56 μm. Beyond this radius the model results confirm that the assumption, implicit in the scaling, that the contribution of bubbles greater than 56 μm is insignificant. This does not confirm the shape of the extrapolated population other than that the numbers of large bubbles must be small. The population was then tuned and bubbles of radius 5μm to 100 μm incorporated to give a more robust population distribution.

Further measurements where made during a second sea trial at the same location in 2002 by Steven Meers[i] and Tim Leighton[i]. Twenty separate measurements were made using a 195 dB source and 500 μs pulses with frequencies between 30 kHz and 200 kHz. The results were then inverted to give the bubble population. The average of the 20 separate results is plotted in Figure 5-20. The original measurements along with the extrapolated and tuned populations used to run the theoretical model are shown next to these new measurements. The new measurements indicate a higher void fraction (more bubbles) than was measured during the first sea trail and are thus linearly scaled to allow a direct comparison between the extrapolated and measured populations. The plot shows excellent agreement between the gradients of the tuned and newly measured population, providing additional confidence in the use of this population in the theoretical model.

[i] Institute of Sound and Vibration Research, University of Southampton

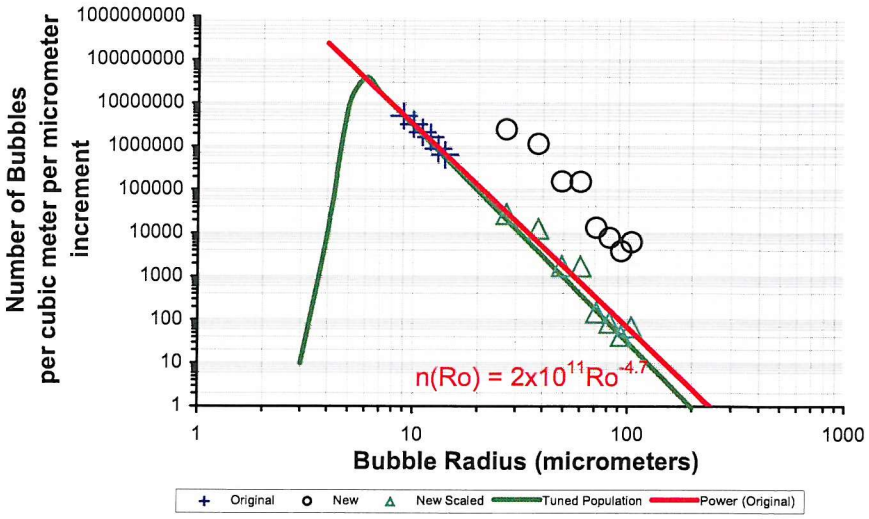

Figure 5-20 Comparison of the extrapolated bubble population measured at Hurst Spit during the sea trial (blue crosses and solid red line) with new measurements made at the site in 2002 (black circles). The new population measurements have been scaled to allow a direct comparison (green triangles). The tuned population is also shown (solid green line).

It is important to stress at this stage that these result are of course valid only for the population distribution measured at the time, and are limited by the frequency range tested. The potential of the various methods of sonar enhancement are thus dependent on the prevalent environmental conditions. For these reasons, the important conclusion to be drawn from the surf-zone trial results is that both Type I short pulse enhancement, and Type III optimum frequency enhancement, can be used to improve target detection. Additionally a-priori knowledge of the bubble population is required to ascertain which technique, or what combination of the two techniques, will give the optimum enhancement.

Finally, Type II novel waveform enhancement must be considered. Firstly, the use of short duration broadband signals resulted in very little change in the attenuation when compared to the long duration broadband signals. Secondly, the attenuation resulting from the chirped and, particularly, the pseudorandom signals, was less than the attenuation from the majority of single frequency pulses used (but greater than the optimum single frequency pulse). The broadband signals were thus the least

successful method of sonar enhancement tested. However, they should not be discarded. In conditions where a-priori knowledge of the bubble population is not available, a broadband signal could be a useful alternative to Type I and Type III methods. This is because it reduces the risk of choosing a particularly bad (in terms of attenuation) single frequency pulse.

In the final chapter, the work discussed in this thesis is summarised and final conclusions drawn.

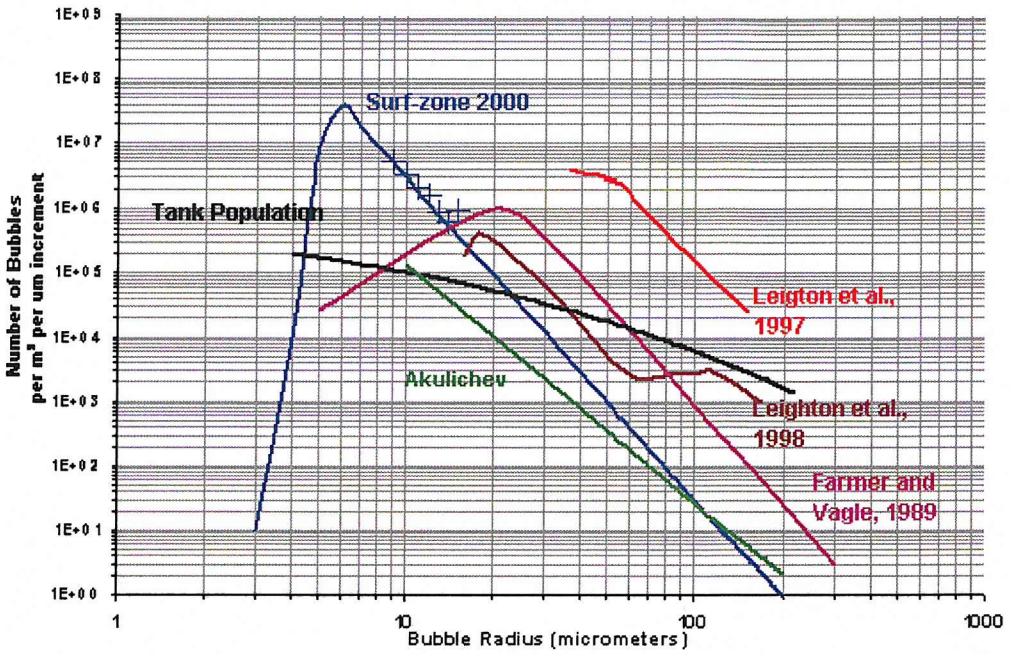

Figure 5-21 A comparison of several experimental measurements of bubble populations. Leighton et al 1998[11] and Farmer and Vagle 1989[72] are two measurements of oceanic bubble population. The tank population is the measurement, using inversion, of the electrolysis bubble cloud generator used in the tank experiments. The population measurement marked surf-zone 2000 is the population measured during the sea trial by inversion. The crosses represent measured data points and the line is an extrapolation of the data. Note the relatively few numbers of large bubbles measured in the surf-zone and the greater numbers of large bubbles measured in the tank population. A final data set is plotted which a previous surf-zone population measurement by Leighton et al 1997[54].

CHAPTER 6

CONCLUSIONS

6 Conclusions

This final chapter discusses the findings of the thesis and presents some suggestion for future work.

6.1 Summary

The aim of this work has been to investigate the enhancement of sonar detection in bubbly environments such as the surf-zone. Previous work on reducing attenuation and scattering of sound by bubbles was reviewed. During the course of this review it was discovered that existing models of the time-dependent scattering and attenuation of bubbles were limited by assumptions such as linearity and restricting the model to resonance conditions only. These existing models relied on linear cross-section theory to calculate the effect of short pulses. They are limited to small amplitude driving signals and single frequency insonification, neglecting the broadening in bandwidth of short pulses. In addition, in these models it is assumed that the bubbles undergo either resonant or off-resonant scattering: the bandwidth of bubbles that are close to, but not at, resonance are not incorporated. These models also cannot calculate the ring-down and so are limited to continuous wave or semi-infinite pulse as driving signals.

In these previous studies it was also hypothesized that the time taken for a bubble to reach steady state oscillation could be exploited to reduce scattering and attenuation. However, only one study by Akulichev[40] measured this phenomenon experimentally.

In the light of the previous work on this topic three different methods of obtaining sonar enhancement were outlined. These methods would need to be tested both theoretically and experimentally under a variety of conditions likely to be

encountered in the oceanic environment. The theoretical study derived a series of bubble cloud models based on the Keller-Miksis non-linear single bubble model. Each model expands on the previous by taking into account the following assumptions:

- Time dependence of the bubble response
- Off-resonant bubble response
- Non-linearity of the bubble response
- Bubble response to an arbitrary waveform
- Attenuation of a driving signal as it propagates through a cloud

The models were also adapted to allow experimentally measured driving signals to be used to allow for distortion effects of acoustic sources. These models are a significant improvement over those used in previous studies[40,42,43] reviewed in chapter 1. A summary of all the models presented in this thesis is shown in *Table 6-1*.

Experimental tests in a laboratory test tank and the surf-zone trial were conducted to test the three types of sonar enhancement identified in this thesis. Type I enhancement utilises short period signals; Type II enhancement uses novel waveforms such as chirps and pseudo-random signals and Type III enhancement relies on finding a minimum in the frequency dependent attenuation of the bubble cloud.

Model	Assumption								
	Linear	Time Independent	Resonance Only	No Off-Resonance Contribution	Ring-Down not Included	Resonant Damping Model Only	No Off-Resonant Transient Response	Driving Signals	Cloud Model
Steady-state	√	√	X	X	√	X	√	CW	Scaling
Akulichev	√	X	√	√	X	√	√	Pulse	Scaling
Pace & Suiter	√	X	X	X	√	√	√	CW	Scaling
Simple Non-linear Cloud Model	X	X	X	X	X	X	X	Any	Scaling
Non-linear Range dependent cloud model (I)	X	X	X	X	X	X	X	Any	Cloud Geometry
Non-linear Range dependent cloud model (II)	X	X	X	X	X	X	X	Any. Inc Signal Atten.	Cloud Geometry

Table 6-1 A table summarising the characteristics of the bubble models used in this thesis. A √ indicates the assumption is valid for this model and a X indicates that the assumption is not valid

The tests in the laboratory were undertaken in a test tank of dimensions 8 m x 8 m x 5 m deep. An artificial bubble cloud generation system, based on electrolysis, was developed to represent oceanic bubble populations in the tank. Care was taken to minimise the amount of large bubbles (> 100 μm) that are produced by normal bubble generation systems such as injection. However, the number of large bubbles produced was still too great when compared with oceanic distributions resulting in a shallower gradient when plotting bubble numbers versus radius.

The artificial bubble cloud generator was used to explore the effect of changing pulse length and sweep rate experimentally in a tank. The non-linear range dependent cloud model was also used to recreate the experimental results using measured waveforms. It was not necessary to account for the attenuation of the driving signal due to the small levels of attenuation measured. A good agreement between model and experiment results was shown. The model was validated by these tests.

No Type I or Type II enhancement was shown experimentally or theoretically with the bubble population distribution used in the laboratory experiments. However, the results would have been wrongly interpreted as showing a Type I enhancement were it not for the ability of the non-linear range dependent cloud model to accept measured time series as a driving signal. The non-linear cloud model was also used to help identify the reason why no Type I or Type II enhancement was detected. It is apparent that the contributions of the near resonant bubbles, which have no ring-up but do have a transient response, masked the ring-up of the resonant bubbles. The importance of the near resonant bubbles (i.e. those bubbles which do not exhibit a steady ring-up to resonance or a steady-state response) could not have been identified using existing linear bubbles models such as those used in previous studies by Akulichev[40], Suiter[42] and Pace[43].

The laboratory experiments did show Type III enhancement. Measurements of the cloud attenuation for frequencies from 15 kHz to 220 kHz have shown that significant increases in target detection range can be achieved by tuning the driving frequency.

The second phase of the experimental measurements involved deployment of a source receiver and target sphere from a beach into the surf-zone at Hurst Spit on the south coast of England in November 2000. It was necessary to move to a beach based trial due to the difficulties of generating realistic populations in the tank. A further goal was to measure the population distribution in the surf-zone. Increased knowledge of the distributions that can occur in this environment was fundamental to this work due to the lack of data on such population distributions and the sensitivity of sonar enhancement to the gradient in the population distribution.

Despite some difficulties, measurements of the surf-zone bubble population were obtained for a narrow bubble population radius range from 9-15 μm. This was extrapolated and the model used to confirm that the extrapolation was valid over a larger bubble population radius range of 5-56 μm. The model showed that this extrapolation was suitable for calculating the bubble cloud response up to 300 kHz. The results of the model were then used to tune the population distribution. Further measurements at the Hurst Spit test site in 2002 agree well with the tuned populations distribution giving further confidence in the results.

The results of the trial were then analysed for the three types of enhancement. Of the three methods tested, Type I and Type III enhancement both showed a reduction in attenuation. In this case careful selection of the frequency could reduce the attenuation by 16 dB and, depending on the frequency, short duration pulses reduced the attenuation by up to 6 dB.

Theoretical models were again compared with experimental data. In this case the non-linear range dependent cloud model, including the attenuation of the driving signal, was used owing to the high levels of attenuation measured in the surf-zone. The model showed close agreement with experimental data lying within the standard deviation of the experimental results for all but the highest frequency pulses (300 kHz to 360 kHz). This deviation at the higher frequencies is attributed to inaccuracies in the numbers of small bubbles measured by inversion. This deviation was then used to tune the population to give a better fit between experimental and theoretical results. The results have also shown the necessity of including signal attenuation into the range dependent model when high levels of attenuation are expected.

In the sea trial the best method of minimising attenuation was by optimising the insonifying frequency. However, care needs to be taken when drawing conclusions from these results. The trial data is only representative of one bubble distribution and the frequency tested was limited by the hardware (transmit/receive array) used. It can be expected that the population distribution will change with environmental conditions such as wind speed[74], the type of breakers[75-76] and the position within the surf-zone. What has been shown is that optimum frequency techniques and short pulses given the right conditions can significantly reduce the attenuation owing to bubble clouds and thus enhance sonar detection in bubble environments.

Both these strategies have been shown to be beneficial, however in practice, the optimum strategy would depend on several issues:-

- Population peaks are not always apparent
- The propagation distance before encountering bubbles could severely limit the use of very high frequencies
- The bandwidth and Q of available sources and receivers
- The population distribution and absolute numbers of bubbles

The models presented in this thesis, in conjunction with suitable knowledge of the environmental conditions and bubble populations, can be used with the guidelines presented here to provide significant gains in the detection of targets using acoustics in bubbly environments.

The work also has potential benefits for measuring bubble populations by inversion. Existing techniques use linear models restricting the driving signal to low amplitude pulses. The models developed in this thesis could be used to determine the attenuation of a bubble to an arbitrary driving signal. This data could be used to invert for bubble populations using broadband and high amplitude driving signals without compromising model assumptions. Indeed this was achieved to a limited degree by tuning the bubble population measured in the surf-zone to improve the agreement between theoretical and experimental results especially above 300 kHz. The benefits of this in the case of high amplitude signals, would be an increased signal to noise ratio and thus increased ability to measure population distributions in areas, such as the surf-zone, where the attenuation due to bubble clouds is large. In the case of broadband signals, their use could allow the numbers of a wide range of bubbles to be measured almost simultaneously rather than stepping through different frequency pulses, during which time the bubble population may have changed.

6.2 Future work

Two issues raised by this thesis are of particular importance for developing this work further. Firstly, the theoretical models presented in this thesis can be further developed to include a full non-linear damping model. Specifically thermal damping needs to be incorporated into the existing Keller-Miksis non-linear bubble model.

Secondly, a sea trial should be conducted using a broader range of frequencies to invert for the bubble population to try and measure a peak in the distribution. A broadband source capable of generating short pulses at the resonant frequency of bubbles at the peak of the population distribution (of order 400 kHz) would need to be obtained. The hypothesis from chapter 2, that insonifying at the distribution peak frequency is the optimum strategy for Type I enhancement, could then be tested experimentally.

APPENDIX A

PHYSICAL PROPERTIES OF GASSES AND LIQUIDS

A Physical Properties of Gases and Liquids

Nitrogen Gas Parameters

$\rho_{gas} = 1.16$ - density (kg/m^3) assuming Nitrogen

molarmass=2x14.0067$x10^{-3}$ - Molar mass (kg/mol) assumed Nitrogen

$\gamma = 1.4$ - Gas specific heat ratio (-)

$Kg = 2.6e^{-2}$ - Thermal conductivity (W/mK)

$Cp = 1.04$ - specific heat of Nitrogen (kJ/kgK)

Oxygen Gas Parameters

$\rho_{gas} = 1.31$ - density (kg/m^3) assuming Oxygen

molarmass=2x15.999x10^{-3} - Molar mass (kg/mol) assumed Oxygen

$\gamma = 1.4$ - Gas specific heat ratio (-)

$Kg = 2.6\text{x}10^{-2}$ - Thermal conductivity (W/mK)

$Cp = 0.91$ - specific heat of Oxygen (kJ/kgK)

Environmental Parameters

$p_{atm} = 1.013x10^5$ - atmospheric pressure (Pa)

$\rho = 1000$ - density (kg/m^3) assuming fresh water

$p_0 = p_{atm} + (9.81\rho h)$ - pressure outside of bubble where h is depth in m (Pa)

c=1480; - speed of sound in fresh water (m/s)

$T_{inf} = 293$ - absolute temperature of liquid surrounding the bubble (K)

$\mu = 0.001$ - shear viscosity coefficient (kg/ms)

$\sigma = 0.0725$ - surface tension (N/m)

$Rg = 8.31441;$ - gas constant (J K^{-1} mol^{-1})

$D_g = \frac{K_g}{1x10^3 \rho_{gas} C_p}$ - thermal diffusivity of gas (cm^2/s)

$K_l = 0.6;$ - Thermal conductivity (W/mK)

$Cp = 4.19;$ - specific heat of water (kJ/kgK)

$D_l = \frac{K_l}{1x10^3 \rho C_p}$ - approximate thermal diffusivity of liquid (cm^2/s)

APPENDIX B

MULTIPLE BUBBLE INTERACTIONS

B Multiple Bubble Interactions

B.1 Introduction

When considering wave propagation and scattering in random media, whether it is acoustic or electromagnetic, it has long been recognised that the wave field from individual scatters could also influence other scatters in the medium. The first attempt to model such interference phenomena was presented by L Foldy in 1944[77] and his model has since been applied extensively to bubbly media by, for example, van Wijngaarden[78] and Catflisch *et al.*[79]. These models have been shown to compare well with theory but only under limited conditions[80]. The main restriction occurs near to bubble resonances when the scattered field from a bubble is a local maximum[81]. Intuitively this is where bubble-bubble interactions are most likely, and it is widely acknowledged that the primary reason for the failure of Foldy's model is that the theory does not correct for multiple scattering processes between bubbles[80]. Several attempts to model multiple scattering have since been made, largely based on Foldy's original theory, to quantify the circumstances under which such interactions become important. The key papers of Feuillade, Zhen Ye and Henyey that address this problem are discussed here.

B.2 Foldy's effective medium theory

Since much of the current work on bubble interactions is an extension of the original work by Foldy, it is reviewed here. The 'effective' medium concept, as it became known, was developed by Foldy[77] and Carstensen[82]. In this, the bubbly water is represented as a homogeneous medium with uniform acoustic properties (i.e. attenuation and phase speed).

Foldy showed that the sound speed in bubbly water, C_T, is a complex quantity and is given by

$$\frac{1}{C_T^2} = \frac{1}{c^2} + \frac{4\pi r n}{\rho\omega^2\left\{\left[\frac{\omega_o^2}{\omega^2} - 1\right] + i\frac{b}{m\omega}\right\}} \qquad \text{[B-1]}$$

Here c is the speed of sound in water, ρ is the density, ω is the angular frequency, n is the number of bubbles per unit volume and the quantities k, m, b are functions of the radius r.

The real and imaginary parts of equation [B.1] represent the dispersion and attenuation, respectively, of the acoustic waves propagating through the medium. If bubbles of different sizes are present, then the number of bubbles per unit volume with a radius range r and $r + d\,r$ is defined as $np(r)d\,r$, where $p(r)$ is a probability density function and [B.1] becomes

$$\frac{1}{C_T^2} = \frac{1}{c^2} + pn\Im \qquad \text{[B-2]}$$

Where

$$\Im = \int_0^\infty \frac{4\pi p(a)da}{\rho\omega^2\left\{\left[\frac{\omega_o^2}{\omega^2} - 1\right] + i\frac{b}{m\omega}\right\}} = \int_0^\infty \frac{p(a)da}{\kappa - \omega^2 m + i\omega b} \qquad \text{[B-3]}$$

B.3 Feuillade correction for the sound speed in bubbly water

Commander and Prosperetti[80] compared the predictions of Foldy's theory with experimental data and showed that, for clouds of high void fractions, narrow size distribution and insonification near to resonance, the level of acoustic attenuation is consistently overestimated.

Feuillade[83,84,85] tries to add terms to equations [B.1] and [B.2] to correct for this problem by considering an external field driving an ensemble of n interacting

bubbles. Thus the total field incident on any one of these bubbles, is a combination of the external field and an aggregate of the scattered fields from all of the other bubbles. A series of equations to describe this can be evolved and written in matrix form. The diagonal of this matrix describes the individual resonance terms, and the remaining elements the radiation coupling terms. Feuillade attempts to solve this matrix for a general case in order to determine the sound speed correction, by determining the eigenvector of the symmetric mode of multiple bubble scattering.[86] Feuillade argues that the acoustic properties of ensembles of closely spaced bubbles insonified at resonance are 'predominantly determined' by the action of the symmetric mode. The antisymmetric mode, where some or all the bubbles oscillate in antiphase, scatters negligible sound. It is also assumed that for a high density bubble cloud the spatial variation of the aggregate field is minimal. Thus the ambient scattered field varies minimally throughout the medium and every bubble responds in an essentially identical manner. Thus an approximate eigenvector generally applicable to all configurations can be formed. This greatly simplifies the problem and allows the average ensemble behaviour to be determined.

Feuillade gives the following general equation for the speed for sound in bubbly liquids

$$\frac{1}{C_T^2} = \frac{1}{c^2} + \frac{\rho n \Im}{1 - \Im \omega^2 \rho n \int_0^\infty r e^{-ikr} dr} \qquad \text{[B-4]}$$

To summarise Feuillade's approach the propagation characteristics of bubbly water have been determined by performing an ensemble average of the effects of the collective symmetric mode over distributions of bubble locations and bubble radii. The method includes all orders of multiple scattering and incorporates the field attenuation (or 'shielding') effect of the intervening bubbly medium as one bubble scatters to another. Comparison with experimental data for bubbles of uniform radius was consistent for higher void fractions from 0.22 - 1%. For lower void fractions 0.22 - 0.0377% the analysis was less consistent even though Feuillade suggests interactions could reasonably be expected. It is also suggested that interactions should rapidly reduce and disappear below a void fraction of 0.377%, although there is no experimental data to support this. Comparison with data for non-uniform bubble sizes

was less successful. The void fraction was ~0.02%, and a better fit to the data was achieved by the original Foldy model with a slightly reduced void fraction. Feuillade suggests that "this implies that multiple scattering plays a much smaller part in the propagation of sound through water containing bubbles of non uniform radius". However it is not clear at what stage the requirement of the assumptions described above (for a large number of bubbles and high uniform density) break down. Hence the statement must be viewed with some caution.

B.4 Zhen Ye's many body theory for bubbly systems

Zhen Ye[87] describes how most studies of the acoustic properties of bubbly liquids have assumed that only the interaction of a single bubble with the medium is considered. For this assumption to be valid the following criteria must be satisfied $n^{2/3}\Omega_{scat} \langle\langle 1$ and $n\Omega_{scat}/k \langle\langle 1$ where Ω_{scat} is the scattering cross-section of the bubbles[81]. This is the case when the void fraction is small and the insonification frequency is far from resonance. To overcome this limitation, and so completely model bubble interactions, would require an indefinite number of interactions and thus an approximate representation must be obtained. Foldy's theory is an example of a model which includes the lowest order iteration only. In order to systematically consider the higher order iterations Zhen Ye utilises the perturbative Feynman-diagram method used in many-body theory which has been used extensively in condensed matter physics. In his paper Zhen Ye has confined his investigation to a second order correction for phase speed and attenuation.

In contrast to Feuillade, Zhen Ye uses the dispersion relation to determine the phase speed and attenuation. Foldy also developed a dispersion relation for a first order iteration

$$K_{eff}^2 = K^2 + 4\pi n f_s \qquad \text{[B-5]}$$

where f_s is the scattering function of a bubble. This is corrected by Zhen Ye to include the second order iteration

$$K_{eff}^2 = K^2\left[1+\frac{4\pi}{K^2}A\left(1-i\frac{2\pi B}{K}\right)\right] \qquad \text{[B-6]}$$

Where

$$A = \int da \left[\frac{n(a)a}{(\omega_0^2/\omega^2) - 1 + i\delta} \right] \qquad \text{[B-7]}$$

$$B = \int da \left[\frac{n(a)a}{[(\omega_0^2/\omega^2) - 1 + i\delta]^2} \right] \qquad \text{[B-8]}$$

As with Feuillade's analysis, the bubble cloud is assumed to be uniformly distributed in three-dimensional space. Results for both single and continuous bubble size distributions are compared for the first and second order theory. Significant differences are indicated for the single bubble size distribution for void fractions as low as 10^{-4} % increasing with decreasing bubble size (suggesting the bubble distribution, and not just the void fraction, is important as increased numbers of bubbles are required to maintain the void fraction). For the continuous distribution the correction is less significant. For the example void fraction of 10^{-2}% and a power law distribution (-4 in this case) although they are still important near resonance.

Since no comparison is made with experimental results, it is difficult to evaluate the improvement gained through the use of the second order correction. However Zhen Ye has shown that high order interactions do contribute significantly to the acoustic properties of bubbly media, particularly near resonance. It is hoped that a comparison with experimental results will be included when the effect of higher order interactions are investigated and published as promised by Zhen Ye.

B.5 Henyey's correction to Foldy's effective medium theory

Henyey[88] uses a similar approach to Zhen Ye in that a correction for the effective dispersion relation K_{eff}, given in equation B.5 above, is sought by consideration of a multiple scattering series. Henyey's paper is particularly interesting since it allows an algebraic comparison of the models of Foldy, Feuillade and Zhen Ye with his own which incorporates some second order interactions neglected by Zhen Ye. Similar assumptions to those of Zhen Ye are also made by Henyey, specifically that only the

mean acoustic field is investigated and thus a uniform density of scatterers is assumed. The effective wave number of a bubbly medium can be given by

$$K_{eff}^2 = K^2 + 4\pi n F_s \qquad \text{[B-9]}$$

where F_s is the effective scattering amplitude function which has the following form for Foldy's, Feuillade's, Zhen Ye's and Henyey's models (equations B.10, B.11, B.12 and B.13 respectively)

$$F_s = f_a \qquad \textit{[B-10]}$$

$$F_s = \frac{f_a}{(1 - 4\pi n f_a I)} \qquad \textit{[B-11]}$$

$$F_s = f_a + 4\pi i n \frac{f_a^3}{2K} \qquad \text{[B-12]}$$

$$F_s = f_a + \frac{4\pi i \ f_a n F^2}{K + K_{eff}} \qquad \textit{[B-13]}$$

where f_a is the scattering amplitude of a single scatterer and $I = \int_0^\infty r e^{iKr} dr$.

It should also be noted that, during this evaluation, Henyey discovered a "spurious quadratic term" and thus Feuillade's results are in error. This appears to have been confirmed through private communication between Henyey and Feuillade. Unfortunately Henyey does not provide any numerical simulations to allow further comparison of the models. However, it is stated that when K_{eff} is large compared to K the results from the model diverge from those of Zhen Ye and are very close to Foldy's.

B.6 Conclusions

Current theory suggests that multiple bubble interactions are important when considering the response of resonant bubbles. The relative importance of these contributions is difficult to quantify due to the scarcity of supporting experimental data, particularly when considering the more recent corrections to the theory. However, comparison of theoretical results of Zhen Ye (with and without corrections for multiple bubble interactions for a 10 μm resonant bubble, with a void fraction of 10^{-4}%) leads to an increase in attenuation of ~20%. The change reduces away from resonance confirming that it is the void fraction of the resonant bubbles that is important when considering multiple bubble interactions.

APPENDIX C

Reverberation Time of the AB Wood Test Tank

C Reverberation Time of the AB Wood Test Tank

C.1 Introduction

An experiment has been conducted to determine the reverb time of the 8 m x 8 x 5 m deep A B Wood laboratory test tank[89].

C.2 Theory

The reverberation time[90], T_{60}, or the time taken for the sound pressure level to reduce by 60 dB, can be determined using equation [C.1].

$$T_{60} = \frac{-55.2V}{S_a c \ln(1 - <\alpha>)} \qquad [C.1]$$

Here V is the volume of the enclosure (m^3), S_a the surface area (of walls and free surface of the tank), c the sound speed (m/s) and $<\alpha>$ is the spatially averaged constant of attenuation.

C.3 Measurement of the reverberation time

To calculate the reverberation time it is necessary to measure the constant of attenuation spatially averaged within the tank enclosure. A source, (B&K 8105) was mounted in one corner of the enclosure and a B&K 8103 hydrophone was placed in six different locations in the tank taking care to remain at least a metre from either the

walls or the source. The source was then excited in third-octave bands of noise, covering the range 60 kHz to 200 kHz. Transmission was stopped at a known time and the ring down in the hydrophone recorded. The reverberation time was then calculated by reverse integration[91] and the results spatially averaged for each of the hydrophone positions.

C.4 Results

The results for the reverberation time obtained by reverse integration were averaged over the six hydrophone positions. The test was then repeated five more times and these data averaged to give the results shown in Figure D.1. The attenuation factors that give the reverberation times shown in Figure D.1 are indicated in Table 1 below.

Centre Frequency (kHz)	Reverberation Time (s)	Attenuation Factor
80	0.029	0.7587
100	0.134	0.2649
125	1.315	0.0309
160	1.144	0.0354

Table C.1 Reverberation time and attenuation factor for the frequency bands tested

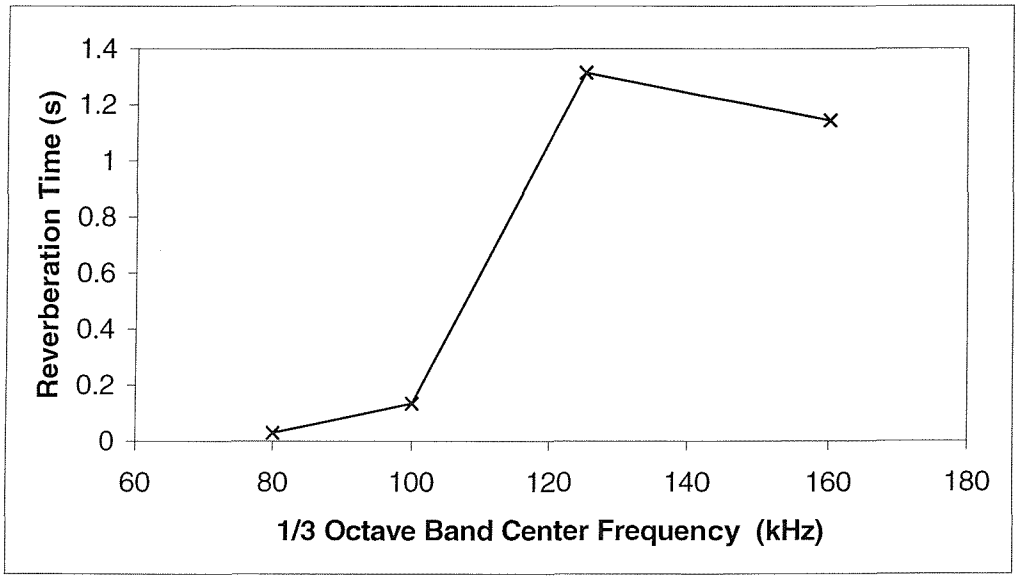

Figure C.1 Reverberation time for the A B Wood test facility for 1/3 octave band centre frequencies of 80, 100, 125 and 160 kHz.

APPENDIX D

SPECIFICATIONS OF HYDROPHONES

D Specifications of hydrophones

This appendix lists the specifications of the sources and receivers used in the tank tests and sea trial discussed in this thesis. The schematics of the Bruel and Kjaer Type 8013 and 8015 hydrophones are shown in Figure D-1 and Figure D-2; the transmit response of the Bruel and Kjaer Type 8105 used as a source in the tank test is plotted in Figure D-3; the directivity patterns of Bruel and Kjaer hydrophones Type 8103 and 8105 are shown in Figure D-4; and a typical calibration for Bruel and Kjaer hydrophone Type 8103 is plotted in Figure D-5.

The UDI wide band transmit receive array used in the sea trial was monostatically mounted with the receiver mounted directly below the transmitter. The transmit and receive elements are 0.07 m by 0.04 m. The units were mounted with the longest dimension horizontal. The transmit and receive calibrations are shown in Figure D-6 and Figure D-7 respectively. The beam patterns in the horizontal plane for the transmit and receive are shown in Figure D-8 and Figure D-9 respectively.

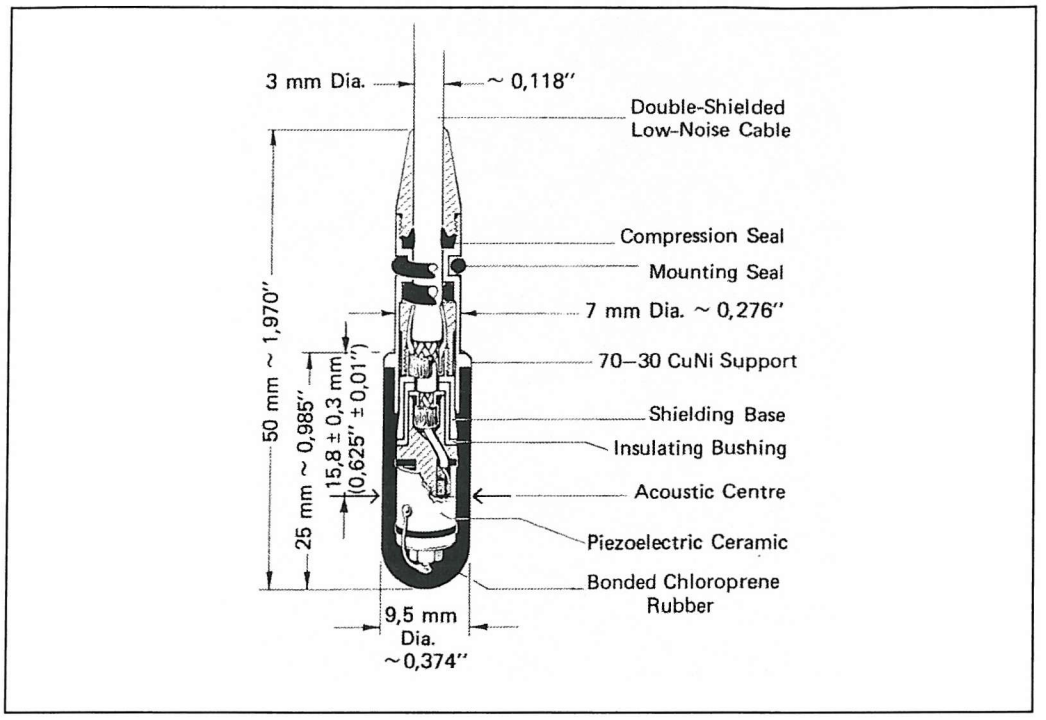

Figure D-1 Dimensions and construction of the Bruel and Kjaer Type 8103 hydrophone[92].

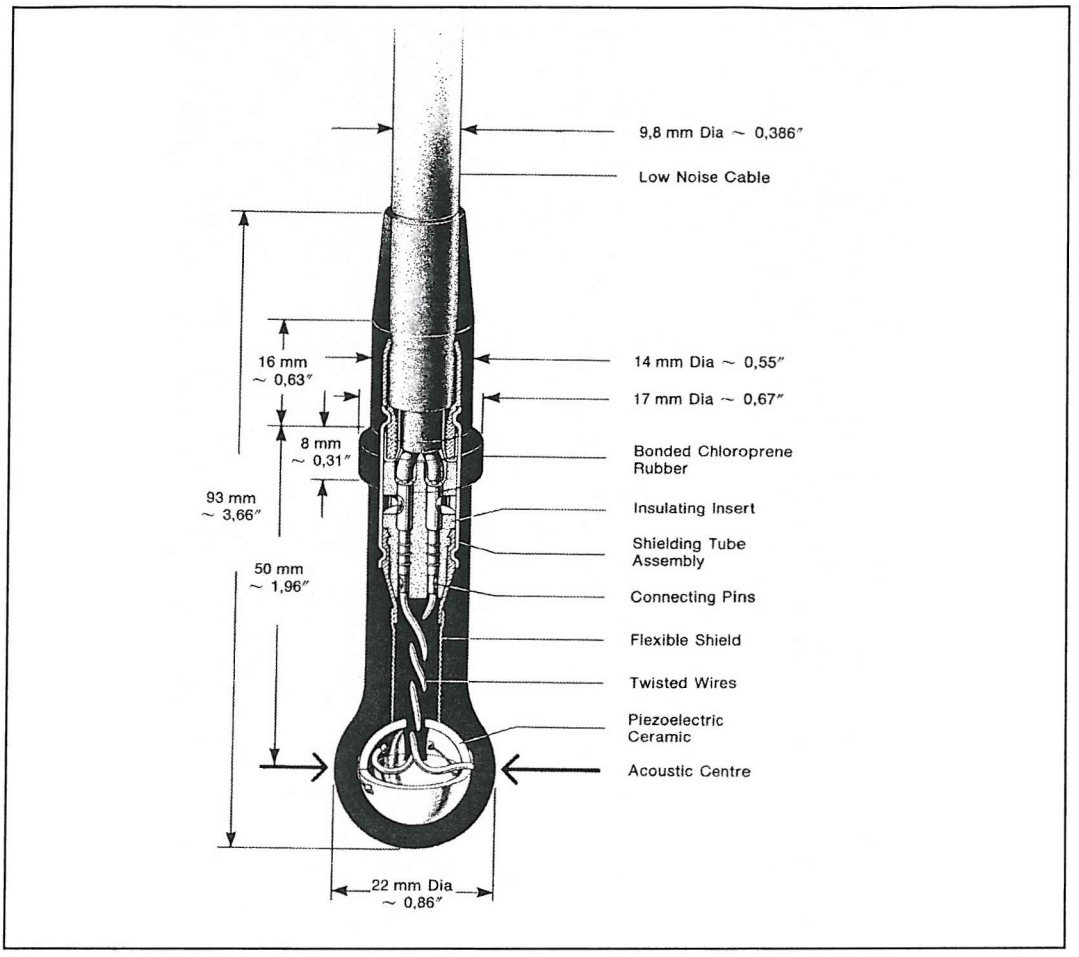

Figure D-2 Dimensions and construction of the Bruel and Kjaer Type 8105 hydrophone[92].

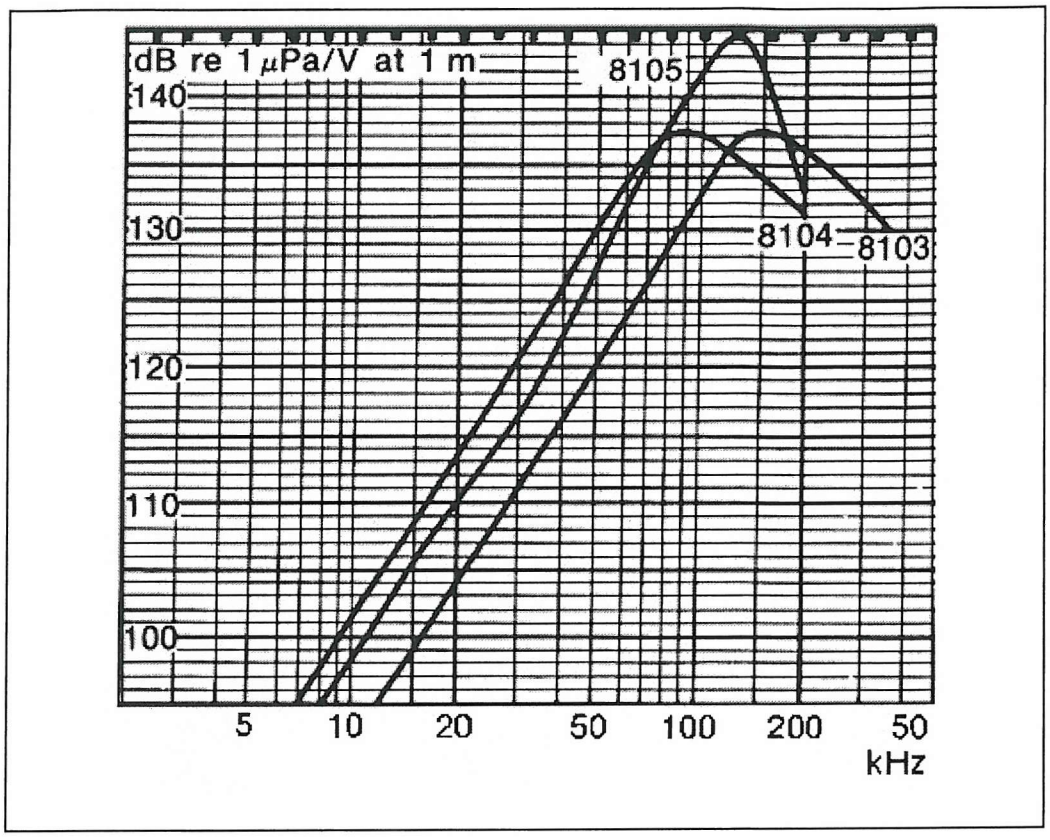

Figure D-3 Typical transmitting response of Bruel and Kjaer hydrophone Types 8103, 8104 and 8105 in dB ref 1 μPa/V at 1 m versus frequency[92].

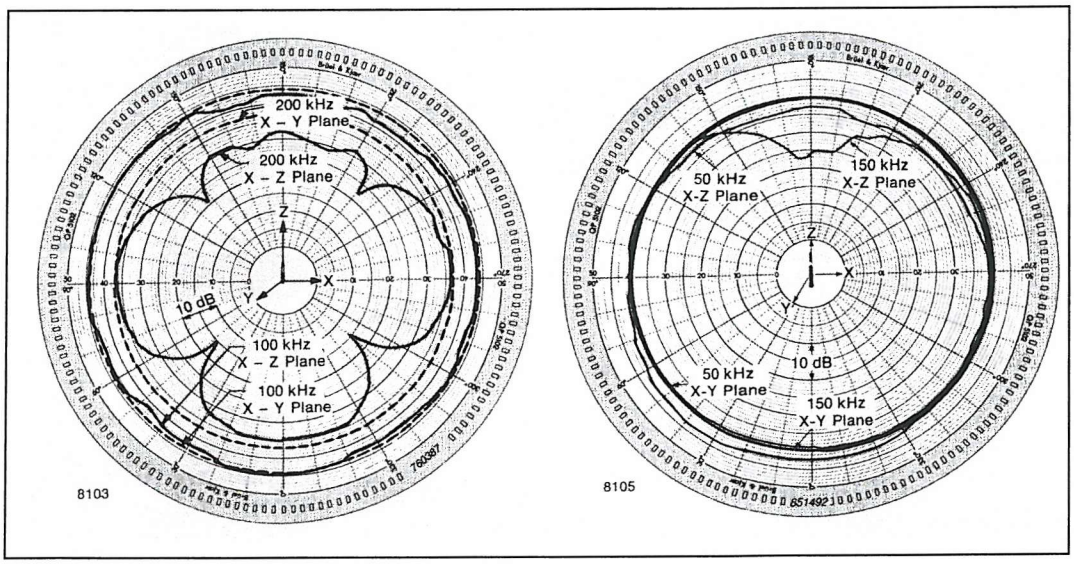

Figure D-4 Typical directivity patterns of Bruel and Kjaer hydrophones Types 8103 and 8105 in the vertical and horizontal planes[92].

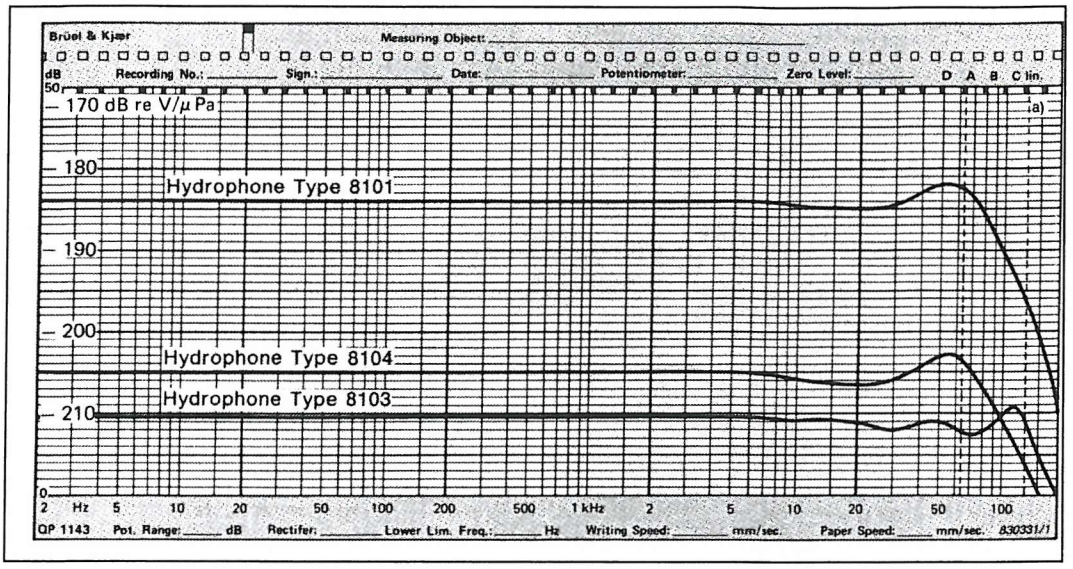

Figure D-5 Typical receiving frequency characteristics of Bruel and Kjaer hydrophones Types 8101, 8103 and 8104[92].

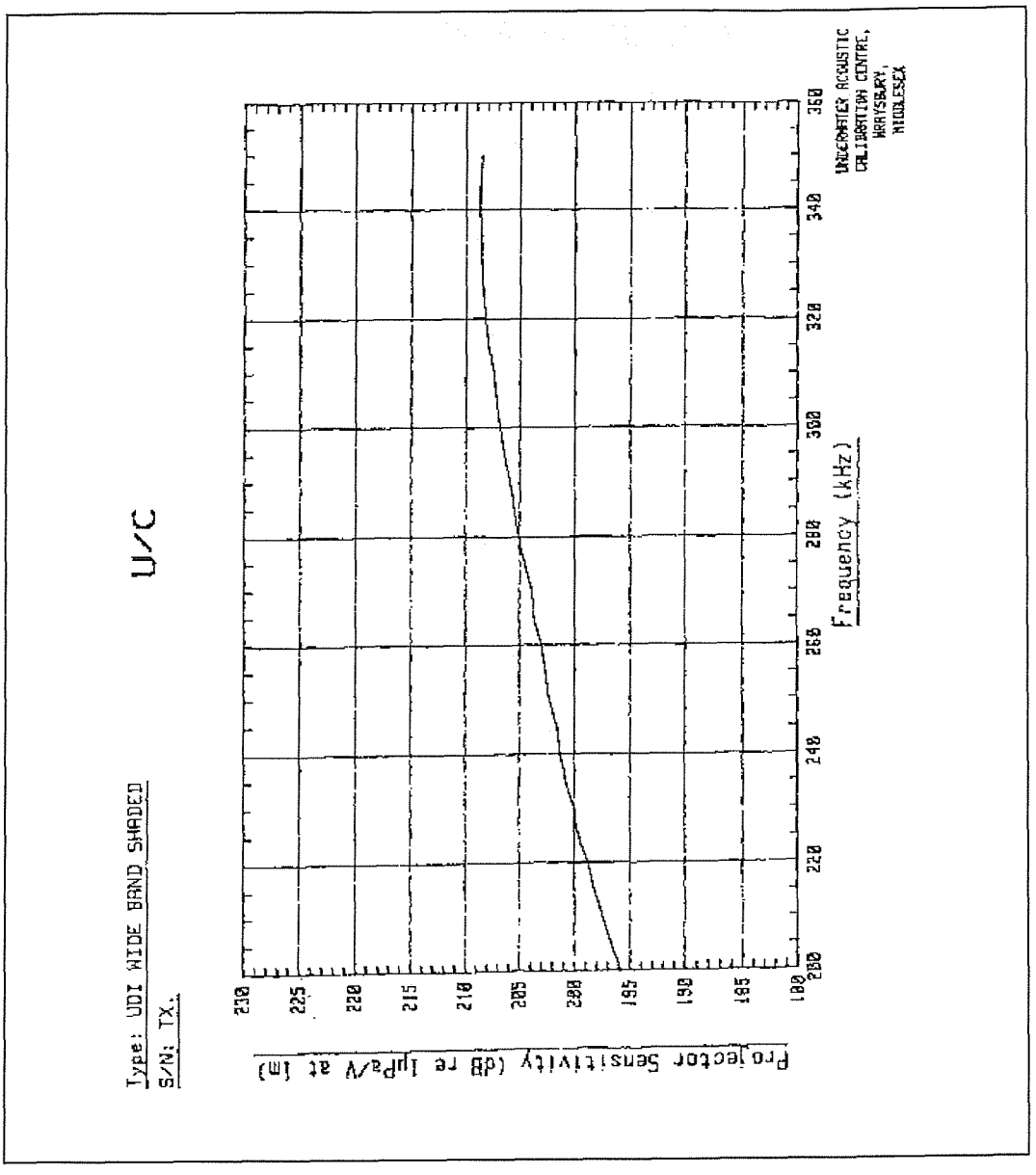

Figure D-6 Transmit calibration for the UDI wide band array. Note pre-amplification was set to x 100 for these calibrations.

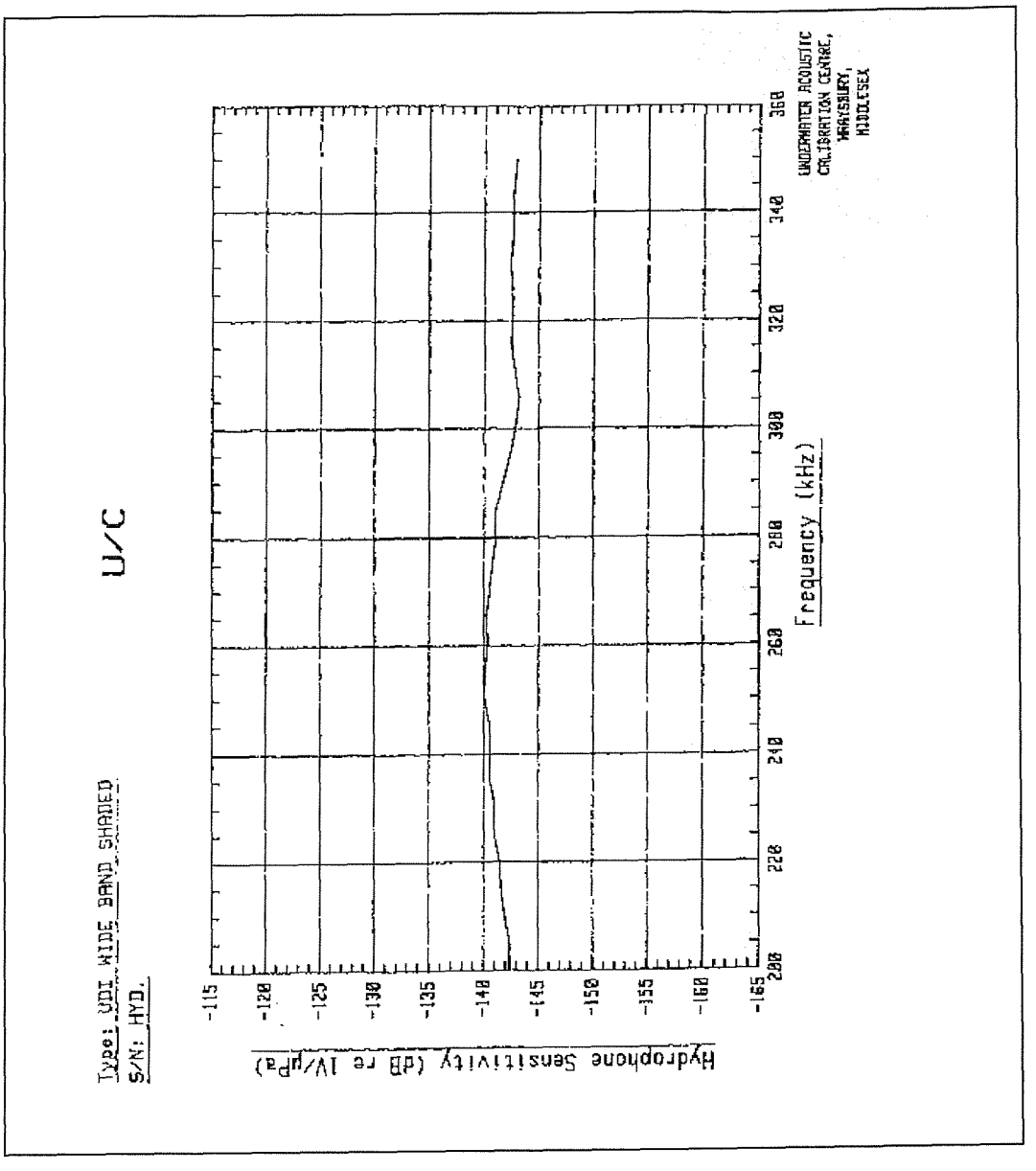

Figure D-7 Receive calibration for the UDI wide band array.

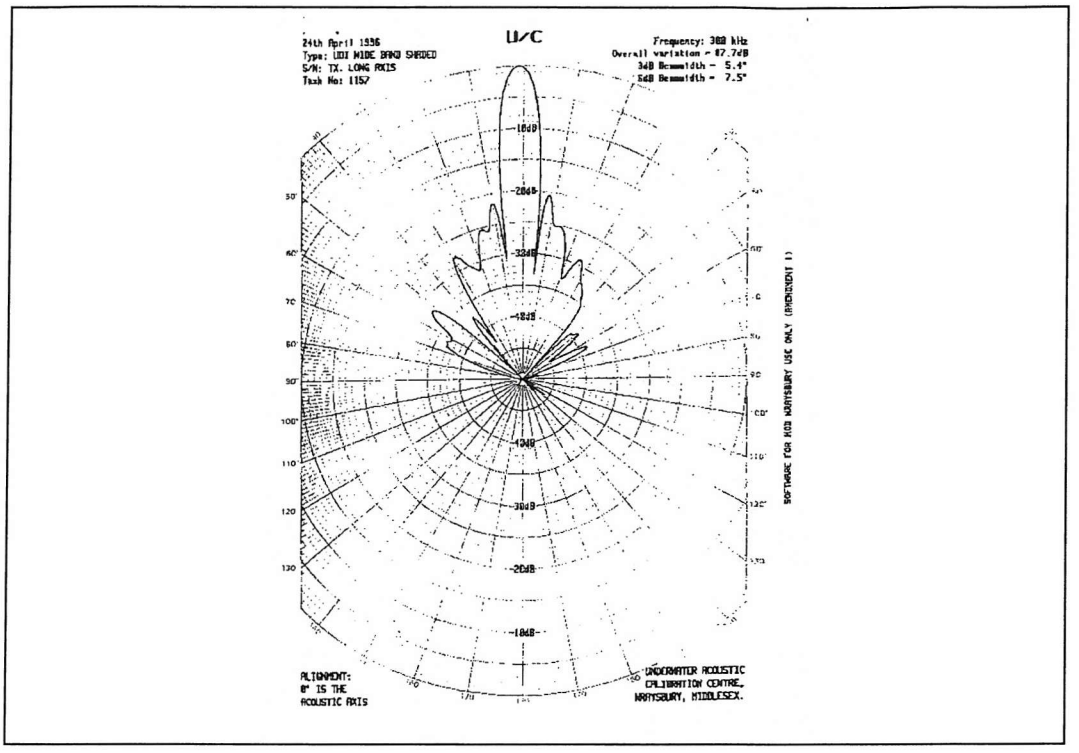

Figure D-8 Transmit beam pattern of the UDI wide band array in the horizontal plane at 300 kHz.

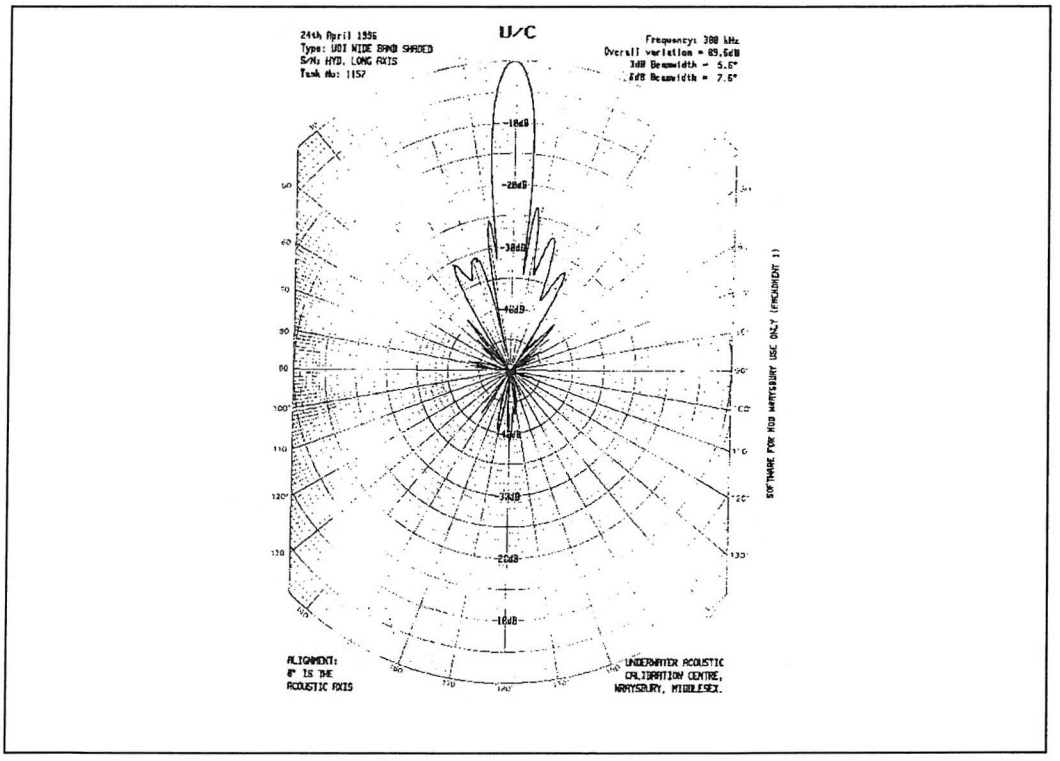

Figure D-9 Receive beam pattern of the UDI wide band array in the horizontal plane at 300 kHz.

APPENDIX E

OTHER OUTCOMES

E Other outcomes

The project has produced the following outcomes:

- The following conference paper was presented by Mr Clarke at the Fourth European Conference on Underwater Acoustics (Rome, Italy; September 1998):

  Clarke J W L, Leighton T G, White P R, Heald G J and Dumbrell H A, The effect of water quality on the damping of bubbles. *Proceedings of the 4th European Conference on Underwater Acoustics, Rome* (ed. A. Alippi, G B Cannelii), 1998, pp. 101-106

- The following conference paper was presented by Mr Clarke at the joint meeting of the Acoustical Society of America and the EAA: Forum Acusticum (Berlin, Germany; March 99):

  Clarke J W L, Leighton T G, Heald G J, Dumbrell H A, Time-dependent scattering from bubble clouds: Implications for the use of acoustic pulses. *Collected papers from the joint meeting "JASA/EAA Berlin 99" (Published on CDRom by Deutsche Gesellschaft für Akustik e.V. Universität Oldenburg, Physik/Akustik D-26111 Oldenburg)*

- The following journal papers have been published:

T. G. Leighton P. R. White, C. L. Morfey, J. W. L. Clarke, G. J. Heald, H. A. Dumbrell, K. R. Holland, The effect of reverberation on the damping of bubbles, J. Acoust. Soc. Am. **112** (4), p 1366-1376, October 2002

Clarke J W L, Leighton T G, A method for estimating time-dependent acoustic cross-sections of bubbles and bubble clouds prior to the steady state, J. Acoust. Soc. Am. 107 (4) p 1922-1929, April 2000

Clarke J W L, Leighton T G, Heald G J , Dumbrell H A, Time-dependent scattering from bubble clouds: Implications fro the use of acoustics pulses, J. Acoust. Soc. Am. 105 (2) p 1254, 1999

Clarke J W L, Leighton T G, Heald G J , Dumbrell H A, Time-dependent scattering from bubble clouds: Implications fro the use of acoustics pulses, Acta Acoustica, 85 sup 1, S328, 1999

Meers S D, Leighton T G, Clarke J W L, Heald G J, Dumbrell H A, White P R,The importance of bubble ring-up and pulse length in estimating the bubble distribution from acoustic propagation measurements, Proc. Institute of Acoustics Vol. 23 Part 2, p 235- 241, 2001

Leighton T G, Meers S D, Simpson M D, Clarke J W L, Yim G T, Birkin P R, Watson Y E, White P R, Heald G J, Dumbrell H A, Culver R L , Richards S D, The Hurst Spit experiment: The characterisation of bubbles in the surf-zone using multiple acoustic techniques Proc. Institute of Acoustics Vol. 23 Part 2, 227-234, 2001.

- Contract reports submitted to DERA Bincleaves (contract no. SSDW1/647):

  Clarke J W L and Leighton T G, The Enhancement of Sonar Detection in Bubbly Environments. Part 1. Preliminary investigation of effect of water quality on damping, and review of prior studies. *ISVR Contract Report No. 98/24, University of Southampton,* 1998.

  Clarke J W L and Leighton T G, The Enhancement of Sonar Detection in Bubbly Environments. Part 2. Effect of salinity on damping and development of models. *ISVR Contract Report No. 98/31, University of Southampton,* 1998.

- The investigations assisted in the MSc project of S. Ponthus who, supervised by Dr Leighton, undertook a study of the response of biomedical echo-contrast agents to ultrasound. This work has received international interest such that Dr Leighton presented an invited paper to the 4th Heart Centre European Symposium on Ultrasound Contrast Imaging (Rotterdam, The Netherlands, January 1999). The following technical memorandum has also been produced:

  Leighton T G, Clarke J W L, Heald G J, Dumbrell H A, Evans R C, Application of the nonlinear acoustic scatter cross-section to the use of clinical ultrasound contrast agents. *ISVR Technical Memorandom No. 835, University of Southampton,* 1999.

- An application for funding in bubble sizing (collaborative between ISVR and ERA) has been submitted and funded by the EPSRC.

APPENDIX F

A METHOD FOR ESTIMATING TIME-DEPENDENT ACOUSTIC CROSS-SECTIONS OF BUBBLES AND BUBBLE CLOUDS PRIOR TO THE STEADY STATE

A method for estimating time-dependent acoustic cross-sections of bubbles and bubble clouds prior to the steady state

J. W. L. Clarke and T. G. Leighton
Institute of Sound and Vibration Research, University of Southampton, Highfield, Southampton SO17 1BJ, United Kingdom

(Received 16 November 1998; revised 11 August 1999; accepted 21 September 1999)

Models for the acoustic cross-sections of gas bubbles undergoing steady-state pulsation in liquid have existed for some time. This article presents a theoretical scheme for estimating the cross-sections of single bubbles, and bubble clouds, from the start of insonation onward. In this period the presence of transients can significantly alter the cross-section from the steady-state value. The model combines numerical solutions of the Herring–Keller model with appropriate damping values to calculate the extinction cross-section of a bubble as a function of time in response to a continuous harmonic sound field (it is also shown how the model can be adapted to estimate the time-dependent scatter cross-section). The model is then extended to determine the extinction cross-section area of multiple bubbles of varying population distributions assuming no bubble–bubble interactions. The results have shown that the time taken to reach steady state is dependent on the closeness of the bubble to resonance, and on the driving pressure amplitude. In the response of the population as a whole, the time to reach steady state tends to decrease with increasing values of the driving pressure amplitude; and with the increasing values of the ratio of the numbers of bubbles having radii much larger than resonance to the number of resonant bubbles. The implications of these findings for the use of acoustic pulses are explored. [S0001-4966(00)01801-4]

PACS numbers: 43.25.Ts, 43.35.Ei, 43.30.Lz [DLB]

INTRODUCTION

It has long been recognized that the high impedance mismatch between an air-filled bubble and the surrounding water provides an excellent acoustic target owing to strong inert scattering. It is also well understood that enhanced scatter and dissipation result from the pulsations into which the bubble will be driven by the sound field. To a first order, this response can be modeled as that of a single degree of freedom system with a resonance frequency, which is dependent on bubble size, where the bubble response is a maximum. It has been convenient to define acoustic extinction and scatter cross-sections for single bubbles, given, respectively, by the ratio of the power lost or reradiated by the bubble to the intensity of an incident plane wave. These have been calculated for the steady state[1] showing that, for a given bubble size, they are maximal at the resonance frequency. It should be noted that the cross-sections are only local maxima at resonance if considered as a function of bubble size for a given insonification frequency. This is because the contribution due to inert scattering will steadily increase with bubble size.

The resonant and off-resonant scattering characteristics of bubbles are well defined and are utilized in a wide number of applications including measurement of oceanic bubble populations[1–4] and research into upper ocean dynamics.[5] However, it is these same characteristics which make acoustic detection of nonbubble targets in areas with high bubble populations (such as the surf-zone) difficult.

One possible solution to this problem utilizes the bubble "ring-up" time, based on the time taken for a bubble to reach steady-state oscillation. Theory suggests that, owing to inertial effects, this ring-up time will be finite and that prior to reaching steady-state oscillation the acoustic scattering will be greatly reduced. A reduction in scattering attributed to "ring-up" time effects was first detected by Akulichev[6] in 1985. However two more recent studies[7,8] have failed to measure any reduction in scattering.

This letter outlines a theoretical scheme which enables the investigation of ring-up times of gas bubbles in fresh water. The model has also been used to determine the extinction cross-section area of bubble clouds of varying population distributions in a 150-kHz sound field assuming no bubble–bubble interactions. This model has been used to help ascertain a possible reason why Suiter[7] and Pace *et al.*[8] did not detect any reduction in scattering.

I. THEORETICAL MODELING OF THE RESPONSE OF A BUBBLE

As discussed in the Introduction, a gas bubble in water, when insonified by a plane wave, will pulsate. The oscillation is, at least to a first approximation, that of a single degree of freedom system, assuming small amplitude oscillations. In this case the restoring force is the elasticity of the gas and the mass is the effective inertia of the liquid component of the oscillating bubble. Damping, and thus energy loss, is introduced into the system by three distinct mechanisms:[9] energy radiated away from the bubble as acoustic waves (radiation damping); energy lost through thermal conduction between the gas and the surrounding liquid (thermal damping); and work done against viscous forces at the bubble wall (viscous damping).

Therefore a simple equation of motion, in the radius-force frame, for such a system driven at a single frequency would be

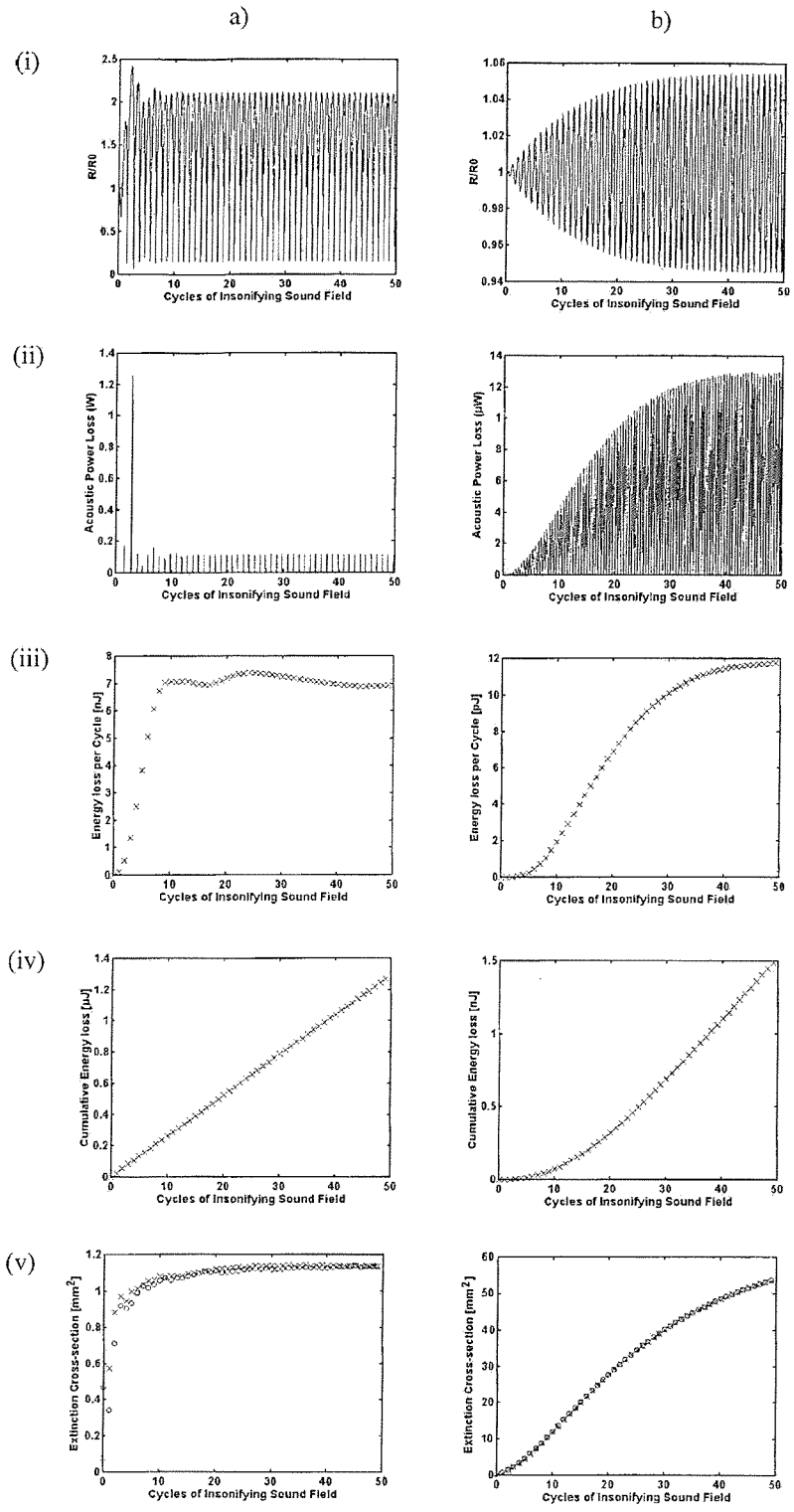

FIG. 1. Simulations of a 20-μm radius bubble in a 150-kHz (a) 1×10^5 Pa, (b) 500 Pa sound field. (i) Bubble wall displacement; (ii) the instantaneous power loss; (iii) energy loss over each cycle of the insonifying sound field; (iv) cumulative total energy loss; (v) extinction cross-sectional area of the bubble over each cycle of the insonifying sound field. For comparison the extinction cross-section calculated using the Gilmore model is also plotted in part (v) ("○" Gilmore, "×" Keller–Miksis). The steady-state extinction cross-sectional area for a 20-μm bubble driven at resonance according to linear theory (Ref. 16) is 6.68×10^{-5} m^2.

$$m_{\rm rad}^{\rm RF}\ddot{R}+b_{\rm tot}^{\rm RF}\dot{R}+kR=-P_A\times4\pi R_0^2\cos(\omega t), \quad (1)$$

where $m_{\rm rad}^{\rm RF}$ is the inertia of the system, $b_{\rm tot}^{\rm RF}$ is the total damping in the radius-force frame, k is the stiffness, R is the radius of the bubble, R_0 is the equilibrium radius, P_A the acoustic pressure amplitude, and ω is the angular frequency of the driving sound field.[10] This is appropriate for bubble pulsations of small amplitude.

The rate of loss of energy (power loss) subtracted from the incident wave by the bubble is:

$$\text{Power}=b_{\rm tot}^{\rm RF}\dot{R}^2. \quad (2)$$

Twice during each bubble oscillation, $\dot{R}=0$. Consider two consecutive times, t_n and t_{n+1} when this occurs. The energy lost from an incident plane wave through viscous, thermal

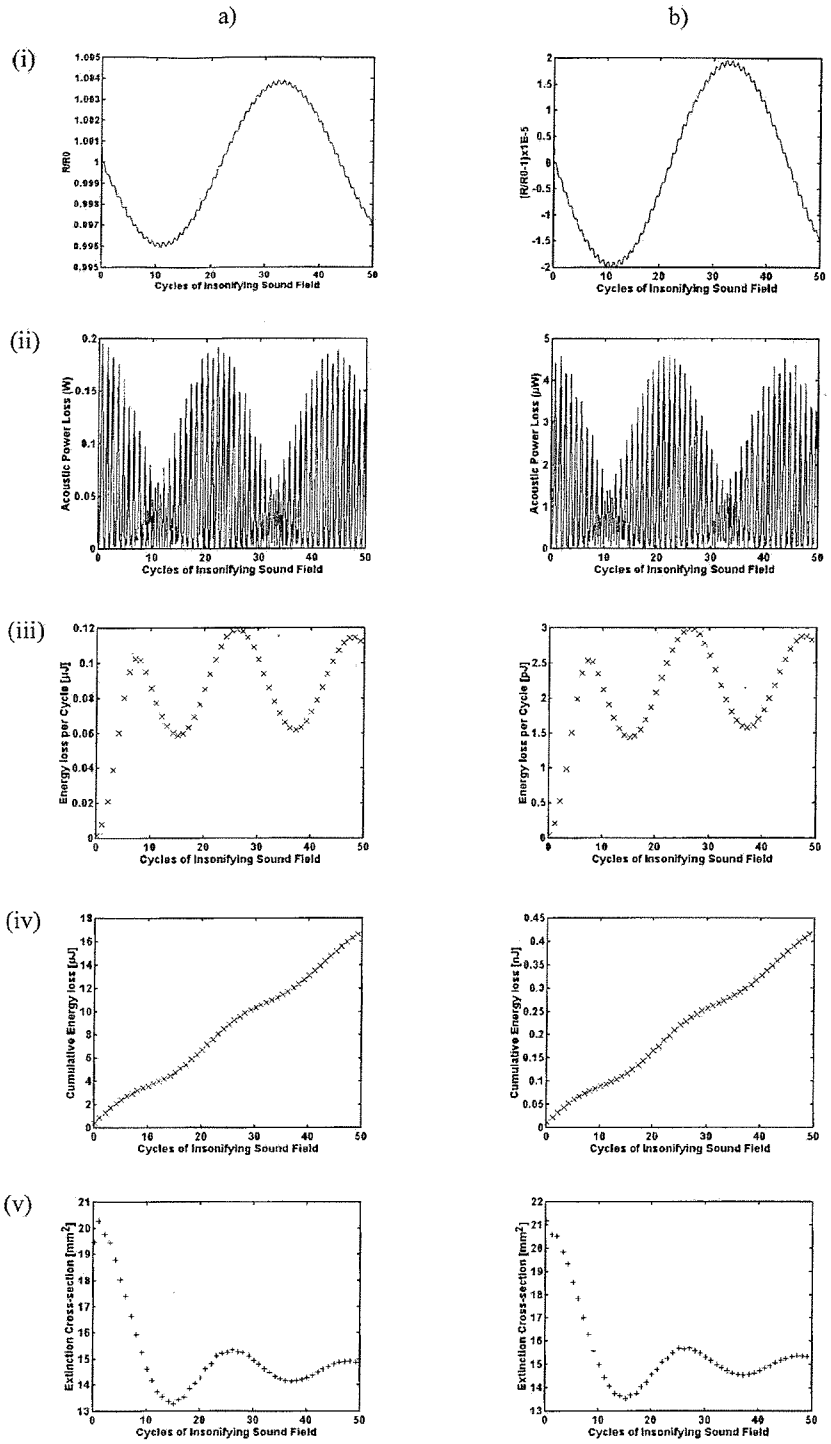

FIG. 2. Simulations of a 1-mm radius bubble in a 150-kHz (a) 1×10^5 Pa, (b) 500 Pa sound field. (i) Bubble wall displacement [for (b) the y-axis has been changed to show (R/R_0-1) so that the axis values can be more clearly shown]; (ii) the instantaneous power loss; (iii) energy loss over each cycle of the insonifying sound field; (iv) cumulative total energy loss; (v) extinction cross-sectional area of the bubble over each cycle of the insonifying sound field. The steady-state extinction cross-sectional area for a 1-mm bubble driven at resonance according to linear theory (Ref. 16) is 1.03×10^{-5} m^2.

and scattering losses in the interval $t=t_n$ to $t=t_{n+1}$ is:

$$\Phi_n=\int_{t=t_n}^{t=t_{n+1}} b_{\mathrm{tot}}^{\mathrm{RF}}\dot{R}^2\,dt, \tag{3}$$

and the average power loss in this interval is:

$$\langle W_n\rangle=\frac{\Phi_n}{t_{n+1}-t_n}. \tag{4}$$

It is then a simple matter to calculate the extinction cross-sectional area, Ω_n, appropriate to the time interval $t=t_n$ to $t=t_{n+1}$. This is given simply by the ratio of the average power loss in this period to the intensity of the incident plane wave:

$$\Omega_n=\frac{\langle W_n\rangle}{I}=\frac{\int_{t=t_n}^{t=t_{n+1}} b_{\mathrm{tot}}^{\mathrm{RF}}\dot{R}^2\,dt}{I(t_{n+1}-t_n)}. \tag{5}$$

It should be noted that if, instead of the total energy loss from the incident beam, it was the power scattered by the

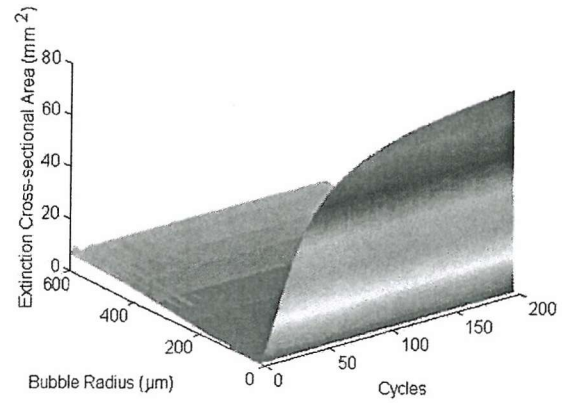

a)

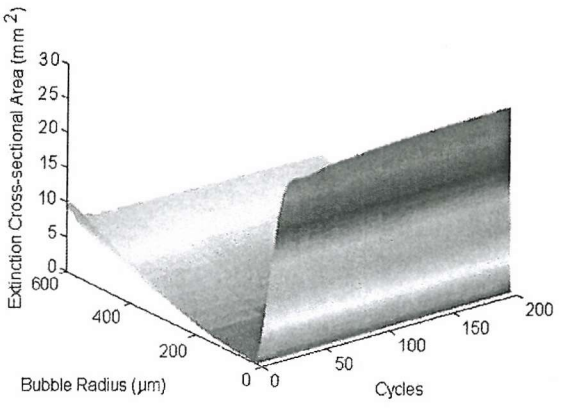

b)

FIG. 3. Extinction cross-sectional area of a single bubble of radius up to 600 μm in a 150-kHz sound field of amplitude (a) 500 Pa, (b) 5000 Pa. For clarity in plotting, the discrete function Ω_n shown in part (v) of Figs. 1 and 2 has been interpolated to provide line plots for the cross-sections shown in this figure and subsequent ones.

bubble which was of interest, then the above formulation can be simply adapted by employing only that component of the damping term $b_{\text{tot}}^{\text{RF}}$ which relates to radiated losses ($b_{\text{rad}}^{\text{RF}}$). This would give the acoustic scattering cross-section. However, a more exact form can be obtained by rewriting the scattered power in Eq. (5) in terms of the emitted pressure field, which can be formulated[10] in terms of the bubble wall motion:

$$\Omega_n = \frac{\langle W_n \rangle}{I} = \frac{4\pi r^2 \int_{t=t_n}^{t=t_{n+1}} \frac{\left(\frac{\rho R}{r}(\ddot{R}R + 2\dot{R}^2)\right)^2}{\rho_0 c} dt}{I(t_{n+1} - t_n)}, \quad (6)$$

where r is the distance from the bubble, ρ_0 is the fluid density, and c is the speed of sound.

Bubbles are nonlinear oscillators and as the following analysis shows the ring-up time is dependent on the bubble equilibrium radius, the driving frequency, and the sound pressure level.

II. TIME-DEPENDENT EXTINCTION CROSS-SECTION OF A SINGLE BUBBLE

To calculate the time-dependent extinction cross-sectional area from Eq. (5), it is necessary to calculate the velocity of the bubble wall over time as well as the total damping in the radius-pressure frame. Although several options are available,[11] in this paper $\dot{R}$ was found using the nonlinear bubble wall velocity determined from the Keller and Miksis equation[12] a form of the equations of motion first introduced by Herring.[13]

The damping term $b_{\text{tot}}^{\text{RF}}$ is obtained using Prosperetti's 1977 analysis.[14] This is a linearized theory for the small amplitude forced pulsation of a bubble, describing the thermal effects in terms of the effective polytropic index and thermal damping constant. This analysis assumes a linear regime. Therefore the only expression of the bubble nonlinearity in this system comes from the Keller–Miksis equation (or equivalent). The resultant is therefore an approximation only. Thus care should be taken when considering the absolute values of $b_{\text{tot}}^{\text{RF}}\dot{R}^2$, especially for higher sound pressure levels when bubble motion is highly nonlinear, as a significant error in the calculation is likely. As discussed in Sec. I, computation of the scattering cross-section need not be limited by such linearizations, since small amplitude expressions for viscous and thermal losses are not required.

Figures 1 and 2 show four illustrative cases, and each figure is subdivided into five subsections [(i)–(v)] showing, against a common time axis, the following: (i) the normalized bubble radius; (ii) the instantaneous power loss determined from Eq. (2); (iii) the energy loss per cycle of the insonifying sound field as determined from Eq. (3) (plotted discretely for each cycle); (iv) a cumulative plot of the energy loss; (v) the time-dependent extinction cross-section area for a single bubble, Ω_n, as calculated by Eq. (5). Plot (iv) is particularly interesting. Were a bubble to immediately attain steady state, this plot would be a straight line of constant positive gradient. However, if the energy loss is less in the ring-up period, the plot will dip below the straight line which would be drawn if the eventual steady-state behavior were extrapolated to time zero.

Figure 1 shows the time-dependent extinction cross-sectional area of a resonant bubble in a 150 kHz sound field of amplitude 10^5 Pa [Fig. 1(a)] and 500 Pa [Fig. 1(b)]. Figure 2 shows the response of a 1-mm radius, off-resonant, bubble in the same sound fields. Further discussion of these results is included in Sec. IV below.

III. TIME-DEPENDENT EXTINCTION CROSS-SECTIONAL AREA OF A BUBBLE CLOUD

The above analysis can be expanded to give a first-order estimation of the time-dependent extinction cross-section of a bubble cloud. It is assumed that the number density is sufficiently small that bubble–bubble interactions can be neglected, as is the reduction in intensity of the incident wave as it propagates through the cloud (although a second-order calculation could include this). This article is restricted to a first-order calculation and thus will underestimate the extinction cross-section near to resonance.[15] After calculating the

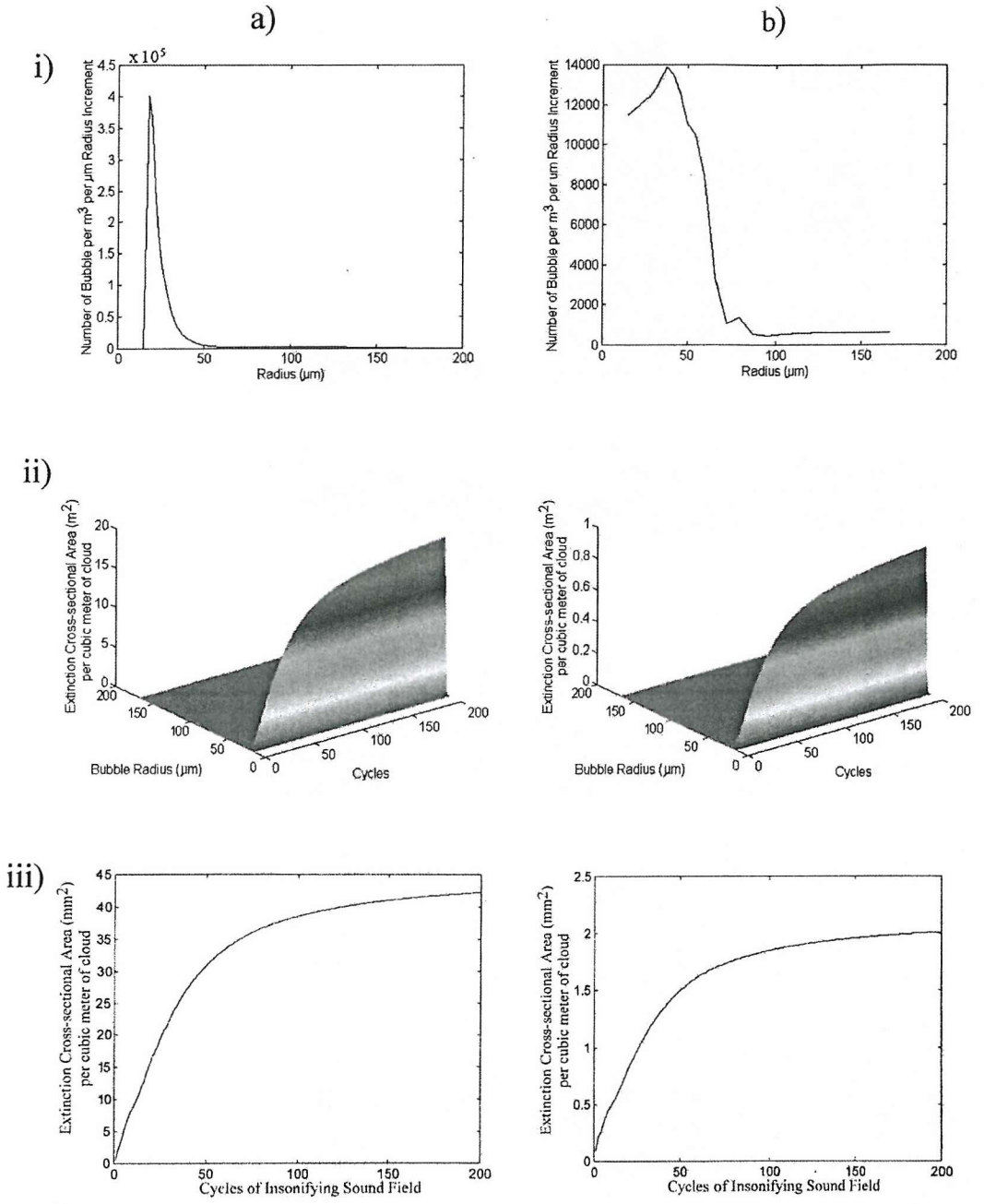

FIG. 4. Response of (a) an example oceanic bubble population (based on the measurements of Phelps and Leighton, Ref. 15); and (b) a laboratory bubble population (based on the measurements of Pace *et al.*, Ref. 8) in a 500-Pa, 150-kHz sound field. Plot (i) shows the bubble population distribution, (ii) is the extinction cross-sectional area oif a 1 m^3 cloud, resolved for each radius bubble assuming no interactions, and (iii) is the extinction cross-sectional area of the 1 m^3 cloud (i.e., summed for all radii for each cycle of the sound field).

extinction cross-sectional area of a single bubble of varying radii and compiling the results as in Fig. 3, the effective response of a bubble layer with a given population distribution can be calculated. The density of the population is used as a scaling quantity given the limitations discussed above.

Therefore the response of a nonuniform bubble distribution can be investigated by multiplying the response [calculated as for Fig. 1(a) and (b)] by a population distribution. In addition the total response of the bubble cloud can be ascertained by integrating to find the area under the extinction cross-section radius curve for each cycle of the insonifying sound field. Figures 4 and 5 show the response for a bubble population typical of an oceanic bubble cloud[16] and an artificially produced bubble cloud (taken from the population measurements of Pace *et al.*[8]) in sound fields of 500 Pa and 5000 Pa amplitude. Since the acoustic attenuation method used for measuring the laboratory population proved unreliable for larger bubble sizes in the data of Pace *et al.*,[8] their population has been extrapolated in Fig. 6, up to a radius of 600 μm, to investigate the effect that this could have on the time dependent extinction cross-sectional area (this is for illustrative purposes only and in no way suggests that this

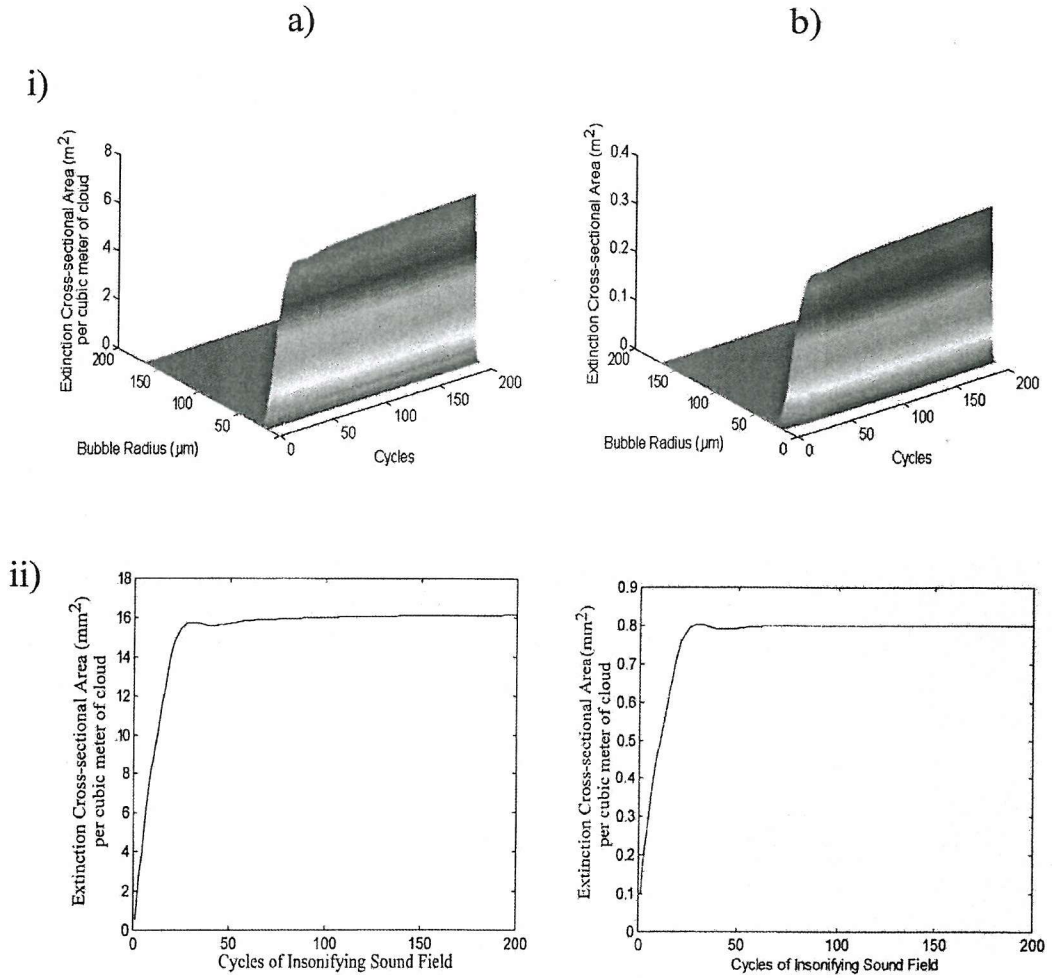

FIG. 5. Response of (a) an example oceanic bubble population (based on the measurements of Phelps and Leighton, Ref. 15) and (b) a laboratory bubble population (based on the measurements of Pace *et al.*, Ref. 8) in a 5000-Pa, 150-kHz sound field. (i) The extinction cross-sectional area of a 1 m^3 cloud, resoved for each radius bubble assuming no interactions. (ii) The extinction cross-sectional area of the 1 m^3 cloud (i.e., summed for all radii for each cycle of the sound field).

extrapolation reflects the true nature of the population).

IV. DISCUSSION

A simple comparison of the bubble wall displacements depicted in Figs. 1 and 2 provides an intuitive guide as to the effect of sound pressure level and the closeness to resonance on ring-up time. It can clearly be seen that the time taken to reach steady state is by far the longest for a resonant bubble in a low amplitude sound field. A gentle build-up to steady state is observed [Fig. 1(b)]. Conversely a resonant bubble in a high amplitude sound field exhibits a distinctly nonlinear response with significant initial transient activity before quickly achieving a steady-state response [Fig. 1(a)]. Examination of the off-resonant bubble wall displacement plots shows a reduced dependence on sound pressure level and a rapid rise time with subsequent reduction and oscillation (Fig. 2).

In the case of the resonant bubbles, the graphs of the extinction cross-sectional area shown in Fig. 1 tend to follow the mean bubble wall response exhibiting a brief, transient, ring-up at high sound pressure levels and a gradual build-up for low sound pressure levels. The latter indicates potential for reducing losses by using short pulses of ultrasound, an effect confirmed by noting that in Fig. 1(b) (iv), in the first 30 cycles the curve dips below a straight line which might be extrapolated back from the steady state (as predicted in Sec. II).

A superposition of natural and driving frequencies is evident in the radius plots [Fig. 2(i)]. The extinction cross-sectional area for these off-resonant bubbles [Fig. 2(v)] is more complicated and can be more easily understood by examining the plots of the acoustic power loss determined from Eq. (2) [Fig. 2(ii)].

Although transients are more evident at the lower driving pressures [Fig. 2(b) (ii)], the tendency in both plots is for the energy loss [Fig. 2(iii)] and extinction cross-section [Fig. 2(v)] to oscillate around the steady-state value at twice the bubble natural frequency, although the cross-section takes much higher values for the first few cycles. Clearly the presence of such bubbles would not be conducive to enhancing acoustic transmission using pulsed fields. Figure 3 summarizes the time-dependent cross-section of single bubbles. A

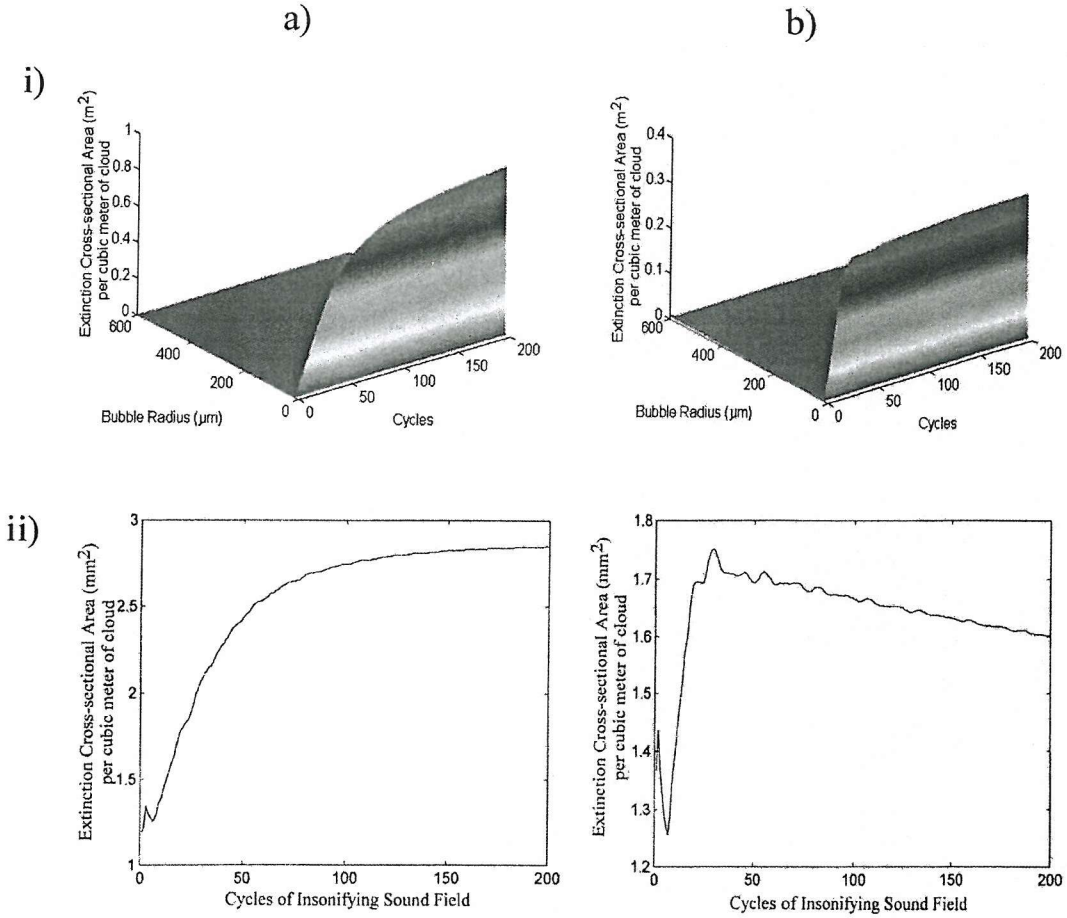

FIG. 6. Response of the laboratory bubble population (based on the measurements of Pace *et al.*, Ref. 8) extrapolated to include potential large bubbles in a 150-kHz, (a) 500 Pa and (b) 5000 Pa sound field. Plot (i) is the extinction cross-sectional area of a 1 m^3 cloud, resoved for each radius bubble assuming no interactions, and (ii) is the extinction cross-sectional area of a 1 m^3 cloud, summed for all radii for each cycle of the sound field.

"geometrical" contribution is seen from the large bubbles, which oscillate for a few tens of cycles following the onset of insonation around the eventual steady-state value. Smaller bubbles contribute a lesser amount except around the resonance condition. Here there is a peak, with a ring-up time which tends to decrease with increasing driving amplitude. Figure 7 shows how the extinction cross-section of a 20-μm radius bubble changes with increasing sound pressure levels. The bubble response quickly deviates from an exponential ring-up with a corresponding decrease in ring-up time. Thus for the simulated response of a bubble cloud, which contain large numbers of small bubbles, to a 150-kHz sound field the response of the resonant bubble is dominant with a well defined ring-up time for low sound pressure levels (Fig. 4). It is evident that an increase in the sound pressure level can significantly reduce the ring-up time. The results shown in Fig. 5 demonstrate this effect. In the case of the extrapolated bubble populations shown in Fig. 6, despite the numbers of large bubbles being relatively few, their presence has a significant effect on the response of the cloud as a whole, particularly during the first few cycles of the insonifying sound field. In this epoch, the early motion of these large bubbles (characterized above as being a fall in the first few cycles following oscillation toward steady state) appears to dominate. Thus the presence of large bubbles and/or high sound pressure levels can be counter-indicative for the enhanced efficiency of penetration of sonar through bubble clouds.

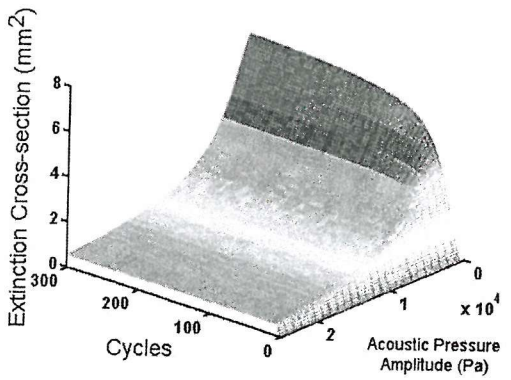

FIG. 7. Extinction cross-sectional area of a single bubble of radius 20 μm in a 150-kHz sound field of varying sound pressure level between 500 and 25 000 Pa.

V. CONCLUSIONS

A theoretical study into the time dependence of the response of air bubbles in fresh water to a continuous wave of 150-kHz sound field has shown that the ring-up time of a bubble is affected by its closeness to resonant oscillation and the amplitude of the driving sound field. Expansion of this theory to investigate the response of a low density bubble cloud of oceanic and laboratory origins has shown that a significant ring-up time should be detectable if the predominant smaller bubbles are insonified at their resonant frequency. Furthermore, higher sound pressure levels can obscure the ring-up time of the resonant bubbles, and the presence of large off-resonant bubbles even in relatively small quantities can enhance this effect significantly.

ACKNOWLEDGMENTS

The authors wish to acknowledge funding from the Defence Evaluation Research Agency (Contract No. SSDW1/647) and are very grateful to G. J. Heald and H. A. Dumbrell of DERA Bincleaves for invaluable scientific and technical input.

[1] H. Medwin, "Counting bubbles acoustically: A review," Ultrasonics **15**, 7–14 (1977).

[2] D. M. Farmer and S. Vagle, "Bubble measurements using a resonator system," in *Natural Physical Processes Associated with Sea Surface Sound*, edited by T. G. Leighton (University of Southampton, 1997), pp. 155–162.

[3] W. K. Melville, E. Terrill, and F. Veron, "Bubbles and turbulence under breaking waves," Natural Physical Processes Associated with Sea Surface Sound, University of Southampton, edited by T. G. Leighton (1997), pp. 135–145.

[4] A. D. Phelps, D. G. Ramble, and T. G. Leighton, "The use of a combination frequency technique to measure the surf zone bubble population," J. Acoust. Soc. Am. **101**, 1981–1989 (1997).

[5] S. A. Thorpe, "Bubble clouds and the dynamics of the upper ocean," Q. J. R. Meteorol. Soc. **118**, 1–22 (1992).

[6] V. A. Akulichev, V. A. Bulanov, and S. A. Klenin, "Acoustic sensing of gas bubbles in the ocean medium," Sov. Phys. Acoust. **32**, 177–180 (1986).

[7] H. R. Suiter, "Pulse length effects on the transmissivity of bubbly water," J. Acoust. Soc. Am. **91**, 1383–1387 (1992).

[8] N. G. Pace, A. Cowley, and A. M. Campbell, "Short pulse acoustic excitation of microbubbles," J. Acoust. Soc. Am. **102**, 1474–1479 (1997).

[9] C. Devin, Jr., "Survey of thermal, radiation, and viscous damping of pulsating air bubbles in water," J. Acoust. Soc. Am. **31**, 1654 (1959).

[10] T. G. Leighton, *The Acoustic Bubble* (Academic, New York, 1994), Sections 3.3.1(b), 3.2.1, and 4.1.2.

[11] For comparison the Gilmore equation was also used to determine $\dot{R}$ with, as Fig. 1(v) illustrates, negligible effect for the parameter range indicated here.

[12] J. B. Keller and M. Miksis, "Bubble oscillations of large amplitude," J. Acoust. Soc. Am. **68**, 628–633 (1980).

[13] C. Herring, "Theory of the pulsations of the gas bubble produced by an underwater explosion," OSRD, Rep. No. 236 (1941).

[14] A. Prosperetti, "Thermal effects and damping mechanisms in the forced radial oscillations of gas bubbles in liquids," J. Acoust. Soc. Am. **61**, 17–27 (1977).

[15] Z. Ye and L. Ding, "Acoustic dispersion and attenuation relations in bubbly mixture," J. Acoust. Soc. Am. **98**, 1629–1636 (1995).

[16] A. D. Phelps and T. G. Leighton, "Oceanic bubble population measurements using a buoy deployed combination frequency technique," IEEE J. Ocean Eng. **23**, 400–410 (1998).

APPENDIX G

THE EFFECT OF REVERBERATION ON THE DAMPING OF BUBBLES

The effect of reverberation on the damping of bubbles

T. G. Leighton,[a] P. R. White, C. L. Morfey, and J. W. L. Clarke
Institute of Sound and Vibration Research, University of Southampton, Highfield, Southampton SO17 1BJ, United Kingdom

G. J. Heald
QinetiQ, Sound Concepts Department, Winfrith Technology Centre, Building A22, Winfrith Newburgh, Dorchester, Dorset DT2 8XJ, United Kingdom

H. A. Dumbrell
QinetiQ, Offshore and Acoustics Department, Newton Road, Bincleaves, Weymouth, Dorset DT4 8UR, United Kingdom

K. R. Holland
Institute of Sound and Vibration Research, University of Southampton, Highfield, Southampton SO17 1BJ, United Kingdom

(Received 27 July 1998; revised 23 January 2002; accepted 26 June 2002)

The measurement of an acoustic emission, or scatter, from a bubble is not difficult. However, an accurate interpretation of that signal in terms of the bubble dynamics may require careful consideration. The study presented here is at first sight relatively simple: comparison of the predicted and measured quality factors of injected bubbles. While the measurement is normally done by monitoring the decay of passive emissions from a bubble, this technique becomes difficult with smaller bubbles. Therefore an active technique is introduced, which removes all the frequency-dependent effects on the measurement (such as transducer response) bar one. That, critically, is the effect of the change in the bubble resonance (frequency and damping) which results from the loading on the bubble due to the reverberant field. The vast majority of theoretical treatments of bubble acoustics assume free field conditions, yet the environmental conditions rarely if ever match these. Therefore measurements of bubble damping are compared both with the established free field theory, and with a new theory relevant to the prevailing reverberant conditions (whether caused by tank surfaces, monochromatic neighboring bubbles, or both). © *2002 Acoustical Society of America.* [DOI: 10.1121/1.1501895]

PACS numbers: 43.30.Jx, 43.30.Ft [DLB]

I. INTRODUCTION

It is usually supposed that one of the simplest experiments in bubble acoustics is the estimation of the equilibrium radius of the bubble (R) and its quality factor (Q) from the exponentially decaying sinusoidal pressure trace obtained when an air bubble is injected into water. The use of formulations resembling those of Minnaert[1] or Devin[2] is almost taken for granted in many tests. For example, to the authors' knowledge, all sparging studies on the use of passive acoustic emissions to characterize the bubble population cite Minnaert's equation at the outset[3–8] (with the exception of those which eschew equations[9,10]). Sparging experiments (and indeed almost all such tank tests involving the low kilohertz regime) include reverberation, yet like the vast majority of papers on bubble acoustics the assumption of free-field conditions, implicit in the underlying formulations, is not questioned. This is true throughout the topic, extending to the application of nonlinear equations of motion describing high amplitude bubble oscillation.

For the particular and common task of inferring bubble size from its resonance or natural frequency, the authors[11] previously showed that the presence of a reverberant field could lead to significant errors if free-field formulations, such as that of Minnaert, were used. In the present paper, the rather more difficult problem of calculating the effect of reverberation on bubble damping is attempted. The importance of this work can be judged by considering the following: There are few end-point equations in bubble acoustics that do not incorporate the resonance frequency and damping; and there are few measurements taken in the strictly free-field conditions upon which the common methods of calculating the resonance characteristics are based. Reverberation can arise from the free surface, or from neighboring bubbles, and even from "anechoically lined" container walls since these have limitations with respect to absorption and frequency range.

The simplest way of describing bubble damping is through use of a dimensionless damping coefficient,[2,12–15] δ_{tot} (otherwise known as a loss factor). This parameter equals the sum of three dimensionless damping coefficients, corresponding to viscous losses (δ_{vis}), thermal losses (δ_{th}), and the acoustic radiation from the bubble itself (δ_{rad}). For linear systems at resonance, δ_{tot} represents the reciprocal of the quality factor, Q. Despite the fact that the damping coefficient is very widely used, it is not always appreciated that the standard formulations[2,14,15] are valid for monochromatic

[a]Electronic mail: tgl@soton.ac.uk

 0001-4966/2002/112(4)/1366/11/$19.00

bubble pulsations only (which means the steady state linear response to a single-frequency excitation) in the free field. Even the more sophisticated studies[16–21] available, which would for example allow the calculation of damping during the interval prior to steady state, still maintain an assumption of free-field conditions.

Section II describes the general theory. This is followed by an image interpretation. The technique for measuring in isolation the effect of reverberation on bubble damping is then described.

II. METHOD

Section II A gives the general theory for the effect of reverberation on the fluid loading impedance on a small bubble in a test tank of rectangular cross section. Section II B describes the implications of this theory with respect to the effect of reverberation on the bubble resonance frequency and radiation damping. Section II C describes an image technique for calculating the effect which the tank surfaces and any neighboring bubbles have on the resonance of each bubble in a population in monochromatic conditions. Section II D describes a new experimental method for taking measurements in a reverberant tank, which eliminates all the effects of reverberation except for the loading on the bubble wall, making it possible to study this effect in isolation.

A. Theory for the radiation loading on a small bubble in a tank

The impedance presented to a spherically pulsating bubble, radius R, is estimated from the average pressure on a sphere of radius R that surrounds a point monopole having the same volume velocity as the bubble. Consider a liquid-filled rectangular tank that has rigid walls except for the upper surface, which is assumed to be pressure-release. The complex eigenvalues of the tank are denoted by K_N^2. These are the forced-mode eigenvalues, and depend in principle on the forcing frequency. However since this paper is concerned only with modes which exhibit low damping and resonant behavior, the exact frequency dependence of K_N^2 is not critical provided its value can be modeled close to resonance. Let $k_0=\omega/c$ be the acoustic wave number corresponding to acoustic phase speed c and angular frequency ω, and η_N be the loss factor for mode N (defined as the ratio of the imaginary and real parts of K_N^2, at resonance). Then (assuming an implicit time factor of $e^{j\omega t}$)

$$K_N^2=k_N^2+jk_0k_N\eta_N \quad (k_N \text{ real};\ N=1,2,3,\ldots). \tag{1}$$

The analysis that follows allows ck_N to be interpreted as the mode resonance frequency, provided $\eta_N \ll 1$. The first stage of the analysis requires derivation of the acoustic impedance presented to a pulsating spherical surface in this environment [Eq. (6)]. This equation is derived in greater detail by Morse and Ingard[22] [their Eq. (9.4.6)], but an outline derivation is given here to assist understanding of the terms in Eq. (6).

The pressure at point $\boldsymbol{x}$ in the tank, due to a point volume velocity source at point $\boldsymbol{x}_0$, is given[22] by

$$p(\mathbf{x})=\frac{j\omega\rho U}{V}\sum_{N=1}^{\infty}\frac{\psi_N(\mathbf{x})\psi_N(\mathbf{x}_0)}{\Lambda_N(K_N^2-k_0^2)}. \tag{2}$$

Here U is the source volume velocity; the mode shape functions, $\psi_N(\mathbf{x})$, are evaluated at the positions of the receiver ($\mathbf{x}$) and the source ($\mathbf{x}_0$); and Λ_N is a normalization constant defined by

$$\int \psi_N^2(\mathbf{x})\,dV=\Lambda_N V, \tag{3}$$

where V is the volume of the tank. The average pressure on a small spherical surface of radius R, centered on the source, can be evaluated explicitly in the low-frequency limit ($k_0R\to 0$) using the expression for $p(\mathbf{x})$ in Eq. (2). The result is[22]

$$\langle p(R)\rangle\approx\frac{j\omega\rho}{4\pi R}U \quad \left(k_0R\to 0;\quad R\ll\frac{k_0^2V}{4\pi}\right); \tag{4}$$

provided that the mode with $k_N=0$ (for a hard-walled cavity) is not included.[23]

Equation (4) is the free-field result, as expected. It follows that if $k_0R\ll 1$ (but has a finite value), and if the tank is sufficiently large for Eq. (4) to be valid (i.e., $k_0^2V\gg 4\pi R$), then an improved approximation is

$$\begin{aligned}\langle p(R)\rangle&\approx\frac{j\omega\rho}{4\pi R}U+\langle p(R)\rangle|_{k_0R}-\langle p(R)\rangle|_0\\&=j\omega\rho U\left(\frac{1}{4\pi R}+\frac{1}{V}\sum_{N=1}^{\infty}\frac{1}{\Lambda_N}\psi_N^2(\mathbf{x}_0)\right.\\&\quad\left.\times\left(\frac{1}{K_N^2-k_0^2}-\frac{1}{K_N^2}\right)\right),\end{aligned} \tag{5}$$

where vector $\mathbf{x}_0$ is the position of the center of the sphere, and the difference between ψ_N at the center and ψ_N on the surface has been neglected.[24] The fluid loading impedance on a small bubble in a tank can now be estimated by dividing both sides of Eq. (5) by U and simplifying:

$$Z_s=\frac{\langle p(R)\rangle}{U}\approx j\omega\rho\left(\frac{1}{4\pi R}+\frac{k_0^2}{V}\sum_{N=1}^{\infty}\frac{\psi_N^2(\mathbf{x}_0)}{\Lambda_N K_N^2(K_N^2-k_0^2)}\right)$$
$$(k_0R\ll 1). \tag{6}$$

This expression is the Morse and Ingard result [Eq. (9.4.6)] for the acoustic impedance presented to a pulsating spherical surface of radius R, which represents a single bubble in the tank.

The first term in the brackets on the right-hand side of Eq. (6) is purely reactive; it dominates in the limit $k_0R\to 0$. However, it simply represents the free-field inertial fluid loading on the bubble. What is more interesting is the deviation from the free-field impedance, as given by the modal summation terms. In particular, the bubble radiation damping comes entirely from the modal summation terms (note that no local viscous or thermal damping has been included at this stage). At low frequencies, the resistance $Z_s^R=\mathrm{Re}(Z_s)$ consists of a sequence of resonant modal peaks. At suffi-

ciently high frequencies the overlap of many modal peaks will produce a smooth curve, corresponding to

$$Z_s^R \approx \frac{\rho c k_0^2}{4\pi}, \tag{7}$$

which is equivalent to the free-field radiation resistance. This last result is derived in the analysis that follows [see Eq. (30)].

The modal loss factors and resonance frequencies can be found experimentally from transmission measurements in the tank. Note from Eq. (2) that, in the neighborhood of a resonance, the pressure at $\mathbf{x}$ due to a point source at $\mathbf{x}_0$ will vary as

$$p(\mathbf{x}) \propto \frac{1}{K_N^2 - k_0^2} = \frac{1}{(k_N^2 - k_0^2) + j\eta_N k_N k_0} = \frac{1}{D}, \tag{8}$$

where the denominator D describes the resonance.

At the modal peak, $k_N = k_0$. Therefore at the half-power points on the resonance curve,

$$|k_N^2 - k_0^2| = \eta_N k_N k_0, \tag{9}$$

i.e.,

$$|k_N - k_0| \approx \tfrac{1}{2}\eta_N k_N \quad (\eta_N \ll 1). \tag{10}$$

It follows that the quality factor for the Nth mode of the tank is equal to η_N^{-1}. Once this is known, the real and imaginary parts of Z_s can be found explicitly from Eq. (6). Provided the loss factors η_N are small, and omitting terms in η_N^2 (except where they occur in $|D|^2$, in the following) the resistance can be approximated by

$$Z_s^R \approx \frac{\rho c}{k_0 V} \sum_{N=1}^{\infty} S_N, \tag{11}$$

where

$$S_N = \frac{\psi_N^2(\mathbf{x}_0)}{\Lambda_N} \frac{(2-\nu_N^2)\eta_N \nu_N^5}{|D|^2}. \tag{12}$$

Here $|D|^2 = (1-\nu_N^2)^2 + (\eta_N \nu_N)^2$ and $\nu_N = k_0/k_N$ is the ratio of the driving frequency to the resonance frequency of mode N. In a similar way the reactance can be approximated by

$$Z_s^I = \mathrm{Im}(Z_s) \approx \frac{\omega\rho}{4\pi R} + \frac{\rho c}{k_0 V} \sum_{N=1}^{\infty} T_N, \tag{13}$$

where

$$T_N = \frac{\psi_N^2(\mathbf{x}_0)}{\Lambda_N} \frac{(1-\nu_N^2)\nu_N^4}{|D|^2}. \tag{14}$$

Note that the modal summation terms S_N in the resistance, Eq. (12), exhibit resonance, while the T_N terms in the reactance vanish at resonance [i.e., when $\nu_N = 1$; Eq. (14)].

For modes of very high order, i.e., $k_N \to \infty$ or $\nu_N \to 0$, the summation terms S_N of Eq. (11) behave like

$$S_N \sim \nu_N^5 \tag{15}$$

and the summation terms T_N of Eq. (13) behave like

$$T_N \sim \nu_N^4. \tag{16}$$

There should therefore be no problem over convergence. We can check this by using the asymptotic relations

$$N \sim k_N^3 \sim \nu_N^{-3}, \quad \frac{dN}{d\nu_N} = n(\nu_N) \sim \nu_N^{-4}. \tag{17}$$

The product of the modal density $n(\nu_N)$ with S_N or T_N remains finite, in the limit $\nu_N \to 0$.

Note that the sums in Eqs. (11) and (13) extend from $N=1$ to $N=\infty$ over integer N. They may be estimated beyond some lower limit N_0 by replacing the sum over N with an integral over ν that involves the modal density $n(\nu)$:

$$\sum_{N=N_0}^{\infty} S_N \approx \int_{\nu_0}^{0} S(\nu) n(\nu) d\nu, \tag{18}$$

and similarly for $\Sigma_{N=N_0}^{\infty} T_N$. The lower limit ν_0 is given by

$$\nu_0 = k_0 L_0, \tag{19}$$

where L_0 is the length that characterizes the tank dimensions. Thus ν_0 is a dimensionless frequency above which the modes of the tank are sufficiently close-spaced to be regarded as a continuum for the purposes of Eqs. (11) and (13). The upper limits of the integrals are zero, corresponding to $k_N \to \infty$.

Note that the modal density $n(\nu)$ follows from the asymptotic mode count $N(k)$:

$$N(k) = \frac{k^3 V}{6\pi^2}, \tag{20}$$

where V is the tank volume. Thus

$$N(k_N) = \frac{k_N^3 V}{6\pi^2} = \left(\frac{k_0}{\nu_N}\right)^3 \frac{V}{6\pi^2}, \tag{21}$$

and

$$\frac{dN}{d\nu} = -\frac{k_0^3 V}{2\pi^2} \nu^{-4} = n(\nu), \tag{22}$$

by definition. In Eq. (22) ν is regarded as a continuous variable. Replacement of the summation step ($\Delta N = 1$) in Eqs. (11) and (13) by an integration increment, $dN = n(\nu)d\nu$, leads to Eq. (18).

The final expression for Z_s, based on summation of Eqs. (11) and (13) up to mode N_0, followed by the integral approximation of Eq. (14) for $N > N_0$, is as follows. The real component of Z_s is

$$Z_s^R = \frac{\rho c}{k_0 V}\left(\sum_{N=1}^{N_0} S_N + \frac{k_0^3 V}{2\pi^2}\int_0^{\nu_0} \frac{(2-\nu^2)\eta\nu}{(1-\nu^2)^2 + \eta^2\nu^2} d\nu\right), \tag{23}$$

and the imaginary component is

$$Z_s^I = \frac{\omega\rho}{4\pi R} + \frac{\rho c}{k_0 V}\left(\sum_{N=1}^{N_0} T_N + \frac{k_0^3 V}{2\pi^2}\int_0^{\nu_0} \frac{(1-\nu^2)}{(1-\nu^2)^2+\eta^2\nu^2} d\nu \right). \quad (24)$$

To obtain Eqs. (23) and (24), Eq. (22) for $n(\nu)$ has been substituted into Eq. (18). The expressions for $S(\nu)$ and $T(\nu)$, Eqs. (12) and (14), have been approximated by replacing $\psi_N^2(\mathbf{x}_0)/\Lambda_N$ with its average value of unity.

Equations (23) and (24) are the main results of the theoretical analysis of this section. Two limiting cases can usefully be distinguished, corresponding to low and high frequencies. In the low frequency limit, defined by

$$k_0 L_0 = \nu_0 \ll 1, \quad (25)$$

the contribution of the integral terms is small compared with that of the summation terms. Note that the integrals in this case do not pass through any resonances.

In the high frequency limit, defined by

$$k_0 L_0 = \nu_0 \gg 1, \quad (26)$$

the contribution of the integral terms is dominant. Provided the overlap of individual-mode responses is sufficient to justify the continuous-distribution model, particularly in the region close to resonance ($\nu \approx 1$) where the integrands are largest, we can estimate the resistance and reactance as follows:

$$Z_s^R \simeq \frac{\rho c k_0^2}{2\pi^2} I_{\text{res}} \frac{\pi}{2} \eta_{\text{res}}, \quad (27)$$

$$Z_s^I \simeq \frac{\omega\rho}{4\pi R}. \quad (28)$$

Note that the integral contribution in Eq. (24) tends to cancel either side of $\nu \approx 1$, which is why Eq. (28) gives just the free field value. In Eq. (27), I_{res} represents the value of the integrand in Eq. (23) at the resonant peak, i.e.,

$$I_{\text{res}} = \frac{1}{\eta_{\text{res}}} \quad (\nu = 1). \quad (29)$$

Thus

$$Z_s^R(\text{high frequency}) \simeq \frac{\rho c k_0^2}{4\pi}, \quad (30)$$

which is the free field value (as expected).

B. Practical implications

The practical implications of the radiation loading result of Eqs. (11) and (13) are interesting, in terms of estimating the bubble radius and damping from the measured acoustic emissions of a single bubble. We define Z_b as the acoustic impedance of the bubble,[25] that is, the ratio of the pressure change Δp to the inwards volume velocity at the bubble wall. If Z_a is the external acoustic impedance due to fluid loading on the bubble, then resonance occurs when

$$Z_a + Z_b = 0. \quad (31)$$

Equation (31) can be used to determine the relationship between the pulsation resonance frequency and the equilibrium bubble radius. For example, since the apparent bulk modulus of the gas within the bubble (of volume V_b) when subject to a pressure change Δp is $B = -V_b \Delta p / \Delta V_b$, then assuming single-frequency simple harmonic motion at circular frequency ω, the acoustic impedance of the bubble at low frequencies ($k_0 R \ll 1$) is

$$Z_b \approx \frac{\Delta p}{-\dot{U}} = \frac{\Delta p}{-j\omega \Delta V_b} = \frac{B}{j\omega V_b}. \quad (32)$$

If the gas within the spherical bubble is assumed to behave polytropically (i.e., $pV^\kappa = \text{constant}$), then $B = \kappa p_0$, where p_0 is the ambient static pressure on the bubble and κ is the polytropic index. The bubble at resonance ($\omega = \omega_0$) is described by Eq. (31) (where in the reverberant conditions of the tank, Z_a is described by Z_s from Sec. II A). If damping is small and hence the resistive terms are neglected, then Z_a and Z_b are almost entirely reactive, ω_0 is real, and Eq. (13) gives

$$\frac{j\kappa p_0}{\omega_0 V_b} \approx j\omega_0 \rho \left(\frac{1}{4\pi R} + \frac{1}{k_0^2 V} \sum_{N=1}^{\infty} T_N \right) \quad (k_0 R \ll 1), \quad (33)$$

where T_N is defined in Eq. (14). The summation term in Eq. (33) represents a reverberant-field correction to the free-field radiation reactance. Neglecting the correction leads to the free-field expression for the resonance frequency of the bubble:[1]

$$\omega_0 \simeq \sqrt{\frac{4\pi R \kappa p_0}{\rho V_b}} = \frac{1}{R}\sqrt{\frac{3\kappa p_0}{\rho}} = \omega_{0f}. \quad (34)$$

An improved approximation is found by evaluating the reverberant correction term at the Minnaert frequency ω_{0f}. The corrected resonance frequency for bubble pulsation in a tank follows from Eq. (34), with the substitution

$$\frac{1}{R} \to \frac{1}{R} + \frac{4\pi c^2}{\omega_{0f}^2 V} \sum_{N=1}^{\infty} T_{Nf} = \frac{1}{R} + \frac{4\pi\rho c^2}{3\kappa p_0 V} R^2 \sum_{N=1}^{\infty} T_{Nf}. \quad (35)$$

Here T_{Nf} denotes T_N of Eq. (14) evaluated at $\omega_0 = \omega_{0f}$. The presence of the summation in Eq. (35) can be seen as a correction which modifies the "free-field" resonance frequency for bubble pulsation. A similar correction factor was used by Leighton *et al.*[11] to modify free-field theory, and thus to estimate the bubble size from the resonance frequency measured in reverberant conditions in a pipe.

However there is a critical difference when calculating how the presence of reverberation changes the bubble damping. As can be seen from Eq. (11) there is no equivalent free-field term: the radiation damping result is entirely made up of the summation terms, and hence the modal structure of the field has to be very well characterized to evaluate this. This can be attempted by measuring the character of the sound field (removing, of course, transducer response, etc., see Sec. II C) and identifying the component modes through

use of Eq. (5). The data can then be converted into effective measurements of the radiation resistance. An alternative but equivalent approach to estimating the reverberation effect is described in Sec. II C. Here an image model is used to calculate the effect of tank surfaces on the radiation impedance of a single oscillating bubble. The technique can also be used to characterize the resonance of each bubble in a *population* driven to steady state by some external source: the effect on each bubble of both the tank's surfaces and of the neighboring bubbles can be incorporated.

C. Method of images

The effect of neighboring reflective boundaries on the radiation impedance of a bubble can be modeled using the method of images. For the specific case of the tank of rectangular cross-section discussed in Sec. II A, the location of the images is calculated from the position of the bubble relative to each wall, the result being an infinite number of images arranged in a grid-like pattern. If the complex pressure reflection coefficient of the various tank walls were of unit magnitude for the frequencies emitted by the bubble, then a continuously emitting bubble would of course generate reverberant acoustic intensities at the bubble surface which would grow with time. This produces a coherent radiation version of Olbers' paradox,[26] by which Halley, Cheseaux, and Olbers realized that, if the number density of stars were constant and the absorption of light in interstellar space were negligible, then unless the universe were finite, the night sky would generate at the observer an intensity equal to the average surface intensity of the stars.

The pressure field radiated by the bubble p consists of a direct field p_d and a reverberant one p_v:

$$p=p_d+p_v, \tag{36}$$

where in the condition $k_0R\ll 1$ the reverberant field is virtually constant over the bubble surface and very similar to that produced at the bubble center location by a point source having the same volume velocity as the bubble. The total acoustic impedance presented to the bubble, Z_a, is

$$Z_a=\frac{p}{U}=\frac{p_d}{U}+\frac{p_v}{U}, \tag{37}$$

where p_d is the direct field on the bubble surface:

$$p_d=\frac{j\rho\omega}{4\pi R}+\frac{\rho\omega^2}{4\pi c} \quad (k_0R\ll 1) \tag{38}$$

(suppressing the harmonic time dependence throughout). Consider two bubbles emitting monochromatic monopole ($kR\ll 1$) radiation, the first having volume velocity U and the second having source strength FU. The pressure at bubble 1 as a result of the radiation from bubble 2 is

$$p_{12}=j\omega\rho FU\left(\frac{e^{-jkr}}{4\pi r}\right), \tag{39}$$

where the bubble separation r introduces both a phase factor and an attenuation. The impedance of Eq. (38) resulting from a population of monochromatic bubbles is therefore

$$\begin{aligned} Z_a&=\frac{j\rho\omega}{4\pi R}+\frac{\rho\omega^2}{4\pi c}+\frac{j\rho\omega}{4\pi}\sum_{m=2}^{m_{\max}}\frac{F_m}{r_m}e^{-jkr_m}\\ &=\frac{j\rho\omega}{4\pi R}+\frac{\rho\omega^2}{4\pi c}+\frac{\rho\omega}{4\pi}\sum_{m=2}^{m_{\max}}\frac{|F_m|}{r_m}(\sin(kr_m-\vartheta_m)\\ &\quad +j\cos(kr_m-\vartheta_m)), \end{aligned} \tag{40}$$

where the subscript $m=2,3,\ldots,m_{\max}$ indicates all bubbles other than bubble 1. These entities may be real bubbles driven linearly at steady state by an external monochromatic source. Equation (40) might also describe the impedance of a single bubble in a tank (where the bubbles $m=2,3,\ldots,\infty$ are images); or indeed be used to calculate the resonance characteristics of each bubble in a monochromatic population within a tank (in which case the population comprises both real and image bubbles). To compare with the calculation of Sec. II A and II B, a single bubble in a rectangular tank would have images characterized by a range term r_m (equal to twice the shortest distance between the real bubble and the wall); and a complex amplitude term $F_m=|F_m|e^{-j(k_mr_m-\vartheta_m)}$ which would depend on the complex reflection coefficient of the boundary in question. Then if the small-damping polytropic conditions of Sec. II B apply, the resonance condition occurs when

$$\begin{aligned} \frac{j\kappa p_0}{\omega_0 V}&\approx\frac{j\rho\omega}{4\pi R}+\frac{\rho\omega^2}{4\pi c}+\frac{\rho\omega}{4\pi}\sum_{m=2}^{\infty}\frac{|F_m|}{r_m}(\sin(kr_m-\vartheta_m)\\ &\quad +j\cos(kr_m-\vartheta_m)). \end{aligned} \tag{41}$$

Equating the imaginary parts gives the resonance frequency

$$\omega_0\approx\frac{(1/R)\sqrt{3\kappa p_0/\rho}}{\sqrt{1+\Sigma_{m=2}^{\infty}(R/r_m)|F_m|\cos(kr_m-\vartheta_m)}}, \tag{42}$$

which reduces to the Minnaert equation [Eq. (34)] when, in the free field, the summation term is zero.

The effect of neighboring bubbles and boundaries on radiation damping can also be calculated by this method. Assume that the radiation damping in free space is to be characterized by the dimensionless damping coefficient, $\delta_{\text{rad,free}}$, which is proportional to the real part of the total acoustic impedance presented to the bubble in free space, $\rho\omega^2/4\pi c=\rho\omega k/4\pi$. The ratio of the damping in reverberant conditions, $\delta_{\text{rad,reverb}}$, to that in free space, equals the ratio of the real parts of the respective total acoustic impedances presented to the bubble. Taking again the case of Sec. II A (a single bubble emitting into a rectangular tank) the ratio of the real component of Eq. (41) to the free-space value is

$$\frac{\delta_{\text{rad,reverb}}}{\delta_{\text{rad,free}}}=1+\sum_{m=2}^{\infty}\frac{|F_m|\sin(kr_m-\vartheta_m)}{kr_m}. \tag{43}$$

For solution of the tank case described in Sec. II A and Eqs. (42) and (43), the spatial distribution of the images is calculated geometrically, and the frequency-dependent complex reflection coefficient associated with each image is simply calculated from the number of reflections from the tank boundaries. The predicted quality factor for a bubble in reverberant conditions is then

$$Q = 1/\delta_{tot} = 1/(\delta_{rad,reverb} + \delta_{th} + \delta_{vis}), \quad (44)$$

where δ_{th} and δ_{vis} are found from the usual monochromatic formulations,[2] and where $\delta_{rad,reverb}$ is calculated by substituting into Eq. (43) the monochromatic value of $\delta_{rad,free}$, again calculated from literature.[2]

With reference to the comments at the start of this section, it should be noted that Eqs. (42) and (43) assume that the emission from the images is steady. If for example the source bubble emits an exponentially decaying sinusoid typical of injection, then the nonsteady nature of the returns introduces an error of order δ_{tot}^2.

D. Experimental measurements

The method used in this paper for measuring the bubble resonance and damping relies upon estimation of the impulse response of bubbles injected one at a time into a tank measuring 0.6 m×0.2 m×0.23 m deep internally, and having glass walls of 6 mm thickness. For the "passive" technique, this consisted of simply measuring the hydrophone signal detected following injection of the bubble through a needle. For the "active" technique, the hydrophone signal of interest is not that emitted by the bubble on injection. Rather, it is the signal scattered by the bubble some time later, when it is driven by band filtered white noise (1–25 kHz, generated using a Bruel and Kjaer Type 2032 dual channel signal analyzer). The bubbles examined in this paper have natural frequencies in the range 4–11 kHz. The bubble rises after injection, and is driven into oscillation by the pseudorandom driving field. Its buoyant passage through a 1 MHz beam triggers the data acquisition from the hydrophone. It is important to know the location of the bubble and hydrophone for comparison with theory. The active technique is particularly useful in measuring the resonance characteristics of the smaller bubbles, whose natural emissions after injection are of insufficient amplitude above the noise to obtain sufficient cycles for a precise measurement of their decay. The following describes how the scattered signal is estimated when the active technique is used.

The received signal at the measurement hydrophone, $y(t)$, in the active configuration, can be considered as the superposition of two components, i.e.,

$$y(t) = y_d(t) + y_s(t), \quad (45)$$

where $y_d(t)$ is the signal due to the direct field (i.e., the signal that is observed in the absence of a bubble), and $y_s(t)$ is the signal arising from the acoustic field generated by scattering from the bubble. In practice the magnitude of the direct field component is sufficient to corrupt measurements of quantities, such as quality factors, based on the raw data $y(t)$. If no bubble is present, then evidently the measured signal is solely due to the direct field component, $y_d(t)$.

Figure 1(a) illustrates a typical example of the spectrum of a signal received at a hydrophone when an active configuration is employed with a bubble being present. The spectrum of the electronic signal used to drive the projector (band limited Gaussian noise) is also shown. The resulting hydrophone signal contains contributions from the direct field and the scattered signal. The "N"-shaped feature at approximately 3 kHz is a result of bubble scattering.[27] The problems of exploiting this data are evident. The comparatively low level of the scattered signal relative to the direct field render the feature difficult to discern even in this relatively small frequency range (its peak is of a similar magnitude to the nonbubble feature at around 6 kHz); and estimation of the bubble quality factor from such a feature is prone to error (see the following). Our methodology aims to reduce the direct field contribution and allow accurate measurements to be made.

To estimate the scattered field we first make measurements in the *absence* of a bubble. A known band limited white noise signal, $x(t)$, is used as an input to the projector and the resulting hydrophone signal is measured. Using standard linear systems theory[28] we can construct an estimate of the system impulse response, $h_d(t)$, from these two measurements. Assuming that the modeling is successful then

$$y_d(t) = h(t) * x(t), \quad (46)$$

where an asterisk is used to denote linear convolution. The accuracy of the model can be assessed as a function of frequency by computing and examining the coherence function.[28]

A bubble is then introduced to the system. Once again a band limited white noise signal, $x(t)$, is used to drive the projector. From the driving signal an estimate of the direct field component of the hydrophone signal is constructed by convolving it with the estimated impulse response, $h(t)$, leading to an estimate of the scattered signal:

$$\hat{y}_s(t) = y(t) - h(t) * x(t). \quad (47)$$

Here $\hat{y}_s(t)$ is an estimate of the contribution of the bubble to the acoustic field. The results of applying this procedure to the data in Fig. 1(a) are shown in Fig. 1(b). The spectrum of the signal after the effect of the direct field has been subtracted shows a distinct peak close to 3 kHz, for which the ratio of center frequency to the bandwidth gives the bubble quality factor. Figure 1(b) illustrates the error that would have been introduced if one had erroneously assumed that Q could be obtained from the equivalent parameters associated with the 3 kHz peak in Fig. 1(a).

This model takes account of any shaping of the excitation spectrum that may occur as a result of a modal field within the tank. This having been removed, what remains is the effect of reverberant loading on the bubble resonance and damping.

III. RESULTS

Figure 2 shows the quality factor of the bubble as a function of its natural (for the "passive" measurements: ■,●) or resonance (for the "active" measurements: □,○,×) frequency. Results from tap, distilled, and newly acquired seawater are shown. The solid curve indicates the quality factor predicted by Devin's theory, which relates to free field conditions. The dashed line indicates the result predicted by Eq. (43), with the dotted lines on either side indicating the maximum and minimum values found by recalculating the prediction repeatedly, allowing the bubble position and the wall reflection coefficient to vary within the limits of uncer-

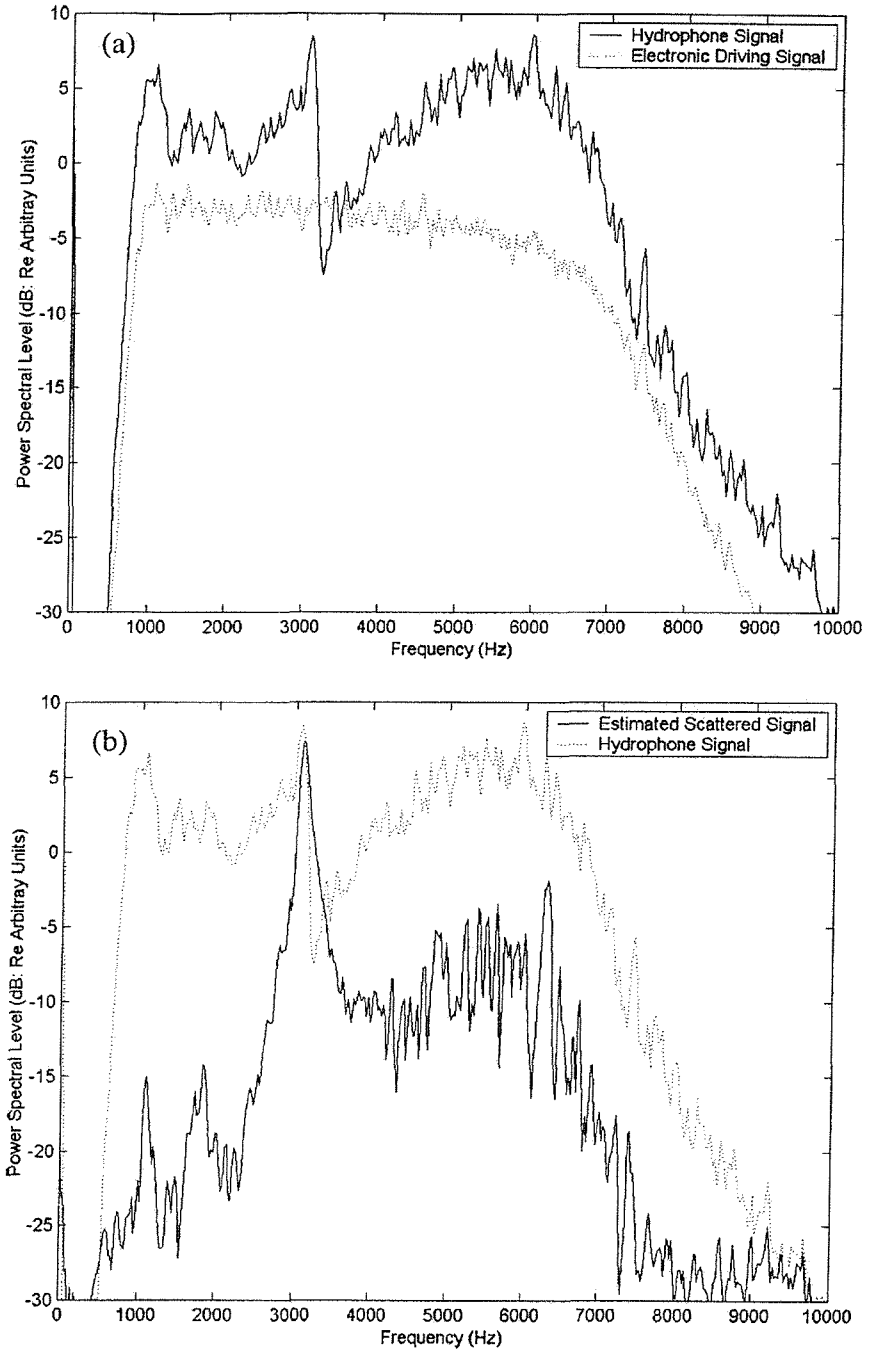

FIG. 1. (a) Spectra of driving signal and hydrophone signal. The driving signal in this example case consists of Gaussian noise, band limited to a frequency range of approximately 1–7 kHz (though 1–25 kHz was required for the data of Fig. 2). (b) Spectra of the hydrophone signal before and after the effect of the direct field has been removed.

tainty of each (the latter having a much smaller contribution that the former, the prediction being fairly robust within the allowed variation of reflection coefficient). For clarity, error bars are not shown (± 75 Hz; ± 1 in Q for $f<6$ kHz; ± 2 in Q for $6<f<9$ kHz; ± 4 in Q for $f>9$ kHz). The lack of passive data above 6 kHz reflects the signal-to-noise problem, described in Sec. II C, which makes the technique difficult for the smaller bubbles. The active technique is not limited in this way.

The discrepancy between observation and the prediction of Devin is less than the error associated with the observation for 26 of the 96 data points. There being negligible uncertainty on this scale in the uncertainty associated with the Devin curve, the conclusion is that Devin's theory is inappropriate for the reverberant conditions found in this typical test tank, in the frequency range most often studied in bubble acoustics. In contrast 76 of the 96 bubbles lie within one error of the theory presented in this paper. This comparison needs interpreting with some caution, as discussed in the following.

IV. DISCUSSION

Although the disagreement between measurement and Devin's theory indicates the need for a theory applicable to reverberant conditions, and while the authors have faith in

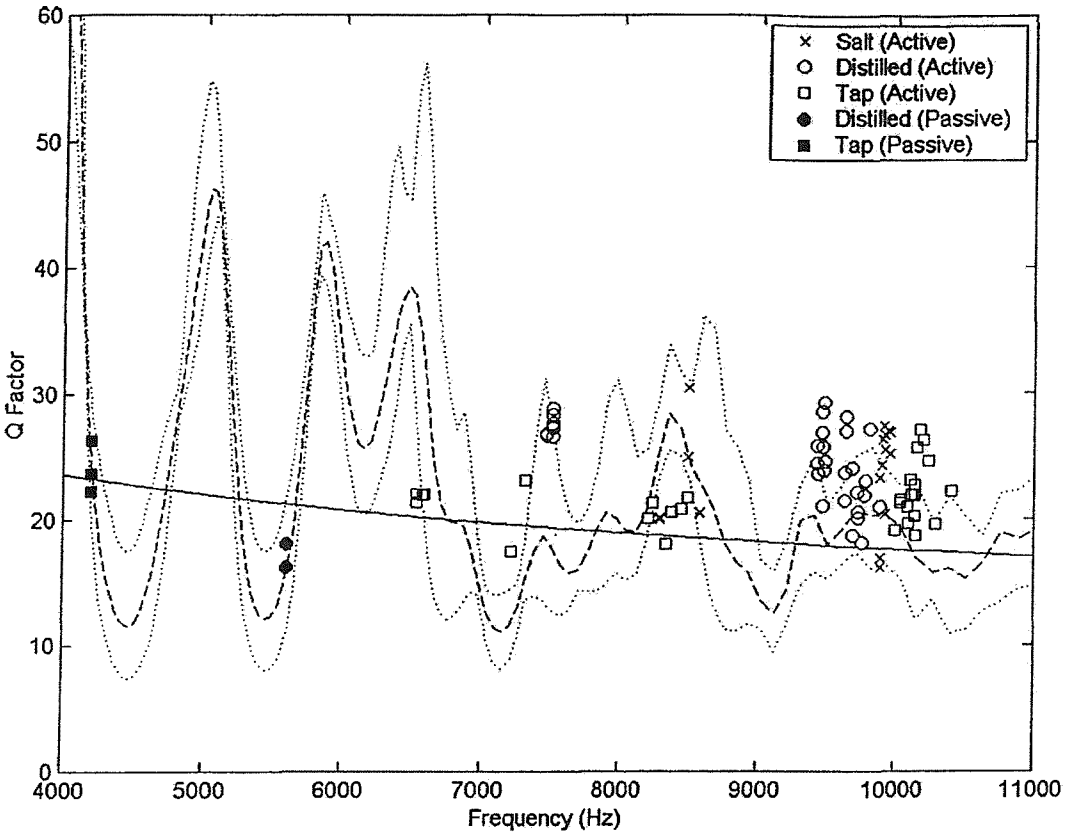

FIG. 2. Graph of the quality factor of the bubble as a function of its natural (for the "passive" measurements, ■, ●) or resonance (for the "active" measurements, □ ○ ×) frequency. Results from tap (■, □), distilled (●, ○) and newly-acquired seawater (×) are shown. For clarity, error bars are not shown (±75 Hz; ±1 in Q for $f<6$ kHz; ±2 in Q for $6<f<9$ kHz; ±4 in Q for $f>9$ kHz). The curves indicate predictions of the theory of Devin (—) and of this paper (---), either side of which is a dotted line indicating the limits of uncertainty in the latter.

the theories of Sec. II, implementation of that theory to calculate the modification to bubble resonance imparted by reverberant loading is not easy. Whereas calculation of the effect on resonance frequency[11] is possible by using Eq. (37), the effect on the damping is very sensitive to details of the reverberation. The resulting uncertainty allows a range of predicted values for Q at each frequency in Fig. 2, while the standard free-field theory predicts a single value. The sensitivity of the prediction to the reverberation parameters is of course greatest at the peaks and troughs in the plots, and hence the extreme predictions of $Q>40$ should be interpreted with caution. For the most part the reverberant theory suggests for this tank there will be deviations from free-field predictions of usually up to $Q\sim 60\%$, and these are observed. In addition the predicted sign of the deviation (which can be positive or negative depending on the frequency) is borne out in the data.

While the magnitude of the discrepancy is difficult to calculate precisely, the form for the quality factor of bubbles in this reverberant environment that is predicted by the method of images technique described in Sec. II C, agrees with the trends expected from the general theory of Sec. II A. Equation (7) predicts that at sufficiently high frequencies, the damping will tend to a smooth function following the "free-field" solution. This is a result of modal overlap. The prediction in Fig. 2 bears this out, although in the range considered the influence of distinct modes is evident. At the lower frequencies the calculation becomes difficult because of convergence problems [note that $|D|^2=(1-\nu_N^2)^2+(\eta_N\nu_N)^2$ in Eqs. (11) and (12) becomes very large when $k_0\to k_N$, then $\nu_N\to 1$]. Paradoxically this means that the effect of reverberation can be easier to calculate in small tanks than in larger ones. This is because the bubbles most often considered in test tanks have natural frequencies of the low kilohertz order (see the following). Therefore unless the tank is sufficiently vast and sufficiently damped that this range is higher than the Schroeder frequency, then to ignore reverberation the bubble natural frequency must be significantly less than that of the first tank mode[11] (depending on the losses, which are generally lowest for these low frequencies). In tanks of several meters on a side this in practice would likely occur only for bubbles resonant at O (10 Hz). Such bubbles would generally be much larger than those typically studied in a test tank. It is well-known that if the intention is to inject single bubbles into a tank for controlled tests, there is a range of bubble size outside of which this process becomes difficult. Bubbles of centimeter-size break up, and bubbles of less than around 200 μm tend to coalesce into larger bubbles at the nozzle.[29] Even exotic methods (e.g., manipulation of the surface tension or pressure head, vibration of the needle, etc.) can only expand this range to a

limited degree. Of course smaller bubbles can be produced by sparging, wave breaking,[30] etc., but these bubbles almost always comprise a subset of a population which includes larger bubbles giving significant natural emissions at roughly 1–10 kHz.

As this paper has shown, this may well be a problematic range: the frequencies may be insufficiently high to generate, via model overlap, the effectively "free-field" solution of Eq. (7); yet they may be so low that anechoic linings are insufficient to remove reverberation. For example, even with the free surface replaced by lining, the "anechoically" lined tank of Bjørnø and Kjeldgaard had a pressure amplitude reflection coefficient of ~0.3 at 10 kHz, the lowest frequency they measured. The actual performance of linings at the frequencies of interest is not always reported in bubble tests.

As an illustration of the problem, a preliminary attempt was made to use the results of Fig. 2 to confirm or counter the suggestion[31,32] that bubble damping may depend on salinity. That suggestion followed from a study of the injection of single bubbles into a tank having "acoustically transparent" walls. This smaller tank was suspended in a larger 2.5 $\times 3.6 \times 3.6$ m^3 water tank, where "the bottom and walls of the [larger] tank were lined with 82-cm high redwood wedges with 30 cm$\times$30 cm bases; these wedges have a large acoustic absorption."[33] Being cognizant that such statements depend on the frequency of interest, an investigation[33] was made to determine which modes could be excited in the largest tank at frequencies of less than 1 kHz, and identified ones at around 540 and 950 Hz.

It is well known that dissolved salt can affect *populations* of bubbles, those formed in salt water tend to be more numerous, particularly regarding the smallest bubbles, and less prone to coalesce than bubbles in fresh water.[34–39] When comparing wave breaking in fresh water with that in salt, it is one thing to attribute acoustic differences to changes in populations of bubbles which, as individuals, have unchanged acoustic properties. That is to say that, even though the collective effect may be affected by differences between the fresh and salt water bubble populations, the single-bubble acoustics is the same (although modifications may be necessary to surface tension and thermal damping terms, etc., as a result of the "dirty" nature of sea water[40]). It is quite another to suggest that the single-bubble dynamics might be different, which is one possible interpretation of the findings of the study[31] mentioned previously. In that, measurements were made of the logarithmic decrement of relatively large single bubbles (1.1–2.4 mm radius) injected into water having a salinity range of 0‰–35‰ (obtained using commercial salt[41]). Both the sound pressure level and the quality factor were observed to change with salinity, but no mechanism for such a single-bubble effect has been proposed. If such a single-bubble effect was robust (and not, as speculated in the following, a by-product of the reverberation), it would have major implications throughout ocean bubble acoustics, for example in measurements of the bubble population[42–46] and the response of bubbles to short acoustic pulses.[47–50]

Prior to the current paper, no account has been taken in test tanks of the effect of the reverberant field on the bubble damping. That two distinct modes at 540 and 950 Hz could be identified in the tank used in the earlier study[33] suggests that the data were taken in the frequency range (roughly 1–3 kHz) at which the effect of reverberation is most problematic, as discussed previously. Taking reverberation into account, the results of Fig. 2 are unable to confirm or deny the earlier proposition that salinity affects the damping of single bubbles: the seawater data ($\times$) show a similar measure of agreement with the prediction of reverberant theory that is exhibited by tap and distilled water. Hence the disagreement which is seen in this paper between the seawater data and the prediction of Devin can be attributed to reverberation. That is not to prove that reverberation was responsible for the earlier finding.[31,32] However the potential for reverberation to complicate the observation is clear. As an example, even small changes in frequency/sound speed can tune in or out of the effect of a given mode, leading to significant changes in Q (Fig. 2). While varying the salinity will change the sound speed in a predictable manner[51] in single-bubble tests, when *populations* are entrained there is a second, and often greater effect. If changes in salinity affect the population of bubbles entrained, for example by a breaking wave, then varying the salinity will indirectly affect both the amount of reverberation and (through the effect of the bubble population on the sound speed) change the modal frequencies of the tank. Figure 2 suggests that mode frequency changes of O (1%) can cause changes in Q of O (10%). Therefore it is strongly recommended that reverberation be considered in tank tests, and other reverberant environments.[52]

The importance of reverberation on bubble resonances should not be underestimated, and its effect cannot be easily dismissed. It is not confined only to frequencies of tank modes: apart from the frequency region well below the first mode,[11] or well above the Schroeder frequency, the effect is potentially very problematic for three reasons.

(1) Calculation of its influence on radiation damping in particular (and, to a lesser extent, on the relationship between the bubble radius and natural frequency) requires detailed knowledge of the reverberation.
(2) Small changes in damping can have major effects close to bubble resonance, and discrepancies from the free field predictions of up to ~60% are here observed.
(3) True free-field conditions are rarely found in bubble acoustics, with even the "open" ocean containing a free-surface, and scatterers which include other bubbles; and "anechoic" fittings can give significant reflections at the resonant frequencies of the larger bubbles.

Finally it should be recalled that the ubiquitous assumption of free-field conditions extends beyond bubble entrainment emissions and linear scattering, to the nonlinear models of bubble motion (such as the Rayleigh–Plesset, Herring–Keller, and Gilmore-Akulichev formulations). Certain scenarios exploit modal fields, such as in measurement of the bubble size distribution.[53–55] Of particular note is the common practice of levitating bubbles in a modal sound field for measurements of, for example, sonoluminescence,[56] rectified diffusion,[57] or (with the comment of this paper particularly in mind) resonance and damping.[58,59] In such circumstances the

effect and validity of the free-field assumption must be assessed.

ACKNOWLEDGMENTS

The authors would like to acknowledge the support of QINETIQ, Bincleaves, UK. T.G.L. is grateful to the Royal Society Leverhulme Trust, and the EPSRC (GR/M38094) for support.

[1] M. Minnaert, "On musical air-bubbles and sounds of running water," Philos. Mag. **16**, 235–248 (1933).
[2] C. Devin, Jr., "Survey of thermal, radiation, and viscous damping of pulsating air bubbles in water," J. Acoust. Soc. Am. **31**, 1654 (1959).
[3] R. His, M. Tay, D. Bukur, and G. Tatterson, "Sound spectra of gas dispersion in an agitated tank," Chem. Eng. J. **31**, 153–161 (1985).
[4] L. S. De More, W. F. Pafford, and G. B. Tatterson, "Cavity sound resonance and mass transfer in aerated agitated tank," AIChE J. **34**, 1922–1926 (1988).
[5] J. W. R. Boyd and J. Varley, "Sound measurement as a means of gas-bubble sizing in aerated agitated tank," AIChE J. **44**, 1731–1739 (1998).
[6] A. B. Pandit, J. Varley, R. B. Thorpe, and J. F. Davidson, "Measurement of bubble size distribution: An acoustic technique," Chem. Eng. Sci. **47**, 1079–1089 (1992).
[7] R. Manasseh, R. F. LaFontaine, J. Davy, I. Shepherd, and Y-G Zhu, "Passive acoustic bubble sizing in sparged systems," Exp. Fluids (in press).
[8] R. Manasseh, A. Bui, J. Sandercock, and A. Ooi, "Sound emission processes on bubble detachment," Proceedings of the 14th Australasian Fluid Mechanics Conference (in press).
[9] T. A. Sutter, G. L. Morrison, and G. B. Tatterson, "Sound spectra in an aerated agitated tank," AIChE J. **33**, 668–671 (1987).
[10] W. R. Usry, G. L. Morrison, and G. B. Tatterson, "On the interrelationship between mass transfer and sound spectra in an aerated agitated tank," Chem. Eng. Sci. **42**, 1856–1859 (1987).
[11] T. G. Leighton, D. G. Ramble, A. D. Phelps, C. L. Morfey, and P. P. Harris, "Acoustic detection of gas bubbles in a pipe," Acta Acust. **84**, 801–814 (1998).
[12] H. Pfriem, "Zur thermischen dämpfung in kugelsymmetrisch schwingenden gasblasen," Akust. Zh. **5**, 202–207 (1940).
[13] Z. Saneyoshi, Electro-technical Journal (Japan) **5**, 49 (1941).
[14] A. I. Eller, "Damping constants of pulsating bubbles," J. Acoust. Soc. Am. **47**, 1469–1470 (1970).
[15] A. Prosperetti, "Thermal effects and damping mechanisms in the forced radial oscillations of gas bubbles in liquids," J. Acoust. Soc. Am. **61**, 17–27 (1977).
[16] R. I. Nigmatulin and N. S. Khabeev, "Heat exchange between a gas bubble and a liquid," Fluid Dyn. **9**, 759–764 (1974).
[17] R. I. Nigmatulin and N. S. Khabeev, "Dynamics of vapour-gas bubbles," Fluid Dyn. **12**, 867–871 (1977).
[18] F. B. Nagiev and N. S. Khabeev, "Heat-transfer and phase transition effects associated with oscillations of vapour-gas bubbles," Sov. Phys. Acoust. **25**, 148–152 (1979).
[19] R. I. Nigmatulin, N. S. Khabeev, and F. B. Nagiev, "Dynamics, heat and mass transfer of vapour-gas bubbles in a liquid," Int. J. Heat Mass Transf. **24**, 1033–1044 (1981).
[20] A. Prosperetti, L. A. Crum, and K. W. Commander, "Nonlinear bubble dynamics," J. Acoust. Soc. Am. **83**, 502–514 (1988).
[21] A. Prosperetti, "The thermal behaviour of oscillating gas bubbles," J. Fluid Mech. **222**, 587–616 (1991).
[22] P. M. Morse and K. U. Ingard, *Theoretical Acoustics* (Princeton University Press, Princeton, 1986), 555 pp.
[23] This mode, if it exists, is labeled $N=0$. It corresponds to a uniform pressure $p_0(\mathbf{x})=\rho c^2 U/j\omega V$. Its contribution in the limit $k_0\to 0$ (i.e., $\omega\to 0$) would be infinite. Since we are dealing with a tank containing a free surface, there is no $N=0$ mode.
[24] This approximation requires $K_N R \ll 1$, and so sets an upper limit to K_N, or equivalently an upper limit to N in the summation. However the limitation becomes important for Z, only if $k_0 R$ is not much less than unity, and therefore will not apply to this paper because the condition $k_0 R \ll 1$ was stated at the outset.
[25] T. G. Leighton, *The Acoustic Bubble* (Academic Press, New York, 1994), Sec. 3.2.1c(iii), 3.3.1(b), 3.5.2, 3.7.3.
[26] M. Rowan-Robinson, *Cosmology*, 2nd ed. (Oxford University Press, Oxford, 1981), p. 56.
[27] T. G. Leighton, A. D. Phelps, D. G. Ramble, and D. A. Sharpe, "Comparison of the abilities of eight acoustic techniques to detect and size a single bubble," Ultrasonics **34**, 661–667 (1996).
[28] J. K. Hammond, "Fundamentals of signal processing," in *Fundamentals of Noise and Vibration*, edited by F. J. Fahy and J. Walker (E&FN Spon, London, 1998), Chap. 6, pp. 311–370.
[29] T. G. Leighton, K. J. Fagan, and J. E. Field, "Acoustic and photographic studies of injected bubbles," Eur. J. Phys. **12**, 77–85 (1991).
[30] A. R. Kolaini, L. A. Crum, and R. A. Roy, "Bubble production by capillary-gravity waves," J. Acoust. Soc. Am. **95**, 1913–1921 (1994).
[31] A. R. Kolaini, "Effects of salt on bubble radiation," in *Natural Physical Processes Associated with Sea Surface Sound*, edited by T. G. Leighton (University of Southampton, Southampton, 1997), pp. 240–249.
[32] A. R. Kolaini, "Sound radiation by various types of laboratory breaking waves in fresh and salt water," J. Acoust. Soc. Am. **103**, 300–308 (1998).
[33] A. R. Kolaini and L. A. Crum, "Observations of underwater sound from laboratory breaking waves and the implications concerning ambient noise in the ocean," J. Acoust. Soc. Am. **96**, 1755–1765 (1994).
[34] J. A. Kitchener, "Foams and free liquid film," *Recent Progress in Surface Science* (Academic, New York, 1964), Vol. I, pp. 51–93.
[35] E. C. Monahan and C. R. Zeitlow, "Laboratory comparisons of fresh-water and salt-water whitecap," J. Geophys. Res. **74**, 6961–6966 (1969).
[36] J. C. Scott, "The role of salt in whitecap persistence," Deep-Sea Res. Oceanogr. Abstr. **22**, 653–657 (1975).
[37] S. A. Thorpe, "The role of bubbles produced by breaking waves in supersaturating the near-surface ocean mixing layer with oxygen," Ann. Geophys. (Gauthier-Villars, 1983–1985) **2**, 53–56 (1984).
[38] L. Memery and L. Merlivat, "Modeling of gas flux through bubbles at the air-water interface," Tellus, Ser. B **37B**, 272–285 (1985).
[39] C. Pounder, "Sodium chloride and water temperature effects on bubbles," in *Oceanic Whitecap and Their Role in Air-Sea Exchange Processes*, edited by E. C. Monahan and G. Mac Niocaill (Reidel, Dordrecht, 1986).
[40] W. M. Carey, J. W. Fitzgerald, E. C. Monohan, and Q. Wang, "Measurement of the sound produced by a tipping trough with fresh and salt water," J. Acoust. Soc. Am. **93**, 3178–3192 (1993).
[41] A. R. Kolaini (personal communication).
[42] N. Breitz and H. Medwin, "Instrumentation for *in situ* acoustical measurements of bubble spectra under breaking waves," J. Acoust. Soc. Am. **86**, 739–743 (1989).
[43] D. M. Farmer and S. Vagle, "Waveguide propagation of ambient sound in the ocean-surface bubble layer," J. Acoust. Soc. Am. **86**, 1897–1908 (1989).
[44] A. D. Phelps, D. G. Ramble, and T. G. Leighton, "The use of a combination frequency technique to measure the surf zone bubble population," J. Acoust. Soc. Am. **101**, 1981–1989 (1997).
[45] W. K. Melville, E. Terrill, and F. Veron, "Bubbles and turbulence under breaking waves," in *Natural Physical Processes Associated with Sea Surface Sound*, edited by T. G. Leighton (University of Southampton, Southampton, 1997), pp. 135–146.
[46] I. N. Didenkulov, S. I. Muyakshin, and D. A. Selivanovsky, "Bubble counting in the subsurface ocean layer," in *Acoustical Oceanography*, Proceedings of the Institute of Acoustics, Vol. 23 Part 2, 2001, edited by T. G. Leighton, G. J. Heald, H. Griffiths, and G. Griffiths (Institute of Acoustics, 2001), pp. 220–226.
[47] V. A. Akulichev, V. A. Bulanov, and S. A. Klenin, "Acoustic sensing of gas bubbles in the ocean medium," Sov. Phys. Acoust. **32**, 177–180 (1986).
[48] J. L. Leander, "A note on transient underwater bubble sound," J. Acoust. Soc. Am. **103**, 1205–1208 (1998).
[49] J. W. L. Clarke and T. G. Leighton, "A method for estimating time-dependent acoustic cross-sections of bubbles and bubble clouds prior to the steady state," J. Acoust. Soc. Am. **107**, 1922–1929 (2000).
[50] S. D. Meers, T. G. Leighton, J. W. L. Clarke, G. J. Heald, H. A. Dumbrell, and P. R. White, "The importance of bubble ring-up and pulse length in estimating the bubble distribution from propagation measurements," in Ref. 46, pp. 235–241.
[51] J. L. Spiesberger and K. Metzger, "New estimates of sound speed in water," J. Acoust. Soc. Am. **89**, 1697–1700 (1991).
[52] Equation (43) was used to correct for reverberation in the surf zone by T. G. Leighton, "Surf zone bubble spectrometry: The role of the acoustic cross section," J. Acoust. Soc. Am. **110**, 2694 (2001).
[53] N. Breitz and H. Medwin, "Instrumentation for *in situ* acoustical measure-

ments of bubble spectra under breaking waves," J. Acoust. Soc. Am. **86**, 739–743 (1989).
[54]M. Y. Su, D. Todoroff, and J. Cartmill, "Laboratory comparisons of acoustical and optical sensors for microbubble measurement," J. Atmos. Ocean. Technol. **11**, 170–181 (1998).
[55]D. M. Farmer, S. Vagle, and A. D. Booth, "A free-flooding acoustical resonator for measurement of bubble size distributions," J. Atmos. Ocean. Technol. **15**, 1132–1146 (1998).
[56]D. F. Gaitan and L. A. Crum, "Observation of sonoluminescence from a single cavitation bubble in a water/glycerine mixture," in *Frontiers of Nonlinear Acoustics, 12th ISNA*, edited by M. F. Hamilton and D. T. Blackstock (Elsevier, New York, 1990), p. 459.
[57]A. I. Eller, "Growth of bubbles by rectified diffusion," J. Acoust. Soc. Am. **52**, 1447–1449 (1972).
[58]L. A. Crum, "The polytropic exponent of gas contained within air bubbles pulsating in a liquid," J. Acoust. Soc. Am. **73**, 116–120 (1983).
[59]L. A. Crum and A. Prosperetti, "Nonlinear oscillations of gas bubbles in liquids: An interpretation of some experimental results," J. Acoust. Soc. Am. **73**, 121–127 (1983).

References

[1] Thorpe S A, On the clouds of bubbles formed by breaking wind-waves in deep water, and their role in air-sea gas transfer, J Fluid Mech, 114, 237-250, (1982)
[2] Medwin H, Clay S C, Fundamentals of Acoustical Oceanography, Ch. 8, Academic Press, (1998)
[3] Melville W K, Terrill E, Veron F, Bubbles and turbulence under breaking waves, Natural Physical Processes Associated with Sea Surface Sound, University of Southampton (T. G. Leighton, editor), 135-145 (1997)
[4] Minnaert M, On musical air-bubbles and sounds of running water, Phil Mag, 16, 235-248 (1933)
[5] Devin C Jr, Survey of thermal, radiation and viscous damping of pulsating air bubbles in water, J Acoust Soc Am, 31, 1654-1667 (1959)
[6] Eller A I, Damping Constants of pulsating bubbles, J Acoust Soc Am, 47, 1469-1470 (1970)
[7] Thorpe S A, Measurements with an automatically recording inverted echo-sounder; ARIES and the bubble clouds, J. Phys. Ocean. 16, 1462-1478 (1986)
[8] Monahan E C, Lu N Q, Acoustically relevant bubble assemblages and their dependence on meteorological parameters, IEEE J. Ocean Eng. 15, 340-345 (1990)
[9] Medwin H, In-situ acoustic measurements of bubble populations in coastal waters, J. Geophys. Res. 75, 599-611 (1970)
[10] Medwin H, In-situ measurements of microbubbles at sea, J. Geophys. Res. 82, 971-976 (1977)
[11] Phelps A D, Leighton T G, Oceanic bubble population measurements using a buoy-deployed combination frequency technique, IEEE J. Oc. Eng. 23(4) (1998)
[12] Leighton T G, The Acoustic Bubble, Ch 3, Academic Press, (1994)
[13] Monahan E C, Kin J P, Wilson M B, Woolf D K, Oceanic whitecaps and the marine microlayer spanning the boundary separating the sub-surface bubble clouds from the aerosol laden marine atmosphere, Whitecap Report 3, University of Connecticut, Avery Point, 1-108 (1987)
[14] Bezzabotnov V Z, Some results on the changes of the structure of sea foam formations in the field, Fiz Atmosfery Okeana 21, 101-104 (1985)
[15] Leighton T G, The Acoustic Bubble, Section 3.2.1, Academic Press (1994)
[16] Kinsler L E, Frey A R, Coppens A B, Sanders J V, Fundamentals of Acoustics 3rd Edition, Ch 7, John Wiley & Sons (1982)
[17] Leighton T G, The Acoustic Bubble, Section 3.4.2b, Academic Press (1994)
[18] Mallock A, The damping of sound by frothy liquids, Proc. Roy. Soc. A84, 391-395, (1910)
[19] Leighton T G, The Acoustic Bubble, Section 3.4.2, Academic Press (1994)
[20] Van Santen G W, Introduction to a study of Mechanical Vibration 2nd Edition, Cleaver Hume Press (1958)
[21] Leighton T G, The Acoustic Bubble, Section 3.2.1c, Academic Press (1994)
[22] Leighton T G, The Acoustic Bubble, Section 3.4.2b, Academic Press (1994)
[23] Leighton T G, The Acoustic Bubble, Section 4.1.2d, Academic Press (1994)
[24] Kinsler L E, Frey A R, Coppens A B, Sanders J V, Fundamentals of Acoustics 3rd Edition, Ch 1, John Wiley & Sons, (1982)

[25] Leighton T G, The Acoustic Bubble, Ch 4, Academic Press (1994)
[26] Prosperetti A, Lezzi A, Bubble dynamics in a compressible liquid. Part 1 first order theory, J. Fluid Mech. 168, 457-478, (1986)
[27] Keller J B, Miksis M, Bubble oscillations of large amplitude, J. Acoust. Soc. Am. 68, 628-633, (1980)
[28] Phelps A D, Ramble D G, Leighton T G, The use of a combination frequency technique to measure the surf zone bubble population J. Acoust. Soc. Am., 101, 1981-1989, (1997)
[29] Neppiras E A, Acoustic cavitation, Physics Report, 61, 159-251 (1980)
[30] Medwin H, Clay S C, Fundamentals of Acoustical Oceanography, Ch. 7, Academic Press, (1998)
[31] Medwin H, Clay S C, Fundamentals of Acoustical Oceanography, Sec. 8.3.2 , Academic Press, (1998)
[32] Kinsler L E, Frey A R, Coppens A B, Sanders J V, Fundamentals of Acoustics 3rd Edition, Ch 15, John Wiley & Sons (1982)
[33] Knudsen V O, Alford R S, Emling J W, Underwater Ambient Noise, J. Mar. Res. 7,410 (1948)
[34] Anderson A L, Gruber G J, Ambient Noise Measurements at 30 , 90 and 150 kHz in Five Ports, J. Acoust. Soc. Am. 49, 928-930 (1971)
[35] Kinsler L E, Frey A R, Coppens A B, Sanders J V, Fundamentals of Acoustics 3rd Edition, Ch 11, John Wiley & Sons (1982)
[36] Farmer D M, Vagle S, Waveguide propagation of ambient sounds in the ocean-surface bubble layer, J. Acoust. Soc. Am. 86, 1897-1908 (1989)
[37] Buckingham M J, On acoustic transmission in ocean-surface waveguides, Phil. Trans. Roy. Soc. A335, 513-555 (1990)
[38] Fisher F H, Simmons V P, Sound absorption in sea water, J. Acoust. Soc. Am. 62, 558-564 (1977)
[39] Urick R J, Principle of Underwater Sound, Ch 2, McGraw-Hill (1983)
[40] Akulichev V A, Bulanov V A , Klenin S A, Acoustic sensing of gas bubbles in the ocean medium, Sov. Phys. Acoust. 32(3), 177-180 (1986)
[41] Leighton T G, The Acoustic Bubble, Section 3.8.2ci, 274, Academic Press (1994)
[42] Suiter H R, Pulse length effects on the transmissivity of bubbly water, J. Acoust. Soc. Am. 91, 1383-1387, (1992)
[43] Pace N G, Cowley A, Campbell A M, Short pulse acoustic excitation of microbubbles, J. Acoust. Soc. Am. 102, 1474-1479, (1997)
[44] Prosperetti A, Thermal effects and damping mechanisms in the forced radial oscillations of bubbles in liquids, J. Acoust. Soc. Am. 61, 17-27 (1977)
[45] Herring C, Theory of the pulsation of the gas bubble produced by an underwater explosion, OSRD, Rep. No. 236 (1941)
[46] Forsythe G E, Malcolm M A, Moler C B, Computer Methods for Mathematical Computations, Prentice-Hall (1977)
[47] Nigmatulin R I, Khabeev N S, Nagiev F B, Dynamics, heat and mass transfer of vapour-gas bubbles in a liquid, Int. J. Heat Mass Transfer, 24, 1033-1044 (1981)
[48] Prosperetti A, Hao Y, Modelling of spherical gas bubble oscillations and sonoluminescence, Phil. Trans. R. Soc. Lond. A, 357, 203-223 (1999)
[49] Vokurka K, On Rayleigh's model of a freely oscillating bubble. I. Basic relations, Czech J. Phys. B35, 28-40 (1985)

[50] Leighton T G, The Acoustic Bubble, Section 4.1.2b, 293, Academic Press (1994)
[51] Terrill E J, Lada G, Melville W K, Surf zone bubble populations, Proceedings Acoustical Oceanography, 23 (2), Institute of Acoustics (2001)
[52] Medwin H, In-situ acoustic measurements of bubble populations in coastal waters, J. Geophys. Res. 75, 599-611 (1970)
[53] Medwin H, In-situ measurements of microbubbles at sea, J. Geophys. Res. 82, 971-976 (1977)
[54] Phelps A D, Ramble D G, Leighton T G, The use of a combination frequency technique to measure the surf zone bubble population J. Acoust. Soc. Am., 101, 1981-1989, (1997)
[55] Phelps A D, Leighton T G, Oceanic bubble population measurements using a buoy-deployed combination frequency technique, IEEE J. Oc. Eng. 23(4) (1998)
[56] Clarke J W L, Leighton T G, A method for estimating time-dependent acoustic cross-sections , J. Acoust. Soc. Am. 107(4) (2000)
of bubbles and bubble clouds prior to the steady state
[57] Longuet-Higgins M S, Kerman B R, Lunde K, The release of air bubbles from an underwater nozzle J. Fluid Mech. **230**, 365-390 (1991)
[58] Clift R, Grace J R, Weber M E, Bubbles drops and particles, Academic Press, 321-339 (1978)
[59] Roy R A, Carey W M, Acoustic scattering from bubble clouds, Natural Physical Processes Associated with Sea Surface Sound, University of Southampton (T. G. Leighton, editor), 221-231 (1997)
[60] Suiter H R, Pulse length effects on the transmissivity of bubbly water, J. Acoust. Soc. Am. **91**, 1383-1387, (1992)
[61] Kozhevnikova I N, Bjorno L, Experimental study of acoustical emission from bubble cloud excitation, Ultrasonics, **30 (1)**, 21-25 (1992)
[62] Muncaster R, A-level Physics 3rd edition, Ch 46, Stanley Thornes Ltd. (1989)
[63] Kolaini A R, Effects of salt on bubble radiation, Natural Physical Processes Associated with Sea Surface Sound, University of Southampton (T. G. Leighton, editor), 171-178 (1997)
[64] Dumbrell H A, Comparison of Excess Attenuation and Backscatter Measurements of Ship Wakes, Natural Physical Processes Associated with Sea Surface Sound, University of Southampton (T. G. Leighton, editor), 171-178 (1997)
[65] Hydrophone Type8103 Instruction Manual, Bruel & Kjaer (1986)
[66] Hydrophone Type8103 Instruction Manual, Bruel & Kjaer (1986)
[67] Charge Amplifier Type 2635 Instruction Manual, Bruel & Kjaer (1986)
[68] Fisher F H, Simmons V P, Sound absorption in sea water, J. Acoust. Soc. Am. 62, 558-564 (1977)
[69] Technical Documentation, Hydrophones Type 8103, 8104, 8105, 8106. Bruel & Kjaer Revised 1992
[70] Commander K W, McDonald R J, Finite element solution of the inverse problem in bubble swarm acoustics, J. Acoust. Soc. Am. 89, (1991)
[71] Leighton T G, The Acoustic Bubble, Section 3.8.1, Academic Press (1994)
[72] Farmer D M, Vagle S, Bubble measurements using a resonator system, in Natural Physical Processes Associated with Sea Surface Sound, T G Leighton Ed. Institute of Sound and Vibration Research: University of Southampton, 155-162 (1997)
[73] Leighton T G, Meers S D, Simpson M D, Clarke J W L, Yim G T, Birkin P R, Watson Y, White P R, Heald G J, Dumbrell H A, Culver R L, and Richards S D, The

Hurst Spit experiment: The characterization of bubbles in the surf zone using multiple acoustic techniques, *Acoustical Oceanography, Proceedings of the Institute of Acoustics Vol. 23 Part 2, 2001,* T G Leighton, G J Heald , H Griffiths and G Griffiths, (eds.), Institute of Acoustics, pp. 227-234.
[74] Thorpe S A, The horizontal structure and distribution of bubble clouds, Sea Surface Sound (Kerman B R ed.) Kluwer Boston, 173-183 (1988)
[75] Galvin C J, Wave breaking in shallow water. Waves on beaches (Meyer R R ed.) Academic Press, New York, 413-456 (1972)
[76] Longuet-Higgins M S, Bubble noise spectra, J Acoust Soc Am, 87(2), 652-661 (1990)
[77] Foldy L L, The multiple scattering of waves, Phys. Rev. 67, 107-119 (1945)
[78] van Wijngaarden L, On equations of motion for mixtures of liquid and gas bubbles, J. Fluid. Mech. 33, 465-474 (1968)
[79] Catflisch R E, Miksis M J, Papanicolaou G C, Ting L, Effective equations for wave propagation in bubbly liquids, J. Fluid. Mech. 153, 259-273 (1985)
[80] Commander K W & Prosperetti A, Linear pressure waves in bubbly liquids: Comparison between theory and experiments, J. Acoust. Soc. Am. 85, 732-746 (1989)
[81] Leighton T G, The Acoustic Bubble, Academic Press 295-298 (1994)
[82] Carstensen E L & Foldy L L, Propagation of sound through a liquid containing bubbles, J. Acoust. Soc. Am. 19, 481-501 (1947)
[83] Feuillade C, The attenuation and dispersion of sound in water containing multiply interacting bubbles, J. Acoust. Soc. Am. 99, 3412-3430 (1996)
[84] Zhen Ye, Comments on " The attenuation and dispersion of sound in water containing multiply interacting bubbles", J. Acoust. Soc. Am. 102, 12391241 (1997)
[85] Feuillade C, Response to "Comments on ' The attenuation and dispersion of sound in water containing multiply interacting bubbles'", J. Acoust. Soc. Am. 102, 1242-1245 (1997)
[86] Feuillade C, Scattering from collective model of air bubbles in water and the physical mechanism of superresonances, J. Acoust. Soc. Am. 98, 1178-1190 (1995)
[87] Zhen Ye, Acoustic dispersion and attenuation relations in bubbly mixture, J. Acoust. Soc. Am. 98, 1629-1636 (1995)
[88] Henyey F S, Corrections to Foldy's effective medium theory for propagation in bubble clouds and other collections of very small scatterers, J. Acoust. Soc. Am. 105, 2149-2154 (1999)
[89] Boyle S P, Reverberation Characteristics of the A B Wood Underwater Acoustics Laboratory, ISVR Technical Memorandum No 714, University of Southampton, 1992
[90] Pierce A D, Acoustics: An Introduction to its Physical Principles and Applications, McGraw-Hill, New York, 1981 (294.)
[91] Schroeder M R, New Method of Measuring Reverberation Time, J. Acoust. Soc. Am., v. 37 (3), 409-12 (1965)
[92] Technical Documentation, Hydrophones Type 8103, 8104, 8105, 8106. Bruel & Kjaer Revised 1992